STUDY OF STRUCTURAL, ELECTRICAL AND OPTICAL PROPERTIES OF LEAD-FREE $(Bi_{0.5}Na_{0.5})TiO_3$ BASED CERAMIC SYSTEMS

A THESIS SUBMITTED TO THE DEPARTMENT OF PHYSICS

IN CONFORMITY WITH THE REQUREMENTS FOR THE

DEGREE OF DOCTOR OF PHILOSOPHY

By

Bishwanath Parija

(Roll No: 50710004)

Under the guidance of

Prof. S. Panigrahi

DEPARTMENT OF PHYSICS

NATIONAL INSTITUTE OF TECHNOLOGY

ROURKELA, ORISSA-INDIA-769008

JUNE – 2012

DEDICATED

TO

MY BELOVED PARENTS

DECLARATION

I hereby declare that the thesis entitled "**STUDY OF STRUCTURAL, ELECTRICAL AND OPTICAL PROPERTIES OF LEAD-FREE $(Bi_{0.5}Na_{0.5})TiO_3$ BASED CERAMIC SYSTEMS**" which is being submitted by me to National Institute of Technology for the award of degree of **Doctor of Philosophy** is original and authentic work conducted by me in the Department of Physics, National Institute of Technology, Rourkela under the supervision of **Prof. S. Panigrahi**, Department of Physics, National Institute of Technology, Rourkela. No part or full form of this thesis work has been submitted elsewhere for a similar or any other degree.

Date: **Bishwanath Parija**

CERTIFICATE

This is to certify that the thesis entitled "**STUDY OF STRUCTURAL, ELECTRICAL AND OPTICAL PROPERTIES OF LEAD-FREE $(Bi_{0.5}Na_{0.5})TiO_3$ BASED CERAMIC SYSTEMS**" submitted by **Bishwanath Parija** to the National Institute of Technology, Rourkela for the award of the degree of Doctor of Philosophy is a bonafide record of research work carried out by him under my supervision. In my opinion, the work fulfils the requirements for which it is being submitted. The contents of the thesis, in full or in parts, have not been submitted to any other Institute or University for the award of any degree or diploma.

Signature of Supervisor
Prof. S. Panigrahi,
Department of Physics,
National Institute of Technology,
Rourkela-769008, India

LIST OF CONTENTS

ACKNOWLEDGEMENTS

The five and half years, I have spent at National Institute of Technology, Rourkela given me a source of most precious experience in my life. I take the opportunity to acknowledge all those who directly or indirectly helped me throughout this difficult journey.

Foremost, I would like to express my deep sense of gratitude to **Prof** (**Dr.) S.Panigrahi** for his guidance, lively discussion, constant encouragement and expert advice, constructive and honest criticism. I am greatly indebted to him for providing me excellent freedom to work on what I was interested in. He is excellent mentor and very supportive throughout the work.

I must acknowledge **Prof.** (**Dr**.) **S. K. Sarangi**, Director, National institute of Technology, Rourkela for providing me a platform to carry out this research.

I extended my heart-felt thanks to **Dr. T.P.Sinha (**BOSE Institute Calcutta**)** for their wholehearted suggestion and cooperation to carry out dielectric measurements. Also extended my heart-felt thanks **to Dr. S. Sarangi, Dr. B. Mallick** (IOP, BBSR) and **Dr. P. K. Sahoo** (NISER, BBSR), for their wholehearted cooperation to carry out Raman and UV data measurements.

I sincerely thank to **Dr. L.S.Cavalcante**, Universidade Federal de S˜ao Carlos, Brazil and **Dr. Manoranjan Kar** (IIT, Patna) for their wholehearted guidance for carryout the XRD Rietvald Refinement.

I also would like to express my gratitude to the rest of my doctoral scrutiny committee members: **Dr.D.Behera, Dr.S.K.Jena, Dr.B.C.Roy** for their invaluable, insightful comments and suggestions that improved the quality of this work.

I am extremely thankful to all the supporting and technical staff of the Department of Physics, Department of Materials and Metallurgical Engineering and Department of Ceramic Engineering for their helps and when required without which I have been in troubled waters.

I extended my heart-felt thanks to **Dr. Pawban Kumar** (NIT, Rourkela), for his wholehearted co-operation carry out data to study the eletromechanical properties.

I would also like to acknowledge the contribution of my friends and colleagues. **Dr. S.K.Rout and Dr. T. Badpanda** deserve special thanks for their timely help and cooperation during this study.

I am thankful to **V.Senthil**, **Subrat**, **Ganesh**, **Prakash**, **Niranjan**, **Naresh** and **Rakesh** for their valuable co-operation and suggestion at every step of my research work.

Finally, I owe a deep sense of indebtedness to my beloved parents **Mr. Gagan Parija** and **Mrs. Basanti Parija** for their affection, wholehearted, untiring and immeasurable support at every stage of my life. I am gratefully indepted to my friends, relatives and colleagues**,** for their unstinted moral support, encouragement and wishes throughout the course of the work. At the end I thankful to my wife **Jyotsna and my son Bishal,** best friend and soul-mate, for their true unconditional love, in my good and bad times.

Bishwanath Parija

ABSTRACT

In view of the processing and environmental issues pertaining to lead-based ferroelectric materials, investigations on lead-free ferroelectrics are carried intensively in recent years. These materials are interesting because they are flexible with respect to structural changes and functional properties. This study focuses on a lead-free, high temperature ceramic capacitor material having the base composition of $(Bi_{0.5}Na_{0.5})TiO_3$. The goal is to modify this base composition to create a material that has diffuse-phase-like dielectric behaviour, while maintaining its inherently good high temperature dielectric properties. This will alleviate some circuit design problems, and will create a component that is less susceptible to drastic environmental changes. Areas of interest include aerospace and weapons system applications, motor control, geological down-hole-drilling equipment and many more. An extensive experimental compositional matrix, along with theoretical modelling, has been investigated to modify the base material to attain the goals set forth.

$(Bi_{0.5}Na_{0.5})TiO_3$, $SrTiO_3$, $BaTiO_3$ and $Ba(Zr_{0.25}Ti_{0.75})O_3$ ceramics were successfully calcined by two stapes conventional solid-state reaction method. The solid-solutions of $(1-x)(Bi_{0.5}Na_{0.5})TiO_3$-$xSrTiO_3$, $(1-x)(Bi_{0.5}Na_{0.5})TiO_3$-$xBaTiO_3$ and $(1-x)(Bi_{0.5}Na_{0.5})TiO_3$-$xBa(Zr_{0.25}Ti_{0.75})O_3$ with concentrations $0 \leq x \leq 0.08$ were prepared successfully by conventional solid-state reaction route. The optimized sintering temperature is found to be 1150^0C for 4 hrs. The X-ray diffraction study shows that all the compositions are having a single phase perovskite structure which confirms that a complete solid-solution is formed. The lattice parameter and cell volume decreases with increase in solid solution. A morphotropic phase boundary (MPB) exists in $(1-x)(Bi_{0.5}Na_{0.5})TiO_3$-$xBaTiO_3$ at $x = 0.07$ and in $(1-x)(Bi_{0.5}Na_{0.5})TiO_3$-$xBa(Zr_{0.25}Ti_{0.75})O_3$ at $x = 0.05$. The same thing is also observed in Raman spectroscopy. The microstructure of all samples shows a change of shape from rectangular to quasi-spherical with decrease in grain size. High dense and smaller grain

size has affected the conductivity and electromechanical property to achieve a higher value of d_{33} and k_p as well as enhanced the ferroelectric behavior in MPB compositions.

The temperature-dependent dielectric study shows increases in dielectric constant in all compositions whereas in (1-*x*)($Bi_{0.5}Na_{0.5}$)TiO_3-*x*$BaTiO_3$ and (1-*x*)($Bi_{0.5}Na_{0.5}$)TiO_3-*x* $Ba(Zr_{0.25}Ti_{0.75})O_3$, increases upto morphotropic phase boundary (MPB) and then decreases with further increase in solid solution. Also, the temperature-dependence of dielectric measurement reveals that the solid-solutions experience two phase transitions from ferroelectric to anti-ferroelectric and from anti-ferroelectric to paraelectric. The dielectric loss decreases with the increase in solid-solution content in the high temperature region. The diffusivity of the ceramics increases with higher content of solid-solution implying that the solid-solution introduces defects and localized strain field.

The impedance spectroscopy study of all compositions shows a dielectric relaxation of non-Debye type and the relaxation frequency shifted to higher frequency side with the increase of temperature and lower frequency side with the increasing concentrations. In ($Bi_{0.5}Na_{0.5}$)TiO_3, (1-*x*)($Bi_{0.5}Na_{0.5}$)TiO_3-*x*$SrTiO_3$ and (1-*x*)($Bi_{0.5}Na_{0.5}$)TiO_3-*x*$BaTiO_3$, only grain effect is observed indicating the uniform distribution and homogeneity in the specimen under study, whereas in (1-*x*)($Bi_{0.5}Na_{0.5}$)TiO_3-*x*$Ba(Zr_{0.25}Ti_{0.75})O_3$, grain and grain boundary effect is observed in the Cole-Cole plot above the temperature 430^0C. The relaxation phenomenon is found to exist due to oxygen vacancies. The activation energy obtained from the impedance, modulus and conductivity data, increases with increasing of solid-solution content. The electrical conductivity studies showed the negative temperature coefficient of resistance (NTCR) character. The optical study shows the variation of optical band gap energy (E_{gap}) in (1-*x*)($Bi_{0.5}Na_{0.5}$)TiO_3-*x*$BaTiO_3$ and (1-*x*)($Bi_{0.5}Na_{0.5}$)TiO_3-*x*$Ba(Zr_{0.25}Ti_{0.75})O_3$ solid-solutions.

Keywords: Ferroelectrics, Piezoelectricity, Diffuse phase transition, Morphotropic phase boundary (MPB), Dielectric relaxation, Raman spectroscopy, Impedance spectroscopy, UV-Visible absorption spectroscopy.

CONTENT

CHAPTER 1: **BACKGROUND AND MOTIVATIONS**

OUTLINE:

CHAPTER 4: STRUCTURAL, ELECTRICAL AND OPTICAL CHARACTERIZATION OF LEAD-FREE PEROVSKITE $(Bi_{0.5}Na_{0.5})TiO_3$-$SrTiO_3$ SYSTEM

OUTLINE:

LIST OF TABLES

LIST OF FIGURES

ABERRAVIATIONS

AFE	Anti-ferroelectric
CIS	Complex Impedance Spectroscopy
CPE	Constant Phase Element
BZT	$Ba(Zr_{0.25}Ti_{0.75})O_3$
BT	$BaTiO_3$
BNT	$(Bi_{0.5}Na_{0.5})TiO_3$
BNT-BT	$(1-x)(Bi_{0.5}Na_{0.5})TiO_3$-$xBaTiO_3$
BNT-BZT	$(1-x)(Bi_{0.5}Na_{0.5})TiO_3$-$xBa(Zr_{0.25}Ti_{0.75})O_3$
BNT-ST	$(1-x)(Bi_{0.5}Na_{0.5})TiO_3$-$xSrTiO_3$
DPT	Diffuse Phase Transition
EDX	Energy Dispersive x-ray
FE	Ferroelectric
JCPDS	Joint Committee on Powder Diffraction Standards
MPB	Morphotropic Phase Boundary
PE	Paraelectric
PND	Polar Nano Domain
PNR	Polar Nano Region
PVA	Poly Vinyl Alcohol
RFE	Relaxor Ferroelectric
SSR	Solid-State Reaction
ST	$SrTiO_3$

SEM	Scanning Electron Microscope
XRD	X-ray diffraction

NOTATIONS

ENGLISH SYMBOLS

a, b, c	Lattice parameters
A	Area of crossection
d_{33}	Piezoelectric constant
f	Frequency
Ea	Activation energy
Ec	Coercive field
k_p	Electromechanical coupling factor
L	Thickness of the sample
M’	Real part of modulus Thickness of the sample
M’’	Imaginary part of modulus
N_p	Frequency constant
Pr	Remnant polarization
Ps	Spontaneous polarization
R_g	Grain resistance
R_{gb}	Grain-boundary resistance
Q_m	Eletromechanical quality factor
t	Tolerance factor
T	Temperature

T_d	Depolarization temperature
T_C	Curie-Weiss temperature
T_f	Freezing temperature of polar-regions
T_m	Temperature corresponding to ε_m
Z’	Real part of impedance
Z’’	Imaginary part of impedance
tanδ	Dielectric loss tangent
V	Unit cell volume

GREEK SYMBOLS

ε_r	Dielectric constant
ε_s	Static dielectric constant
ε_∞	Dielectric constant at high temperature
ε_m	Maximum value of dielectric constants
ω	Probe frequency
$\omega(cm^{-1})$	Mode position in Raman Spectrum
ω_{max}	Angular frequency corresponding to Z'_{max} and M'_{max}
δ	Indicators of degree of relaxation
γ	Diffuseness exponent
σ	Conductivity
Φ	Phase angle
τ	Relaxation time
$\Gamma(cm^{-1})$	Line-width of a mode in Raman-Spectrum

INTRODUCTION

Chapter 1 introduces the basic concepts of dielectricity, piezoelectricity and ferroelectricity. The classification of crystal systems and the interrelationship between the piezoelectrics and subgroups with respect to symmetry of crystal structure is presented. A brief review of the classification of dielectrics, theory of dielectric classification and theory of the dielectric polarization phenomenon is well presented. The phenomena of ferroelectricity and piezoelectricity are discussed in detail. The basic understanding of the perovskite structure is elaborated and systems that possess this structure are discussed. The literature surveys have been briefly presented and finally, the objective of the present work is highlighted.

Chapter 2 contains details of all the experimental techniques used for preparation, structural characterization as well as to measure the dielectric, piezoelectric, ferroelectric and optical properties of materials.

Chapter 3 elaborates structural study of $(Bi_{0.5}Na_{0.5})TiO_3$ (abbreviated as BNT) ceramics has done with the help of x-ray diffraction and its Reitveld-refinement analysis. The microstructural and compositional study was done by scanning electron microscopy (SEM) and energy dispersive x-ray (EDX) spectroscopy, respectively. Vibrational study was carried out by Raman spectroscopy of the sample. The dielectric study of $(Bi_{0.5}Na_{0.5})TiO_3$ reveals that the composition shows diffuse phase transition behavior. Also, BNT shows two phase transitions Viz., ferroelectric to anti-ferroelectric and anti-ferroelectric to paraelectric, with rising temperature. The impedance study shows single arcs within the studied temperature range. The sample shows negative temperature coefficient of resistivity (NTCR) effect as the

bulk resistance decreases with increase in temperature. The ferroelectric properties studied by *P~E* loop tracer, have indicated that the sample exhibited typical ferroelectric nature at room temperature. The piezoelectric properties have been studied by d_{33} meter and the piezoelectric coefficient was found to be 41 pC/N. The electromechanical properties studied by resonance and anti-resonance method, the electromechanical coplanar factor (k_p) and mechanical quality factor (Q_m) was found to be 10.7533% and 108 respectively. The optical band gap was determined by the UV-Visible spectroscopy and found to be 2.94 eV.

Chapter 4 elaborates structure, microstructure and electrical properties of (1-*x)* $(Bi_{0.5}Na_{0.5})TiO_3$-*x*$(SrTiO_3)$ (abbreviated as BNT-ST) ceramics. The polycrystalline (1-*x)* $(Bi_{0.5}Na_{0.5})TiO_3$-*x*$(SrTiO_3)$ ceramic with $0 \leq x \leq 0.09$ has been prepared by solid-state reaction route. The sample shows that well-developed grain shape changes from rectangular to quasi-spherical as the $SrTiO_3$ content increases and the size of the grains decreases with the increase in $SrTiO_3$ concentration. Phase formation and structural study by XRD Rietveld-refinement method revealed that ST diffused into the BNT lattice. The UV-Visible spectroscopy study revealed that the optical energy band-gap slightly increases with increasing ST concentrations. Dielectric study revealed that dielectric constant increases, loss decreases, T_C shifts towards lower temperature and diffusivity co-efficient increases with increasing $SrTiO_3$ concentration. The impedance data show single semicircles in Nyquist plot within the studied temperature range indicating the contribution of only grains. It is observed that the conductivity decreases with increasing ST concentration. The variation of dc conductivity with temperature follows Arrhenius behavior. Ferroelectric and piezoelectric properties of the ceramics showed degenerated behavior with increase in ST content in the studied composition range at room temperature.

Chapter 5 elaborates structure, ferroelectric and piezoelectric properties of (1-x)($Ba_{0.5}Na_{0.5}$)TiO_3-$x$$BaTiO_3$ (abbreviated as BNT-BT) ceramic system. The polycrystalline (1-x)($Ba_{0.5}Na_{0.5}$)TiO_3-$x$$BaTiO_3$ ($0 \leq x \leq 0.08$) ceramic has been successfully prepared by the solid-state reaction route. The samples were found to be well crystallized in single phase. The XRD and its Rietveld-refinement shows a morphotropic phase boundary (MPB) between rhombohedral and tetragonal phases located at $x = 0.07$, which is also confirmed by the Raman spectroscopy study. The scanning electron microscopy (SEM) micrographs suggest that materials comprise of polycrystalline microstructure and the concentration of $BaTiO_3$ affects the microstructure. The dielectric response indicates the typical diffuse phase transition behavior and the magnitude of dielectric constant (ε') increases, loss tangent ($tan\delta$) slightly decreases, T_C shifts towards lower temperature up to MPB composition ($x = 0.07$) and then alters the variation. It is seen that the loss tangent decreases rapidly at high temperature. Also T_d is minimum at MPB composition. The diffusiveness coefficient and the dielectric dispersion value increase significantly with increase in $BaTiO_3$ content. The electrical properties of the samples have been studied by impedance spectroscopy, which shows non-Debye nature of the samples and grain effect only. The activation energy, obtained from the impedance, modulus and conductivity data, increases with increasing of BT content, but at $x = 0.07$, suddenly the activation energy decreases. The ferroelectric and piezoelectric properties are well generated with increasing the $BaTiO_3$ concentration. The electromechanical properties are optimized at MPB composition, which is studied by resonance and anti-resonance method.

Chapter 6 elaborates structural, electrical and optical study of (1-x)($Bi_{0.5}Na_{0.5}$)TiO_3-$x$$Ba(Zr_{0.25}Ti_{0.75})O_3$ (abbreviated as BNT-BZT) lead-free piezoelectric ceramic system. The

solid-state reaction technique has been employed for the synthesis of the polycrystalline (1-x)($Bi_{0.5}Na_{0.5}$)TiO_3-xBa($Zr_{0.25}Ti_{0.75}$)O_3 (abbreviated as BNT-BZT) ceramic with $0 \leq x \leq 0.08$. All the compositions are well sintered at 1150^oC for 4 hrs in air. The XRD and its Rietveld-refinement revealed that morphotropic phase boundary exists at x = 0.05, which is also confirmed by Raman spectroscopy study. Also, XRD data indicate increase of lattice parameters/unit cell volume with increasing BZT concentrations. The SEM micrographs indicate that the shape and size (decreases) of the grains changes with increasing BZT content. The optical band gap values, estimated from the UV-Visible spectra, suggested the presence of intermediary energy levels (shallow holes) within the band gap. The dielectric study shows diffuse phase transition behavior and the dielectric permittivity increases with increases in BZT content up to the composition x = 0.05. The depolarization temperature (T_d) and critical temperature (T_C) decrease and attain minimum value at x = 0.05 and then increase. The electrical properties of the sample have been studied by impedance and modulus spectroscopy. The grain boundary effects appeared with increasing BZT content at higher temperature data. The activation energy, obtained from the impedance, modulus and conductivity study, increases with increasing of BZT content, but at x = 0.05, suddenly the activation energy decreased. Ferroelectric and piezoelectric properties are maximal at x = 0.05 composition. The optimal electromechanical properties are observed at MPB composition.

Chapter 7 presents major conclusions of the research work, drawn after in depth-discussion in individual chapters. A brief report on the scope for future work is also presented**.**

CHAPTER 1

BACKGROUND AND MOTIVATIONS

OUTLINE: This chapter covers an overview of the electrical properties of ferroelectric materials, the historical developments in piezoelectric materials, literature survey and discussion on $(Bi_{0.5}Na_{0.5})TiO_3$-based ceramics, and finally emphasizes on the motivations and objective of this research work.

1.1 DIELECTRICITY

Dielectrics are non-conducting, insulating materials with a large energy gap. Dielectrics are described by relative permittivity (ε_r), the material parameter that makes the bridge between externally applied electric field **E,** electrical polarization **P** and dielectric displacement **D**. Homogeneous electric field **E** induces homogeneous polarization **P**,

$$\mathbf{P} = \chi\varepsilon_0\mathbf{E}, \tag{1.1}$$

where ε_0 is the permittivity of vacuum, and χ is the dielectric susceptibility. Relative permittivity, ε_r, of an isotropic or cubic medium is defined by the relation

$$\varepsilon_r = (\varepsilon_0 E + P)\big/\varepsilon_0 E = 1 + \chi \tag{1.2}$$

where $\varepsilon_0\mathbf{E} + \mathbf{P} = \mathbf{D}$ is the dielectric displacement [1, 2].

The dielectric function complex permittivity, $\varepsilon^* = \varepsilon_r$, is sometimes loosely referred to as dielectric constant of the material. In fact, it is not a constant. It depends on frequency, temperature, pressure, entropy, mechanical and electrical stresses/strains, etc., $\varepsilon^* = \varepsilon^*(f, T, p, x, \ldots)$.

When time-dependent electric field is applied (let us further consider harmonic function with a constant angular frequency, ω), moving charges cause frequency-dependent phase shift between the applied field and the charge displacement. Relative dielectric permittivity is then written as a complex function,

$$\varepsilon_r(\omega) = \varepsilon^*(\omega) = \varepsilon'(\omega) - i\varepsilon''(\omega) \quad (1.3)$$

where, ε' and ε'' are the real and imaginary parts of dielectric constants, respectively.

The total polarization of dielectric materials results from four contributions, as follows [1, 2]:

- Electronic polarization (displacement of the negatively charged electron shell against the positively charged nucleus),
- Ionic polarization (mutual displacement of the positive and negative sub lattices under the influence of an applied electric field),
- Orientation polarization (alignment of permanent dipoles), and
- Space charge polarization (polarization effect in a dielectric material showing spatial in homogeneities of charge carrier densities).

Each contribution stems from a short-range movement of charges that respond to an electric field on different time scales, hence, through a Fourier transform in different frequency regimes. Schematic dispersion of the real and imaginary part of the dielectric function is shown in Fig.1.1. Each of the contributions has characteristic frequency (where maximum of dielectric loss function appears, see lower part of Fig.1.1).

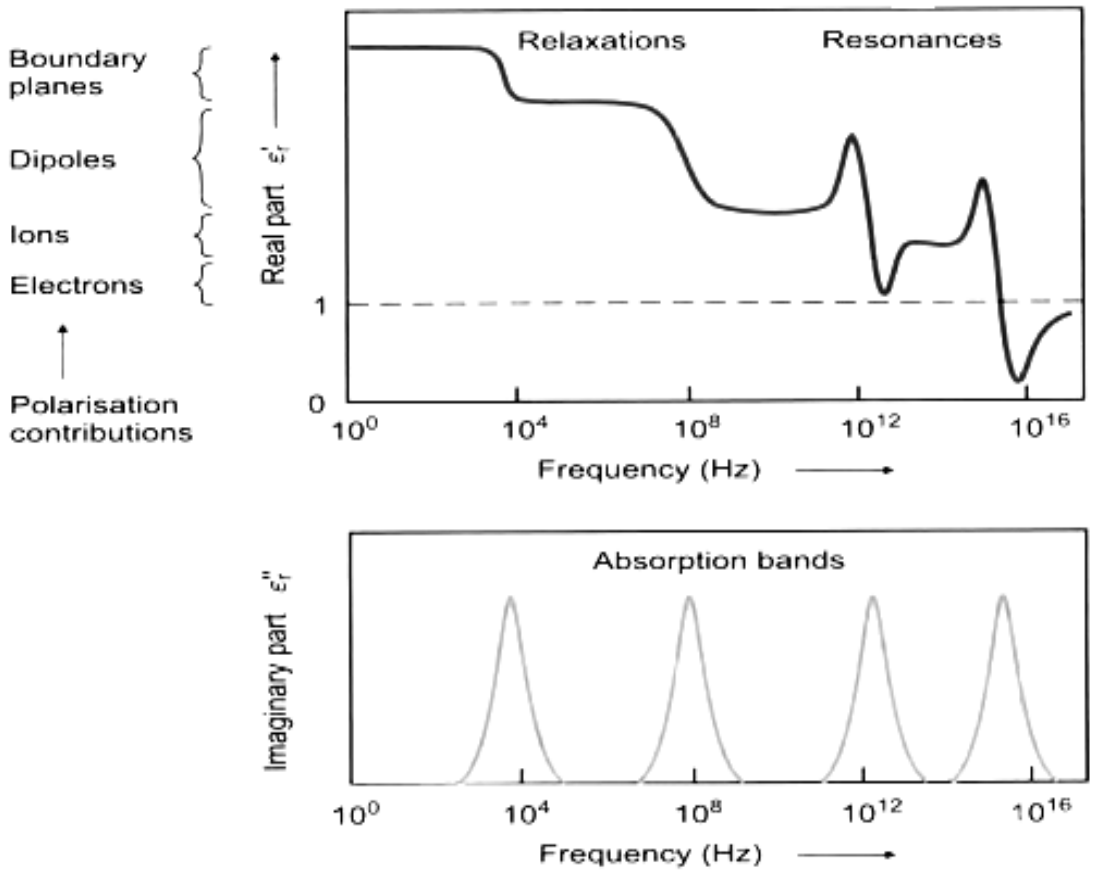

Fig.1.1: Frequency-dependence of the real (top) and the imaginary (bottom) part of dielectric function [1]

The different polarization mechanisms not only take place on different time scales but also exhibit different frequency dependence. Depending whether the oscillating masses experience a restoring force or not, we distinguish between resonance effects and relaxation effects, respectively. Resonances are observed for the ionic (molecular vibrations and ionic lattices in the infrared (IR) region, 10^{11}-10^{13} Hz) and electronic polarization (above 10^{13} Hz), while relaxation effects are found for orientational polarization (electric dipoles from mHz up to GHz) and space charge polarization (from mHz up to MHz).The polarization mechanisms of dielectric phenomena with frequency are clearly shown in Fig.1.2.

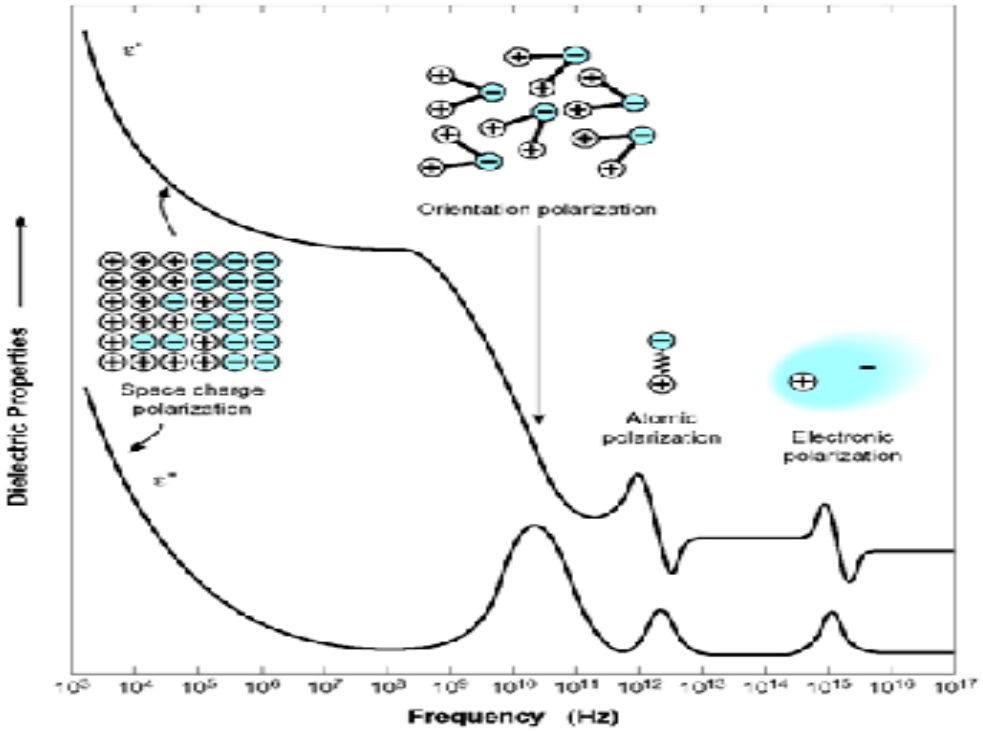

Fig.1.2: The frequency-dependent dielectric constant measures the response of a material to a time varying external electric field [3]

1.2 CLASSIFICATION OF CRYSTAL CLASSES

Of the 32 possible crystal classes (i.e. point groups), 11 are centro-symmetric and thus cannot exhibit polar properties. The remaining 21 lack a centre of symmetry and thus can posses one or more polar axes. Of these, 20 classes are piezoelectric (the one exception being the cubic class) (Fig. 1.3). Piezoelectric crystals have the property that the application of mechanical stress induces polarization, and conversely, the application of an electric field produces mechanical deformation. Of the 20 piezoelectric classes, 10 have a unique polar axis and thus are spontaneously polarized, i.e. polarized in the absence of an electric field. Crystals belonging to these 10 classes are called pyroelectric. The intrinsic polarization of pyroelectric crystals is often difficult to detect experimentally because of the neutralization of the charges on the crystal surfaces by free charges from the atmosphere and by conduction within the

crystal. However, because the polarization is a function of temperature, it is often possible to observe the spontaneous moment in these crystals by changing the temperature, hence the name pyroelectrics. Ferroelectric crystals belong to the pyroelectric family, but they also exhibit the additional property that the direction of the spontaneous polarization can be reversed by the application of an electric field. Thus, we have the following simple definition for a ferroelectric crystal: A ferroelectric crystals is a crystal that possesses reversible spontaneous polarization as exhibited by a dielectric hysteresis loop. A more detailed discussion on ferroelectrics is given in the subsequent sections. The Fig.1.3 also reflects that the dielectric property is the umbrella of all electrical properties of ceramic materials.

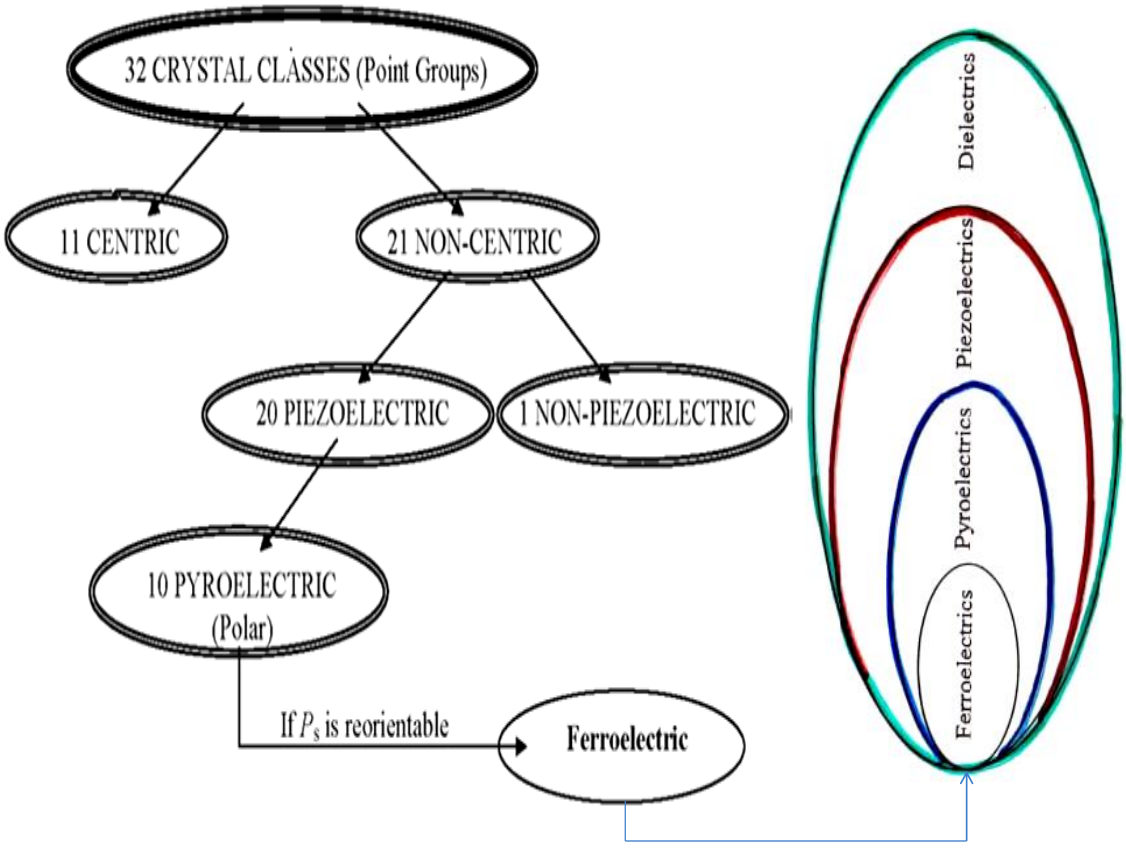

Fig.1.3: A classification scheme for the 32 crystallographic point groups [4]

1.3 PIEZOELECTRICITY

The first experimental demonstration of a connection between macroscopic piezoelectric phenomena and crystallographic structure was published in 1880 by Pierre and Jacques Curie. Their experiment consisted of a conclusive measurement of surface charges appearing on specially prepared crystals (tourmaline, quartz, topaz, cane sugar and Rochelle salt among them) which were subjected to mechanical stress [5, 6]. The phenomenon was later named “piezoelectricity" where “piezo" is a Greek derivative meaning “to press" [5].The Curies later experimentally confirmed this effect and provided proof of the linear and reversible nature of piezoelectricity.

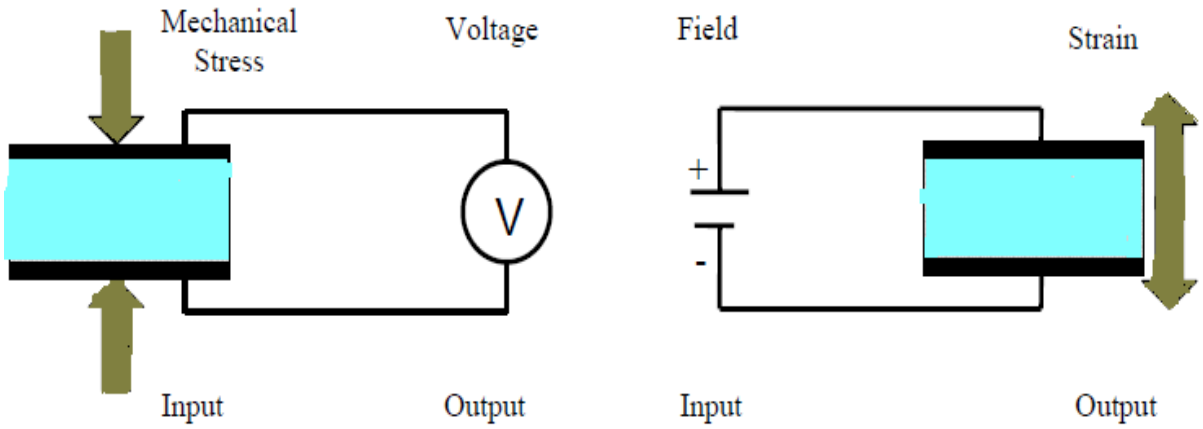

Fig.1.4: Polarization of ceramic material to generate piezoelectric effect [7]

In ordinary solids, a stress causes a strain proportional to an elastic modulus. Piezoelectricity is creation of an electric charge in addition to a strain, both of which are proportional to the applied stress [8]. This phenomenon is known as the direct piezoelectric effect (Fig.1.4), and can be described in tensor notation by:

$$P_i = d_{ijk} T_{jk} \qquad (1.4)$$

where P_i is the polarization (charge per unit area), generated along the i-axis in response to the applied stress T_{jk}, and d_{ijk} is the piezoelectric coefficient. It is clear from Eq.1.4 that there is a linear relationship between the electrical and mechanical properties [9]. The converse piezoelectric effect describes an induced strain (S_{ij}) which is proportional to an applied electric field E_k. This relationship is described in tensor notation as:

$$S_{ij} = d_{kij}E_k \tag{1.5}$$

The proportionality constant is numerically identical for both the direct and reverse effects, and is called the piezoelectric coefficient [8]:

$$d = P/T = S/E \tag{1.6}$$

A simplified notation is often used where one of the subscripts is dropped, and the piezoelectric coefficient becomes d_{ij}. Equations 1.4 and 1.5 then become:

$$P_i = d_{ij}T_j \tag{1.7}$$

$$S_j = d_{ij}E_j \tag{1.8}$$

Convention states that the subscript i in Eq. (1.7) and (1.8) indicates the z-axis which is perpendicular to the plane of the electrodes, and the subscript j indicates the direction of the applied stress, or piezoelectrically induced strain. The most commonly measured and cited values are d_{33}, where the field and strain (or stress and polarization) are applied and measured in the same plane, and d_{31}, where the application and measurement planes are perpendicular. Both of these piezoelectric coefficients can be measured using a commercial d_{33} meter, which measures the charge developed on a sample for a given applied force.

The d constants can also be calculated from:

$$d = k\,(\varepsilon^T s^E)^{½} \tag{1.9}$$

where k is the electromechanical coupling coefficient, ε^T is the relative dielectric constant (at constant stress), and s^E is the compliance (at constant field) [8]. The piezoelectric effect is present in varying degrees in nearly all of the non-centrosymmetric crystal classes.

1.4 FERROELECTRICCITY

The permanent electric dipole moment is possessed by all pyroelectric (polar) materials. In certain cases it can be reoriented by the application of an electric field. Such properties of crystal are called ferroelectric properties and the phenomenon is known as ferroelectricity. The phenomenon of ferroelectricity was discovered by Valasek [10]. Thereafter, many essential features of the ferroelectric phenomenon were studied and described. Since then, many excellent books introducing a number of phenomenological theories of ferroelectricity and various ferroelectric material systems have been published [8, 11-14]. Rochelle salt ($NaKC_4H_4O_6$. H_2O) was the first material found to show ferroelectric properties on cooling below a transition temperature (T_C-Curie temperature). In the ferroelectric phase, modifications to the cation and anion positions occur to give relative displacements of ions inside the unit cell, resulting in reversible spontaneous dipole moments.

1.5 CHARACTERISTICS OF FERROELECTRIC MATERIALS

As mentioned earlier, some of the most important unique characteristics of ferroelectric crystals are spontaneous polarization below Curie temperature, polarization hysteresis and ferroelectric domains, which will be briefly discussed in the following sections.

1.5.1 Phase Transitions

One of the main characteristics of most ferroelectric materials is the existence of a phase transition from a ferroelectric (polar) to a paraelectric (non-polar) phase, at a so-called Curie

point, T_C. Above this transition temperature, the dielectric constant of the ferroelectric material follows Curie-Weiss law:

$$\varepsilon' \cong C/(T-T_C) \qquad (1.10)$$

where ε' is dielectric constant, C is the Curie constant, T is the temperature, and T_C the Curie-Weiss temperature. The dielectric constant shows a maximum at the transition temperature, and as explained earlier, above the transition temperature, the material is non-polar with zero spontaneous polarization and higher symmetry point group.

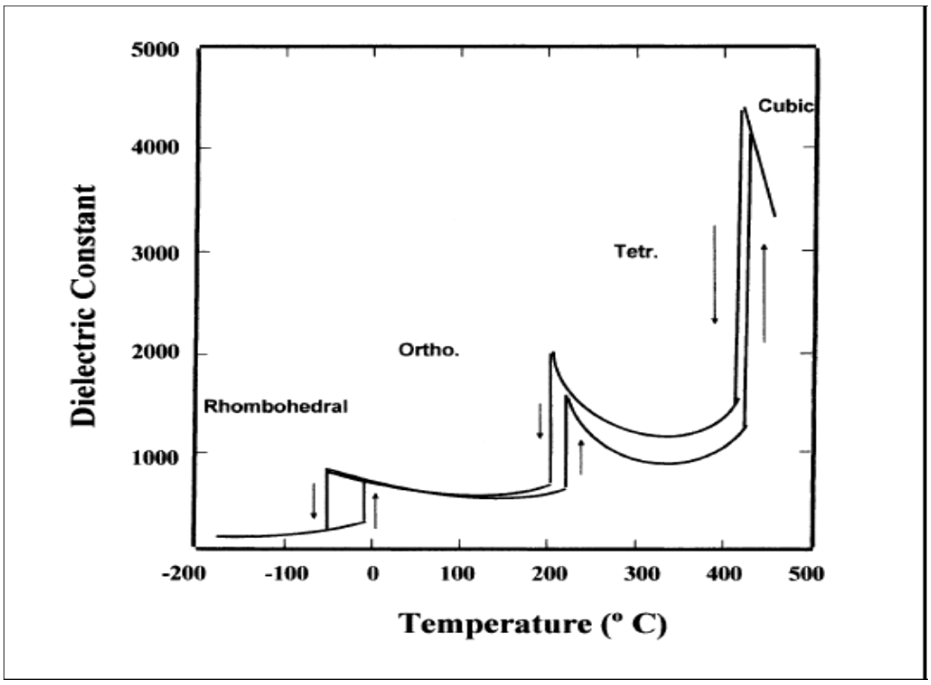

Fig.1.5: Dielectric constant as a function of temperature for $BaTiO_3$[15]

The transition into a ferroelectric phase usually leads to strong anomalies in the dielectric, elastic, thermal and other properties of the material [16] and is accompanied with changes in the dimensions of the crystal unit cell. The associated strain is called the spontaneous strain x_S. It represents the relative difference in the dimensions of the ferroelectric and paraelectric unit cells [17, 18].

1.5.2 Polarization Hysteresis

One of the easiest ways to inspect ferroelectricity in a material is the observation of polarization hysteresis. Application of an electric field, and cycling through negative and positive directions in a ferroelectric, results in a hysteretic behaviour as shown schematically in Fig.1.6. The polarization initially increases from zero to a saturation polarization, P_{sat} and upon decreasing the electric field, reduces to a remanent polarization, P_r. The electric field required to reduce the polarization back to a zero value, is called coercive field, E_C. **[**17**]**.

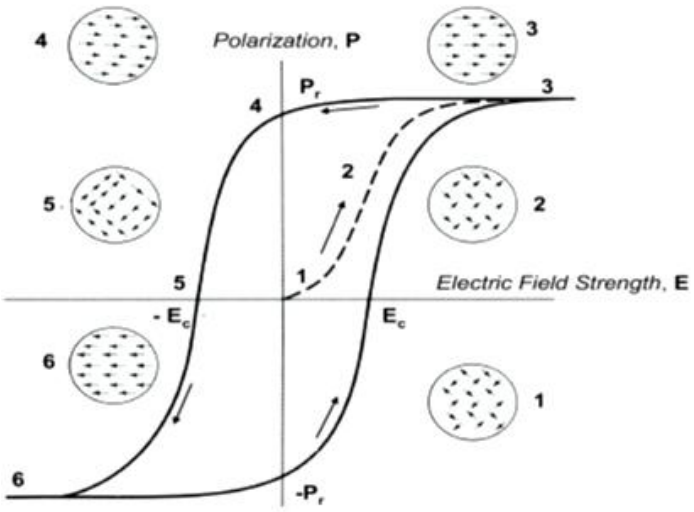

Fig.1.6: Polarization hysteresis in a ferroelectric material [**19**]

1.5.3 Ferroelectric Domains

A ferroelectric crystal often consists of regions called domains within each of which all dipole moments are aligned in the same direction, while this direction may differ from an adjacent domain. The individual dipoles, and as a result, the spontaneous polarization are generated upon cooling the crystal below the Curie point. The region between two domains is called the domain wall. The walls between domains with oppositely orientated polarization are called

180^{o} walls and those between regions with mutually perpendicular polarization are called 90^{o} walls **[**20**]**. As the temperature is reduced down to the Curie point, the generation of spontaneous polarization leads to formation of surface charge and this surface charge in turn produces a so-called depolarizing field, E_d, whose direction is the opposite of the spontaneous polarization. In principle, ferroelectric domains form to minimize the electrostatic energy of depolarizing fields and the elastic energy associated with mechanical strain generated in the ferroelectric material as it is cooled through paraelectric-ferroelectric phase transition **[**21**]**. The electrostatic energy generated as a result of depolarizing field may be minimized in two ways. The first is involved with the ferroelectric materials into domains with oppositely oriented polarization and the second with depolarizing charge being compensated for by electrical conduction through the crystal or by charges from the surrounding. On the other hand, 90^{o} domain walls are considered responsible for minimizing the elastic energy. A combination of electric and elastic boundary conditions to which a crystal is subjected as it is cooled through the ferroelectric phase transition temperature usually leads to a complex domain structure with many 90^{o} and 180^{o} walls. This is schematically described in Fig.1.7.

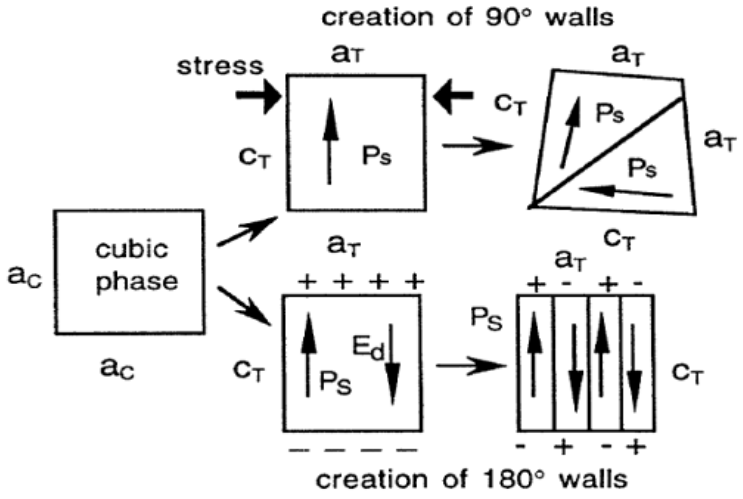

Fig.1.7: Creation of ferroelectric domains [**15**]

1.6 CLASSIFICATION OF FERROELECTRIC MATERIAL

Depending on the temperature variation of dielectric constant or Curie constant C, ferroelectrics (*FE*) can be divided into two groups. In one group, the compounds undergoing order-disorder type transition have a Curie constant of the order 10^3 while for others, which undergo displacive type transition, it is of the order of 10^5. Initially, ferroelectric materials were broadly classified into two categories: (a) soft (KH_2PO_4 - type) and (b) hard ($BaTiO_3$ - type). The phase transition in soft (H-bonded) ferroelectrics is of order-disorder type whereas in hard ones it is displacive type. The phase transition in soft ferroelectrics involves not only the ordering of the disordered hydrogen atom, but also the deformation of the atomic groups like SO_4^{2-}, Se_4^{2-} and PO_4^{3-}. In case of displacive type of transition a small atomic displacement of some of the atoms is mainly responsible for phase transition, which has been found in some of the perovskites. However, the difference between displacive and order-disorder type of transitions becomes uncertain when the separation of relevant disorder becomes comparable with the mean thermal amplitude of those atoms. The character of ferroelectrics is represented in terms of the dynamics of phase transition.

1.6.1 Diffuse Phase Transition

Many phase transitions in macroscopic homogeneous materials are characterized by the fact that the transition temperature is not sharply defined. In these, so-called diffuse phase transitions (DPT), the transition is smeared out over a certain temperature interval, resulting in a gradual change of physical properties in this temperature region. Though this phenomenon is observed in several types of materials [22], however, the most remarkable examples of DPT are found in ferroelectric materials [23]. Ferroelectrics diffuse phase transitions (FDPT) were first mentioned in the literature in the early 1950's [24]. Some characteristics of the DPT are:

(a) broadened maxima in the permittivity- temperature curve, (b) gradual decrease of spontaneous and remanent polarisations with rising temperature, (c) transition temperatures obtained by different techniques do not coincide, (d) relaxation character of the dielectric properties in transition region and (e) no Curie-Weiss behaviour in certain temperature intervals above the transition temperature. The diffuseness of the phase transition is assumed to be due to the occurrence of fluctuations in a relatively large temperature interval around the transition. Usually, two kinds of fluctuations are considered: (a) compositional fluctuation and (b) polarisation (structural) fluctuation. From the thermodynamic point of view, it is clear that the compositional fluctuation is present in ferroelectric solid-solutions and polarisation fluctuation is due to the small energy difference between high and low temperature phases around the transition. This small entropy difference between ferroelectric and paraelectric phase will cause a large probability of fluctuation. According to Fritsberg [25], substances of less stability are expected to have a more diffuse transition. For relaxor as well as other FDPT, the width of the transition region is mainly important for practical applications. Smolensky and Rolov have introduced a model calculation, based on the concept of Gaussian distribution for both the compositional and polarisation fluctuation, from which the diffuseness parameter can be calculated [26, 27]. Complex perovskite type ferroelectrics with distorted cation arrangements show DPT, which is characterised by a broad maximum for the temperature dependence of dielectric constant (ε') and dielectric dispersion in the transition region [26,28]. For DPT, ε' follows the modified temperature dependence

$$1/\varepsilon' - 1/\varepsilon_m = (T - T_m)^{\gamma}/ C' \qquad (1.11)$$

where T_m is the temperature at which ε' reaches maximum, ε_m is the value of ε' at T_m, C' is the modified Curie-Weiss-like constant and γ is the critical exponent, which explains the

diffusivity of the materials, and lies in the range $1 < \gamma < 2$ [29]. The smeared-out ε' vs. T response has generally been attributed [26, 30, 31] to the presence of micro regions with local compositions varying from the average composition over the length scale of 100 to 1000 Å. Different micro-regions in a macroscopic sample are assumed [31] to transfer at different temperature, the so-called Curie range, leading to DPT which is due to compositional fluctuations. The dielectric and mechanical properties of FE system below their T_C are functions of the state of polarisation and stress. So ferroelectrics have major applications today because of their characteristic electro-optic, dielectric and hysteresis properties.

For many practical applications, it is desired to use the very-large-property maxima in the vicinity of the ferroelectric phase transition, to move the transition into the temperature range of interest and to broaden and diffuse the very large sharp peak values. In DPT the dielectric maxima are now much rounder and polarisation persists for a shorter range of temperature above T_m.

1.7 PEROVSKITE CRYSTAL STRUCTURE

Most of the useful ferroelectrics, such as barium titanate ($BaTiO_3$), lead titanate ($PbTiO_3$), lead zirconate titanate (PZT), lead lanthanum zirconate titanate (PLZT), and potassium niobate ($KNbO_3$), have the perovskite structure. Perovskite is the mineral name of calcium titanate ($CaTiO_3$). Its simplest structure is cubic, which is the high temperature form for many mixed oxides of the ABO_3 type. The simple cubic structure (space symmetry Pm-3m) consists of corner sharing oxygen octahedra (BO_6) arranged in three dimensions with smaller, highly charged cations (B: Ti^{4+}, Zr^{4+},Sn^{4+},Nb^{5+},Ta^{5+},W^{6+} , etc.) located in the middle of the octahedra, and lower-charged, larger cations (A:Na^{+}, K^{+},Ca^{2+}, Ba^{2+}, Pb^{2+}, etc.) in between the octahedra. The structure is shown in Fig.1.8. Most perovskite-type ferroelectrics are compounds with

either $A^{2+}B^{4+}O_3^{2-}$ or $A^{1+}B^{5+}O_3^{2-}$-type formula [32]. The perovskite structure can be also regarded as a cubic close-packed arrangement of large A and O ions with smaller B ions filling the octahedral interstitial positions. The structure is also very tolerant to cation substitution to both A and B sites of lattice, and hence may lead to more complex compounds, such as $(K_{1/2}Bi_{1/2})TiO_3$,$Pb(Fe_{1/2}Ta_{1/2})O_3$, $Pb(Co_{1/4}Mn_{1/4}W_{1/2})O_3$, $Pb(Mg_{1/3}Nb_{2/3})O_3$, and $Pb(Zn_{1/3}Nb_{2/3})O_3$ [17,27].

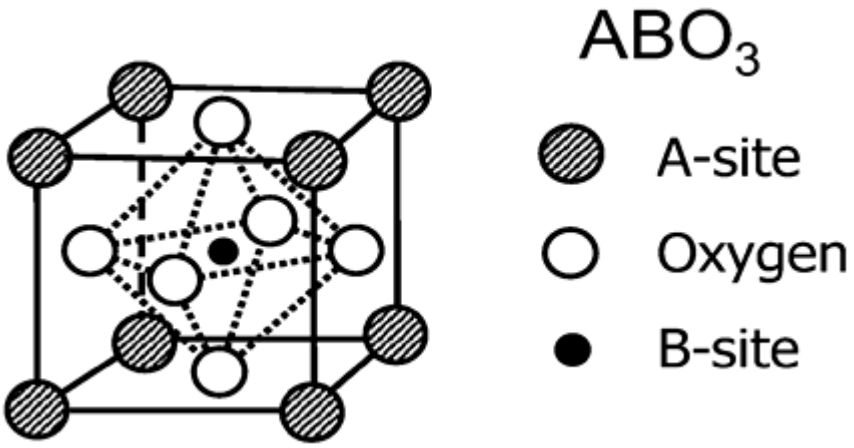

Fig.1.8: A cubic ABO_3 perovskite-type unit cell [**33**]

1.7.1 Goldschmidt Tolerance Factor

The concept of tolerance factor (*t*) is the arrangement of interpenetrating octahedra and dodecahedra in perovskite structure (ABO_3 type), introduced by Goldschmidt [34], which is given by:

$$t = \frac{R_a + R_o}{\sqrt{2}(R_b + R_o)} \tag{1.12}$$

where R_a, R_b, and R_o are the ionic radii of cations A, B and oxygen, respectively. The t value also provides an indication about how far the atoms can move from the ideal packing positions

and be still "tolerated" in the perovskite structure. It reflects the structural modification such as distortion, rotation and tilt of the octahedra [35]. These structure factors consequently affect the electric property. Recently, some investigations are trying to find out the relation between the *t* and some material properties. For example, Reaney *et al*. have shown that the temperature coefficient of dielectric constant (τ_ε) is controlled by the tolerance factor (t).

1.8 REVIEW OF PREVIOUS WORK

Recently ferroelectric perovskite-type compounds are being studied more, as these materials are involved in the fabrication of many devices, such as transducers, capacitors, electro-acoustic transformers, signal processing devices, ultrasonic miniature motors, micropositioners, deformable mirrors in optical switching, etc. [36-38] The properties of these materials can be controlled either by doping or compositional change. The latter is connected with the onset of cationic disorder which strongly influences the properties, mainly due to the dependence of nature of the phase transition [39]. Among the various lead free ferroelectric materials, $(Bi_{0.5}Na_{0.5})TiO_3$ (BNT) is considered as a possible candidate for different industrial applications due to its large polarization, high temperature dielectric constant and high piezoelectric behavior. Various methods have been explored by researchers to improve the piezoelectric and dielectric properties of BNT-based material by doping at A and/or B site as well as forming solid-solutions.

1.8.1 Sodium Bismuth Titanate-$(Na_{0.5}Bi_{0.5})TiO_3$ (BNT)

$(Bi_{0.5}Na_{0.5})TiO_3$ is one of the important lead-free piezoelectric materials with perovskite structure discovered by Smolenskii et al in 1961 [34]. Its dielectric and optical property measurements of BNT were reported in the 1990s by various researchers [40-42]. Isupov *et al.*

[43] summarized that there are three phase transitions in the temperature dependent dielectric study. The transition of ferroelectric to anti-ferroelectric at temperature 473 K is named as ferroelectric (FE) transition. The transition of anti-ferroelectric to ferroelastic at temperature 593 K is named as anti-ferroelectric (AFE) transition. The transition of ferroelastic to paraelastic at temperature 813 K is named as ferroelastic transition. East *et al.* [44] reported that the bulk permittivity of BNT did not show any peak in the region 450 to 540^{o}C, confirming that the tetragonal polymorph is non-polar. . The structural phase transitions in bismuth sodium titanate with the variation of pressure (upto 19 GPa) has been investigated using Raman spectroscopy by Kreisel *et al*. [45]. The complex impedance, electric modulus, dielectric loss and conductivity analyses of BNT were carried out by Saradhi *et al.* [46]. The relaxor ferroelectric nature of BNT was studied using Brillouin scattering by Schmidt *et al.* [47]. The peak in dielectric constant of $(Bi_{0.5}N_{0.5})TiO_3$ at 320^{0}C is associated with relaxation processes which can be recognized as the results of interaction (both of electric and mechanical nature) between polar-regions and non-polar matrix, but cannot be a phase transition i.e., no changes in structure, specific heat, domain structure, etc. are observed at this temperature [48]. Suchanicz [49] explained the deformed hysteresis loops above 200^{o}C of BNT in terms of electro-mechanical interaction between polar-regions and nonpolar matrix.

1.8.2 Effect of Dopant in BNT

BNT is a good material for various applications because it can be modified to enhance a specific desirable behavior. Many studies have been performed to show the affect of A-site or/and B-site dopants on the structural and electrical properties of BNT. Some studies focus on dielectric properties, while others focus on piezoelectric properties.

The phase transition temperature, electrical properties and the relationship between the substituted divalent ions (Ca^{2+}, Sr^{2+} and Ba^{2+}) in $(Bi_{0.5}Na_{0.5})TiO_3$-based ceramics were investigated by Watanabe *et al.* [50]. The phase transition temperature and dielectric permittivity of A-site ion (A = Pb, Sr) substituted-$(Bi_{0.5}Na_{0.5})TiO_3$ solid solutions with the aid of structural analysis have been investigated by Lee *et al.* [51]. They observed first-order phase transition with the increase in the substitutions of Pb. Structure and dielectric properties of Sr^{2+}-doped $(Bi_{1/2}Na_{1/2})TiO_3$ were studied by Park *et al.* [52]. The decrease of T_{max} and typical relaxor ferroelectric phase transition behavior was found above 18 % of Sr^{2+} concentration. Dorcet *et al.* [53] studied the nanoscale structure and local structure due to the A-site order-disorder in BNT using transmission electron microscopy (TEM). The structure of $(Bi_{0.5}N_{0.5})TiO_3$ and Ba modified $(Bi_{0.5}N_{0.5})TiO_3$ was studied using diffuse x-ray scattering by Thomas *et al.* [54]. Ranjan *et al.* [55] studied structural and dielectric properties of $(Bi_{0.5}Na_{0.5})_{1-x}Ba_xTiO_3$ with $0 \leq x \leq 0.1$. The above system shows rhombohedral structure up to x = 0.055 and above that it becomes nearly cubic. Lin *et al.* [56] studied the dielectric properties of silver-particles-incorporated $(Bi_{0.5}Na_{0.5})TiO_3$. The dielectric constant increases with the increase in the amount of metallic silver particles, which is ascribed to the effective electric fields developed between the dispersed particles in the matrix and the percolation effect. Kim *et al.* [57] observed that the coercive field decreases in La modified $(Bi_{0.5}Na_{0.5})TiO_3$ (BNT) for the composition $Bi_{0.5}Na_{0.51-x}La_xTiO_3$ with $0 \leq x \leq 0.1$. Dielectric and piezoelectric properties of yttrium-modified $(Bi_{0.5}Na_{0.5})_{0.94}Ba_{0.06}TiO_3$ was studied by Zhou *et al.* [58]. Yi *et al.* [59] have investigated the microstructure of lanthanum-doped BNT and it was found that the substitution of La^{3+} ions at the A-site (Bi^{3+} or Na^{+} ions), inducing A-site vacancies, resulted in inhibition of grain growth as well as improvement of densification. The

depolarization temperature (T_d) decreased, T_{max} increased and diffusivity of the phase transition increased with incorporation of La in BNT as observed by Barick *et al.* [60]. The Bi-doped BNT was studied by Wang *et al.* [61] and they reported that it reduces poling leakage current, enhances the piezoelectric properties and increases the dielectric constant and the dielectric loss of the BNT ceramics. Raghavender *et al.* [62, 63] studies the effect of Ce^{3+} and Sm^{3+}substitution on electrical properties $Bi_{0.5}Na_{0.5}TiO_3$.

Kumari et al. [64] reported that the addition of ZrO_2 to BNT increases the T_m as well as T_d to higher temperature and decreases the dielectric loss. The effect of Zr/Ti ratios on dielectric properties of $(Bi_{0.5}N_{0.5})TiO_3$ was studied by Jaiban *et al.* [65]. The dielectric relaxation and electrical conduction in the Zr-doped BNT systems were studied by Lily *et al.* [66]. Microstructures and mechanical properties of zirconium doped BNT ceramics were studied by Watcharapasorn *et al.* [67]. Piezoelectric coefficients and thermal stability of Fe and Mn substituted BNT ceramics were studied at high temperature by Davies *et al.* [68]. The reduction of domain size of Mn-doped $(Bi_{0.5}Na_{0.5})TiO_3$ crystal with enhanced dielectric, piezoelectric and ferroelectric properties was observed in comparison with that of pure $(Bi_{0.5}Na_{0.5})TiO_3$ crystal [69]. The addition of Mn decreases the Tc and increases the resistivity of the BNT [70]. Prasad *et al.* [71] reported that the addition of WO_3 to $(Bi_{0.5}N_{0.5})TiO_3$ shifts the phase transition temperature and depolarization temperature to a higher temperature with the influences of phase transition and microstructure. The dielectric properties of $Bi_{0.5}Na_{0.5}Ti_{1-x}(Ni_{1/3}Nb_{2/3})_xO_3$ with $0 \leq x \leq 0.04$ were studied by Zhou *et al.* [72]. They observed that the grain size decreases with increasing x. The piezoelectric constant increases, up to x = 0.03 and then decreases with increasing x with a maximum value of 101 pC/N. The substitution of $(Mg_{1/3}Nb_{2/3})^{4+}$ at B-site of $(Bi_{0.5}Na_{0.5})TiO_3$-based piezoelectric ceramic by a

conventional ceramic technique and its effect on the microstructure, dielectric and piezoelectric properties were investigated [73].

1.8.3 Effect of Solid-solution in BNT

It is observed from the above section that there is enhancement in dielectric and piezoelectric properties by doping various dopants in BNT based ceramics. As mentioned previously, another useful method for the enhancement of properties is by forming solid-solutions. This section discusses the structure and properties of several lead-free binary and ternary solid-solution material compositions.

Senda *et al.* [74] compared the properties of lead based and lead-free BNT composition of BNT-PT, BNT-BKT systems. A relaxor-like behaviour was observed for BNT-rich materials and attributed to cation disorder in the 12-fold co-ordination sites. The compound (1-*x*)$(Bi_{0.5}N_{0.5})TiO_3$-*x*$(Bi_{0.5}K_{0.5})TiO_3$ for *x* = 0.50, showed high piezoelectric properties, high T_d and low dielectric loss as reported by Zhao *et al.* [75]. Buhrer *et al.* [76] reported that the Curie temperature went through a minimum at *x* = 0.1-0.2 for the solid solutions of (1-*x*)$Bi_{0.5}Na_{0.5}TiO_3$-*x*$K_{0.5}Bi_{0.5}TiO_3$, while the lattice parameters grew with *x*. The diffused phase transitions in the BNT-BKT system are due to structural disorder as well as compositional fluctuations in the crystal structure and relaxation phenomena are Maxwell-Wagner type as reported by Li *et al.* [77]. Hiruma *et al.* [78] determined the depolarization temperature T_d, rhombohedral-tetragonal phase transition temperature T_{R-T}, and the temperature of maximum dielectric constant T_m from the temperature dependent dielectric and piezoelectric properties of $(Bi_{0.5}Na_{0.5})TiO_3$-$(Bi_{0.5}A_{0.5})TiO_3$, where A=Li and K. The solution of (1-*x*)BNT-*x*$PbMg_{1/3}Nb_{2/3}O_3$ has been investigated by Lee *et al.* [79]. It is postulated that the addition of

PMN promotes the piezoelectric response by decreasing the coercive field and the dielectric loss of BNT. Hiruma *et al.* [80] demonstrated the relationship between various phases and the electrical properties of solid solutions of $(Bi_{0.5}Na_{0.5})TiO_3$ with $NaNbO_3$ and $KNbO_3$ substitutions. The addition of bismuth aluminate ($BiAlO_3$) increases the broadness of dielectric peak and reduces the coercive field as reported by Yu *et al.* [81]. Boucher *et al.* [82] studied the structure and ferroelectric properties of $(Bi_{0.5}Na_{0.5})TiO_3$-$BiScO_3$ system. The T_d and T_{R-T} decrease, while T_m increases linearly with increase in $BiCrO_3$ contents in BNT as reported by Selvamani *et al.* [83]. The compound $(1-x)(Bi_{0.5}Na_{0.5})TiO_3$-$xBaNb_2O_6$ shows diffuse phase transition character and the diffuse character increases with increasing concentration of $BaNb_2O_6$ [84]. Li *et al.* [85] observed that the crystalline structure varies from rhombohedral to cubic with the increase in concentration of $KNbO_3$. The phase transition temperatures decreased and compounds showed relaxor ferroelectric behavior due to the introduction of $KNbO_3$. Electrical properties of $(Bi_{0.5}Na_{0.5})TiO_3$-$Ba(Hf_{0.05},Ti_{0.95})O_3$, (BHT5) were studied by Tian *et al.* [86].

Sakata *et al.* [87] reported the AFE properties of the BNT phase above 473 K in the BNT-$SrTiO_3$ solid solutions. Rout *et al.* investigated various phase transformations in a solid solution series of $(100-x)(Bi_{0.5}Na_{0.5})TiO_3$-$xSrTiO_3 (0 \leq x \leq 40)$ by x-ray diffraction, dielectric, and Raman scattering techniques [88]. The relationship between depolarization temperature and maximum permittivity temperature, influence of non-stoichiometry and doping on the structures and piezoelectric properties of $(Bi_{0.5}Na_{0.5})TiO_3$-$BaTiO_3$ ceramics were studied by Chu *et al.* [89]. Kim *et al.* [90] studies the electrical properties of $(1-x)(Bi_{0.5}Na_{0.5})TiO_3$-$xBaTiO_3$ with $0 \leq x = 0.1$ powders synthesized by the emulsion method. The change in crystal structure of $(Bi_{0.5}Na_{0.5})_{0.94}Ba_{0.06}TiO_3$-$Ba(Zr_{0.04}Ti_{0.96})O_3$ from rhombohedral to tetragonal

symmetry along with increasing $Ba(Zr_{0.04}Ti_{0.96})O_3$ content was studied by Chen *et al.* [91]. Setasuwon *et al.* [92] reported the synthesis of $Ba(Zr_{0.05}Ti_{0.95})O_3$ anisotropic particles with grain orientation by conversion of $(Bi_{4.5}Na_{0.5})Ti_4O_{15}$ crystals.

Zhu *et al.* [93] studied the effect of sintering temperature on $74(Bi_{1/2}Na_{1/2})TiO_3$-$20.8(Bi_{1/2}K_{1/2})TiO_3$-$5.2BaTiO_3$ ceramics. They observed that with the increase in Curie-Weiss temperature T_C, the sintering temperature increases, and the depolarization temperature T_d decreases. The composition (1-3*x*)BNT-2*x*KBT-*x*BT shows the morphotropic phase boundary at $0.025 \leq x \leq 0.035$ between rhombohedral and tetragonal phase as reported by Li *et al.* [94]. Phase Transitions in $(Bi_{0.5}Na_{0.5})TiO_3$-$SrTiO_3$-$PbTiO_3$ solid solution were studied by Dunce *et al.* [95]. This composition shows relaxation depending on various concentrations of $PbTiO_3$. The dielectric constant of Nd_2O_3-doped $0.82Bi_{0.5}Na_{0.5}TiO_3$-$0.18Bi_{0.5}K_{0.5}TiO_3$ lowers with an increase in the Nd_2O_3 content [96]. Zhou *et al.* [97] studied the relaxor behavior of $(Bi_{0.5}N_{0.5})TiO_3$-$(Bi_{0.5}K_{0.5})TiO_3$-$BiFeO_3$ ferroelectrics. The ternary system, $(Bi_{0.5}Na_{0.5})TiO_3$-$NaNbO_3$-$BaTiO_3$ ceramics, which shows pseudo-cubic crystal structure, was studied by Wu *et al.* [98].

1.8.4 MPB (Morphotropic phase boundary) in BNT based solid-solution

The most useful piezoelectric materials display a transition region (or coexisting region) in their composition phase diagrams; known as a morphotropic phase boundary (MPB), where the crystal structure changes abruptly and the electromechanical properties are maximal.

Sasaki *et al.* reported that a MPB between rhombohedral (BNT-rich) and tetragonal (BKT-rich) structures occurs in BNT-BKT solid solution in the region of 16-22 mol% BKT which

shows improvement in the piezoelectric constant, dielectric constant, and the coupling factor [99]. Since this solid solution contains several elements that volatilize easily, such as K, Na, and Bi, the sintering conditions used play a large role in the final piezoelectric properties achieved in these materials as reported by Zhang et al. [100]. In the case of a combination of BNT with KNN, several different MPBs have been reported. In a BNT-rich system, Kounga *et al.* reported an MPB at 6-7 mol% KNN between a rhombohedral FE phase (BNT-rich) and a tetragonal AFE phase [101]. Although the addition of KNN made the material more antiferroelectric in its behavior, it also led to a much higher unipolar strain [102]. On the contrary, with a KNN rich solution, an MPB was reported at 2-3% BNT between ferroelectric orthorhombic and tetragonal phases [103]. This composition leads to a high piezoelectric constant and electromechanical coupling factor. Takenaka *et al.* [104] has reported the MPB at x = 0.06-0.07 in $(1-x)(Bi_{0.5}Na_{0.5})TiO_3$-$xBaTiO_3$ system. The composition of $(Bi_{0.5}N_{0.5})TiO_3$-$Ba(Zr_{0.05}Ti_{0.95})O_3$ shows an MPB and improves piezoelectric properties in the range of 3 to 12 mol% $Ba(Zr_{0.05}Ti_{0.95})O_3$ [105]. Chen *et al.* [106] studied the electrical properties of $(1-x)(Bi_{0.5}N_{0.5})TiO_3$-$xBa(Zr_{0.04}Ti_{0.96})O_3$ solid solutions and they reported that the solid solutions showed an MPB with the addition of 6 mole percent $Ba(Zr_{0.04}Ti_{0.96})O_3$ in BNT.

The composition $(1-3x)$BNT-$2x$KBT-xBT shows a morphotropic phase boundary (MPB) between rhombohedral and tetragonal phase located in the range of x = 0.025-0.035 and show a relatively low coercive field of Ec = 4.55kVmm^{-1}. The transformation of relaxor type ferroelectrics to normal ferroelectrics increases with increase of KBT and BT concentration [107]. Shieh *et al.* [108] studied the switching characteristics of the MPB compositions of the $(Bi_{0.5}Na_{0.5})TiO_3$-$BaTiO_3$-$(Bi_{0.5}K_{0.5})TiO_3$ system by examining their polarization and strain hysteresis. There exists a morphotropic phase boundary (MPB) between rhombohedral and

tetragonal lattices in the range of $0.18 < x < 0.21$ and $0 < y < 0.05$ in $(0.97-x)$BNT-xBKT-0.03BF and $(0.82-y)$BNT-0.18BKT-yBF systems as reported by Zhou *et al.* [109].

Plenty of research results for the BNT-based lead-free piezoelectric ceramics have been discussed above and the compositions (MPB) with optimal piezoelectric and dielectric properties of some systems are summarized in Table 1.

Table 1.1: The optimal piezoelectric constant (d_{33}), electromechanical coupling factor (k_p) and relative permittivity (ε_r) of the composition in various BNT-based piezoelectric ceramics

BNT based solid-solution	d_{33} (pC/N)	K_p	ε_r	Reference
$(1-x)(Na_{0.5}Bi_{0.5})TiO_3$-$xBiAlO_3$	130	0.23	2500	Yu *et al.* [81]
Nd_2O_3 doped $0.82Bi_{0.5}Na_{0.5}TiO_3$-$0.18Bi_{0.5}K_{0.5}TiO_3$	134	0.27	925	Yang *et al.* [96]
0.94BNT-$0.06BaTiO_3$	122	0.29	601	Takenaka *et al.* [104]
$(1-x)(Bi_{1/2}Na_{1/2})TiO_3$-$xNaNbO_3$	83	---	2300	Hiruma *et al.* [80]
$(1-x)$BNT-xBHT5	135	--	---	Tian et al. [86]
$0.88Na_{0.5}Bi_{0.5}TiO_3$-$12K_{0.5}Bi_{0.5}TiO_3$	100	----	1237	Mahboob et al. [110]
$0.98(Bi_{0.5}Na_{0.5})TiO_3$-$0.02NaNbO_3$	88	----	624	Li *et al.* [111]
$(1-x)BaTiO_3$-$x(Bi_{0.5}K_{0.5})TiO_3$ + $MnCO_3$ (BTBK-5 + Mn)	117	---	2300	Takenaka *et al.* [112]
$(Bi_{0.5}Na_{0.5})TiO_3$-$Ba(Ti,Zr)O_3$	147		8814	Yoo *et al.* [113]
$0.985(Bi_{0.5}K_{0.5})TiO_3$-$0.015LiNbO_3$	75	0.18	2800	Zuo *et al.* [114]
$0.975Bi_{0.5}Na_{0.5}TiO_3$-$0.025BiCoO_3$	107	---	3000	Guo *et al.* [115]
0.91BNT-$0.09Ba(Ti_{0.942}Zr_{0.058})O_3$	147	--	881.4	Peng *et. al. [105]*
0.88BNT-$0.12PbTiO_3$	106.6	0.332		Sakata *et al.* [116]
0.84BNT-$0.16(Bi_{0.5}K_{0.5})TiO_3$	--	0.314	--	Sasaki *et. al.[99]*
0.9BNT-$0.05(Bi_{0.5}K_{0.5})TiO_3$-$0.05BaTiO_3$	163	0.28	---	Li *et al.* [117]

1.9 RESEARCH MOTIVATION AND OBJECTIVES

BNT is a promising candidate in the field of piezoelectric applications due to its high piezoelectric constant and high Curie temperature. It is mostly suitable for ultrasonic applications on account of its low acoustic impedance that ensures maximum efficiency. BNT-based materials show high anisotropic electromechanical coupling property and a high frequency constant as compared to lead-based piezoelectric ceramics (useful in the field of electronic devices). However, pure BNT suffers from a large coercive field E_c = 73 $kVcm^{-1}$ at room temperature as well as a rhombohedral to tetragonal phase transition below the Curie point, both of which limit its usefulness in the transducer industry. Also, pure BNT ceramics are limited by some of their other shortcomings in electrical properties such as low relative permittivity (ε_r), narrow sintering temperature range and high conductivity at room temperature. In order to obtain useful lead-free piezoelectric ceramics some modification in the BNT ceramics have proven to be helpful by forming solid-solution with other perovskite systems [118-122]. This is a trade-off to make use of the solid-solution technique to substitute the individuals and seek for the merits of the selected materials.

The perovskite-type ferroelectric materials are enormously tolerant to variations in composition and distortions due to their ability to adapt a mismatch between the equilibrium A-O and B-O bond lengths, allowing the existence of a large number and variety of stoichiometric compounds. There are lots of reports on the solid-solution of many pervoskite materials with BNT as discussed in literature review. Most of the work shows that the property of the BNT based materials enhances near the morphotropic phase boundary. So the main objective of the thesis is to form BNT based solid-solutions with various pervoskites with special emphasize on the morphotropic phase boundary.

Among of the perovskite ferroelectric materials, most of the work has been done on $SrTiO_3$ and $BaTiO_3$ ceramics. So we have chosen $SrTiO_3$ and $BaTiO_3$ perovskite materials to form solid-solution with BNT because of their high dielectric constant and low loss factor. $SrTiO_3$ (ST) has a perovskite-type cubic structure with space group (Pm3m) and paraelectric nature at room temperature [123]. Below -168ºC, a transition to tetragonal structure is reported by Jauch and Palmer [124]. Its high dielectric permittivity combined with low dielectric loss can be interesting for various microwave application [125]. $BaTiO_3$ is one of the most investigated ferroelectric materials having high electro-optic coefficients, broad wavelength sensitivity range, high crystalline uniformity, and it displays a large variety of non-linear optical effects. Also, barium titanate displays superior dielectric, ferroelectric, piezoelectric, pyroelectric, polaron-semiconducting and electro-optical properties [126-129]; therefore it has been the base material for many important and widely-applied ceramic components and devices. Many reports are available on the existence of MPB in $(1-x)(Bi_{0.5}Na_{0.5})TiO_3$-$xBaTiO_3$ system with maximum value of piezoelectric constant and dielectric constant. Chu *et al*. reported the maximum value of piezoelectric constant and dielectric at 7% and 8.3% of BT respectively, Where as Pengpat *et al*. observed the MPB at 10% of BT in their work on the (1-*x*)BNT-*x*BT system [130,131]. Takanaka et al. observed relatively good piezoelectric properties in (100-*x*)BNT-*x*BT system at the MPB around the composition of x = 6-7 [132]. Hosono *et al*. reported maximum dielectric constants and piezoelectric coupling factors in the composition range x = 5-9 on single crystals [133]. Jo *et al.* reported maximum piezoelectric coefficient occurs at x = 7, in (100-*x*)BNT-*x*BT solid-solution. Even if a number of studies have been carried out to improve the properties of BNT-BT system near the MPB compositions; however, exclusive studies regarding MPB are rare in the literature. Rietveld refinements and

Raman spectroscopy have been used as effective techniques to investigate the structural evolution in perovskite solid-solutions. However, limited reports are available on Raman spectroscopy studies but Rietveld refinements are not well reports of BNT-based systems.

There are very few reports on the solid-solution of complex pervoskite with BNT material. The modified $BaTiO_3$ pervoskite have been investigated to develop high quality lead free ceramics. One of the major problems with BT is that there is a conflict between the significant hysteresis in the strain and the electric field dependence of the material which leads to increasing difficulty in controlling $BaTiO_3$ based piezoelectric components. It is reported that the properties of $BaTiO_3$ can be tailored by substituting or doping at A and/ or B site of the prervoskite. Substitution of cations in the A-site can either increase or decrease the transition temperature without significantly broadening the transition. Substituting cations into the B-site can disrupt ferroelectric domains, broaden structural transition considerably, significantly reduce transition temperature and increase the permittivity maximum. Many studies shows that the substitution of Ti^{+4} by Zr^{+4} in $BaTiO_3$ can significantly improve overall properties of the material as Zr^{+4} is more stable than Ti^{+4} [134-137]. $Ba(Zr_{0.25}Ti_{0.75})O_3$ (BZT), which is a B-site complex perovskite-type cubic structure with space group (Pm3m) and relaxor ferroelectric [138]. The compounds have a wide range of applications such as transducers, capacitors, electro-acoustic transformers, signal processing devices, ultrasonic miniature motors, micropositioners, deformable mirrors in optical switching, etc. Again it is also reported in literature is the BNT exhibits relaxor ferroelectric behavior. So BNT-BZT solid-solutions have been prepared to improve its relaxor behavior along with dielectric, ferroelectric and piezoelectric properties.

The main objective of the proposed work is to improve the property of BNT by preparing solid-solutions with various pervoskite (ST, BT and BZT) with general formula (1-*x*)($Bi_{0.5}Na_{0.5}$)TiO_3-*x*$SrTiO_3$, (1-*x*)($Bi_{0.5}Na_{0.5}$)TiO_3-*x*$BaTiO_3$ and (1-*x*)($Bi_{0.5}Na_{0.5}$)TiO_3-*x*Ba($Zr_{0.25}Ti_{0.75}$)O_3, *x* ranging from 0.0 to 0.08. Their detailed structural study is studied by x-ray diffraction, Rietveld refinement and Raman spectroscopy with special attention paid to the MPB composition. Their dielectric, impedance spectroscopy, ferroelectric, electro mechanical and piezoelectric will be studied. The presence of MPB is also confirmed by dielectric and piezoelectric behavior. For various industrial applications electromechanical properties of the solid-solutions showing MPB will be studied. The optical properties will be studied by UV-Visible spectroscopy.

CHAPTER 2

EXPERIMENTAL TECHNIQUES

OUTLINE: This chapter describes the experiments that were designed to fulfill the objectives set out in Chapter 1. The whole Thesis has investigated $(Bi_{1\2}Na_{1\2})TiO_3$ (BNT) and its three different BNT-based solid-solutions systems: (i) $(1-x)(Bi_{1\2}Na_{1\2})TiO_3$-$xSrTiO_3$, (ii) $(1-x)(Bi_{1\2}Na_{1\2})TiO_3$-$xBaTiO_3$ and (iii) $(1-x)(Bi_{1\2}Na_{1\2})TiO_3$-$xBa(Zr_{0.25}Ti_{0.75})\ TiO_3$.

For the remainder of this Thesis, these three systems will be abbreviated as (1-*x*)BNT-*x*ST (or BNT-ST), (1-*x*)BNT-*x*BT (or BNT-BT) and (1-*x*)BNT-*x*BZT (or BNT-BZT), respectively, where *x* refers to the amount of non-BNT compounds added with BNT. Pure $(Bi_{1\2}Na_{1\2})\ TiO_3$ ceramics (abbreviated as BNT) were also prepared and characterized as a baseline for comparison of the effectiveness of the additives. The materials and methods used to synthesize and characterize the ceramics are given in the following sections.

2.1 MATERIALS AND POWDER SYNTHESIS

Commercially available high purity (greater than 99% purity), ultra-fine grain size (≤1μm) starting reagents (powders) of bismuth oxide (Bi_2O_3), titanium oxide (TiO_2), sodium carbonate (Na_2CO_3), strontium carbonate ($SrCO_3$), barium carbonate ($BaCO_3$) and zirconium oxide (ZrO_2) were used as the starting materials in the fabrication of the BNT and the above three BNT systems (Table 2.1).

Ceramic materials are one of the major groups in the field of Materials Science because of their direct and indirect applications in day-to-day life. Hence, the synthesis of new ceramic powders is of great importance in the progress of Materials Science.

Table 2.1: Raw materials used in the synthesis of BNT and BNT-based solid-solutions

Chemical Name	Chemical Formula	Purity	Particle (mesh) Size	Source
Bismuth oxide	$Bi_2 O_3$	99.9%	10 µm	S.D. Fine Chemical Ltd., Mumbai
Sodium carbonate	Na_2CO_3	≥99.99%	_	Loba Chemicals Pvt. Ltd., Mumbai
Titanium oxide	TiO_2	99.9%	_	E.Merck Specialties Pvt. Ltd., Mumbai
Barium carbonate	$BaCO_3$	≥99.8%	2.09 µm	S.D.Fine ChemicalLtd., Mumbai
Strontium carbonate	$SrCO_3$	≥99.9%	13.13 µm	S.D.Fine ChemicalLtd., Mumbai
Zirconium oxide	ZrO_2	99.8%	10.27 µm	Loba Chemicals Pvt. Ltd., Mumbai

2.1.1 Solid-Solution

A solid-solution is formed when two materials are completely soluble in liquid state and also completely soluble in solid state. In other words, when homogeneous mixtures of two or more kinds of atoms occur in the solid state, they are known as solid-solutions. The more abundant atomic form is referred as solvent and the less abundant atomic form is referred as solute. Also as the dopant concentration rises, above ~0.1 to 1 percent, it is a common practice to refer to the materials as solid solutions rather than as doped materials. Solid-solutions are of two types. These are: (a) Substitutional solid-solutions and (*b*) Interstitial solid-solutions.

(a). Substitutional Solid-Solutions

The atom or ion that is being introduced directly replaces an atom or ion of the same charge in the parent structure. In other words, if the atoms of the solvent or parent metal are replaced in the crystal lattice by atoms of the solute metal then the solid solution is known as substitutional solid-solution, as shown in Fig.2.1.

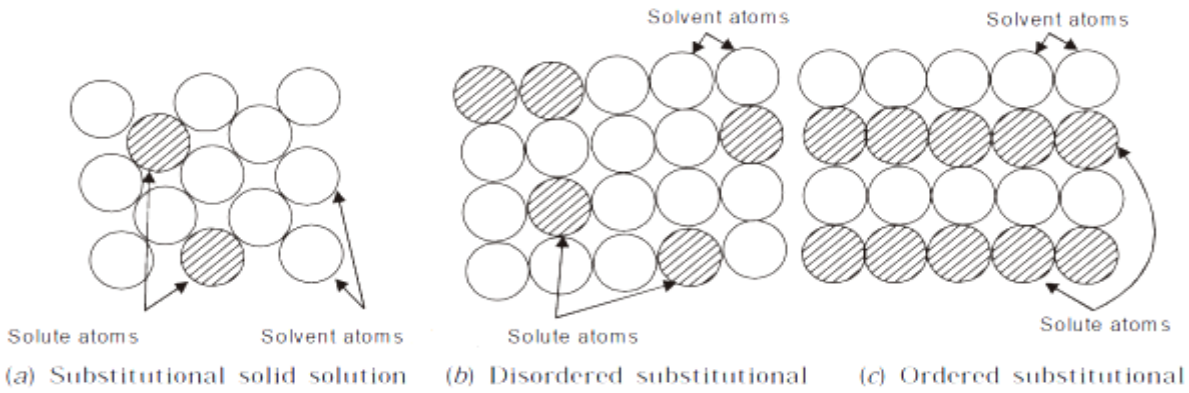

Fig.2.1: Substitutional solid-solutions

(b). Interstitial Solid-Solutions

The introduced species occupies a site that is normally empty and no ions or atoms are left out. In other words, in interstitial solid-solutions, the solute atom does not displace a solvent atom, but rather it enters one of the holes or interstices between the solvent atoms. Normally, atoms which have atomic radii less than one angstrom are likely to form interstitial solid-solutions (see Fig.2.2).

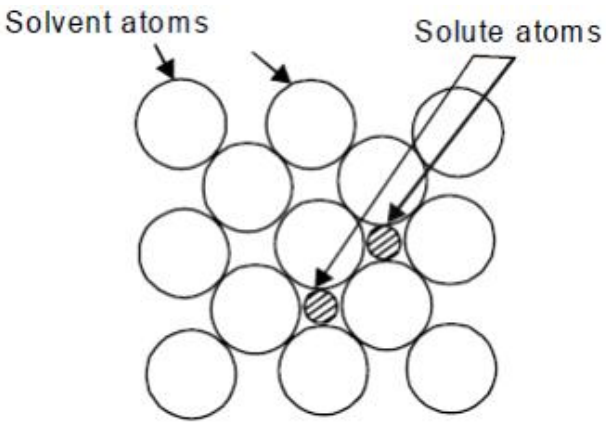

Fig.2.2: Interstitial solid-solutions

2.1.2 Solid-State Reaction

There are several methods of preparation such as the mechanical method, which includes solid-state reaction, and ball-milling, etc., and the chemical method, which includes sol-gel,

wet-dry and polymer-sol-gel, etc. To achieve a quality product with respect to purity, homogeneity, reactivity, particle size, etc., each method finds its own advantages and disadvantages. In this context, the solid-state reaction is found to be the easier, convenient and low cost technique among other available methods as regards to performance, reliability, reproducibility and economy.

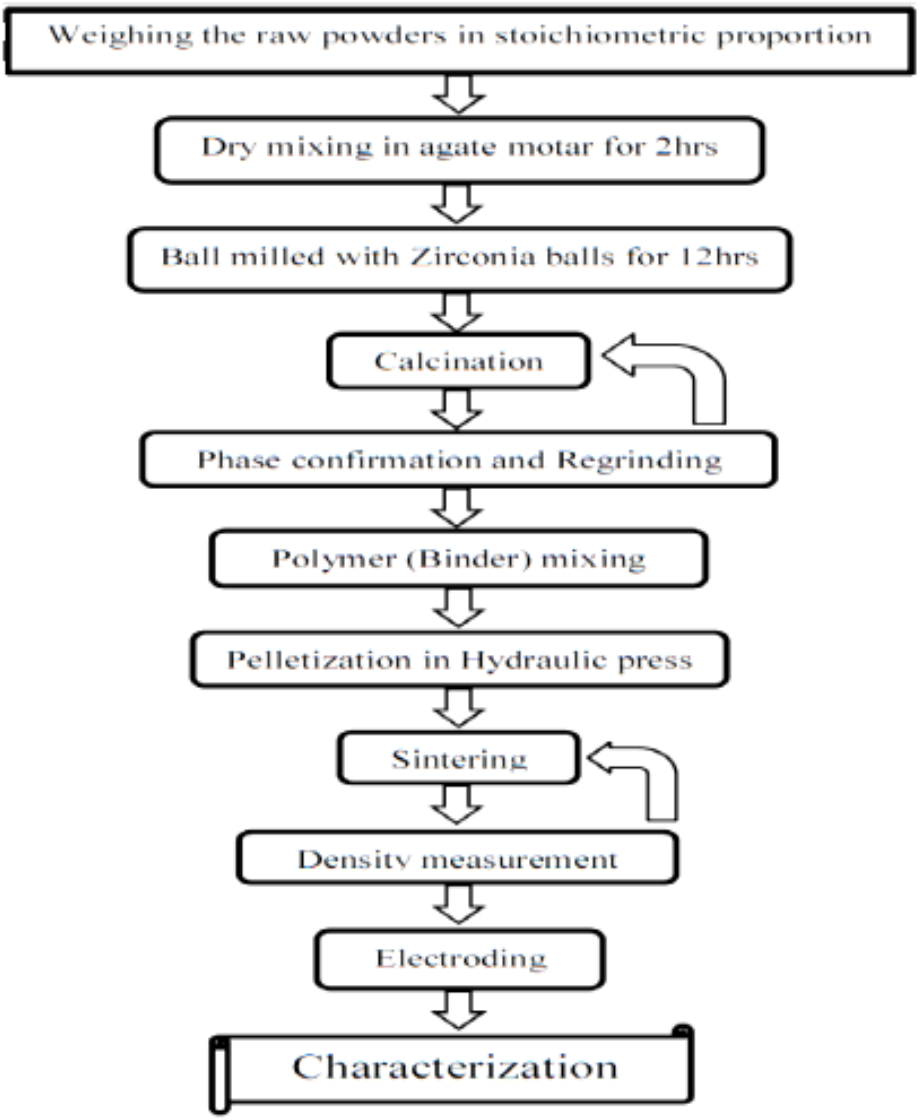

Fig.2.3: Flow chart of sample preparation

The various steps in the solid-state reaction process are represented as a flow chart shown in Fig. 2.3 In the present work, raw chemicals with high purity were used for the material

preparation. The constituents of the required specimen were taken in a stoichiometric ratio and dry mixed followed by wet mixing with distilled water as the medium. The mixing was accomplished using agate mortar and pestle. The amount of water used was just enough to form slurry to prevent the selective sedimentation of the reagents.

After proper mixing, mixed powders were calcined at different temperatures (detailed heat treatments are cited in the text) by an indigenous programmable furnace with intermediate grinding to avoid agglomeration of the particles. The calcined powders were used for the study of their phase formation as well as their reaction mechanism. After studying the phase formation, the powders were again grinded and mixed with polyvinyl alcohol (PVA) (which acts as a binder) to reduce the brittleness, and to have better compactness amongst the granules of the materials. To get uniform and fine grains, the granules were passed through a 73 μm sieve. The residues after sieving were again crushed in an agate mortar and passed through the sieve. The process was repeated till all the granules became less than 73 μm. The green pellets of dimension 11 mm diameter and 1 mm thickness were made using uniaxial press with the help of tungsten carbide dye.

2.2 STRUCTURAL CHARACTERIZATION

The following characterizing tools were used to study the structural, electrical and optical study of the ceramics.

2.2.1 X-Ray Diffraction Study

X-ray diffraction (XRD) technique is a powerful tool for material characterization as well as for detailed structural elucidation. As the physical properties of solids (electrical, optical, magnetic, ferroelectric, etc.) depend on atomic arrangements of materials, determination of the crystal structure is an indispensable part of the characterization of materials, mainly the

identification of the chemical species. x-ray diffraction patterns are used to establish the atomic arrangement or structure of the materials because the d spacing of diffraction planes is of the order of x-ray wavelength λ, the various orders n of reflection occur only at the precise values of the angle θ, which satisfies the Bragg equation given by $n\lambda = 2d\sin\theta$. The powder profile of a substance, even without further interpretation, can be used for identification of materials. The accurate determination of lattice parameters provides an important basis in understanding various properties of the materials. The calculation of lattice constants from the line positions or d-spacing can be done from a general formula:

$$\frac{1}{d_{hkl}^2} = V^2[h^2b^2c^2\sin^2\alpha + k^2c^2a^2\sin^2\beta + l^2a^2b^2\sin^2\gamma] \quad (2.1)$$

where; V = volume of the unit cell

$$= abc(1-\cos^2\alpha -\cos^2\beta -\cos^2\gamma+\cos\alpha\cos\beta\cos\gamma)^{1/2} \quad (2.2)$$

where a, b, c, α, β and γ are lattice parameters and h, k, l are the Miller indices. Using the above formula, lattice parameters for all the compositions were found out. The kinematics theory of x-ray diffraction describes that for a perfect cause the spread in the intensity distribution curves, the nature and the extent of the intensity spread is an obvious measure of crystal imperfection present in the sample under study. Since the different types of defects may be co-existent in crystalline materials, the problems that arise are of separation of different types of defects and identification and quantitative estimation of the extent and distribution of each type of defects. The different factors affecting the diffraction intensities can be grouped into a single expression for use in calculating the relative intensities of reflections. For the powder method, the intensity (I) is given by

$$I = J\ \frac{1+Cos^2 2\theta}{4Sin^2\theta Cos\theta}\ F^2\ A\ (\theta) \quad (2.3)$$

where J is the multiplicity factor and F is the structure factor, which can be written as

$$F = \sum_j f_j \exp 2\Pi i\,(hx_i + ky_j + lz_j) \qquad (2.4)$$

where f_j = atomic scattering factor and $A(\theta)$ = absorption coefficient = $\frac{1}{V}\int e^{-\mu x} dx$

where μ is the linear absorption coefficient of the specimen, x is the distance traversed by the beam and V is the volume of the crystal exposed to x-rays. A very important aspect of the intensity distribution among the reflections is to relate the extinction, which is a deciding factor for the symmetry elements involved in the material. The translations involved in these symmetry elements and centered lattices add a new periodicity in the patterns, which shows itself by extinguishing certain classes of x-ray spectra. Each type of extinction is characteristic of a particular space group. Therefore, the absence of such characteristic spectra from the diffraction data is a major criterion for the determination of the lattice type and the space group.

The following information can be obtained from the x-ray powder diffractogram:

(i) Quality and confirmation of the prepared samples

(ii) The interplaner spacing d of the reflections

(iii) The intensities of the reflections

(iv) The unit cell dimensions and lattice type.

In the present case, calcined powders were characterized with respect to phase identification, phase quantity measurement, crystallite size determination and lattice parameter measurement, etc., all by using Cu-Kα XRD (Xpert MPD, Philips, UK). For quantitative estimation of phases, calcined powders were uniformly mixed and the resulting mixture was analyzed using a step size of 0.02^o, 2θ with 10 second/step. The relative weight fractions were quantified from the ratio of peak areas. The phases giving maximum peak area at a particular temperature were considered as 100% formation of those phases at that temperature. Considering that area as

100%, the relative percentages of the respective phases were calculated. On the basis of XRD line broadening at half maxima of the 100% RI peak, crystallite sizes of the phases were estimated using the Scherer equation:

$$P=k\lambda/\beta_{1/2}\ \mathrm{Cos}\ \theta_p \qquad (2.5)$$

where P: linear particle size, k: 0.89, θ_p: peak position, $\beta_{1/2}$: half-peak width.

2.2.2 Rietveld-Refinement Analysis

The Rietveld-refinement is a method in which the profile intensities are obtained from step-scanning measurements of the ceramics rather than from integrated powder peak intensity and allow estimating an approximate structural model [139]. There is a simple relationship between the individual scale factor determined, considering all refined structural parameters of individual phases of a multiphase sample, and the phase concentration (volume/weight fraction) in the mixture. The structure refinement along with size-strain broadening analysis was carried out simultaneously by adopting the standard procedure. Particle size and lattice strain values of all the phases were found to be isotropic. The process of successive profile refinements modulates different structural and microstructural parameters of the simulated pattern to fit the experimental diffraction pattern. Refinement continues till convergence is reached with the value of the quality factor.

Initially, the positions of the peaks were corrected by successive refinements of systematic errors taking into account the zero-shift error and sample displacement error. The *U*, *V*, *W* parameters of instrumental broadening, instrumental asymmetry and Gaussianity of reflections were estimated for the present setting of the instrument using a specially prepared Si standard and found to vary with scattering angle in different manners. Structure and microstructure refinements were carried out simultaneously by refining, scale factors, lattice parameters,

occupancy factors, variable fractional atomic coordinates, particle size, r.m.s. lattice strain, preferred orientation factors, etc. of individual phases. Considering the integrated intensity of the peaks as a function of structure/microstructure parameters only, the Marquardt least-squares procedures were adopted for minimizing the difference between the observed and simulated powder diffraction patterns. The minimization was carried out by using the reliability index parameters given by

The profile R-factor $$R_p = \frac{\sum_i |y_{io} - y_{ic}|}{\sum_i y_{io}} \quad (2.6)$$

The weighted Rp $$R_{wp} = \left[\frac{\sum_i w_i (y_{io} - y_{ic})^2}{\sum_i w_i y_{io}^2} \right]^{\frac{1}{2}} \quad (2.7)$$

The Bragg R-factor $$R_B = \frac{\sum_i |I_{ko} - I_{kc}|}{\sum_i I_{ko}} \quad (2.8)$$

The expected Rf $$R_{\exp} = \left[\frac{N - P}{\sum_i w_i y_{io}^2} \right]^{\frac{1}{2}} \quad (2.9)$$

The goodness of fit $$GOF = \frac{\sum_i w_i (y_{io} - y_{ic})^2}{N - P} = \left(\frac{R_{wp}}{R_{\exp}} \right)^2 \quad (2.10)$$

Volume fraction $$V = \frac{SV_e^2}{\sum_p (SV_e^2)_p} \quad (2.11)$$

Weight fraction $$m = \frac{SZMV_e^2}{\sum_p (SZMV_e^2)_p} \quad (2.12)$$

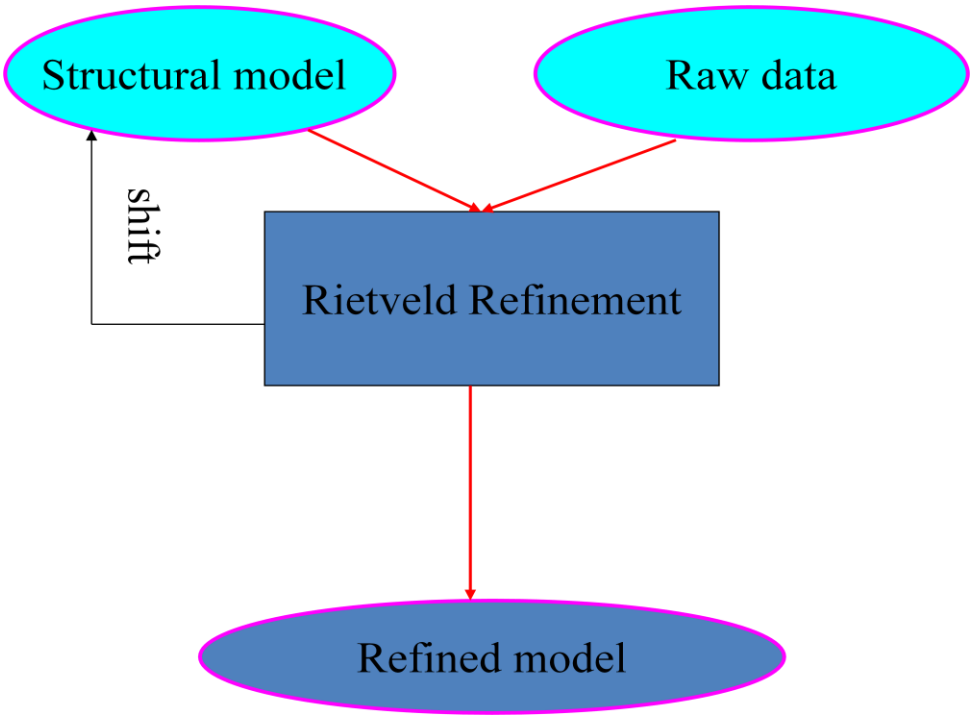

Fig.2.4: Flow chart of Rietveld-refinement

Use the correct occupancies: N = occupancy / max # of Wyckoff positions. Z is the number of formula units per cell, M is the atomic weight of the formula unit and V_e is the volume of the unit cell. The goodness of fit (GOF) is established by comparing R_{wp} with the expected error, R_{exp}. The weight fraction (m) for each phase was obtained from the refinement relation.

In this work, the Rietveld-refinement was performed through the GSAS program [140]. In the Rietveld analysis, the refined parameters were scale factor, background, shift lattice constants, profile half-width parameters (u, v, w), isotropic thermal parameters, strain anisotropy factor, occupancy, atomic functional positions, bond lengths and bond angles. The background was corrected using a Chebyschev polynomial of the first kind. The diffraction peak profiles were better fitted by the Thompson-Cox-Hastings pseudo-Voigt (pV-TCH) function and by the asymmetry function described by Finger *et al*. [141]. The strain anisotropy was corrected by the phenomenological model described by Stephens *et al*. [142].

2.2.3 Sintering

Density of the electronic ceramics is a very sensitive parameter and that directly affects their properties. Therefore, proper sintering of the pellets is essential for electrical measurement. All the pellets were taken in an alumina plate and sintered at different temperature in a programmable furnace at a heating rate of 5^oC per minute with an intermediate shocking of 2 hours at 600^oC for organic binder removal in the initial heat treatment.

2.2.4 Density Determination

After the heat treatment on the samples, the dry weights of the pellets were measured by a digital electronic balance. Then the samples were given different identification to avoid any confusion and kept together in a glass beaker. The samples-containing beaker was kept in a vacuum oven and heated at 100^oC. At this temperature water starts boiling and simultaneously vacuum was also created by the use of a suction pump. By heating the samples in the vacuum for 30 minutes, the pores present in the pellets were completely filled with water. The heater of the oven was switched off and the vacuum was slowly released. Now the beaker was taken out of the oven. The weight of the pellets was taken in a digital electronic balance and interpreted as soaked weight. After the soaked weights were taken, the samples were suspended in water with the help of a specially designed hanger to hang the pellets inside water and the measured weight was interpreted as suspended weight. The experimental bulk density and apparent porosity were measured by using Archimedes principle;

$$\text{Bulk Density} = D / (W-I) \tag{2.13}$$

$$\text{Apparent Porosity} = (W-D) / (W-I) \tag{2.14}$$

where, D:Dry weight, W:Soaked weight and I:Suspended weight.

X-ray densities were calculated as suggested by B.D. Cullity:

$$\rho = \frac{\sum A}{NV}$$

$$= 1.66042 \frac{\sum A}{V} \quad (2.15)$$

where ρ is X-ray density (g/cc), $\sum A$ is the sum of the atomic weights of all the atoms in the unit cell, N is Avogadro's number and V is the volume of a unit cell. If the composition is of atomic weight A, then

$$\sum A = n_1 M \quad (2.16)$$

where n_1 is number of molecules per unit cell and M is molecular weight

The macroscopic density or the experimental bulk density of a particular specimen, determined from Archimedes principle, is usually less and that can't be exceeded by the X-ray density because the macroscopic specimen usually contains some cracks and pores.

2.2.5 Scanning Electron Microscopy (SEM) and Energy Dispersive X-ray Spectroscopy (EDX)

The scanning electron microscopy (SEM) is a useful technique to study the topography, morphology and composition of the materials with much higher resolution. When a beam of highly energetic electrons strikes the sample, the secondary electrons, x-rays and back-scattered electrons are ejected from the sample. These electrons are then collected by the detector and converted into a signal that displays on a screen. In the present study, the SEM micrograph was taken on the fractured surface of the sample using a scanning electron microscope (SEM: JSM-840 scanning microscope JEOL). As the samples were non-

conducting, a thin layer of platinum was coated using a sputter coater. The average grain sizes of the samples were determined using the line-intercept method on micrographs taken using the SEM. Minimum 10 lines, each having the length not less than 200 micrometers were drawn on the different places of a single micrograph and average grain sizes were calculated to minimize the error. The chemical composition of the samples has been determined by energy dispersive x-ray spectrometry (EDX).

The energy dispersive x-ray spectroscopy (EDX or EDS) is a method used to determine the energy spectrum of x-ray radiation. This technique is used in conjunction with SEM and is not a surface science technique. An electron beam strikes the surface of a conducting sample. The energy of the beam is typically in the range 10-20 keV. This causes x-rays to be emitted from the point of material. The energy of the x-rays emitted depends on the material under examination. The x-rays are generated in a region about 2 microns in depth. By collecting and analyzing the energy of the x-rays, the constituent elements of the specimen can be determined. The output of an EDX analysis is an EDX spectrum. An EDX spectrum normally displays peaks corresponding to the energy levels for which the most x-rays have been received. Each of these peaks is unique to an atom and therefore corresponds to a single element.

The higher the peak in a spectrum, the more concentrated element is in the specimen. Elements of low atomic number are difficult to detect by EDX. This analytical tool allows simultaneous non-destructive elemental analysis on the sample.

An EDX spectrum plot not only identifies the element corresponding to calls of its peak, but the type of x-ray to which it corresponds as well. For example, a peak corresponding to the amount of energy possessed by x-rays emitted by an electron in the *L*-shell going down to the

K-shell is identified as a K_α peak. The peak corresponding to x-rays emitted by *M*-shell electrons going to the *K*-shell is identified as a K_β peak.

2.2.6 Raman Spectroscopy

Raman spectroscopy is an appropriate tool to get more insight into the local distortions, disorder and the strain present in the system because the vibrational spectrum has shorter characteristic length scale than required for the diffraction experiment. Raman scattering is also a useful tool to study the dynamics of structure by analyzing the characteristic modes associated with nano regions. The selection rules are very sensitive to the local and global symmetries. In crystalline solids, the Raman effect deals with phonons instead of molecular vibrations. A phonon can be active only in the crystals with no centre of inversion.

The Raman spectra are usually plotted in intensity versus the difference in wave number between the incident beam and the scattered beam and the peaks are in correspondence to the phonon frequency. Due to the small wave vector of the optical photons, the phonons involved in the Raman scattering of crystalline solids have (from the wave vector conservation law) a very small momentum compared with the Brillouin zone. So only the zone-centered phonons participate to the Raman scattering.

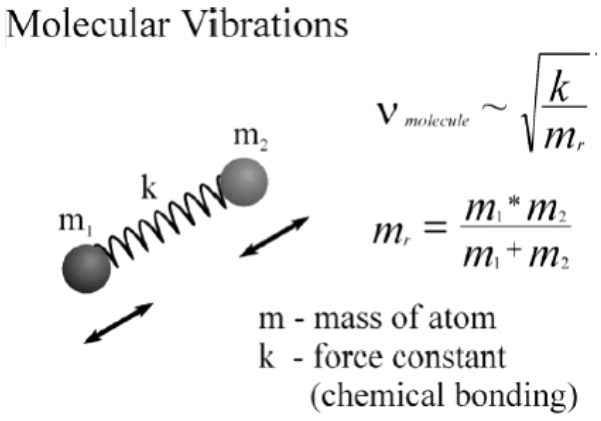

Fig.2.5: Model for the molecules

Light is treated as an electromagnetic wave and the molecules are modeled as small spheres connected by the spring as shown in the Fig.2.5.

2.3 ELECTRICAL PROPERTIES

The electromechanical properties were measured to evaluate the different additives to the BNT ceramics in terms of how much they improved or changed the properties. The following parameters were determined:

1. Dielectric constant (ε_r) and losses (tan δ)

2. Electrical impedance (Z), modulus (M) and conductivity (σ)

3. Piezoelectric coefficient (d_{33}) (poling properties)

4. Coercive field (E_C) and remanent polarization (P_r) (P~E loop).

For electrical characterization the sintered ceramics were painted with a lead-free, sliver-based electrode on their surfaces according to the manufacturer's instructions.

2.3.1 Electroding

The selection of suitable electrode for the test materials is important. In our case the contacting, conducting, thin-film electrode method is adopted because: (i) it causes minimum error caused by air gap between the electrode and surface of the test material, which is more in case of contacting rigid-metal electrode method, and (ii) procedures to measure dielectric constant are simple, which are relatively complex in non-contacting electrode method. In our case, all the ceramic bodies after sintering were polished well and coated on both sides with conducting silver paste. For organic removal printed disks were kept on an alumina plate and fired at 500^oC for 20 minutes. This procedure was repeated twice for better electroding.

2.3.2 Dielectric Measurement

There are several types of polarizations, each of which can be explained by its intrinsic physical mechanism. The three basic types of polarizations are electronic, ionic and orientational. When an insulator is placed in an external electric field, electrons of the atoms are displaced slightly with respect to the nuclei, so induced dipole moments result and cause the electronic polarization. When the atoms of a molecule do not share their electrons symmetrically, the electron-clouds will be displaced eccentrically towards the stronger binding one. Thus the ions acquire charges of opposite polarity. These net charges will tend to change the equilibrium positions of the ions themselves under the action of an external electric field. This displacement of charged ions or groups of ions with respect to each other creates a second type of induced dipole moment. It represents the ionic polarization of the unlike partners of molecule giving rise, in addition to permanent dipole moments, which exist even in the absence of an external electric field. Such dipoles experience a torque in an electric field that tends to orient them in the direction of the field. Consequently, an orientation (or dipole) polarization can arise. These three mechanisms of polarization are due to charges locally bound in atoms, molecules or in the structure of solids. In addition to all these, there usually exist charge carriers that can migrate for some distance through the dielectric. Generally, carriers are impeded in motion because of being trapped in the materials interfaces. Hence, they cannot freely discharge at the electrodes and space charges result. Such distortion appears as an increase in the capacitance of the sample and may be distinguishable from a rise of the dielectric constant. Thus, a fourth polarization, called the space charge (or interfacial), comes into play. For electronic and ionic polarizations, the frequency effect is negligible upto about 1010 Hz. As the optical range of frequencies is reached, electronic contribution becomes the

sole contributor. The effect of temperature on both electronic and ionic polarizations is small. At higher temperatures, polarization increases due to ionic and crystal imperfection mobility. The combined effect produces a sharp rise in the dielectric constant at low frequency with increasing temperature corresponding to both dipole orientation effects and space charge effects. The total polarization is a sum of these four polarizations (assuming that they act independently) [13].

When the dielectric is placed in alternating fields, these polarizations are set up and give rise to the dielectric constant. A temporal phase shift is found to occur between the driving field and the resulting polarization and a loss current component appears giving rise to the dielectric loss of the sample. Here this polarization, *P*, as well as the electric displacement, *D*, vary periodically with time. In general, however, *P* and *D* may lag behind in phase relative to electric field *E*, so that

$$D = D_0\cos(\omega t - \delta) = D_1\cos\omega t + D_2\sin\omega t \qquad (2.17)$$

where δ is the phase angle and slightly less than 90°,

$$D_1 = D_0\cos\delta \quad \text{and} \quad D_2 = D_0\sin\delta$$

The ratio of displacement vector to electric field (D_0 / E_0) is, in general, frequency dependent for most of the dielectrics. Hence, we can introduce two frequency-dependent dielectric constants:

$$\varepsilon'(\omega) = (D_0 / E_0)\cos\delta \qquad (2.18)$$

$$\varepsilon''(\omega) = (D_0 / E_0)\sin\delta \qquad (2.19)$$

These two constants can be expressed in terms of a single complex dielectric constant, $\varepsilon^* = \varepsilon' - j\varepsilon''$. As the applied voltage (*V*) varies periodically with time as:

$$V = V_0 e^{i\omega t}$$

the total current, $I = \frac{dQ}{dt} = \frac{d(CV)}{dt} = j\omega C\,V = j\omega\varepsilon C_0 V$ (2.20)

where, C and C_0 are the capacitance in a dielectric medium and vacuum, respectively. Therefore,

$$I = j\omega C_0 V(\varepsilon' - j\varepsilon'') = \omega\varepsilon'' C_0 V + j\,\omega\varepsilon' C_0 V' = I_l + I_c \quad (2.21)$$

The tangent loss is given by $\tan\delta = I_l / I_c = \varepsilon'' / \varepsilon'$ (2.22)

The total current I through the capacitor can be resolved into two components, a charging current (I_c) in quadrature with voltage and conduction current I_l in phase with the voltage. The vector resolution of the total current is shown in Fig. 2.6.

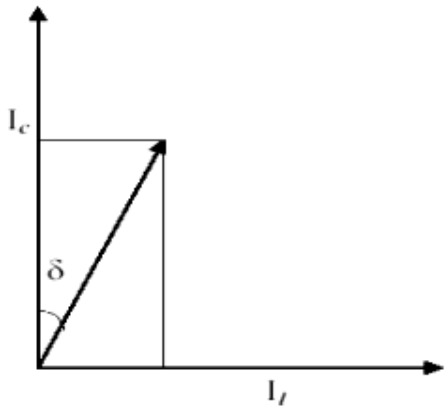

Fig.2.6: The vector resolution of ac current in a capacitor

For a parallel plate capacitor with sinusoidal applied voltage, loss current density is given by

$$J_l = \omega\,\varepsilon_0\,\varepsilon''\,V = \sigma\,V \quad (2.23)$$

$$\text{where } \sigma = \omega\,\varepsilon'\,\varepsilon_0 \tan\delta \quad (2.24)$$

is the dielectric conductivity. The effective conductivity defined in this manner depends upon frequency and is always greater than dc conductivity. The loss factor is the primary criterion for the usefulness of a dielectric as an insulator. So, for application purposes where high capacitance in the smallest physical space in required, materials with high dielectric constant and low tangent loss (tanδ) must be used. The dielectric properties of ferroelectrics depend on the field strength at which they are measured. This is a consequence of non-linear relation between polarization and electric field.

To measure the relative permittivity (dielectric constant) and dielectric loss, LCR meter can be used. In this work, LCR Tester (Hioki 3532, Japan, 42*Hz*-1*MHz*) was used to measure the dielectric constant and dielectric loss. The electrode samples were used to make the measurements. The LCR meter was interfaced with the computer and the data (capacitance and *D* factor) were collected as a function of temperature at different frequencies. The measured capacitance was then converted into dielectric constant using the following formula:

$$C = \varepsilon_0 \varepsilon_r \frac{A}{d} \tag{2.25}$$

$$\varepsilon_r = (C\ d)/(\varepsilon_0 A) \tag{2.26}$$

where, *C:* Capacitance in farad (*F*)

ε_0*:* Permittivity of free space in farad per meter ($8.854 \times 10^{-12} F/m$)

ε_r : Dielectric constant or relative permittivity of the sample

A: Area of each plane electrode in square meters (m^2)

d: Separation between the electrodes in meters (*m*).

The measured capacitance and conductance were then converted into dielectric loss using the following formula:

$$\tan\delta = \frac{G}{\omega C} \tag{2.27}$$

where *G*: Conductance of the sample (Ω^{-1}), *C*: Capacitance in farad (*F*) and ω: Angular frequency (rad/sec)

2.3.3 Impedance Spectroscopy

The complex impedance spectroscopy is a powerful tool to investigate the electrical properties of the complex perovskite oxides. The main advantages of the technique are i) it involves

relatively simple electrical measurements that can readily be automated, ii) the measurements can be implemented by using arbitrary electrodes, iii) the results can be often correlated with the properties such as composition, microstructure, defects, dielectric properties, chemical reaction, etc. of the sample and iv) the resistance of the grain boundaries and that of grains can be easily separated in most of the polycrystalline samples. AC measurements are often made with a Wheatstone-bridge-type of apparatus (impedance analyzer or LCR meter) in which the resistance *R* and capacitance *C* of the sample are measured and balanced against variable resistors and capacitors. The impedance $|Z|$ and the phase difference (θ) between the voltage and current are measured as a function of frequency for the given sample and the technique is called impedance spectroscopy. Analysis of the data is carried out by plotting the imaginary part of the impedance $Z''=|Z|cos\theta$ against the real part $Z'=|Z|sin\theta$ on a complex plane called the impedance plot. An impedance plot with linear scale is used to analyze the equivalent circuit as follows. Impedance plot of a pure resistor is a point on real axis and that of pure capacitor is a straight line coinciding with the imaginary axis. The impedance of a parallel *RC* combination is expressed by the following relation,

$$Z^* = Z' - jZ'' = R / 1+j\omega RC \qquad (2.28)$$

After simplification, one gets

$$(Z' - \tfrac{R}{2})^2 + Z''^2 = (\tfrac{R}{2})^2 \qquad (2.29)$$

which represents the equation of a circle with radius *R/2* and centre at (*R/2*, *0*). Thus, a plot of *Z'* vs. *Z''* (as parametric function of Ω) will result in a semicircle of radius *R*/2 as shown in Fig.2.7 (a) and the equivalent circuit is shown in Fig.2.7 (b). (This plot is often called a Nyquist plot). The time constant of the simple circuit is defined as $t = RC = 1/\omega_m$. This corresponds to the relaxation time of the sample and the characteristic frequency lies at the

peak of the semi-circle. In an ideal polycrystalline sample, the impedance plot exhibits an arc at high frequency corresponding to the bulk property of the sample, an arc at low frequency corresponding to the grain boundary behavior and a spike at the lowest frequency corresponding to the electrode effect. Fig.2.8 (a) shows a typical impedance plot for a polycrystalline sample and Fig.2.8 (b) represents the equivalent circuit. In the present work, impedance measurements have been performed using Hioki LCR tester in the frequency range 42 Hz – 1 *MHz* at different temperatures.

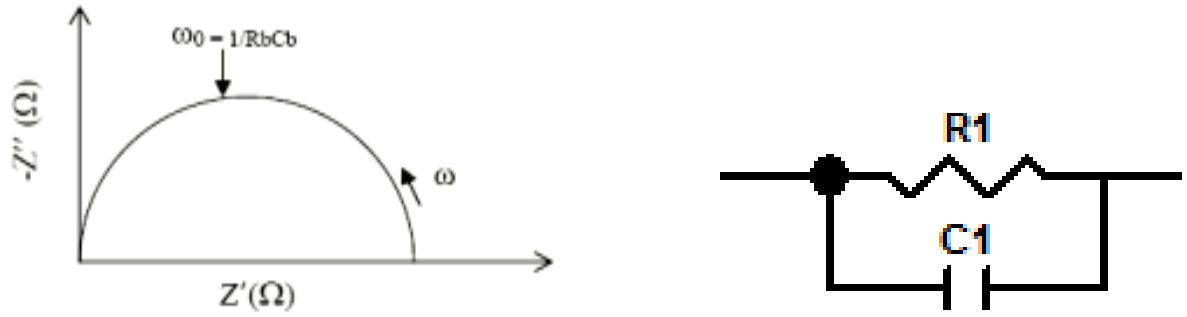

(a) (b)

Fig.2.7: (a) The impedance plot for the circuit of a resistor and a capacitor in parallel and (b) the corresponding equivalent circuit

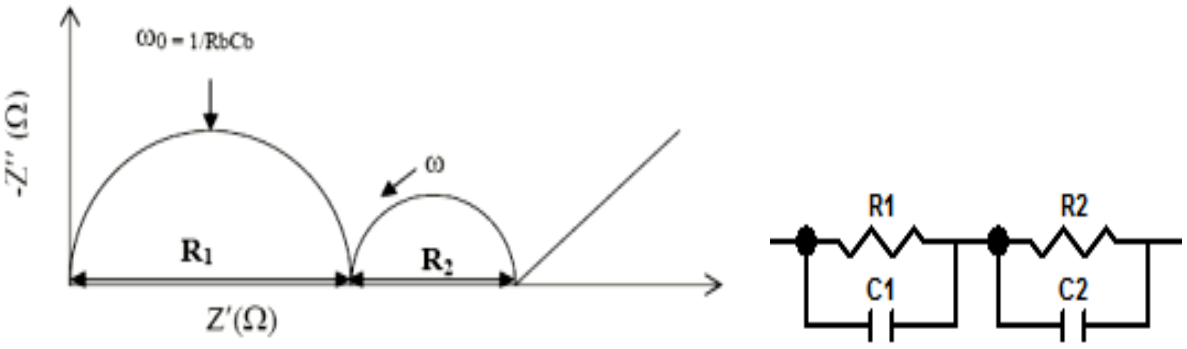

(a) (b)

Fig.2.8: (a) The impedance plot for an ideal polycrystalline sample and (b) the corresponding equivalent circuit

2.3.4 Modulus Spectroscopy

The complex modulus spectroscopy study is an informative and powerful technique in materials research which gives vital information regarding the distribution parameters of different micro regions in the polycrystalline materials, such as grain, grain boundary and electrode interface. Different mechanisms involved in the relaxation as well as in ac conduction process can be resolved by plotting the modulus at different frequencies in a complex plane, and is found very effective in separating the contributions of various factors such as bulk effect, grain boundary effect and interfaces. Also, the use of modulus spectroscopy plot is particularly useful for separating the components with similar resistance but different capacitance. The other advantage of electric modulus formalism is that the electrode effect is suppressed. Due to the above reasons, complex electric modulus formalism has been opted. Dielectric relaxation studies have been carried out in the complex modulus *M** formalism. The real and imaginary parts of electric modulus were obtained from the impedance data in accordance with the relation:

$$M' = \omega C_o Z'' \tag{2.30}$$

$$M'' = \omega C_o Z' \tag{2.31}$$

2.3.5 Piezoelectric Properties

The poling process is used to align the domains of a piezoelectric material. During this process, an electric field is applied to the material for a length of time, and then removed. The time interval between poling and the d_{33} measurement is usually not reported in the literature. In the present research, it was noted that there was some aging that occurred, where the d_{33} decreased over several days. Consequently, all d_{33} measurements were made within three

hours of poling. Many researchers report poling in the range of 3 to 4 kV/mm at temperatures ranging from 30 to 120°C, and times ranging from 5 to 30 minutes [104, 143-146]. These higher temperatures reportedly facilitate domain movement, but are accompanied by an increase in the leakage current. Higher temperatures in the neighborhoods of 140°C are known to depole BNT-based ceramics.

In the present research, the dc poling was conducted for 20 minutes at temperatures of 30, 60 and 100°C. Poling fields of 3 - 3.5 kV/mm were used at each of these poling temperatures. The sample was placed between two electrical contacts supported by a Teflon jig for poling. The Teflon jig was immersed in a beaker of silicon oil, which was set on a hotplate equipped with a magnetic stir bar .The oil bath was heated on the hotplate, and the oil temperature was monitored with a temperature probe. When the desired temperature was reached, the hotplate and stirrer were shut off, and the poling field was applied for 20 minutes. During this time, there was some cooling of the oil, but the temperature stayed within ± 6°C of the target value.

A High Voltage Amplifier (Trek Inc., Medina, NY) was used to supply the high voltage field up to 20 kV across the sample. The amplifier output voltage was controlled by a dc control voltage supplied to the amplifier input ports. The control voltage was generated by a dc power supply fitted with a 10-turn potentiometer, which allowed the control voltage and therefore, the high-voltage output to be gradually increased to the desired level. Both the output current (sample leakage current), and output voltage of the high voltage amplifier were monitored with multimeters connected on the monitoring ports on the amplifier. After poling for 20 minutes, the high-voltage was shut off, the sample was removed, and the d_{33} measured at room temperature using a Piezo-d_{33} meter (YE2730A d_{33} meter, NTPL\018\08-09).

After poling room temperature Impedance (Z) and Phase (θ) verses frequency with steps in the range 100 Hz to 1 MHz were measured using Hioki 3532 impedance-phase gain analyzer. A decrease in impedance and the appearance of resonance is an indication that the sample was poled. The electro mechanical coupling factor k is measure of the electromechanical energy efficiency:

$$k^2 = \frac{Electrical\ Energy\ in\ put}{Mechancal\ Energy\ out\ put} \tag{2.32}$$

The planar coupling coefficient (K_p) mechanical quality factor (Q_m) and frequency constant (N_p) can be calculated using the following formulas [147]:

$$K_p = \left[\frac{0.395 f_r}{(f_a - f_r) + 0.574}\right]^{-\frac{1}{2}} \tag{2.33}$$

$$Q_m = f_a^2 \left[2\pi R_f C f_r \left(f_a^2 - f_r^2\right)\right]^{-1} \tag{2.34}$$

$$N_p = \left(\frac{\pi d}{3.4}\right) f_r \tag{2.35}$$

where f_r and f_a are resonant and anti-resonant frequencies, and R_f, C and d are resonant impedance, electrical capacitance and diameter of the pellet respectively.

2.3.6 Ferroelectric Properties (Polarization vs. Electric Field)

Samples were submerged in a silicon oil bath at room temperature while dc voltage was applied by a precision work station. In the present study, precision work station standardized ferroelectric test system with high voltage limit 4 kV was used to record the polarization vs. electric field loops on the ceramic samples (Radiant Technologies). The test configuration was

the same as in the dielectric measurements. Vision can construct complex programs with any number of tests to characterize all aspects of the sample in one execution while keeping track of the measurement results and the history of the sample being tested. The maximum limit of frequency for measurement of electric field was 200 Hz.

2.4 OPTICAL PROPERTIES

The optical properties were measured to evaluate the different additives to the BNT ceramics in terms of how much they improved or changed the properties. The following parameters were determined:

1. The optical band gap energy (E_{gap})

2. Electronic transitions in different energy levels.

2.4.1 Ultraviolet-Visible Absorption Spectroscopy

The UV-Visible spectroscopy deals with the recording of absorption of light in the visible and ultraviolet regions of the spectrum. Light of wavelength between 4000 *Å* and 7500 *Å* (400-750 *nm*) is visible. Just beyond the red end of visible spectrum (wavelength more than 750 *nm*) starts the infrared region and just beyond the violet end of the visible spectrum (wavelength less than 400 *nm*) lies the ultraviolet region. Thus, ultraviolet region starts at the blue end of the visible light (about 4000 *Å*) and ends at 2000 *Å*. This region is further sub-divided into near-ultraviolet region and far-or vacuum-ultraviolet region (region below 2000 *Å*). When radiant energy impinges upon a solution it may be absorbed, transmitted and/or reflected. In spectro-photometry, the absorbed light is determined. However, because of the difficulty of directly measuring the absorbed energy, the transmitted energy is measured and the amount

absorbed is indirectly determined by subtracting the transmitted from the initial energy. The relationship is $E=h\upsilon$, where E is the transition energy from the stable to excited state, h is the Planck's constant, and υ is the frequency. The energy of ultraviolet and visible radiation corresponds to that required for electronic transitions of the outer electrons. Since these are the valance electrons of the molecules or ions, the absorption spectra reflect the bonding characteristics of these particles. It is frequently impossible to obtain resolution of the numerous close absorption lines, and the plot of absorption vs. wavelength yields a broad, smooth band spectrum.

CHAPTER 3

STUDY OF STRUCTURAL, ELECTRICAL AND OPTICAL PROPERTIES OF $(Bi_{0.5}Na_{0.5})TiO_3$ LEAD-FREE PIEZOCERAMIC

OUTLINE: This chapter aims to study the various physical properties of $(Bi_{0.5}Na_{0.5})TiO_3$ lead-free piezoceramic. This chapter starts with synthesis followed by characterization of compounds. The sample is synthesized by the solid-state reaction mechanism method and then characterized by XRD, Raman, SEM and EDX. The optical properties are studied by UV. The electrical properties are studied by dielectric, piezoelectric, elecrtomechanical, ferroelectric and impedance spectroscopy.

3.1 SAMPLE PREPARATION

$(Bi_{0.5}Na_{0.5})TiO_3$ (abbreviated as BNT) ceramic was prepared by the solid-state reaction route. For this synthesis, we have used Bi_2O_3 (S.P. Fine Chemical Ltd., Mumbai, India), Na_2CO_3 (Loba Chemicals Pvt. Ltd., Mumbai, India) and TiO_2 (Merck Specialties Pvt. Ltd., Mumbai, India) as the starting raw materials in the fabrication of $(Bi_{0.5}Na_{0.5})TiO_3$ ceramic. The oxide and carbonate powders were weighed according to their respective stochtiometric proportions, and then mixed by ball mill with zirconia media in acetone medium for a period of 16 hrs. The mixed powders were calcined at different temperatures for different durations to study the phase formation with repeated cycles of mixing and grinding. Finally, the pure BNT phase was obtained at 850^oC and pellets have been made.

In the mixing process, the calculated relevant proportions of constituents were weighed according to the formulae given below (Eq.3.1):

$$0.25(Na_2CO_3) + 0.25(Bi_2O_3) + TiO_2 \rightarrow (Bi_{0.5}Na_{0.5})TiO_3 + 0.25CO_2(g). \quad (3.1)$$

3.2 CHARACTERIZATION

The sample was characterized by the following tools to study of structural, electrical and optical behavior.

3.2.1 Phase Formation and Rietveld-Refinement Study

Phase formation studies as a function of heat treatment temperature and duration were done. The phase purity and crystallinity of the ceramic compounds were confirmed by x-ray powder diffraction (XRD) method.

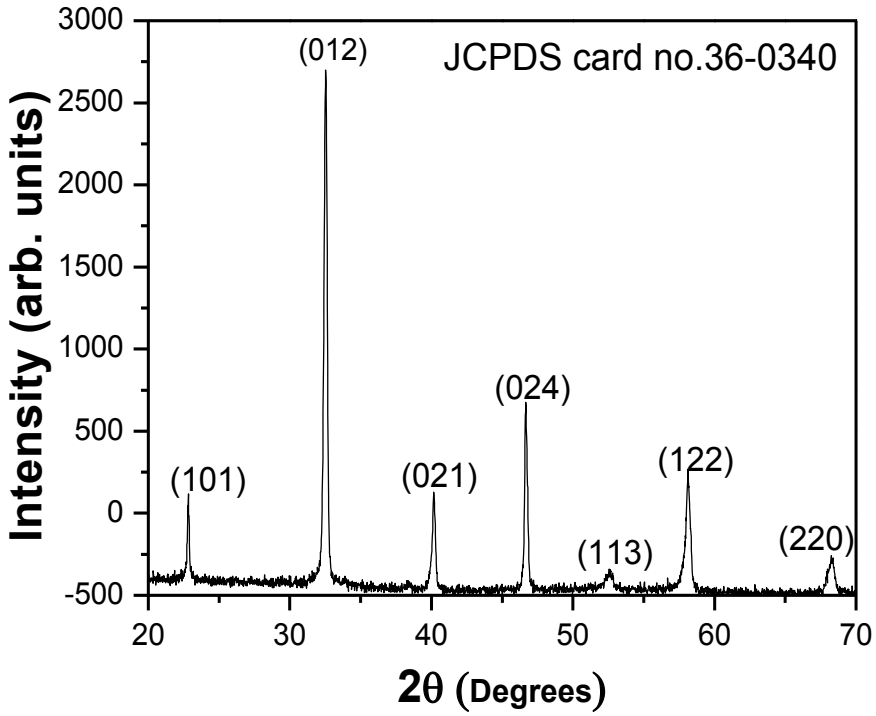

Fig.3.1: Room temperature powder x-ray diffraction pattern of $(Bi_{0.5}Na_{0.5})TiO_3$ ceramic calcined at 850^{o}C, for 4 hrs

The x-ray diffraction analysis of the calcined powder (Fig.3.1) shows that the sample $(Bi_{0.5}Na_{0.5})TiO_3$ (abbreviated as BNT) are single phase and maintain the rhombohedral structure with space group R3c, in agreement with the respective Joint Committee on Powder Diffraction Standards (JCPDS) card No. 36-0340 [148]. The lattice parameters are found to be a= 5.5158 Å, b=5.5158 Å, c = 13.4642 Å and the cell volume is found to be 347.2 $Å^3$.

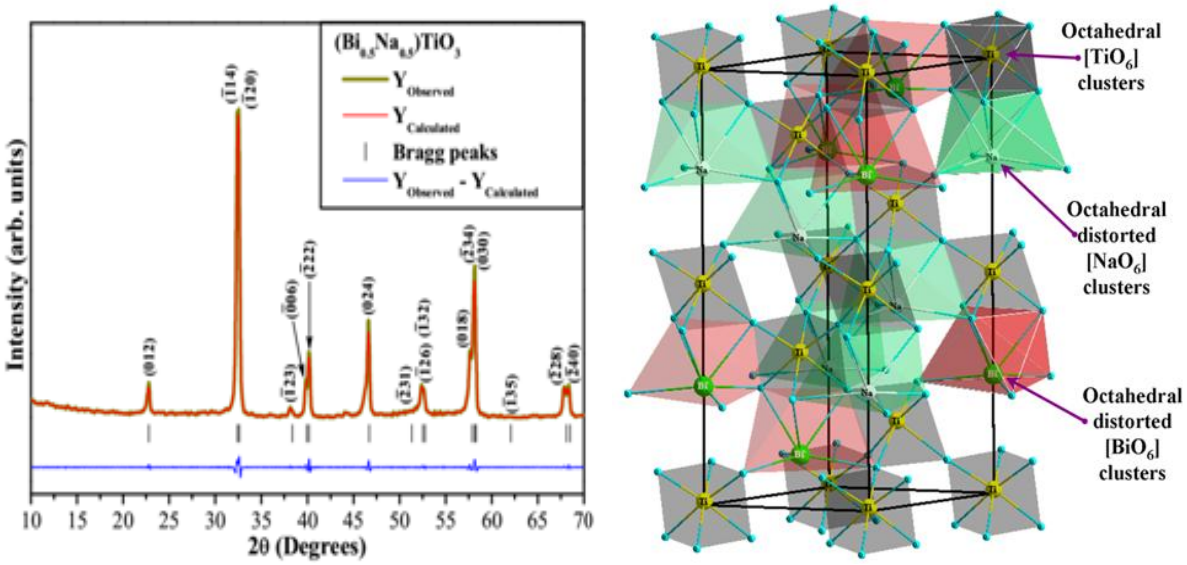

Fig.3.2: (a) Rietveld-refinement plots and (b) Super cell model of pure BNT ceramic

The rhombohedral structure of $(Bi_{0.5}Na_{0.5})TiO_3$ ceramics was structurally refined by Materials Analysis Using Diffraction (MAUD) software version 2.33 [149,150] using the Rietveld-refinement method [151]. The results obtained from the Rietveld-refinement method have shown a good agreement between the observed XRD patterns and theoretical results (Fig.3.2 (a)). Moreover, the difference between the profiles of the XRD patterns experimentally observed and theoretically calculated dates display small differences near to zero in scale of intensity as illustrated by a line ($Y_{Observed}$ - $Y_{Calculated}$). The lattice parameters and atomic positions obtained from the Rietveld-refinement are presented in Table 3.1.

Table 3.1: Lattice parameters, unit cell volume, atomic coordinates and site occupation obtained by Rietveld-refinement for the $(Bi_{0.5}Na_{0.5})TiO_3$ ceramics

Atom	Wyckoff	Site	x	y	z
Bi	6a	3	0	0	0.211331
Na	6a	3	0	0	0.286520
Ti	6a	3	0	0.5	0.0410742
O1	18b	1	0.0903385	0.175109	0.0910219

*R3c (*161) - rhombohedral ($a = b$ = 5.4614(6); c = 13.4797(2) Å; c/a = 2.4682; V = 348.19 Å^3) *Rp* = 9.82%; *Rwp* = 5.2%; *Rexp* = 2.2% and χ^2 = 2.36

In this Table, the fit parameters (R_p, R_{wp}, R_{exp}, and χ^2) suggest that the refinement results are well-reliable. However, the difference between the measured and calculated patterns is considered a way to verify the success of the structural refinement. In our work, the optimized parameters were scale factor, background with exponential shift, exponential thermal shift and polynomial coefficients, basic phase, microstructure, crystal structure, size-strain (structure solution model (genetic algorithm SDPD)), shift lattice constants, profile half-width parameters (*u*, *v*, *w*), texture, lattice parameters (*a*, *b*, *c*), factor occupancy and atomic site occupancies (Wyckoff) [152-154]. In the Rietveld-refinement, the measured diffraction patterns were well adjusted to the Crystallographic Information File (CIF) No. 154040 and 80874, for $(Bi_{0.5}Na_{0.5})TiO_3$ structures [55]. In fact, the results arising from structural refinements are commonly acceptable under the following criteria: (a) *Rw* < 10% - medium complex phases (tetragonal, orthorhombic, rhombohedral and hexagonal); (b) *Rw* < 15% - highly complex phases (monoclinic and triclinic); (c) *Rw* < 8% - cubic structure (high symmetry and few diffraction peaks). Also, the low χ values (< 2) are indicative of good accuracy for the obtained refinement results [155]. As it can be seen in the Table, there is a good fit obtained with the CIF's reported. Therefore, the calculated XRD patterns prove the accuracy of the structural refinements performed on the BNT ceramics Rietveld refinements results are displayed in Table 3.1. These parameters were employed to model these unit cells

of BNT ceramics by means of the Diamond Crystal and Molecular Structure Visualization program (Version 3.2g for Windows) [156]. The rhombohedral structure of the BNT ceramics exhibits a space group (R3c), with point-group symmetry (C^6_{3v}) and two clusters per unit cell (Z = 2) [157]. In this unit cell, the bismuth (Bi) and sodium (Na) atoms are coordinated to six oxygen (O) atoms, forming the distorted octahedral [BiO_6] and [NaO_6] clusters (6-vertices, 6-faces and 12-edges) [158]. In this unit cell, the titanium (Ti) atoms are hexacoordinated to six O atoms, represented by the octahedral [TiO_6] clusters (Fig. 3.2(b)).

3.2.2 Raman Spectroscopy Study

As per the group theory analysis BNT (rhombohedral symmetry with space group R3c (C^6_{3v})) should show 13 Raman active modes; in irreducible representation $\Gamma_{Raman} = 7A_1+6E$ [38]. In the Fig. 3.3 could be deconvoluted 11 Raman peaks from 5 Raman-active vibrational modes. Therefore, among the 13 Raman-active vibrational modes it is possible to observe 11 Raman-active modes from fitting deconvolution of the Raman spectrum of BNT ceramics with the Gauss and Lorentzian Area function.

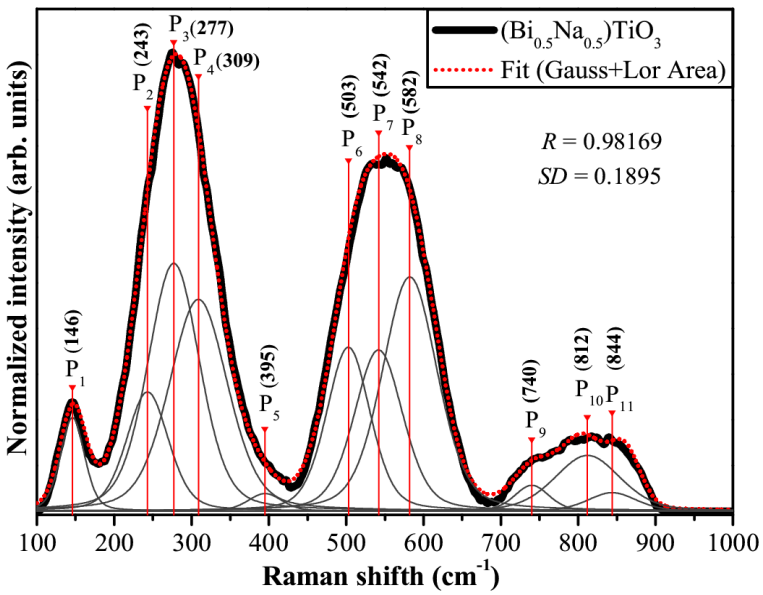

Fig.3.3: Deconvoluted Raman spectrum of BNT ceramics

In the Fig.3.3, the first Raman-active mode at around (146 cm^{-1}) is related to network modifiers or distorted octahedral [BiO_6] and [NaO_6] clusters. The second Raman-active mode can be deconvoluted in three Raman peaks in the regions of 249, 281, and 318 cm^{-1}. This mode is assigned to stretching arising from the bonds due the presence of octahedral [TiO_6] clusters at short-range. The third Raman-active mode with low intensity is related to short-range electrostatic forces associated with the lattice ionicity [159]. According to Dobal *et al*. [160], the mode situated at around 542 cm^{-1} is ascribed to the (←O←Ti→O→) stretching symmetric vibrations of the octahedral [TiO_6] clusters. Also, the fourth Raman-active mode can be deconvoluted in three Raman peaks in the regions of 503, 542, and 582 cm^{-1}.Finally, the mode found at 812 cm^{-1} is due to the presence of the sites within the rhombohedral lattice pre containing octahedral distorted [TiO_6] clusters [161]. This Raman-active mode also can be deconvoluted in three Raman peaks in the regions of 740, 812, and 844 cm^{-1}.

3.2.3 Sintering and Microstructure Analysis

In this study, the densities of sintered BNT ceramics heated at 1075^{o}C, 1100^{o}C, 1125^{o}C and 1150^{o}C for 4 hrs were found to be 54, 64, 90 and 94%, respectively of their theoretical density. Fig.3.4 shows the density and apparent porosity of the sintered samples at various temperatures. This indicates that the sintering temperature of 1150^{o}C for 4 hrs yielded the highest density of the sintered ceramics. However, the sintering temperature has influence on the morphology and microstructure of sintered BNT ceramics. As shown in Fig.3.4, the density of the BNT ceramics increased sharply as the sintering temperature increased from 1075 to 1150^{o}C and the porosity decreased with increase in sintering temperature. A maximum density of 5.72 g/cm^3, which is 94% of the theoretical density, was obtained for samples sintered at 1150^{o}C. However, the density drops when the temperature is further

increased to 1175°C. The densification behavior of the BNT ceramics at different sintering temperatures can be explained in terms of defect chemistry and the creation of oxygen vacancies. At lower sintering temperatures, the number of oxygen vacancies is small and the ability of atoms to diffuse is also small, which results in poor densification. The lower density of the BNT ceramics sintered at 1050°C is due to poor atomic diffusion and insufficient sintering of the ceramics. It has been demonstrated, both theoretically and experimentally, that the number of vacancies increases with increase in sintering temperature. As a result, better atomic diffusion during the sintering process occurs and thus promotes densification. However, the low density at a higher sintering temperature of 1175°C may be due to evaporation of the volatile alkali metal [162, 163].

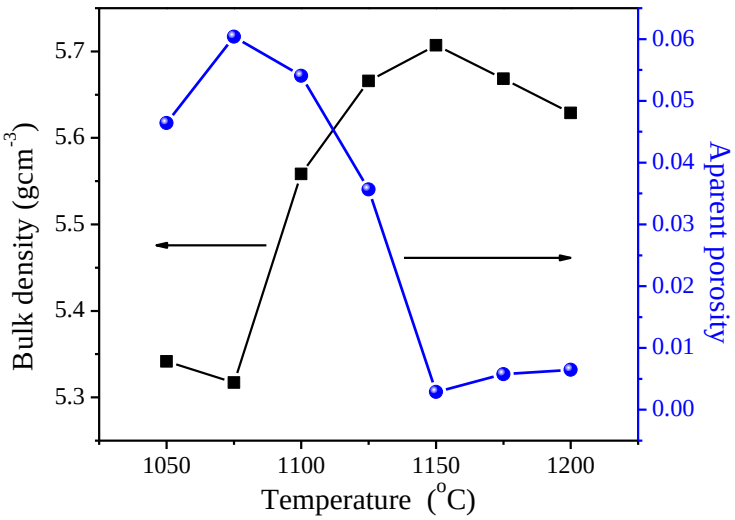

Fig.3.4: Bulk density and apparent porosity at different temperature of BNT pellets

Fig.3.5 (a-f) shows SEM micrograph taken on natural surface of BNT ceramics sintered at 1050°C, 1075°C, 1100°C, 1125°C, 1150°C and 1175°C for 4 hrs. The micrograph suggests that the material comprises of polycrystalline microstructure and the grains are distributed non-homogeneously throughout the natural surface.

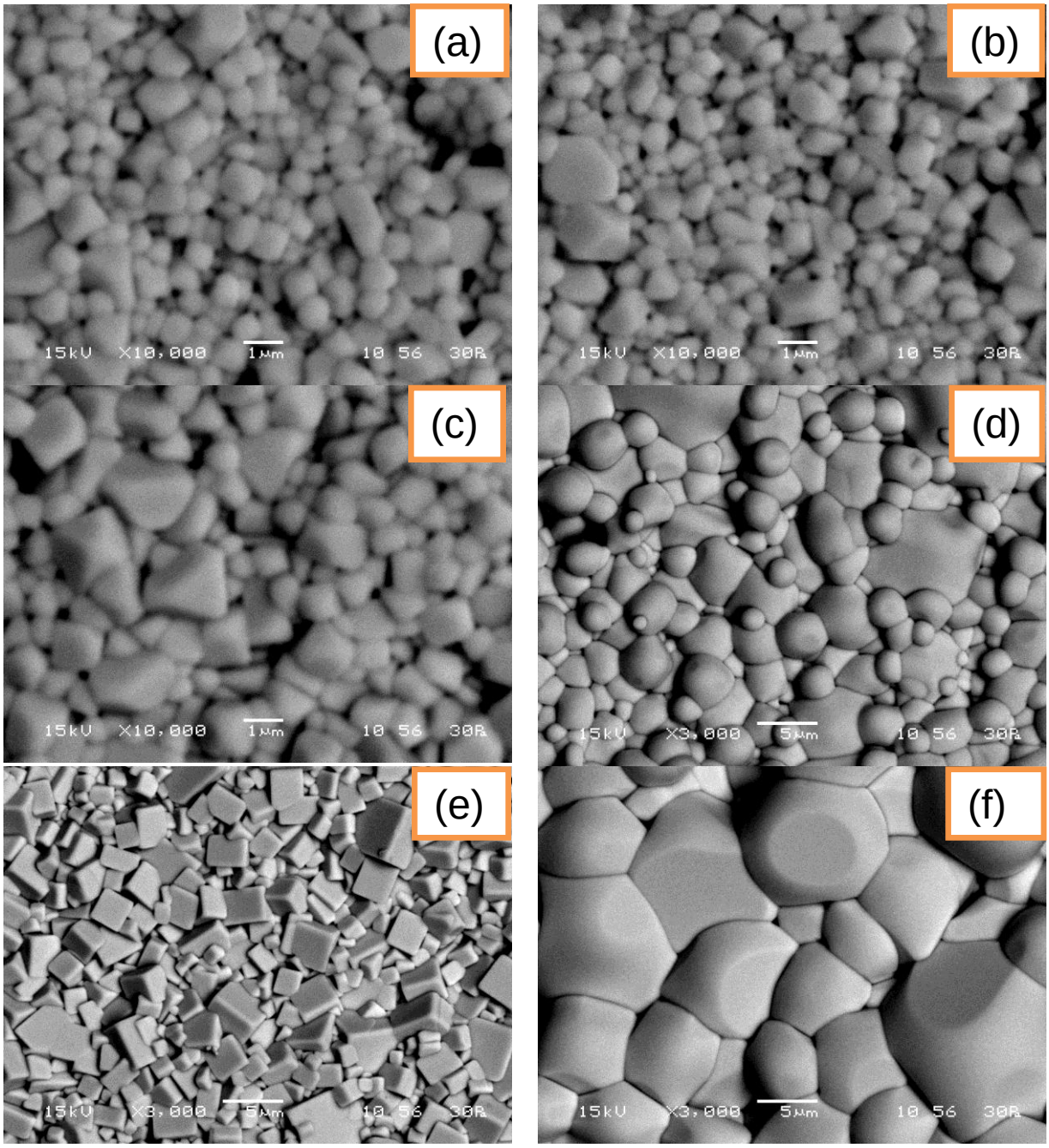

Fig.3.5: SEM of BNT pellets sintered at (a) 1050^{o}C, 4 hrs; (b) 1075^{o}C, 4 hrs; (c) 1100^{o}C, 4 hrs; (d) 1125^{o}C, 4 hrs; (e) 1150^{o}C, 4 hrs; (f) 1175^{o}C, 4 hrs

It was found that the average grain size of sintered BNT ceramics at 1075-1150^{o}C for 4 hrs were approximately 1-5 μm. The particles are agglomerate and basically irregular in shape (Fig.3.5 (a,b)). Some spherical particles are ranging in diameter from 0.2 to 1.0 μm. A sintered

surface ceramics with fine grained, non-uniform microstructure was obtained in BNT ceramics (Fig. 3.5(c, d)), with average grain size ranging from 1 to 5 μm. It can be concluded that lower sintering temperature with longer sintering time produced smaller grain size ceramics.

The elemental composition of the BNT ceramic is confirmed by EDX spectrum as shown in Fig.3.6. Although a reliable quantitative composition analysis is difficult through EDX measurement, the values calculated in the present system indicate that the stoichiometry of the sample is almost maintained after sintering process. The compositions are found to be 49.21%, 5.33%, 19.45% and 26.01%, whereas the theoretical calculated values 49.32%, 5.427%, 19.6% and 25.655% weight % for Bi, Na, Ti and O, respectively.

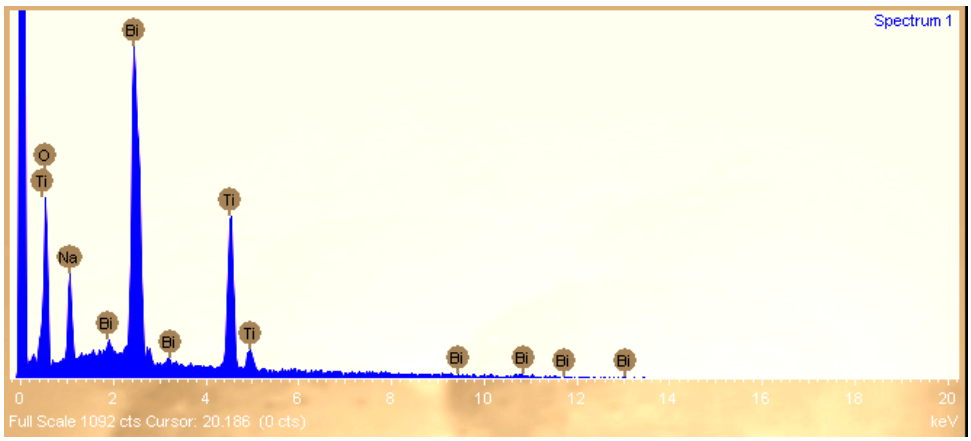

Fig.3.6: Elemental analyses (EDX) spectrum of BNT pellet sintered at 1150^{o}C

3.3 OPTICAL PROPERTIES STUDY

3.3.1 Ultraviolet-Visible Absorption Spectroscopy Analysis

Fig.3.7 shows the UV-Visible absorbance spectrum of BNT ceramic sintered at 850^{o}C for 4 hrs. The optical band gap energy (E_{gap}) was estimated by the method proposed by Wood and Tauc [164]. According to these authors, the optical band gap is associated with the absorbance and photon energy by the following equation:

$$h\upsilon\alpha \;\; \alpha \;\; \left(h\upsilon - E_{gap}\right)^{n} . \qquad (3.2)$$

where α is the absorbance, h is the Planck constant, v is the frequency, E_{gap} is the optical band gap and n is a constant associated to the different types of electronic transitions (n = 1/2, 2, 3/2 or 3 for direct allowed, indirect allowed, direct forbidden and indirect forbidden transitions, respectively). Thus, the E_{gap} value of BNT ceramic was evaluated extrapolating the linear portion of the curve or tail. In our work, the UV-Visible absorbance spectrum suggests an indirect allowed transition and, therefore, the $n = 0.5$ was used in Eq.3.2.

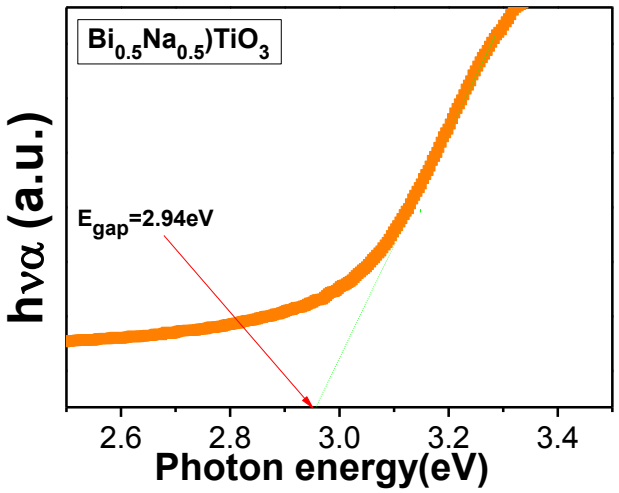

Fig. 3.7: UV-Visible spectrum of BNT powder

In principle, we believe that the obtained E_{gap} value for the BNT ceramic can be associated to a structural order-disorder effect into the lattice due to a symmetry break between the O-Ti-O bonds and/or distortions on the [TiO_6] clusters. A plausible explanation for the origin of this symmetry break can be related to the synthesis method. It is possible to conclude on this hypothesis that the high temperatures employed in the solid-state-reaction (SSR) during the sintering process are not sufficient to avoid the presence of structural defects (symmetry break between bonds or distortions) into the BNT structure, mainly those arising from the repeated cycles of grinding.

3.4 DIELECTRIC PROPERTIES STUDY

3.4.1 Temperature-Dependent Dielectric Constant (ε') and Loss (tanδ)

Temperature-dependence of relative dielectric constant at measuring frequencies of 1 kHz, 10 kHz, 100 kHz and 1 MHz is shown in Fig.3.8. There are two ε_r peaks in the graph, which appear at 210°C and 320°C, respectively, and we call these two temperatures as characteristic temperature. The conventional explanation, regarding this phenomenon, is that different phase transformation process occurs at two characteristic temperature, ferroelectric to anti-ferroelectric transformation process at 210°C and anti-ferroelectric to paraelectric transformation process at 320°C [165]. Fig.3.8 shows the temperature dependence of the tanδ for pure BNT ceramics at different frequencies. The T_d near 150°C can be derived from the temperature of the tanδ first peak at a certain frequency and, accordingly, depends on the determining frequency.

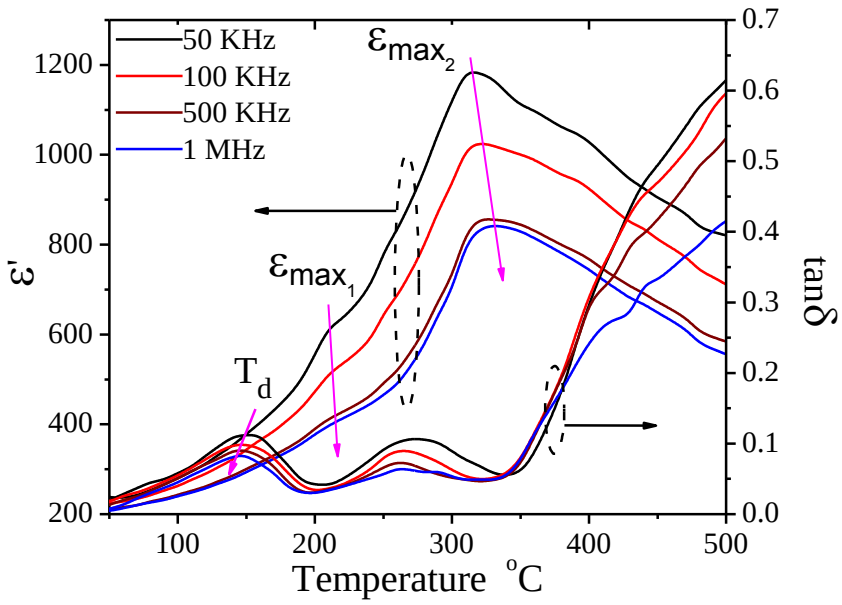

Fig.3.8: Temperature-dependence of dielectric constant ε_r and loss tangent (tanδ) of BNT ceramic

The relative dielectric constant increases slowly with the increasing temperature below 210°C, and more rapidly above 210°C until the temperature T_{max} of maximum dielectric constants $\varepsilon_{\max_1}$. Rapid increases in ε_r occurred near 316°C on the heating run, which is the structural phase transition temperature from the rhombohedral to the tetragonal phase. Another feature in Fig.3.8 is that the temperature T_{max} increases with measuring frequencies; they are: 320°C, 330°C, 335°C and 340°C at frequencies of 50 kHz, 100 kHz, 500 kHz and 1 MHz, respectively. Also, value of the dielectric constant decreases as the measuring frequency increases, showing evidence of a diffuse phase transition with a straight frequency dispersion occurring around the temperature T_{max}. Peak broadening may be quantified by the parameter δ, which is related with permittivity and temperature as follows [31]:

$$\frac{1}{\varepsilon'} - \frac{1}{\varepsilon'_m} = \frac{(T - T_m)^2}{2\varepsilon_m \delta^2} \quad . \tag{3.3}$$

The δ parameter of two different frequencies is calculated by fitting permittivity-temperature data and found to be 221.5 for 50 kHz and 217.9 for 100 kHz and the fitting is shown in Fig.3.9 (a).

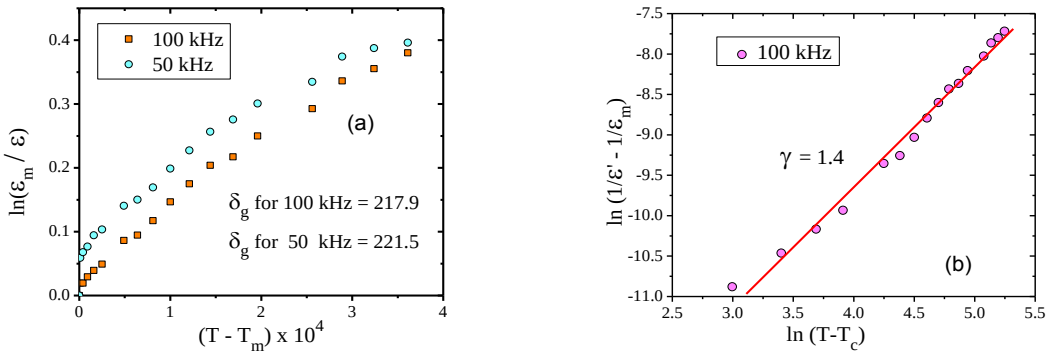

Fig.3.9: (a) $\ln(\varepsilon_m/\varepsilon)$ vs. $(T-T_m)$ for 50 kHz and 100 kHz of BNT ceramic (b) log $(1/\varepsilon'-1/\varepsilon_m)$ vs. log $(T-T_m)$ of BNT ceramic at 100 kHz

The diffusivity (γ) parameter is applied to characterize the relaxor behavior and it is expressed by a modified Curie-Weiss law [166]

$$\frac{1}{\varepsilon'} - \frac{1}{\varepsilon'_m} = \frac{(T - T_m)^{\gamma}}{C} \quad . \tag{3.4}$$

where γ and C are constants for diffusion factor and Curie-Weiss constants, respectively. In general, the diffusion factor is in between 1 and 2, representing the normal ferroelectric phase transition and completed diffusion phase transition. In the case of γ = 1, a normal Curie-Weiss law is obtained. The diffusion factor can be employed to describe the diffusion phase transition. The plot of $\ln(1/\varepsilon' - 1/\varepsilon'_m)$ as a function of $\ln(T - T_m)$ for the BNT samples is shown in Fig.3.9(b). The diffusion factor is found to be 1.4 at 100 kHz.

3.4.2 Frequency-Dependent Dielectric Constant (ε') and Loss (tanδ)

The angular frequency $\omega\ (=2\pi\nu)$ dependence of the dielectric constant ε' of BNT at various temperatures is shown in Fig. 3.10(a). The nature of the dielectric permittivity for free dipoles oscillating in an alternating field may be described in the following way. At very low frequencies ($\omega \ll 1/\tau$, τ = relaxation time), dipoles follow the field and we have $\varepsilon' = \varepsilon_s$ (value of the dielectric constant at quasistatic fields). As the frequency increases (with $\omega < 1/\tau$), dipoles begin to lag behind the field and ε' slightly decreases. When frequency reaches the characteristic frequency ($\omega = 1/\tau$), the dielectric constant drops (relaxation process). At very high frequencies ($\omega \gg 1/\tau$), dipoles can no longer follow the field and $\varepsilon' \approx \varepsilon_\infty$ (high-frequency value of ε'). Qualitatively, this behavior has been observed in Fig.3.10 (a). The dielectric constant at low frequency is rather high, and is found to decrease with frequency at first and then becomes more or less stabilized. The high value of ε' at frequencies lower than 1 kHz,

which increases with decreasing frequency and increasing temperature, corresponds to bulk effect of the system.

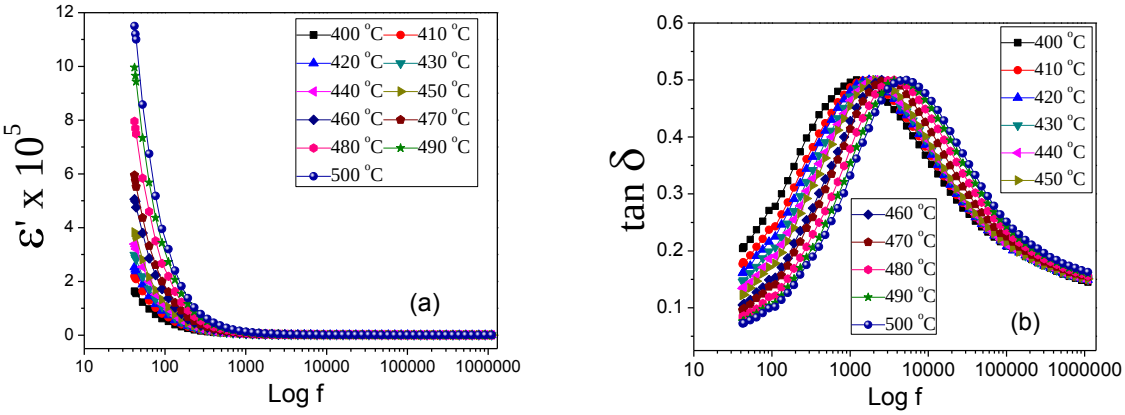

Fig. 3.10: Frequency-dependence of (a) dielectric constant *ε'* and (b) dielectric loss *(tanδ)* of BNT at various temperature

Fig.3.10 (b) shows the variation of dielectric loss *(tanδ)* with frequency at various temperatures. It is obvious that two peaks are superimposed on an apparent background increasing with the measuring temperature but decreasing with frequency. The positions of the peaks apparently shift towards higher frequency with the increase of the peak height when temperature increases. This characteristic indicates that these peaks are associated with a thermally activated relaxation process.

3.5 ELECTRICAL CONDUCTIVITY STUDY

3.5.1 Impedance Study

Fig.3.11 (a) shows the variation of the real part of impedance (*Z'*) with frequency at various temperatures. It is observed that the magnitude of *Z'* decreases with the increase in both frequency as well as temperature, indicating an increase in *ac* conductivity with the rise in temperature and frequency. The *Z'* values for all temperatures merge above 100 kHz. This

may be due to the release of space charges as a result of reduction in the barrier properties of the material with the rise in temperature and may be a responsible factor for the enhancement of *ac* conductivity of material with temperature at higher frequencies. Further, at low frequencies, the *Z'* values decrease with rise in temperature and show negative temperature coefficient of resistance (NTCR) type behavior like that of semiconductors. The coincidence of the impedance (*Z'*) at higher frequencies at all the temperatures indicates a possible release of space charge as a reduction in barrier properties of the material with rise in temperature [167].

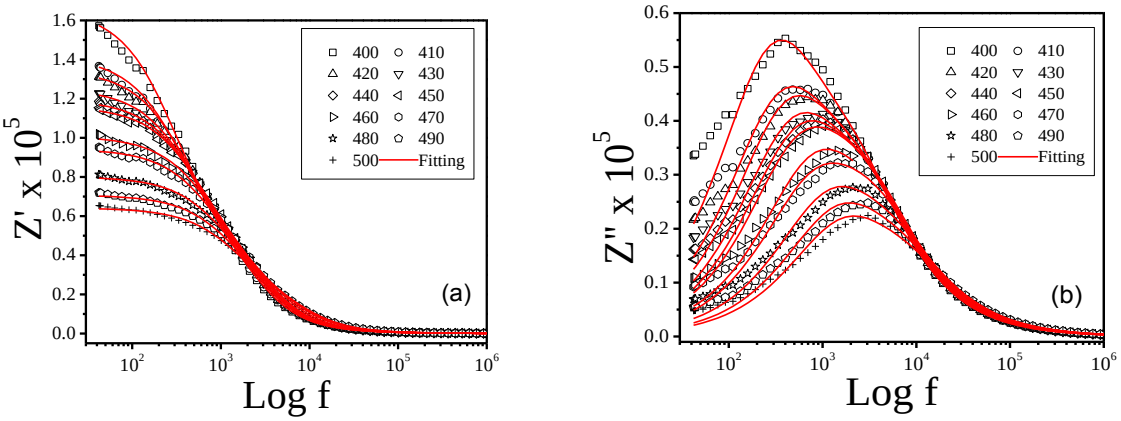

Fig.3.11: Variation of the (a) real part (*Z'*) and (b) imaginary part (*Z''*) of impedance with frequency at various temperatures

Fig. 3.11(b) shows the variation of the imaginary part of impedance (*Z''*) with frequency at different temperatures. The curves show that the *Z''* values reach a maxima peak (Z''_{max}) and the value of Z''_{max} shifts to higher frequencies with increasing temperature. A typical peak broadening, which is slightly asymmetrical in nature, can be observed with the rise in temperature. The broadening of peaks in frequency explicit plots of *Z''* suggests that there is a spread of relaxation times, *i.e.*, the existence of a temperature dependent electrical relaxation phenomenon in the material [168].

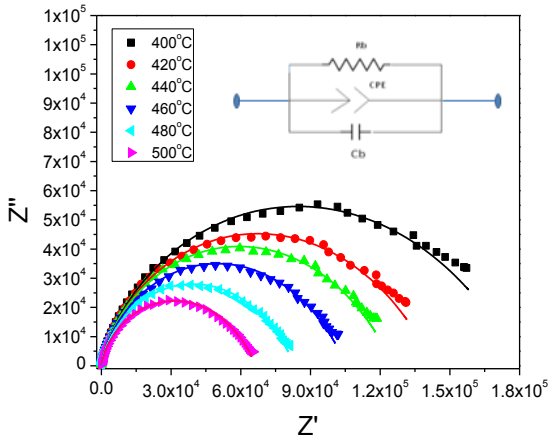

Fig.3.12: Cole-Cole plots of the BNT ceramics at various temperatures (Inset shows the appropriate equivalent electrical circuit)

Fig.3.12 shows the complex impedance plot (Nyquist plot) of BNT at different temperatures between 400°C and 500°C. The symbols represent the experimental data and the lines represent the theoretical fitting by Eq. (3.5). It is observed that with the increase in temperature the radius of the semicircles decreases. It can be also seen from this Fig. that the complex impedance data are represented by depressed semicircle (i.e., centers of semicircle lie below the real axis). The Debye's expression is modified in such a situation by introducing a factor *n*. This modification leads to the Cole-Cole empirical behavior described by the following equation [169]:

$$Z^* = \frac{R}{1+(j\omega/\omega_0)^{1-n}} \qquad (3.5)$$

where *n* represents the magnitude of the departure of the electrical response from an ideal condition and can be determined from the location of the centre of the Cole-Cole circles. This equation shows that the centre of the semicircle obtained from the data plotted in the complex plane is located below the real axis, indicating the polydispersive non-Debye type dielectric

relaxation. When *n* goes to zero *{i.e. (1-n) → 1}*, Eq. (3.5) reduces to the classical Debye's formalism where centre of the semicircle should lie on the real Z'-axis. Least squares fitting to the complex impedance data gives the value of n>0 at all the temperatures, suggesting the dielectric relaxation to be of polydispersive non-Debye type. This may happen due to the presence of distributed elements in the material electrode system [170] that results in the deviation from the pure semicircle in complex impedance plots.

Table 3.2: Parameters obtained from Cole-Cole plots of BNT ceramics at different temperature

T (^{o}C)	C_b (nF)	R_b (Ω)	$\tau = C_b R_b$ (s)	$\sigma_b = t/R_b A$ (Ωcm)$^{-1}$
400	0.4296	1.804×10^{5}	7.75×10^{-5}	7.1×10^{-7}
420	0.3964	1.433×10^{5}	5.68×10^{-5}	8.91×10^{-7}
440	0.3711	1.259×10^{5}	4.81×10^{-5}	1.02×10^{-6}
460	0.3322	1.055×10^{5}	3.5×10^{-5}	1.215×10^{-6}
480	0.3114	8.834×10^{4}	2.751×10^{-5}	1.45×10^{-6}
500	0.2954	6.68×10^{4}	1.973×10^{-5}	1.92×10^{-6}

3.5.2 Modulus Study

We have adopted the impedance as well as the modulus formalism to study the relaxation mechanism in BNT ceramic.

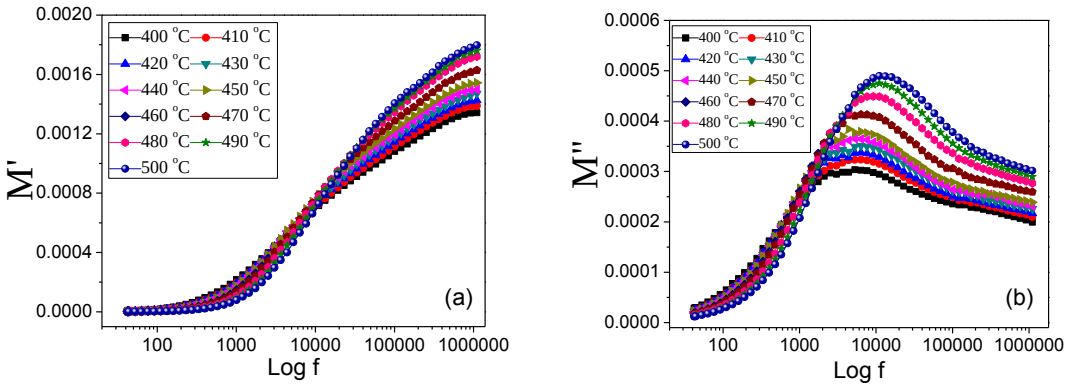

Fig.3.13: Variation of (a) real part (M') and (b) imaginary part (M'') of electric modulus with frequency at different temperature

Fig. 3.13((a) and (b)) shows the real and imaginary part of electric modulus over a wide range of frequency at different temperatures. This graph shows that the modulus peaks shift towards higher frequency side on increasing temperature. Fig. 3.13((a) and (b)) displays the frequency (angular) dependence of *M'(ω)* and *M''(ω)* for BNT as a function of temperature. *M'(ω)* shows a dispersion tending toward M_∞ (the asymptotic value of *M'(ω)* at higher frequencies (Fig. 3.13(a)), while *M''(ω)* exhibits a maximum M''_{max} (Fig. 3.13(b)) centred at the dispersion region of *M'(ω)*. It may be noted from Fig.3.13 (b) that the position of the peak M''_{max} shifts to higher frequencies as the temperature is increased. The asymmetric broadening of the peak indicates the spread of relaxation with different time constant, and relaxation in the material is of non-Debye type The frequency region below peak maximum *M''* determines the range in which charge carriers are mobile on long distances. At frequency above peak maximum *M''*, the carriers are confined to potential wells, being mobile on short distances. The complex electric modulus spectrum (M' vs. M'') is shown in Fig.3.14 (a).

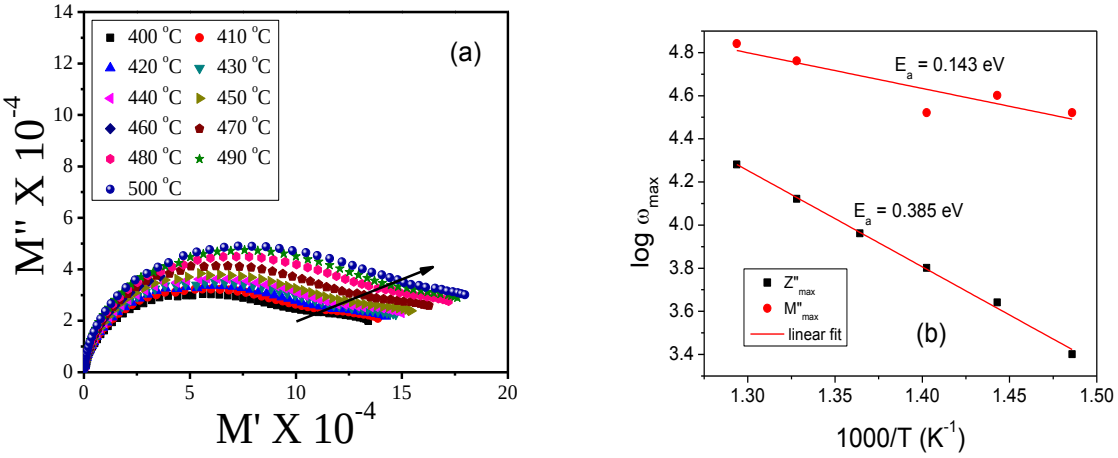

Fig.3.14: (a) Variation between real (M') and imaginary (M'') parts of the electrical modulus and (b) Variation of characteristic of *log* ω_m vs. *1000/T (K)* (Arrhenius plot)

The frequency ω_m (corresponding to Z''_{max} and M''_{max}) gives the most probable relaxation time τ_m from the condition $\omega_m\tau_m = 1$. The most probable relaxation time follows the Arrhenius law, given by

$$\omega_m = \omega_0 \, exp\left(\frac{-E_a}{k_B T}\right) \tag{3.6}$$

where ω_o is the pre-exponential factor and E_a is the activation energy.

Fig. 3.14(b) shows a plot of the *log* ω_m versus *1/T*, where the dots are the experimental data and the solid line is the least-squares straight-line fit. The activation energy E_a is calculated from the least-squares fit to the points. From Fig. 3.14(b), it can be seen that the activation energy calculated from the Arrhenius relation is E_a = 0.14 eV for relaxation of *Z''* and E_a = 0.38 eV for *M''*.

3.5.3 AC and DC Conductivity

Fig. 3.15(a) shows the plot of *ac* conductivity with frequency at different temperatures. The frequency dependence of conductivity of the material at room temperature exhibits both low and high frequency dispersion phenomena. This obeys the Jonscher's power law equation given by

$$\sigma(\omega) = \sigma_{dc} + A\omega^n \tag{3.7}$$

where *n* is the frequency exponent in the range of $0<n<1$, *A and n* are thermally activated quantities, hence electrical conduction is a thermally activated process. According to Jonscher [171], the origin of the frequency dependence of conductivity lies in the relaxation phenomena arising due to mobile charge carriers. When a mobile charge carriers hops to a new site from its original position, it remains in a state of displacement between two potential energy

minima, which includes contributions from other mobile defects. After a sufficiently long time, the defect could relax until the two minima in lattice potential energy coincide with the lattice site. Also, the conduction behavior of the materials obeys the power law $\sigma(\omega) \alpha \omega^n$ with a slope change governed by *n* in the low temperature region.

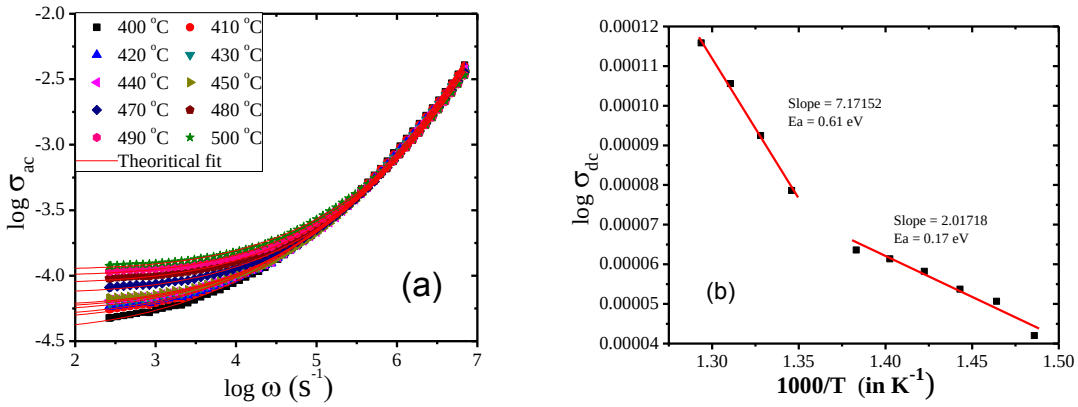

Fig. 3.15: (a) Frequency dependence of the ac conductivity at various temperatures and (b) temperature (*1000/T (K)*) dependence of the dc conductivity of BNT ceramic

Fig. 3.15(b) shows the variation of σ_{dc} against the $10^3/T$. The value of bulk conductivity of the material is evaluated from the *ac* conductivity plot of the sample at different temperatures by theoretical fitting using Joncher's power law (Eq.3.7). At higher temperature, the conductivity versus temperature response is more or less a straight line and can be explained by a thermally activated transport of Arrhenius type;

$$\sigma_{dc} = \sigma_0 \exp\left(\frac{-E_a}{k_B T}\right) \tag{3.8}$$

where σ_o, *Ea* and k_B represent the pre exponential term, the activation energy of the mobile charge carriers and Boltzmann's constant, respectively. At lower temperature, a small deviation from the linear behavior of conductivity has been noticed and can be attributed to Mott's hopping type phenomena.

The electric conductivity is controlled by the migration of charge species under the action of electric field and by the defect-ion complexes, the polarization field, the relaxations, etc. At lower temperatures the defect-ion complexes may exist and they are present in a polarization field (i.e., the polarization field responsible for ferroelectricity). The polarization field may aid the charge species to migrate, thereby contributing to the conductivity. However, the defect ion complexes may cause distortions. The grain boundaries may also contribute to the conduction mechanism. The defect ion complexes tend to dissociate. The activation energy may be due to the migration energy for the charges.

Hence, there are distinct values of activation energy in the different temperature ranges; (i) from temperature 400°C to 440°C, the activation energy, found to be 0.17 eV, may be attributed to the small polarons created by the electron and/or hole-phonon interaction [172] and (ii) from 460°C to 500°C, the activation energy is found to be 0.61 eV. The higher value of activation energy (0.61 eV) may be due to the oxygen vacancy [173]. Also, the motion of domain wall occurs with the increase in temperature, but pinning of the motion of domain walls arises due to the deposition of excess oxygen vacancy at higher temperature.

3.6 POLARIZATION AND PIEZOELECTRIC STUDY

Fig. 3.16 (a) shows the room temperature *P*~*E* hysteresis loop of BNT ceramic sintered at 1150°C. The *P*~*E* hysteresis loop indicated that the sample exhibited typical ferroelectric nature. The remnant polarization (P_r) and coercive field (E_c) of BNT ceramics evaluated from the saturated ferroelectric hysteresis loop at various electric fields is summarized in Fig.3.16 (a). The values of P_r and E_c of BNT ceramic are shown in Table 3.3. It is observed that the ceramic shows a lower E_c value than that of the value reported in the literature.

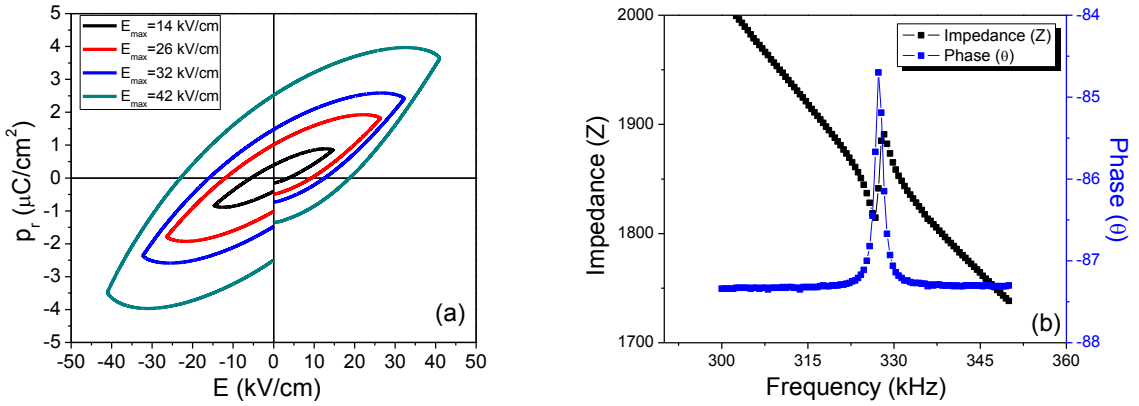

Fig.3.16: (a) P~E hysteresis loop of pure BNT ceramic in different field and (b) The frequency vs. impedance/phase spectrum of pure BNT ceramic

Table 3.3: Variation of P_r and E_c as a function of applied field (E_{max}) of pure BNT

Maximum Field (E_{max}) kV/cm	E_c (kV/cm)	P_r (μC/cm^2)
14	5.5	0.4
26	12	1.02
32	16.1	1.48
42	23	2.55

Fig. 3.16 (b) shows the measured resonance-antiresonance curve of the BNT ceramics. From that figure one can see that the piezoelectric resonance curve of the BNT ceramics is excellent, which indicates that the ceramics has good piezoelectric response. The dynamic piezoelectric constant (d_{33}) (poling field 3 kV/mm for 20 min.) of BNT ceramic at room temperature is found to be 41 pC/N. The measurement of resonance (the magnitude of impedance is minimum) and anti-resonance (the magnitude of impedance is maximum) frequencies from Fig.3.16 (b) provides the means to evaluate the electromechanical coupling factors of the specimens. These coupling factors represent the strength of the material for device application. The electromechanical planar coupling factors, quality factor, and frequency constant were

calculated from the resonance and the anti-resonance frequencies using equations (2.33), (2.34) and (2.35) (given in chapter 2, section 2.3.5) respectively. BNT ceramic gives good performances with electromechanical planar coupling factor (k_p) = 10.7533 %, quality factor (Q_m) = 108 and frequency constant (N_p) = 3034.65.

Main result of this chapter have been published in
1. *Bull. Mater. Sci., 35(2) (2012) 197*
2. Phys. Express, 2 (2012) 21

CHAPTER 4

STRUCTURAL, ELECTRICAL AND OPTICAL CHARACTERIZATION OF LEAD-FREE PEROVSKITE $(Bi_{0.5}Na_{0.5})TiO_3$-$SrTiO_3$ SYSTEM

OUTLINE: In this chapter the influence of $SrTiO_3$ content on $(Bi_{0.5}Na_{0.5})TiO_3$ ceramic with regards to the structural, electrical and optical properties has been studied.

4.1 SAMPLE PREPARATION

The samples were prepared by a conventional mixed-oxide process. In the first step, $(Bi_{0.5}Na_{0.5})TiO_3$ (abbreviated as BNT) and $SrTiO_3$ (abbreviated as ST) master batches were made from bismuth oxide (Meark, India), sodium carbonate (Merck, India), strontium carbonate (Loba Chem., India) and titanium oxide (Merck, India). Appropriate amount of reagents were mixed in zirconia media for 12 hrs using a laboratory designed ball milling unit. The BNT sample was calcined at 850^{o}C for 4 hrs with intermediate grinding and mixing. The ST sample was calcined at 1250^{o}C for 4 hrs with intermediate grinding and mixing. The phase purity of both the master samples was investigated using x-ray diffraction (XRD), (Xpert MPD, Philips, UK). Appropriate amounts of BNT and ST were mixed thoroughly in agate mortar using isopropyl alcohol (IPA) to obtained $(1-x)(Bi_{0.5}Na_{0.5})TiO_3$-$xSrTiO_3$ (abbreviated as BNT-ST hereafter) ceramics, where x is ranging from 0.01 to 0.09. The mixed powders were ball-milled for 16 hrs in acetone medium. The intension of using ball-milled is proper mixing of powder. After ball milling, the powders were dried at room temperature. Then the dried

powders were again grinded for 2 hrs in agate mortar. The granules were made by adding 3% polyvinyl alcohol (PVA) as a binder. The granules were sieved and uniaxially cold pressed with a load of 6 tonnes to obtain discs with a diameter of 11 mm. The discs were decarbonized at 550°C and then sintered between 1050°C and 1175°C for 4 hrs. The optimum sintering temperature was determined by investigating the linear shrinkage and bulk density of the sintered pellets. The bulk density and apparent porosity were investigated using the Archimedes principle (water immersion technique).The pellets were sintered at optimized temperature 1150^{o}C for 4 hrs in a programmable furnace (Table 4.1).

Table 4.1: The optimized sintering temperature, bulk density and apparent porosity of (1-x)($Bi_{0.5}Na_{0.5}$)TiO_3-$x$$SrTiO_3$ ceramic

Composition (x)	Sintering Temp. (°C)	Bulk Density	Apparent Porosity
0.01	1150	5.661	0.0012
0.02	1150	5.643	0.0014
0.03	1150	5.831	0.0014
0.04	1150	5.764	0.0011
0.05	1150	5.755	0.0016
0.06	1150	5.592	0.0012
0.07	1150	5.773	0.0031
0.08	1150	5.611	0.0014
0.09	1150	5.566	0.0013

For electrical measurement, disk-shaped samples are prepared and fired at elevated temperatures. The linear shrinkage of different compositions as a function of temperature has been recorded and shown in Fig.4.1. The diameter of all the pallets is found to decrease with

increasing temperature and shows stable behavior above 1150^{o}C. The bulk density of the pellets sintered at 1150^{o}C was measured using water immersion technique and found to be ~97% of their theoretical density. This indicates that all the compositions of BNT-ST are well sintered above 1150^{o}C. The sintering temperature slightly increases with the addition of ST due to its higher melting temperature than BNT. Similar observation is reported by Krauss, *et al.* [174] on the sintering kinetics of the BNT ceramics with higher concentration of ST using the dilatometry technique.

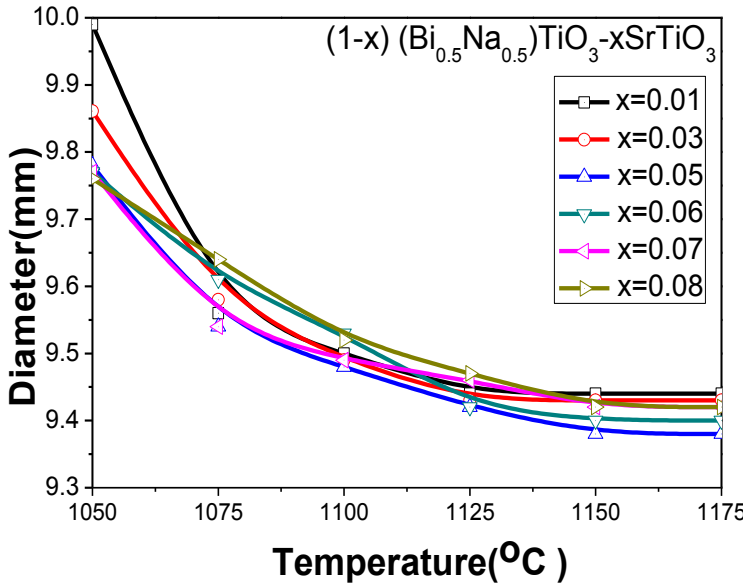

Fig.4.1: Linear shrinkage of (1- *x*)($Bi_{0.5}Na_{0.5}$)TiO_3-*x*$SrTiO_3$ ceramics

4.2 CHARACTERIZATION

The selected samples were characterized by the following tools and the results were discussed.

4.2.1 Phase Formation and Rietveld-Refinement Study

Fig.4.2 (a,b) shows the Rietveld-refinement plots for $SrTiO_3$ (ST) ceramics and its super cell model, respectively. According to the Rietveld-refinement analysis and XRD patterns illustrated in the Fig.4.2 (a), the ST ceramics can be indexed to a perovskite-type cubic

structure with the space group (Pm3m). The rhombohedral structure of $(Bi_{0.5}Na_{0.5})TiO_3$ ceramics (Chapter 3 (Section 3.3.1)) and cubic of $SrTiO_3$ ceramics was structurally refined by using the Rietveld-refinement method [151]. The results obtained from the Rietveld-refinement method show a good agreement between the observed XRD patterns and theoretical results (Fig.3.2 (a) and Fig. 4.2(a)). Moreover, the profiles of the XRD patterns experimentally observed and theoretically calculated data display small differences near to zero in scale of intensity as illustrated by a line ($Y_{Observed}$ - $Y_{Calculated}$). The lattice parameters and atomic positions obtained from the Rietveld-refinement have been presented previously (Table 3.1) for BNT and in Table 4.2 for ST.

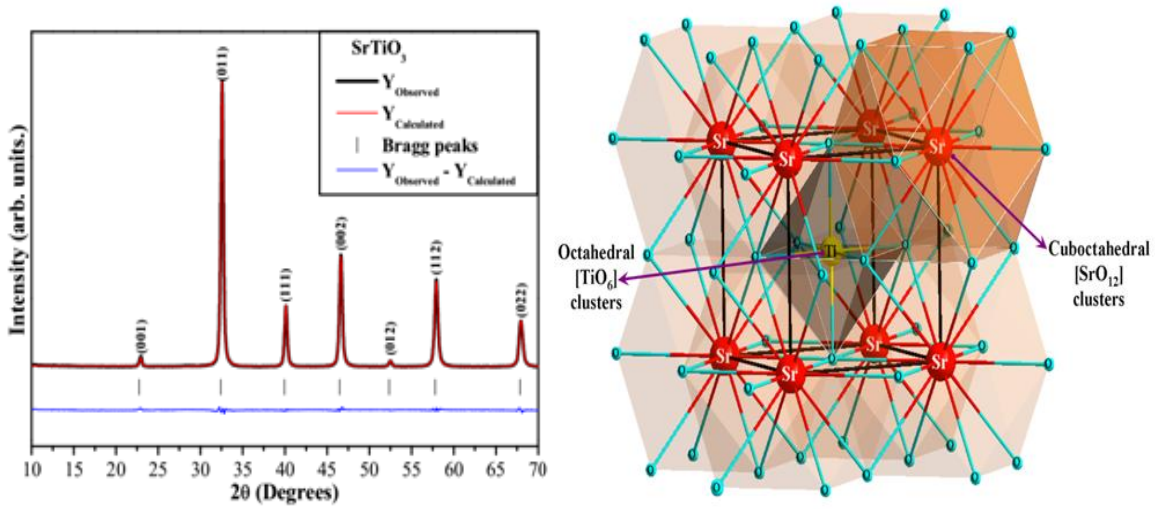

(a) (b)

Fig.4.2: (a,b) (Free colour on-line) Rietveld-refinement plots of ST ceramics and representations of ST unit cells

Table 4.2: Lattice parameters, unit cell volume, atomic coordinates and site occupation obtained by Rietveld-refinement for ST ceramics

Atoms	Wyckoff	Site	*x*	*Y*	*z*
Sr	1a	*m*-3*m*	0	0	0
Ti	1a	4/*mm.m*	0.5	0.5	0.5
O	3b	*mm*2.	0	0.5	0.5

Pm3m (221)-cubic ($a = b = c$ = 3.9038(4) Å; c/a = 1; V = 59.49 Å^3) Rp = 3.35%; R_{wp} = 5.08%; R_{exp} = 4.3% and χ = 1.18

In this Table 4.2, the fit parameters (R_w, R_{wp}, R_{exp}, and χ) suggest that the refinement results are well-reliable. In the Rietveld-refinement, the measured diffraction patterns are well adjusted to the Crystallographic Information File (CIF) No. 154040 and 80874, for BNT (Chapter 3) and ST structures, respectively [55, 175]. Also, the low χ values (< 2) are indicative of good accuracy for the obtained refinement results [155]. As it can be seen in the Table, there is a good fit obtained with the CIF's reported. Therefore, the calculated XRD patterns prove the accuracy of the structural refinements performed on the BNT and ST ceramics Rietveld-refinements results are displayed in Table 3.2 (Chapter 3) and Table 4.2, respectively. In Fig. 4.2(b), a cubic structure for the ST ceramic is observed. This lattice presents a space group (Pm3m), point-group symmetry (O_h^1) and one cluster per unit cell (Z = 1). In this cell, the strontium (Sr) atoms are coordinated to twelve oxygen atoms forming the polyhedrons with cuboctahedral configuration for the [SrO_{12}] clusters. The cuboctahedron presents twelve identical vertices, formed by the meeting of two triangles and two squares, fourteen faces and twenty-four identical edges, each separating a triangle from a square [158, 176]. While the Ti atoms are bonded to six O atoms, forming a polyhedron called octahedron, which is written as [TiO_6] clusters [176].

Fig.4.3 shows the room temperature x-ray diffraction patterns of the (1-*x*)BNT-*x*ST ceramics. A single phase perovskite structure is observed for all compositions, with no trace of nonstoichiometry induced second phase. This suggests that Sr^{2+} have diffused into the BNT lattices, and occupied the $(Bi_{0.5}Na_{0.5})^{2+}$ sites to form a homogeneous solid-solution. As increasing the ST content, the peaks shift towards lower angle slightly, suggesting the change in lattice parameters. The little increase in lattice parameters is due to incorporation of higher radii Sr^{2+} in place of the host $(Bi_{0.5}Na_{0.5})^{2+}$. Similar to the BNT ceramic, all the BNT-ST

ceramics showed a rhombohedral symmetry, indicating that the substitutions Sr^{2+} do not cause any significant change to the crystalline structure in the studied composition range.

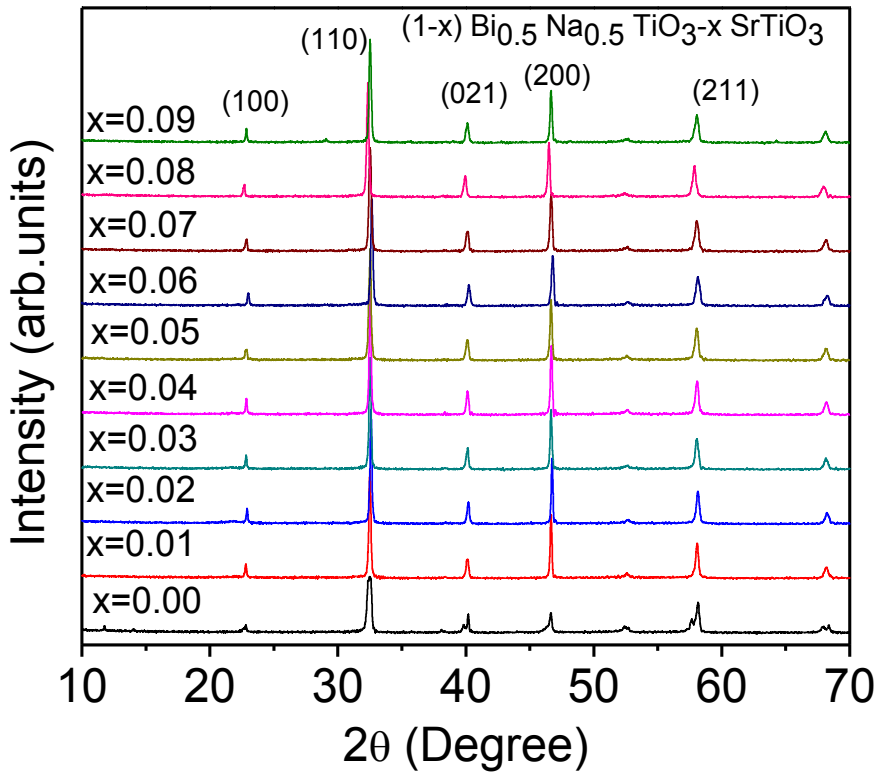

Fig.4.3: (Free colour on-line) XRD patterns of the (1-*x*)BNT-*x*ST ceramic composites with ($0 \leq x \leq 0.09$), respectively

4.2.2 Raman Scattering Spectroscopy Analysis

Fig.4.4 shows the room temperature Raman spectra of (1-*x*)BNT-*x*ST ceramics with $x = 0$, 0.03, 0.05, 0.07 and 0.09, the structural order-disorder degree at short range can be evaluated by micro-Raman scattering spectroscopy [177, 88]. In Fig. 4.4, the Raman peaks are relatively broad, which can be caused by the distorted octahedral [BiO_6] and [NaO_6] clusters or disorder in A-site of rhombohedral structure, the overlap of Raman peaks is observed in all the compositions of the solids solutions ceramics due to the lattice anharmonicity. The first

Raman-active A1(TO1) mode at around (146 cm^{-1}) is related to network modifiers or distorted octahedral [BiO_6] and [NaO_6] clusters. In addition, we also observe that there is a reduction in the intensity of this mode with the increase of the cuboctahedral [SrO_{12}] clusters in the (1-*x*)($Na_{0.5}Bi_{0.5}$)TiO_3-*x*$SrTiO_3$ solid-solution ceramics with $x = 0.03$.

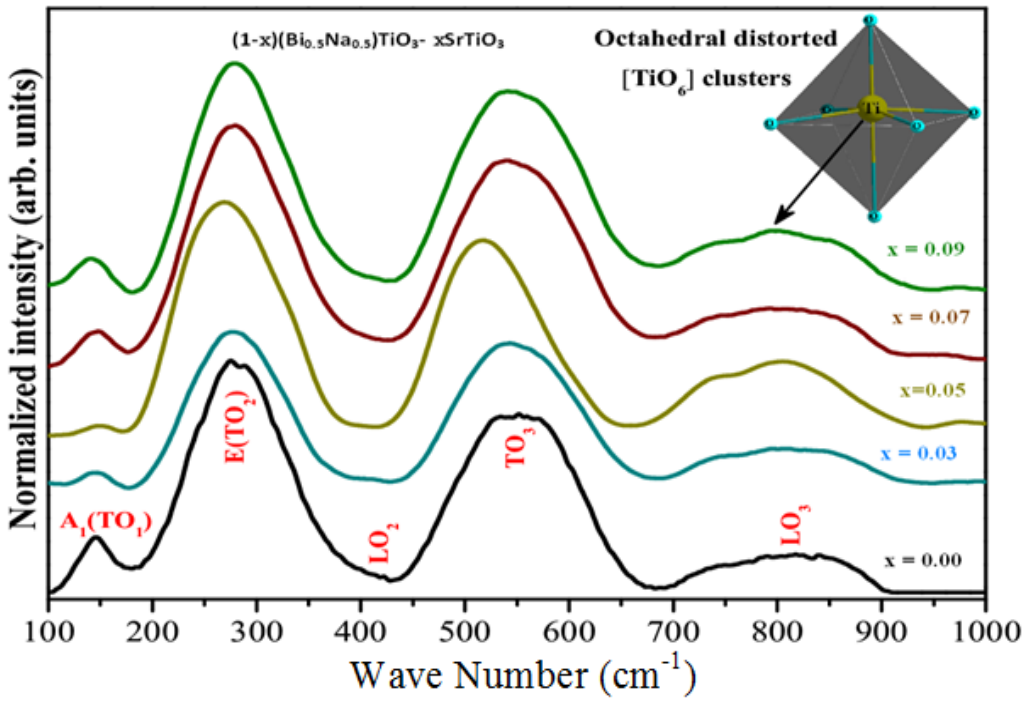

Fig.4.4: (Free colour on-line) Raman spectra of (1-*x*)BNT-*x*ST ceramics composites

The second Raman-active E(TO2) mode can be deconvoluted in three Raman peaks in the regions of 249, 281, and 318 cm^{-1}. This mode is assigned to stretching arising from the bonds due the presence of octahedral [TiO_6] clusters at short-range. The third Raman-active (LO2) mode with low intensity is related to short-range electrostatic forces associated with the lattice ionicity [159]. According to Dobal *et al*. [160], the (TO3) mode situated at around 542 cm^{-1} is ascribed to the (←O←Ti→O→) stretching symmetric vibrations of the octahedral [TiO_6] clusters. This mode is common in materials with perovskite-type structure. Finally, the (LO3) mode found at 812 cm^{-1} is due to presence of the sites within the rhombohedral lattice pre-containing octahedral distorted [TiO_6] clusters [161]. These modes are classified into

longitudinal (LO) and transverse (TO) components because of the electronic structure with polar character of lattice. However, in Fig. 4.4, it is possible to detect that all the Raman peaks are very broad in BNT ceramics and (1-*x*)BNT-*x*ST solid-solutions. This behavior can be caused by the presence of the structural disorder or distorted octahedral [TiO_6] clusters at short-range in both (rhombohedral and cubic) lattices.

4.2.3 Microstructure Analysis

Fig.4.5 shows the SEM micrograph images of natural surface for (1-*x*)BNT-*x*ST ceramics. The pure BNT sample presents rectangular grain morphology while the higher concentration of ST changes the grain shape to spherical one. The microstructure of all the compositions shows well compact and almost free from pore. The BNT sample present rectangular grains having average grain size ~4μm. It can also be seen that the grain size reduces with increase in ST content in the compositions. The reason may be that Sr^{2+} abounds in crystal boundary, which prevents the ion migration and restricts the grain growth. The average grain size decreases from ~ 4μm (for x = 0.0) to ~2μm (for different compositions), which was determined by linear interception method.

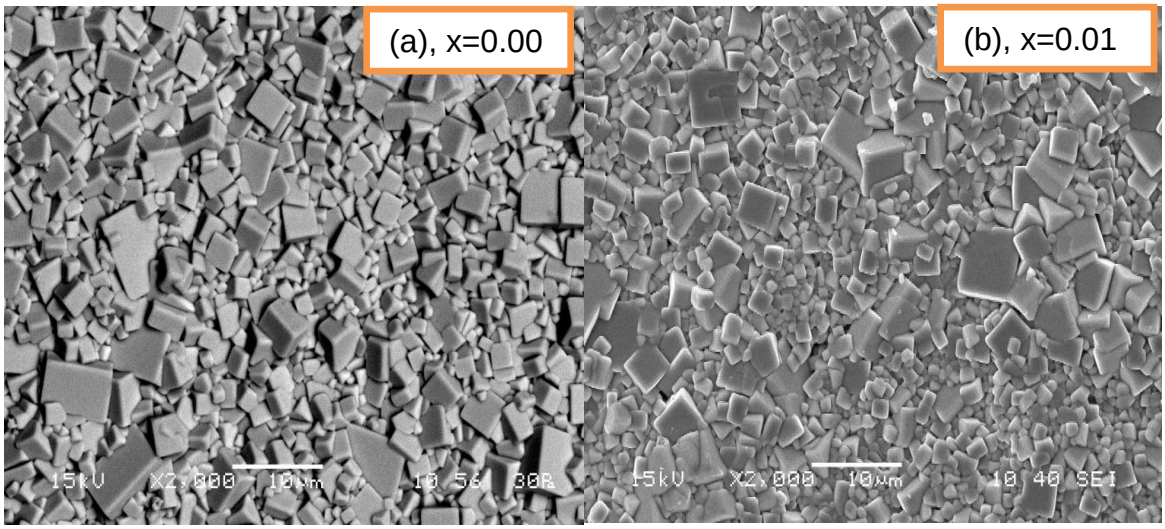

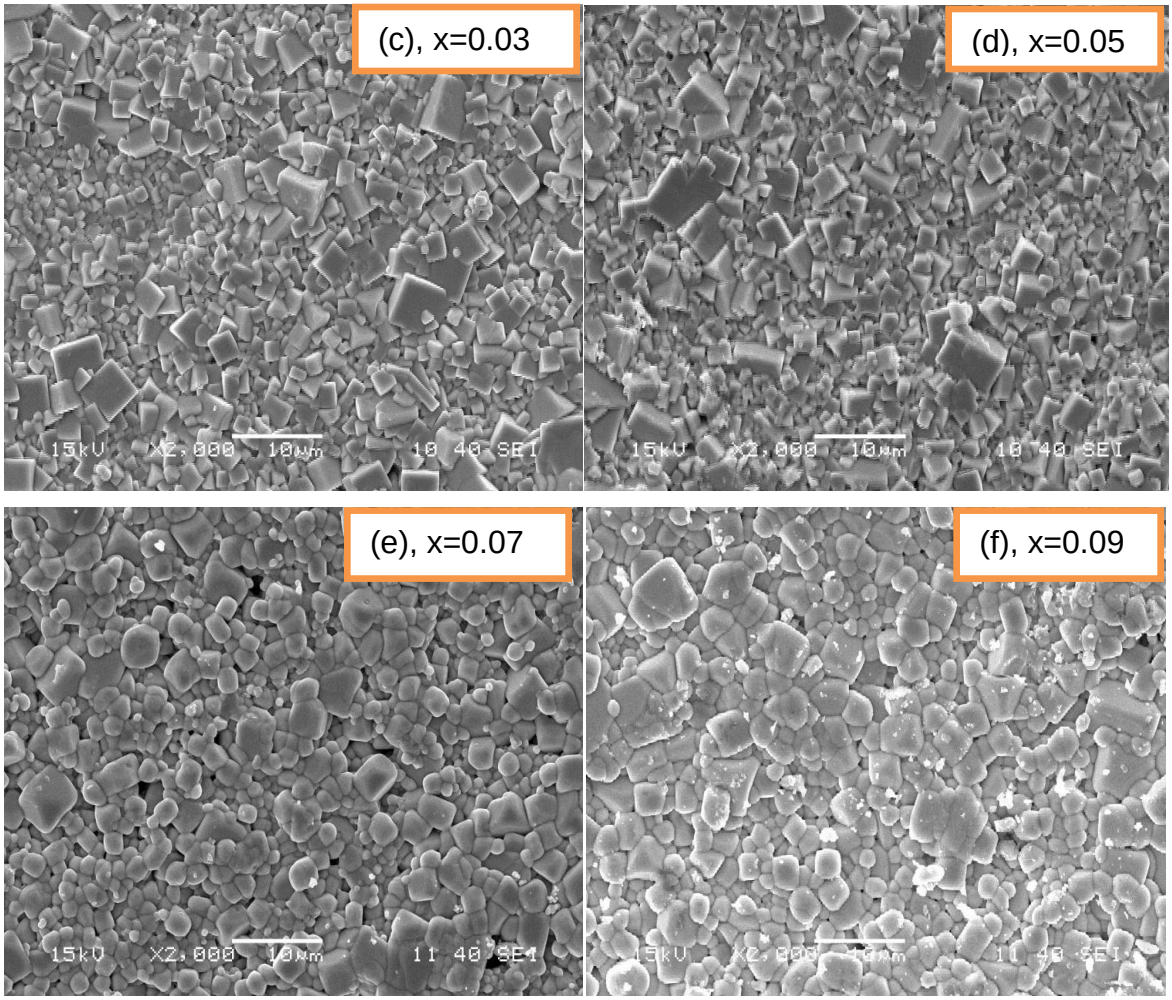

Fig.4.5: (a-f) Representative SEM images of (1-*x*)BNT-*x*ST ceramics.

Energy dispersive X-ray spectroscopy (EDS) is a chemical microanalysis technique used in conjunction with SEM and is not a surface science technique. The EDS technique detects x-rays emitted from the sample during bombardment by an electron beam to characterize the elemental composition of the analyzed volume. The spectra show the EDS of $SrTiO_3$ substituted BNT compositions (Fig. 4.6(a-d)). The spectra show that the elements present in the prepared compositions are Na, Bi, Sr, Ti and O only. With increasing $SrTiO_3$ content, the weight percentage of Sr^{2+} increases in the composition (Table 4.3). Hence energy dispersive x-ray analysis (EDX) (Fig. 4.6 and Table 4.3) confirmed that all the samples are in stoichiometry ratio.

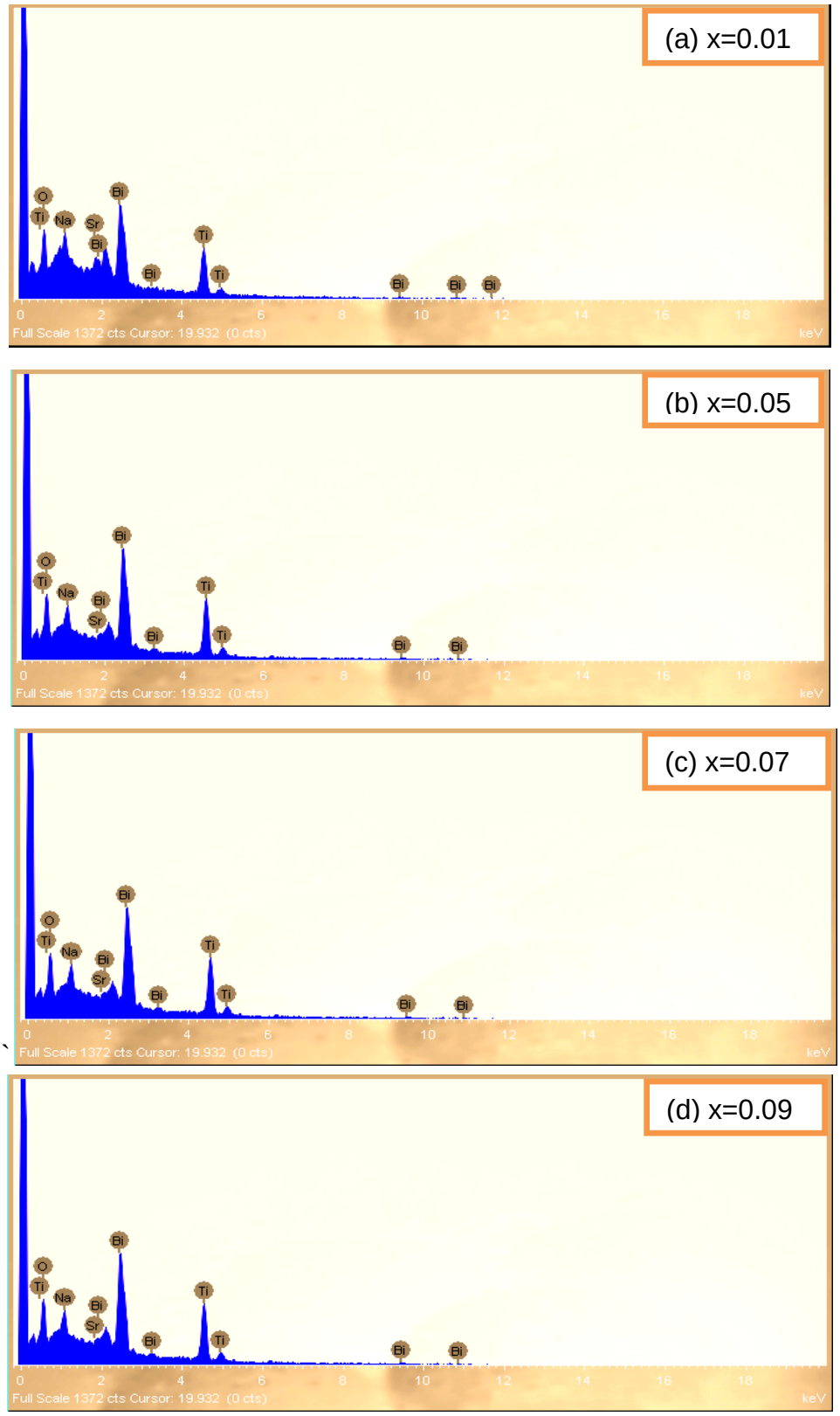

Fig.4.6: (a-d) Energy dispersive x-ray spectroscopy compositional patterns of the (1-*x*)BNT-*x*ST ceramics sintered at 1150^{o}C for 4 hrs

Table 4.3: Compositional analysis of (1-*x*)BNT-*x*ST ceramics from energy dispersive x-ray spectroscopy

Compositions (*x*)	Elements	Theoretical Weight%	Weight% from EDS
0	O K	25.6554	26.01
	Na K	5.4256	5.33
	Ti K	19.6	19.45
	Bi M	49.32	49.21
0.01	O K	25.7596	26.90
	Na K	5.263	4.58
	Ti K	19.7	19.57
	Sr L	1.4342	1.45
	Bi M	47.84	47.49
0.05	O K	25.829	26.55
	Na K	5.1833	4.68
	Ti K	19.773	19.73
	Sr L	2.393	2.23
	Bi M	46.85365	46.80
0.07	O K	25.898545	26.95
	Na K	5.0458	4.03
	Ti K	19.842	19.94
	Sr L	3.346467	3.90
	Bi M	45.867	45.17
0.09	O K	25.968	27.12
	Na K	4.9373	4.45
	Ti K	19.9113	20.03
	Sr L	4.3026	4.15
	Bi M	44.88	44.26

4.3 *OPTICAL PROPERTIES STUDY*

4.3.1 Ultraviolet-Visible Absorption Spectroscopy Analysis

The optical band gap nature and value was estimated for (1-*x*)BNT-*x*ST ceramics by using the method proposed by Wood and Tauc [164] and is presented in Fig.4.7. According to these

authors, the optical band gap is associated with the absorbance and photon energy by the following equation 4.1:

$$(\alpha h\nu)^r = A(h\nu - E_{gap}) \quad (4.1)$$

where α is the absorbance, h is the Planck constant, A is a constant, ν is the frequency, E_{gap} is the optical band gap and r is a constant associated to the different types of electronic transitions (r = 2, 1/2, 2/3 or 1/3 for direct allowed, indirect allowed, direct forbidden and indirect forbidden transitions, respectively).

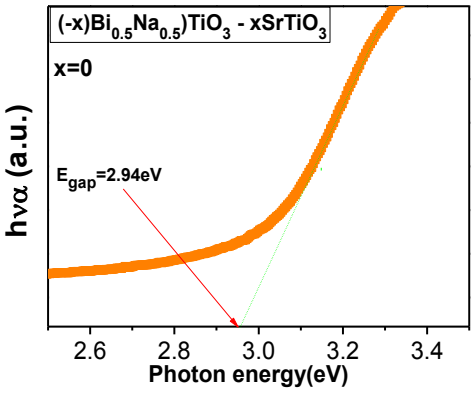

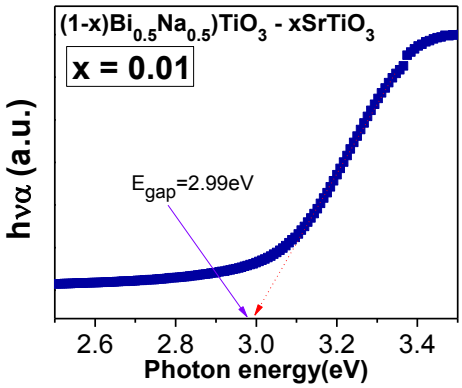

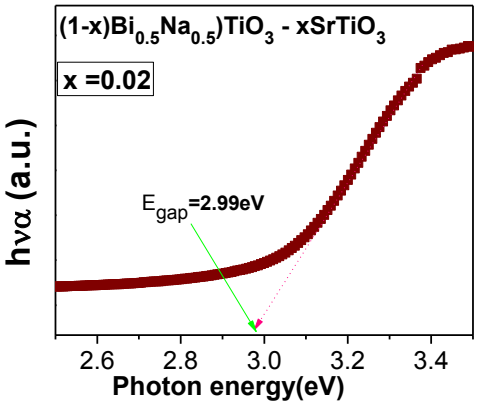

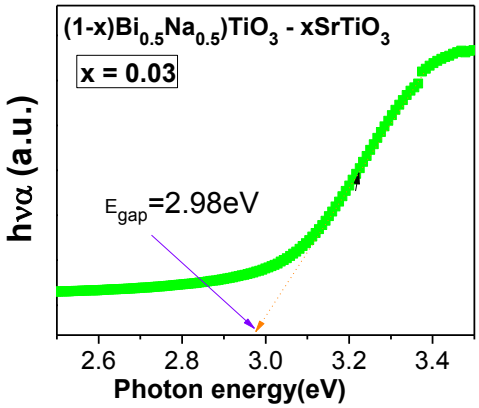

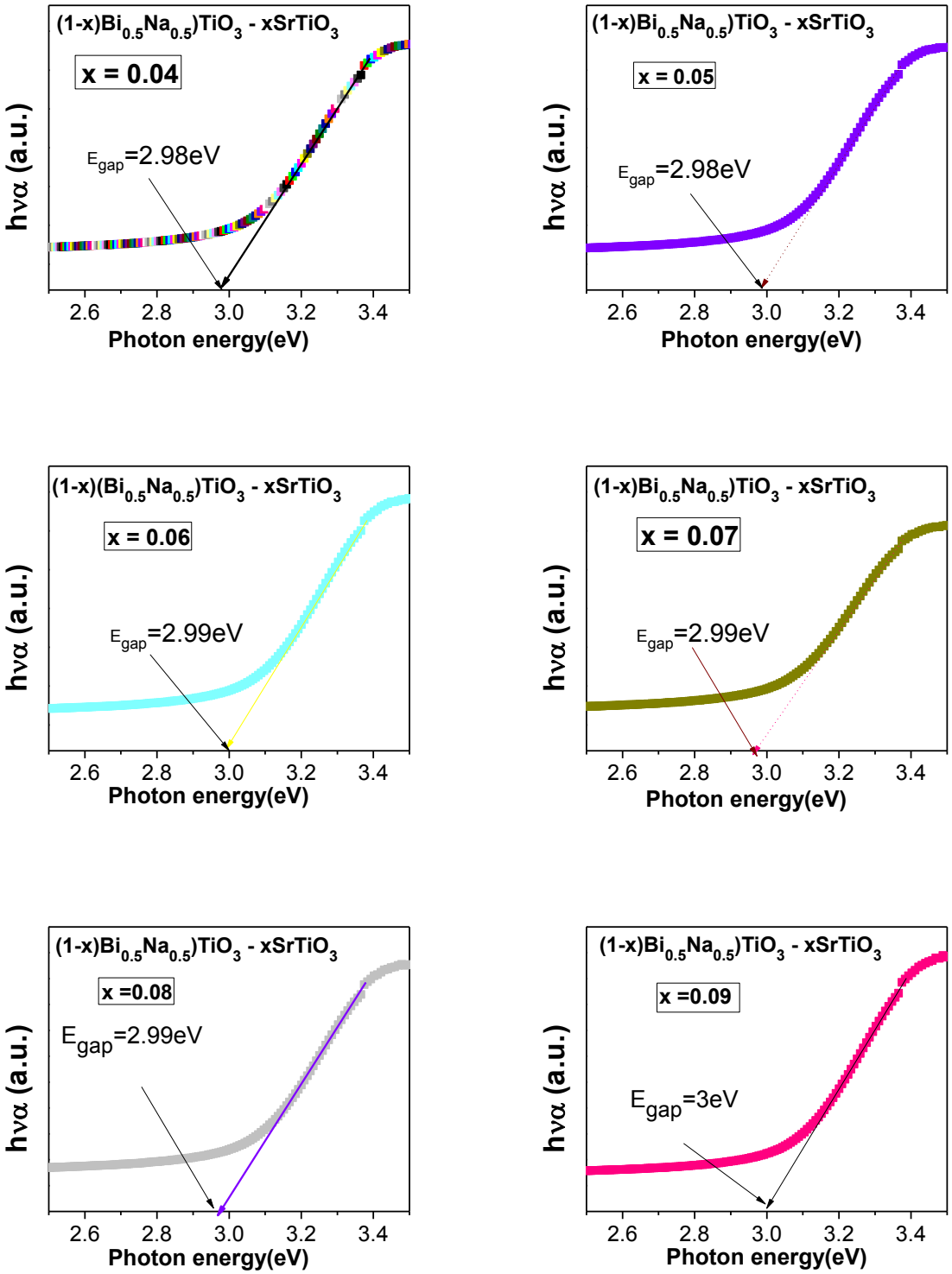

Fig.4.7: Optical band gap calculated by extrapolating the linear portion of the absorption spectra for (1-*x*)BNT-*x*ST ceramics

In our work, the UV-Visible absorbance spectra indicated an indirect allowed transition and, therefore, the value of $r = 1/2$ is used in the above equation. The literature [178] describes that the band gap energy is indirect when the electronic transitions occur from maximum-energy states located near or in the valence band (VB) to minimum-energy states below or in the conduction band (CB), but in different regions in the Brillouin zone. Thus, the E_{gap} value for BNT-ST powders was evaluated by extrapolating the linear portion of the curve or tail. Such method gives a rather good idea of the optical band gap with an accuracy of about ± 0.05 *eV* (depending on the way the tangent is defined). Slightly increased optical band gap is observed with the increase in ST content in BNT-ST ceramics in the studied composition range.

In principle, this behavior indicates the existence of different intermediary energy levels within the band gap of these materials, which can be arising from the structural order-disorder into the lattice. Thus, the increase of ST content is able to induce a structural rearrangement, reducing the presence of these energy levels within the band gap and increasing the E_{gap} values. Based on this hypothesis, we believe that the intermediary energy levels are composed of deep and shallow holes [179].

4.4 *DIELECTRIC PROPERTIES STUDY*

4.4.1 Temperature-Dependent Dielectric Constant (ε') and Loss (tanδ)

Fig.4.8 (a,b) show the typical temperature-dependence of relative permittivity for (1-*x*)BNT-*x*ST solid-solutions at 100 kHz and 1 MHz, respectively. The dielectric constant increases, transition temperature decreases and peaks become slightly broader as ST content increases. It is reported that when $x = 0.04$, the curves exhibit two dielectric anomalies at T_d and T_m. Wang, *et. al*. [180] studied the dielectric behavior of BNT-ST ceramics and observed a strong

frequency dependent T_m. The T_m move towards higher temperature as frequency increases while presented a maximum value of ε decreases, suggesting that the ceramics are relaxor ferroelectrics. These authors suggested that the observed relaxor behavior in BNT-ST ceramics is due to the random distribution of octahedral [SrO_{12}] clusters, which are coordinated to twelve oxygen atoms in A-site in perovskite-type cubic structure, analogous to the other well-known relaxor [181]. Himura, *et al*. [182] reported the composition-dependent phase transition temperatures and found that the transition temperature from rhombohedral to tetragonal phase decreases with increase in ST content and becomes equal to T_d at about x = 0.02. Our dielectric results are in good agreement with those reported earlier.

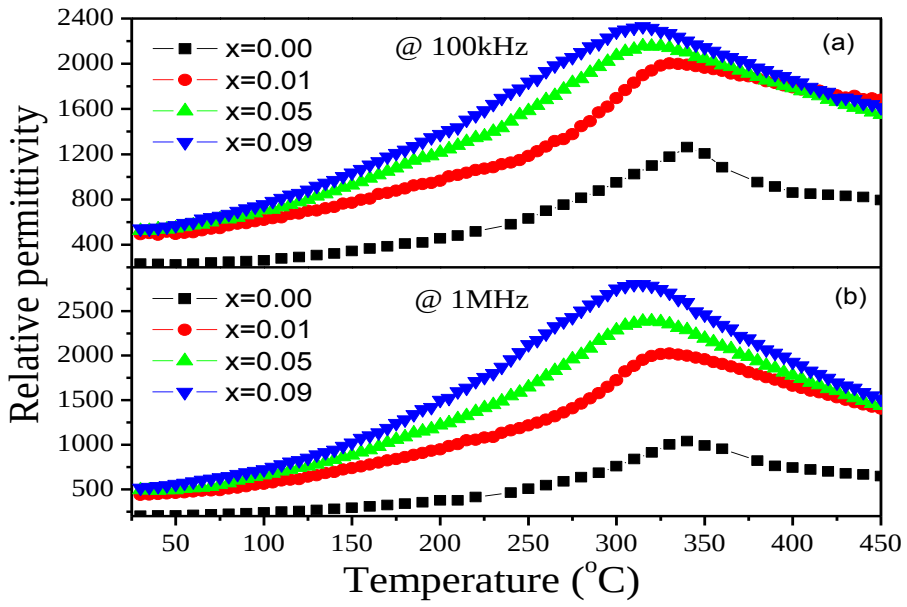

Fig.4.8: (a, b) Temperature-dependence of the relative permittivity for (1-*x*)BNT-*x*ST ceramics

The temperature co-efficient of permittivity (α) is calculated by using the formula in equation 4.2 and that value are given in Table 4.4.

$$\alpha = \frac{\varepsilon_r(T) - \varepsilon_r(T_R)}{(T - T_R)\varepsilon_r(T_R)} \qquad (4.2)$$

where $\varepsilon_r(T_R)$ is the permittivity at room temperature, $\varepsilon_r(T)$ is the permittivity at 100° C and α is the temperature coefficient of permittivity.

Fig.4.9 (a) (phase angle vs. temperature) shows the depolarization temperature (T_d) of (1-*x*)BNT-(*x*)ST ceramics given in the Table 4.4, which is not so clear in ε_r vs. temperature plot for all the compositions. This depolarization temperature decreases with increasing ST concentration, which indicates that the stability in the materials increases. Fig.4.9 (b) shows the Log $(1/\varepsilon'-1/\varepsilon_m)$ vs. log $(T-T_m)$ plot of (1-*x*)$(Bi_{0.5}Na_{0.5})TiO_3$-*x*$SrTiO_3$ ceramic at the frequency 100 kHz. The diffusion coefficient (γ) increases with increasing ST content (given in Table 4.4); it signifies the relaxor properties of (1-*x*)BNT-*x*ST ceramics generated with ST content in the studied composition range. These results are in good agreement with those reported earlier.

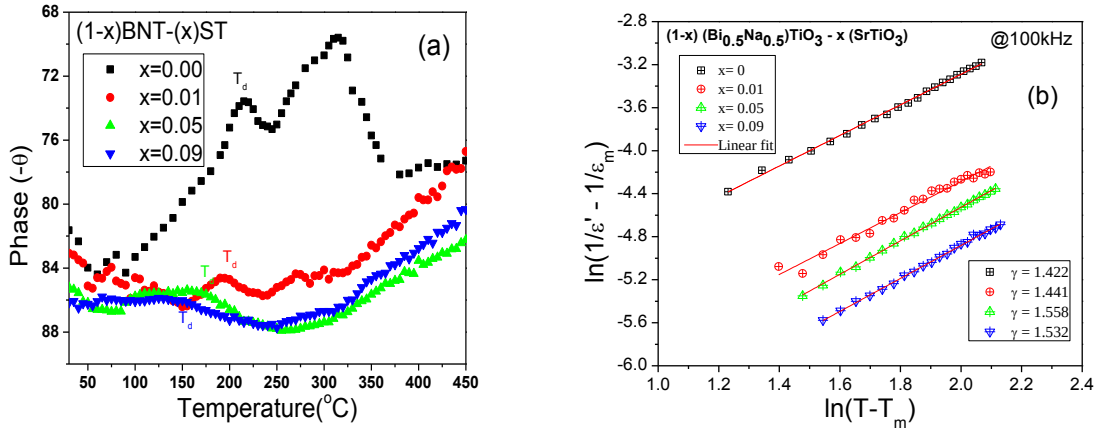

Fig.4.9: (a) Variation of phase angle with temperature and (b) Log $(1/\varepsilon'-1/\varepsilon_m)$ vs. log $(T-T_m)$ frequency at 100 kHz of (1-*x*)$(Bi_{0.5}Na_{0.5})TiO_3$-*x*$SrTiO_3$ ceramic

Fig.4.10 (a, b) show the temperature-dependence of the dielectric loss for BNT-ST solid-solutions at 100 kHz and 1 MHz, respectively. In Fig.4.10 (a, b), it can be noted that the presence of two loss peaks appears in the temperature range from 100 to 175°C and from 250

to 300°C. When the temperature is kept on rising beyond 350°C, the leakage current becomes dominant in the materials, which results in the sharp increase of dielectric loss. This phenomenon may be explained on the basis of the existence of polar micro-region [183]. As the materials suffer a transition from ferroelectric state, to anti-ferroelectric state then to paraelectric state, the anti-ferroelectric phase changes from macro-domain to micro-domain, then to a polar micro-region, cause a sharp increase in dielectric loss [84].

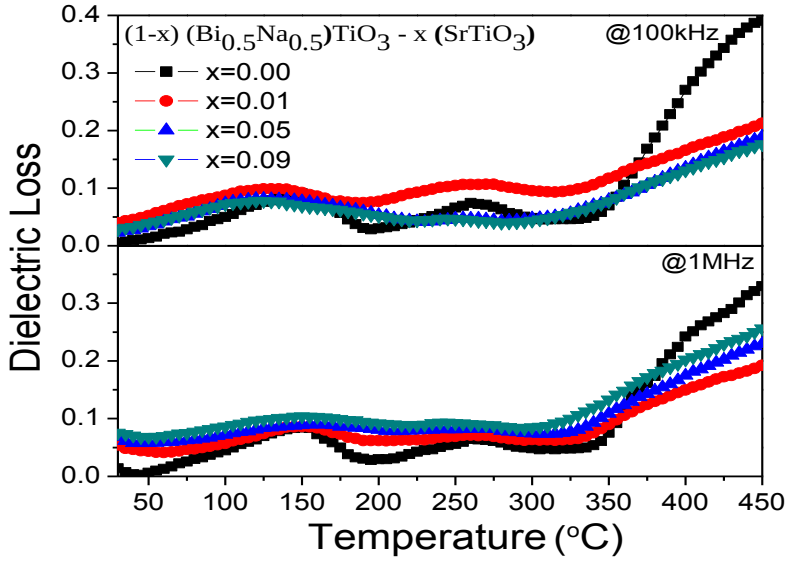

Fig.4.10: (a, b) Temperature-dependence of the dielectric loss for (1-*x*)BNT-*x*ST ceramics

Table.4.4: Dielectric coefficient of (1-*x*)($Bi_{0.5}Na_{0.5}$)TiO_3-*x*$SrTiO_3$ ceramic at 100 kHz frequency

Composition (*x*)	T_d (°C)	T_C (°C)	α ($°C^{-1}$)	ε_m	γ	tanδ
0.00	210	333	2.17 X 10^{-3}	1115	1.42	0.045
0.01	195	325	3.66 X 10^{-3}	2005	1.44	0.09
0.05	170	320	4.99 X 10^{-3}	2156	1.55	0.052
0.09	160	315	6.10 X 10^{-3}	2332	1.53	00.5

4.4.2 Frequency-Dependent Dielectric Constant (ε') and Loss (tanδ)

Fig.4.11 (a, b) show the frequency dependence of the relative permittivity and dielectric loss, respectively, of (1-*x*)BNT-*x*ST ceramics at room temperature. In Fig. 4.11(a), the relative permittivity shows very high value in the low frequency region, and decreases with increase in frequency up to 6 kHz in all compositions. At high frequency, permittivity shows stable behavior for all the compositions. The high value of the permittivity at low frequency is may be due to presence of all type of polarization including space charge [184]. It can also be noticed that with increase in ST content permittivity increases in the high frequency region but decreases in low frequency region. The high frequency behavior can be explained on the basis of; (1) the increase in concentration of high permittivity ST, and (2) due to the increase in polarizability of the atoms in the structure. When a higher radius Sr^{2+} replaces lower radii $(Bi_{0.5}Na_{0.5})^{2+}$ in the structure, there is an increase in lattice parameter yielding the increase of dipole moment in perovskite structure [185].

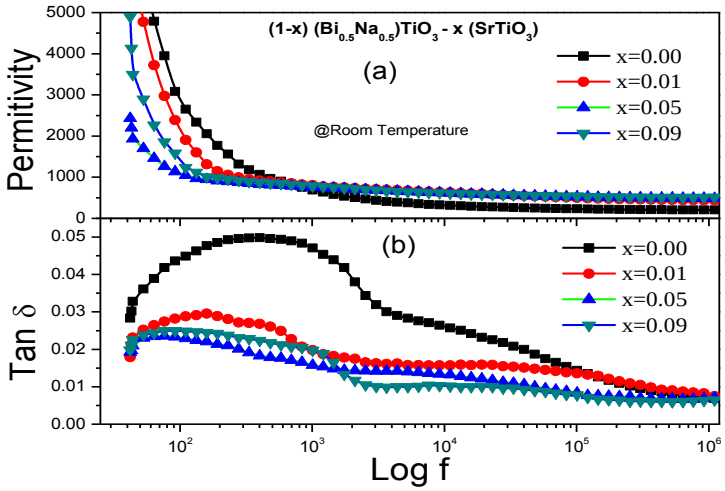

Fig.4.11: Room temperature frequency-dependence of; (a) relative permittivity, (b) dielectric loss for (1-*x*)BNT-*x*ST ceramic

However, to explain the low-frequency behavior, frequency-dependent dielectric loss for BNT-ST is plotted and is shown in the Fig. 4.10(b). At low frequency, with increase in ST content, the dielectric loss decreases. This characteristic combined with frequency-dependent permittivity (Fig. 4.11(a)), it can be ascribed to the Maxwell-Wagner effect. BNT contains lots of point defects due to volatility of Na and Bi. These contribute to the Maxwell-Wagner effect and, therefore, high dielectric constant and high dielectric loss are observed in the low frequency range. Decrease in dielectric loss with ST substitution may be considered due to the decrease in defects (vacancy, mobile ions or leaky grain boundary, etc.) [186].

4.5 ELECTRICAL CONDUCTIVITY

4.5.1 Impedance Study

Fig.4.12 shows the variation of the real part of the impedance (Z') vs. frequency at different temperatures.

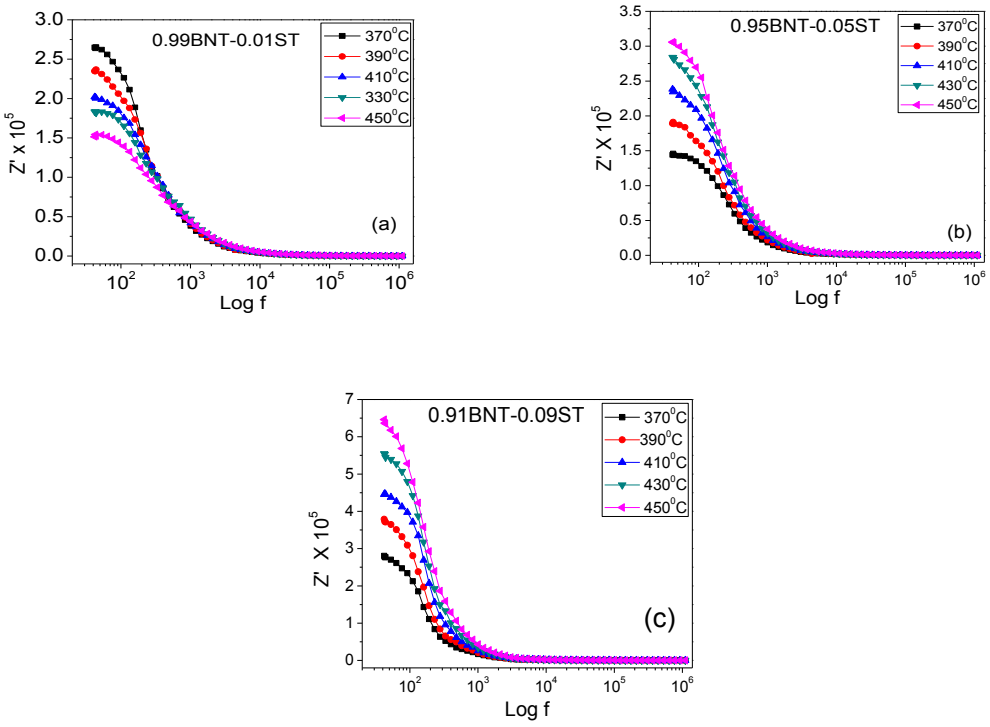

Fig.4.12: Frequency explicit plot of Z' of (a) x = 0.01, (b) x = 0.05, and (c) x = 0.09 for (1-x) BNT-xST specimen at different temperatures

The magnitude of Z' (i.e., resistance) is observed to decrease with increasing temperature and frequency, which indicates the possibility of an increase in the ac conductivity with increasing temperature and frequency [187]. At higher frequency, the space charge has lesser time to relax and the recombination would be faster. The space charge polarization is reduced at higher frequency at the studied temperature. So, the curves merge in higher frequency. Further, at low frequencies, the Z' values decrease with increasing temperature, and the compound exhibits a negative temperature coefficient of resistance (NTCR)-type behavior like that of semiconductors [188].The magnitude of the real part of impedance (Z') increases with increasing $SrTiO_3$ content in BNT. Fig.4.13 shows the imaginary part of the impedance (Z'') as a function of frequency at different temperatures. It can be seen that the curves display broad and low intensity peaks with asymmetrical shape. The broadening of the peak and half widths of the peaks indicate multiple relaxations and deviations from Debye behavior.

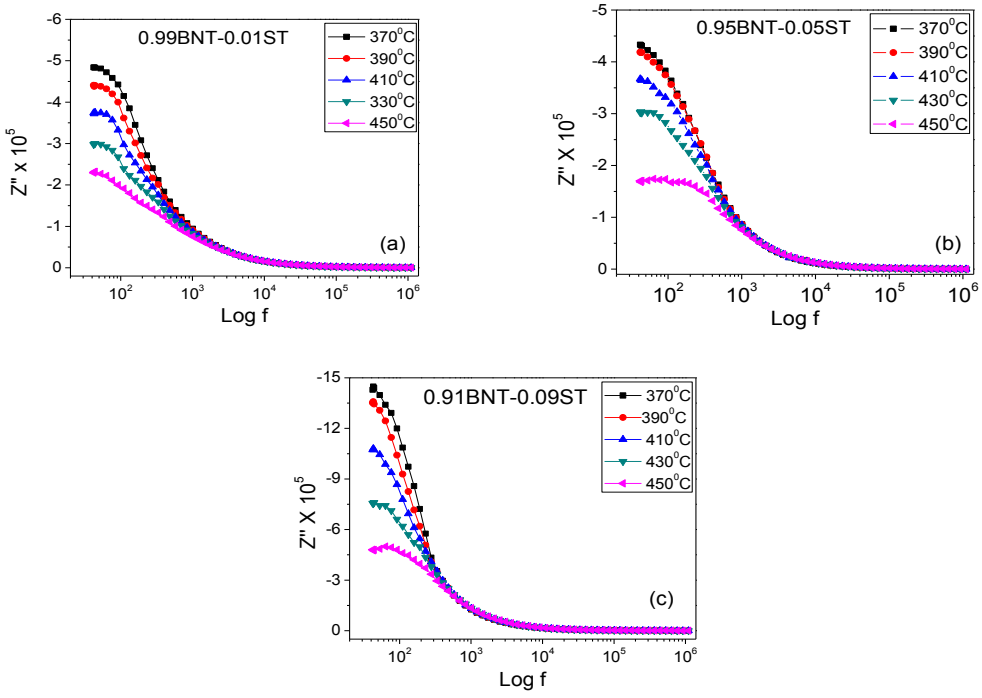

Fig.4.13: Frequency explicit plot of Z'' of (a) x = 0.01, (b) x = 0.05, and (c) x = 0.09 for (1-x) BNT-xST specimen at different temperatures

A significant broadening of the peak with increasing temperature suggests a temperature-dependent electrical relaxation phenomenon in the material [189]. Generally, the relaxation process may be due to the presence of immobile species at lower temperatures and of defects at higher temperatures.

Fig. 4.14 shows Cole-Cole plots (a plot drawn between imaginary and real parts of the impedance) at various temperatures.

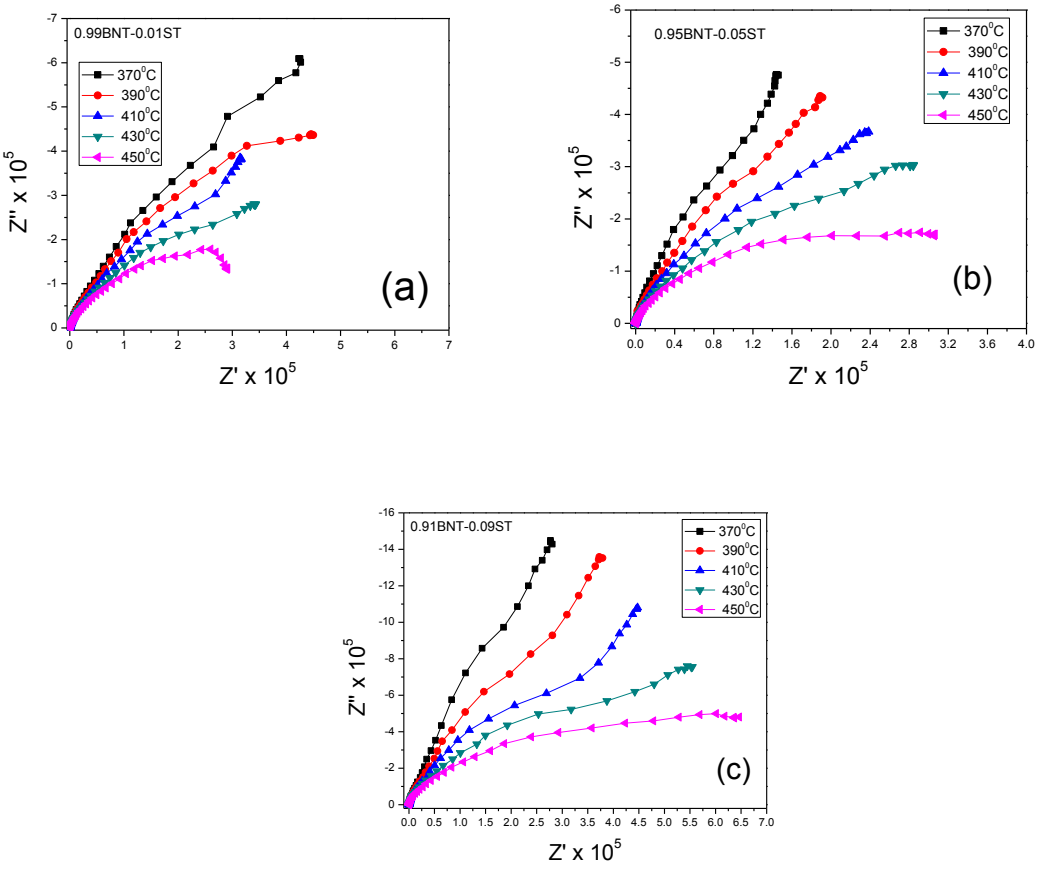

Fig.4.14: (a,c) Cole-Cole (*Z*'-*Z*'') plots of (1-*x*)BNT-*x*ST specimens at different temperatures for x = 0.01, 0.05 and 0.09

As temperature increases, the graphs turn approximately from a pitch arc to semicircles for all the studied compositions. Although not all the plots are depressed semicircles, it also can be

seen that the centers of the circles do not fall on the real axis, but fall on a straight line below the real axis. The relaxation time τ is then not single valued, but is distributed continuously or discretely around a mean value of τ, i.e. τ_m. The angle by which such a semicircular arc is depressed below the real axis is related to the width of the relaxation time distribution. This indicates the non-Debye nature of these samples [77]. The parameters from Cole-Cole plots are given in Table 4.5, fitted by single circuit, which indicates grain effect only in BNT-ST samples. Fig.4.15 (a, b) shows the Cole-Cole (*Z*'-*Z*'') plots of (1-*x*) BNT-*x*ST specimen at different temperature. The area of the semi-circles increases with increasing $SrTiO_3$ content in BNT, which indicates the fall of conductivity and non-Debye nature of these samples.

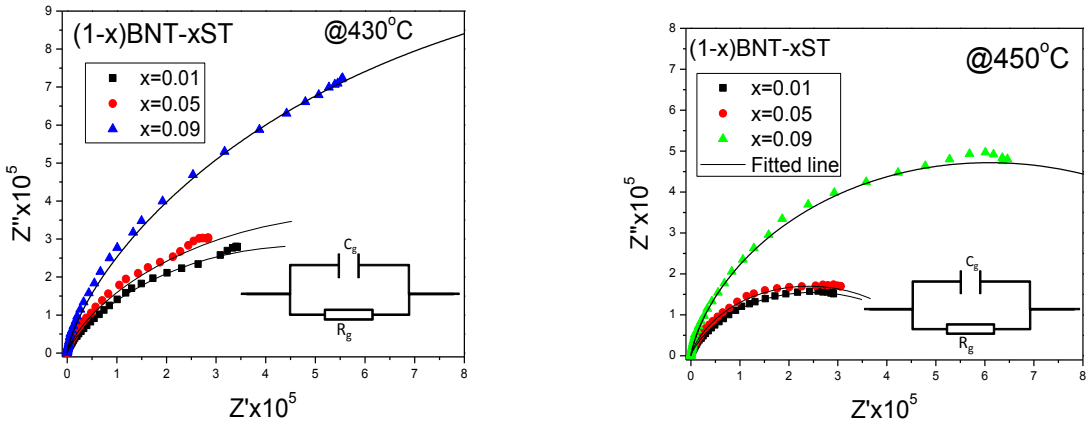

Fig.4.15: (a, b) Cole-Cole (*Z*'-*Z*'') plots of (1-*x*)BNT-*x*ST specimens at temperatures 430°C and 450°C

Table 4.5: the parameters from Cole-Cole (*Z*'-*Z*'') plots of (1-*x*) BNT-*x*ST specimens

Composition (*x*)	Temperature (°C)	R_g(MΩ)	C_g (nF)	$\tau(\text{sec}) = \frac{1}{\omega_{max}} = C_g R_g$
0.01	430	1.013	56	0.05673
	450	0.5144	43.6	0.02243
0.05	430	1.639	20.56	0.0337
	450	0.915	20.4	0.0187
0.09	430	3.073	21.7	0.0667
	450	1.258	8.742	0.011

4.5.2 Modulus Analysis

Fig.4.16 (a-c) shows the variation of real part of electrical modulus M' as a function of frequency at various temperatures for the studied compositions. It is evident that for each temperature, at lower frequencies the real part of impedance M' approaches to zero, confirming the presence of an appreciable electrode and/or ionic polarization in the studied samples. With increasing the ST content in (1-*x*)BNT-*x*ST solid-solution, there is no significant change of M' in the studied composition range.

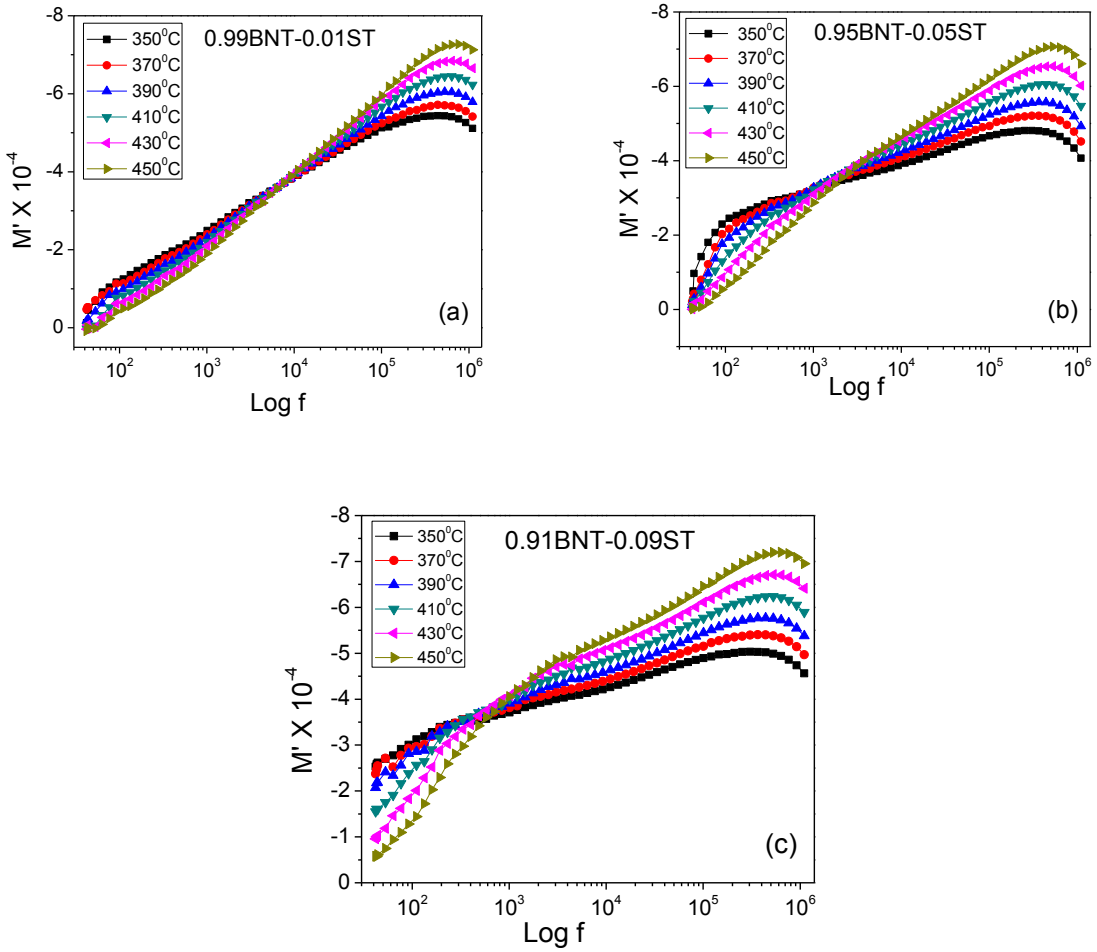

Fig.4.16: (a-d) Variation of real part of electrical modulus M' as a function of frequency at various temperatures of (1-*x*)BNT-*x*ST ceramics

4.5.3 AC and DC Conductivity Analysis

The log-log plot of electrical conductivity vs. frequency at different temperature is shown in Fig.4.17 (a-c). The plot shows that conductivity increases with increase of temperature for all the specimens. Frequency-independent behavior of the conductivity in the low-frequency region is observed but that becomes sensitive in the high-frequency region, which is generally known as hopping frequency, shifted towards higher frequency side with increasing of temperature. In the higher-frequency region, the conductivity increases due to the hopping of charge carriers in finite clusters. Frequency-independent ac conductivity observed at the high temperature indicates the long-range movement of mobile charge carriers.

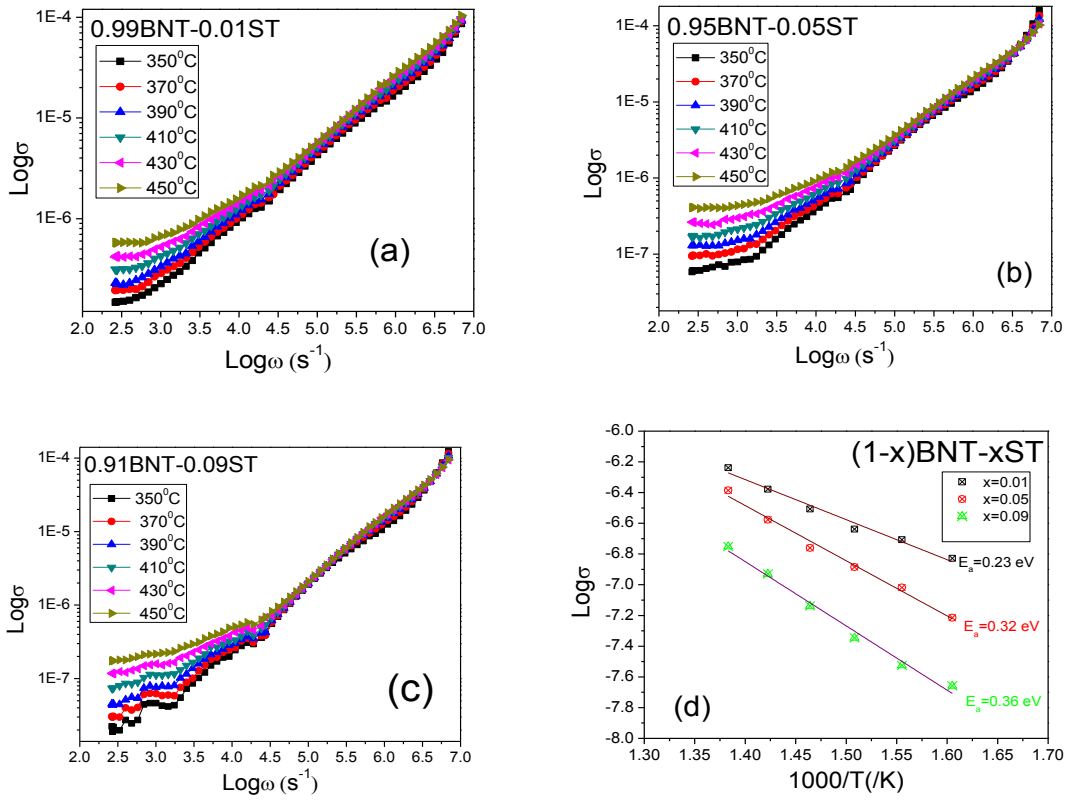

Fig.4.17: (a-c) Frequency explicit plot of conductivity (σ) of (1-*x*) BNT-*x*ST specimens at different temperatures and (d) Temperature-dependence of the dc conductivity for (1-*x*) BNT-*x*ST specimens (the dots are the experimental points and the solid line is the least-squares straight-line fit)

The frequency dependence of conductivity in the dispersive regions for all the compositions of the (1-*x*)BNT-*x*ST samples at various temperatures were analyzed using the Universal Jonscher's power law (Eq.3.7). Fig.4.17 (a-c) shows frequency dependence of ac conductivity at various temperatures. It can be seen that in low frequencies and high temperatures we observe plateaus of $\sigma\ (\omega)$ *or* σ_{ac}, i.e. frequency independent values of conductivity, which corresponds to the dc conductivity (σ_{dc}).

The dc conductivity estimated from the bulk response of the material has been observed as a function of temperature for all the specimens as shown in the Fig.4.18. At higher temperatures, the conductivity vs. temperature response for all the specimens is linear and can be explained by a thermally activated transport of Arrhenius type governed by the relation:

$$\sigma_{dc} = \sigma_0 exp(E_a | k_B T) \qquad (4.2)$$

where σ_o, *E*a and *k* represent the pre-exponential factor, the activation energy of the mobile charge carriers and Boltzmann constant respectively. The activation energy was found to be 0.23 *eV*, 0.32 *eV* and 0.36 *eV* for all the studied specimens shown in the Fig.4.17 (d). The activation energy increases with increasing ST content.

4.6 POLARIZATION AND PIEZOELECTRIC STUDY

Fig.4.18(a) shows the hysteresis loop of (1-*x*)BNT-*x*ST ceramics in a maximum applied field of about 42 kV/cm for all compositions at room temperature and 4.18(b) shows the variation of coercive field and remnant polarization with maximum applied field for a particular composition (*x* = 0.09). All the compositions show a typical ferroelectric behavior. In the studied compositions, with the increasing of ST content both coercive field (E_c) and remnant polarization (P_r) increase. The ionic radius of Sr^{2+} is larger than the ionic radius of $(Bi_{0.5}Na_{0.5})^{2+}$, these network modifiers are located in A-site, which has weakened the coupling

between TiO_6 octahedron and, as a result, the ferroelectric properties of samples degenerated. It is well known that ST is paraelectric at room temperature. Addition of paraelectric phase into the ferroelectric lattice may be another reason for decrease in ferroelectric behavior. Similar degenerated behavior of BNT ceramics has been reported in the literature [190, 191]. Together with the temperature dependence of dielectric and room temperature ferroelectric properties, it has been suggested that the *P~E* loop were resulted from the electro-mechanical interaction between the polar and non-polar regions, which coexisted in the BNT-based ceramics [192].

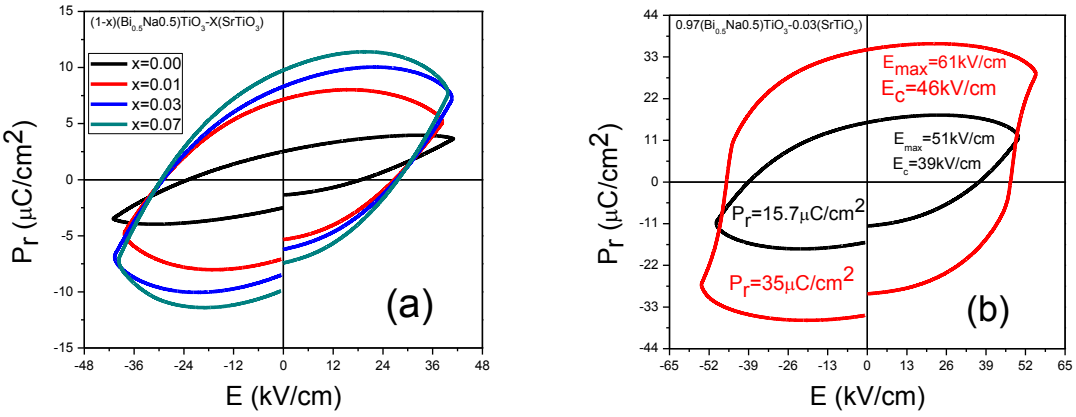

Fig.4.18: (a,b) Hysteresis loop (P~E) of (1-*x*)BNT-*x*ST ceramics recorded at room temperature

Table 4.6: Variation of P_r and E_c as a function of ST content and with E_{max} in (1-*x*) BNT-*x*ST ceramics

Maximum Field (E_{max})	Composition (*x*)	E_C (kV/cm)	P_r (μC/cm^2)
41 kV/cm	0	20	2.55
	0.01	27.5	7.2
	0.05	28	8.4
	0.09	27.2	10
51 kV/cm	0.09	39	15.7
61 kV/cm	0.09	46	35

In Fig. 4.19, we can observe that the increase of ST content promotes a decrease in d_{33}, since the ST lattices have a cubic structure with a high symmetry. Therefore, the undistorted octahedral [TiO_6] clusters and cuboctahedral [SrO_{12}] clusters inhibit the improvement of piezoelectric properties. The observed d_{33} values in the studied composition range are smaller than those reported in the literature [193, 194]. This behavior is due to use of low electric field during polling process. Piezoelectrical properties degenerated in the studied composition range of BNT-ST, which may be due to the paraelectric nature of $SrTiO_3$ ceramics.

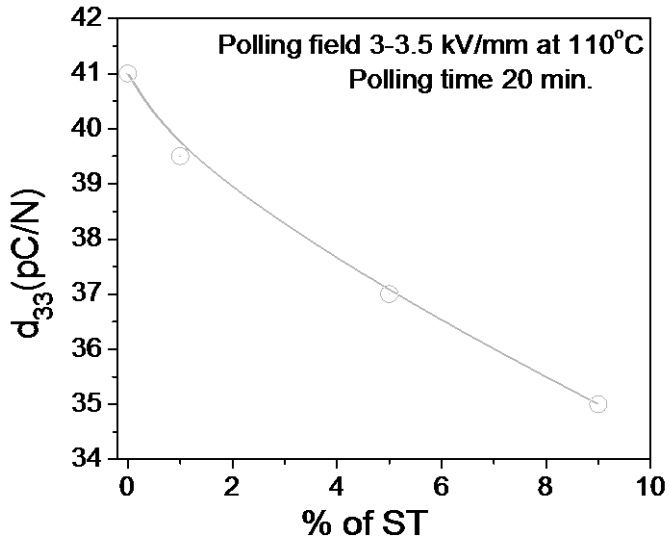

Fig.4.19: Compositional dependence of d_{33} for (1-*x*)BNT-*x*ST ceramics at room temperature

Main result of this chapter have been published and accepted in

1. **Journal of Applied Physics A, 109 (3), (2012) 715-723**
2. **Asian Journal of physics (Accepted)**

CHAPTER 5

MORPHOTROPIC PHASE BOUNDARY (MPB), ELECTRICAL AND OPTICAL STUDY OF $(Bi_{0.5}Na_{0.5})TiO_3$-$BaTiO_3$ LEAD-FREE PIEZOELECTRIC CERAMIC SYSTEM

OUTLINE: In this chapter the influence of $BaTiO_3$ content on $(Bi_{0.5}Na_{0.5})TiO_3$ ceramic with regards to its structural, electrical and optical properties has been studied. Particular emphasis has been given to study the enhanced properties in the morphotropic phase boundary (MPB) region.

5.1 SAMPLE PREPARATION

The samples were prepared by a conventional mixed oxide process. In the first step, $(Bi_{0.5}Na_{0.5})TiO_3$ (BNT) and $BaTiO_3$ (BT) master batches were made from Barium Carbonate - $BaCO_3$ (reagent grade, Meark, India), Titanium Oxide -TiO_2 (reagent grade, Merck, India), Bismuth Oxide - Bi_2O_3 (reagent grade, Meark, India) and Sodium Carbonate - Na_2CO_3 (reagent grade, Merck, India). Appropriate amounts of reagents were mixed in a zirconia media for 12 hrs using a laboratory designed ball milling unit. The BNT sample was calcined at 850^{o}C for 4 hrs with intermediate grinding and mixing. The BT sample was calcined at 1300^{o}C for 4 hrs with intermediate grinding and mixing. The phase purity of both the master samples was investigated using x-ray diffraction (XRD), (Xpert MPD, Philips, UK). Appropriate amounts of BNT and BT were mixed thoroughly in agate mortar using isopropyl alcohol (IPA) to obtain $(1-x)(Bi_{0.5}Na_{0.5})TiO_3$-$xBaTiO_3$ (abbreviated as BNT-BT hereafter) ceramics, where x ranges from 0.01 - 0.08. The mixed powders were ball milled for 12 hrs in

acetone medium. The intension of using ball milled is proper mixing of powder. After ball milling the powders were dried at room temperature. Then the dried powders were again grinded for 2 hrs in agate mortar. The granules were made by adding 3% polyvinyl alcohol (PVA) as a binder. The granules were sieved and uniaxially cold pressed with a load of 6 tonnes to obtain discs with a diameter of 11mm. The discs were decarbonized at 550°C and then sintered between 1050 and 1175°C for 4 hrs. The optimum sintering temperature was determined by investigating the linear shrinkage and bulk density of the sintered pellets. The bulk density and apparent porosity were investigated using Archimedes principle (water immersion technique).The pellets were sintered at the optimized temperature of 1150^{o}C for 4 hrs in a programmable furnace (Table 5.1).

Table 5.1: The optimized sintering temperature, bulk density and apparent porosity of (1-x)($Bi_{0.5}Na_{0.5}$)TiO_3-$x$$BaTiO_3$ ceramic

x	Sintering temperature (°C)	Bulk density (gm/cm^3)	Apparent porosity
0.01	1150	5.86	0.002
0.02	1150	5.71	0.004
0.03	1150	5.43	0.003
0.04	1150	5.63	0.002
0.05	1150	5.69	0.005
0.06	1150	5.49	0.004
0.07	1150	5.61	0.003
0.08	1150	5.32	0.006

Fig.5.1 shows that all the compositions of (1-x)($Bi_{0.5}Na_{0.5}$)TiO_3-$x$$BaTiO_3$ solid-solution ceramics were well sintered at 1150°C with a high density ratio in around 97% of the theoretical density for 4 hrs in air.

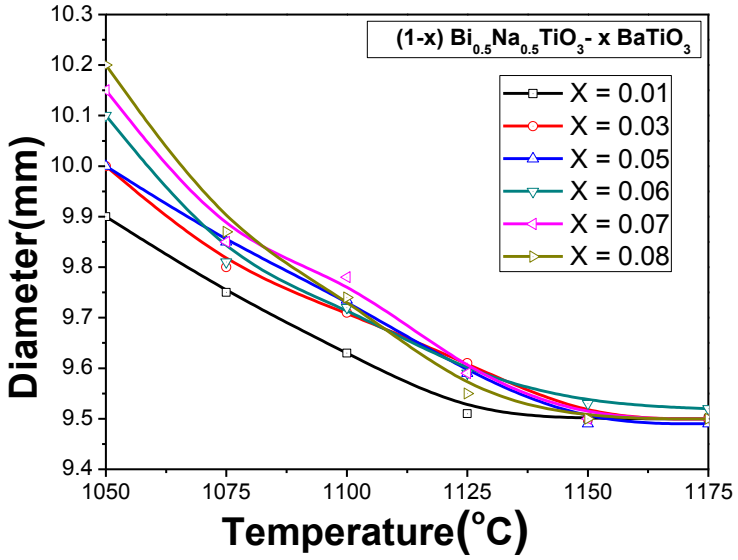

Fig.5.1: Linear shrinkage of (1-*x*)($Bi_{0.5}Na_{0.5}$)TiO_3-*x*$BaTiO_3$

5.2 STRUCTURAL CHARACTERIZATION

The selected samples were characterized by the following tools and the results are discussed.

5.2.1 Phase Formation and Rietveld-Refinement Study

Here we employed the Rietveld-refinement to identify the crystal structure and phase formation of $BaTiO_3$ ceramics, as shown in Fig.5.2 (a), and for BNT ceramics previously in details described in Chapter 3. The Rietveld-refinement requires an approximate structural model for the actual structure. The initial Rietveld-refinement was done by the zero-point shift, the unit-cell, and background parameters. After a good match, the peak position was achieved and the peak profile parameters including the peak asymmetry were refined. The final residual of least-squares refinement (R_p = 15.1%), weighted residual-factors (R_{wp} = 19.5%), expected R-factor (R_{exp} = 11.9%) and the goodness of fit indicator, χ (=R_{wp}/R_{exp} = 1.6) were found.

In the Table 5.2, the given fitting parameters indicated a good agreement between the refined and observed XRD patterns for the $BaTiO_3$ phase. The refined lattice parameter values (a = b = 3.9837 Å, c = 4.0247 Å, ($\alpha = \beta = \gamma = 90^o$)), unit cell volume (V = 63.8702 $Å^3$), bond angles and the bond lengths (given with unit cell in Fig. 5.2(b)) confirmed that the $BaTiO_3$ phase has a tetragonal structure of space group P4mm (70).

Table 5.2: Rietveld-refinement results and atomic coordinates employed to model the $BaTiO_3$ super cells

Atom	Wyckoff	*X*	*Y*	*Z*
Ba1	1a	0	0	0
Ti1	1b	0.5	0.5	0.537
O1	1b	0.5	0.5	-0.06304
O2	2c	0.5	0	0.51997

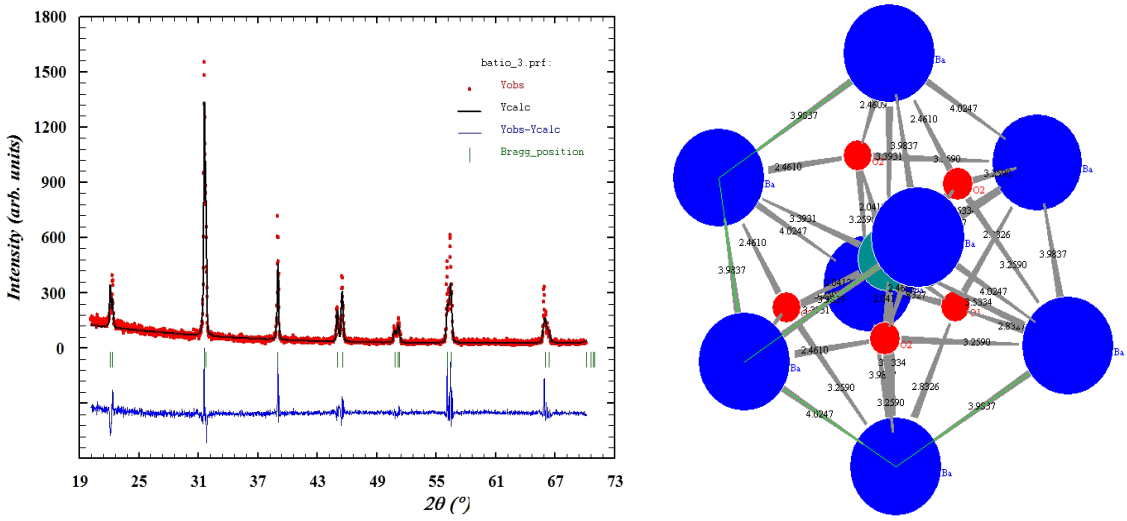

Fig.5.2: (a, b) (Free colour on-line) Rietveld-refinement plots of $BaTiO_3$ ceramics and representations of its unit cell

Fig 5.3 (a) shows the XRD patterns of $(1-x)(Bi_{0.5}Na_{0.5})TiO_3$ - $xBaTiO_3$ ceramics with $0 \leq x \leq 0.08$, sintered at 1150°C for 4 hrs. All the compositions exhibit a pure perovskite structure and no second phases are observed, which implies that $BaTiO_3$ (BT) ceramic has diffused into the

$(Bi_{0.5}Na_{0.5})TiO_3$ lattices to form a solid solution. All the peaks in the XRD pattern of (1-*x*) BNT-*x*BT correspond to the BNT phase with rhombohedral structure as reported by different researchers [43,195,196].

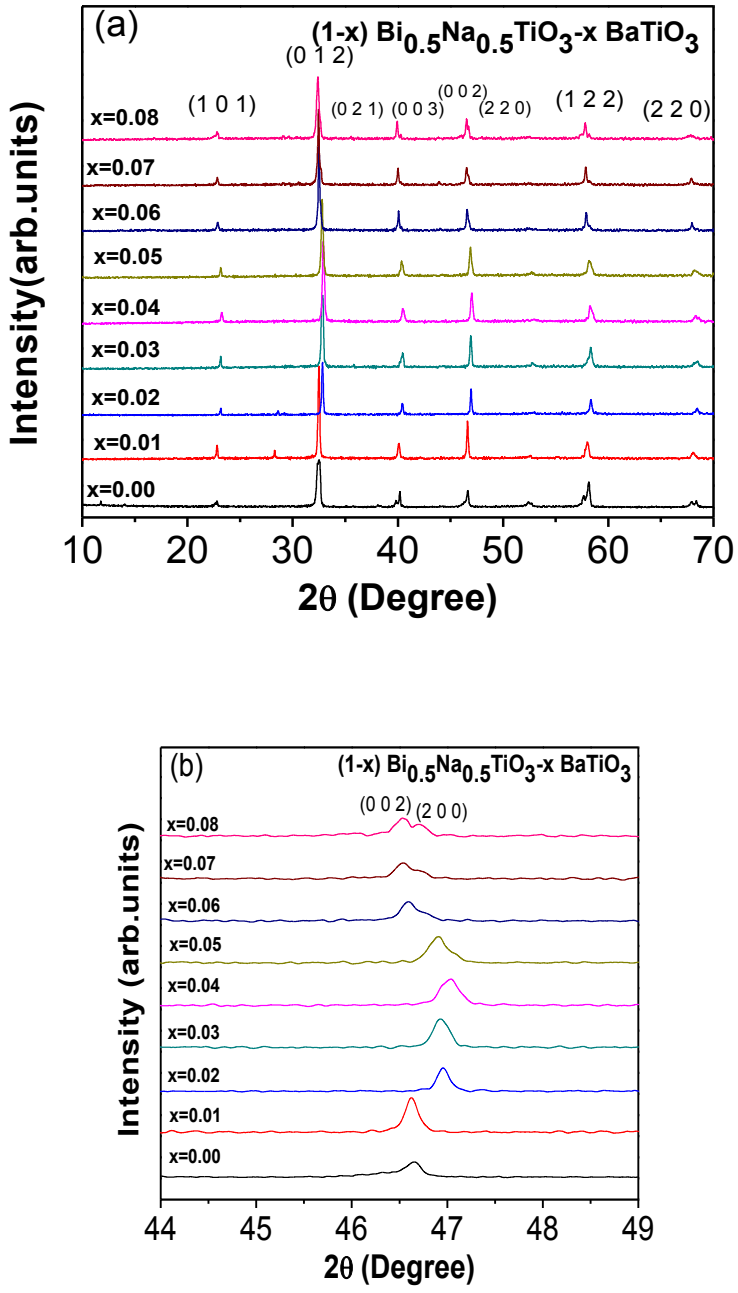

Fig.5.3: (a) x-ray diffraction pattern and (b) Reduced x-ray diffraction pattern of (1-*x*) $(Bi_{0.5}Na_{0.5})TiO_3$-*x*$BaTiO_3$ ceramics

With the increasing of BT content, the peak positions shift towards lower angle and the peaks also get broadened, which implies that crystallite size decreases and lattice parameters increases with increasing BT concentrations. Fig.5.3 (b) shows the XRD patterns of the ceramics in the 2θ range of 38-48 degrees. The rhombohedral symmetry of BNT ceramic at room temperature can be characterized by a (0 0 3)/(0 2 1) peak splitting between 39 and 41 degrees and a single peak of (0 2 4) between 44 and 49 degrees. The rhombohedral (0 0 3)/(0 2 1) peak splitting remains until x = 0.05 and then combines into a slightly asymmetric peak at x = 0.07. On the other hand, the (0 2 4) peak became broad and asymmetric at x = 0.04. A distinct (0 0 2)/(2 0 0) peak splitting appears when x = 0.05, referring to a tetragonal symmetry. These results suggest that the rhombohedral-tetragonal morphotrophc phase boundary (MPB) of (1-x)BNT-xBT ceramics lies near x = 0.07.

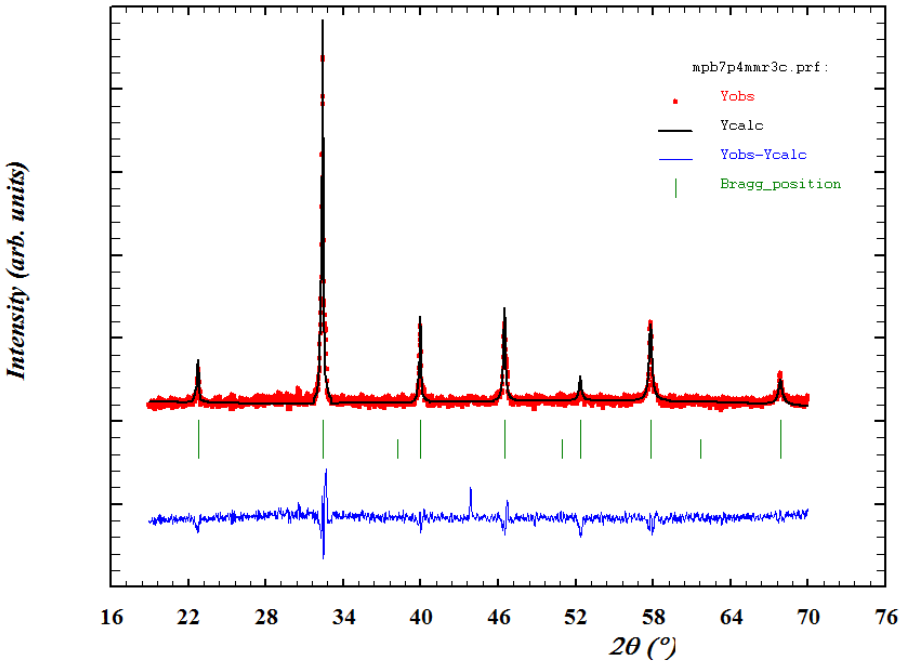

Fig.5.4: Rietveld-refinement plot of $0.93(Bi_{0.5}Na_{0.5})TiO_3$-$0.07BaTiO_3$ ceramics (MPB region)

Table 5.3 and Table 5.4 summarize the Rietveld-refinement result carried out in the MPB (co-existing of BNT and BT phase) composition of the present work. Replacing the refined phase by the coexisting rhombohedral and tetragonal phases resulted in a good fitting between the observed intensities and the calculated intensities of $0.93(Bi_{0.5}Na_{0.5})TiO_3$-$0.07BaTiO_3$ as shown in Fig.5.4, where the final *R*-factor (R_p), weighted *R*-factor (R_{wp}), and χ^2 value are found to be 10.25%, 10.8%, and 2.54, respectively. The result indicates that 0.93BNT-0.07BT is composed of 41.2% rhombohedral phase and 58.8% tetragonal phase, so that 0.93BNT-0.07BT is confirmed to be an MPB composition.

Table 5.3: Rietveld-refinement results and atomic coordinates of $0.93(Bi_{0.5}Na_{0.5})TiO_3$-$0.07BaTiO_3$ ceramics (MPB region)

Phase	Atom	*x*	*y*	*z*	Biso
Rhomb. (R3c)	Bi	0	0	0.2903(13)	0.3840(18)
	Ba	0	0	0.2903(13)	0.3840(18)
	Na	0	0	0.2903(13)	0.3840(18)
	Ti	0	0	0.0177(14)	0.2840(19)
	O1	0.1596(15)	0.3297(16)	0.8866(17)	0.9834(20)
Tetra.(P4mm)	Bi	0	0	0	0.3201(16)
	Ba	0	0	0	0.3201(16)
	Na	0	0	0	0.3201(16)
	Ti	0.5	0.5	0.5356	0.2485(17)
	O1	0.5	0.5	-0.10931	0.5447(18)
	O2	0.5	0	0.41957	0.0374(19)

(The reliability factors are R_p=10.25%, R_{wp}=10.8%, χ^2=2.54, R_{exp}=11.5% and R_{Bragg}=8.1%)

Table 5.4: Refinement-results (phase percentage, cell parameter and cell volume) of the crystal structure of $0.93(Bi_{0.5}Na_{0.5})TiO_3$-$0.07BaTiO_3$ ceramics

x	Crystal system	Space group	Phase %	Lattice parameters		Cell volume ($Å^3$)
				a=b (Å)	c (Å)	
0.07	Rhomb.	R3c	(41.2)	5.5201(3)	13.5229(5)	356.8(9)
	Tetra.	P4mm	(58.8)	3.9025(5)	3.9048(3)	59.4 (6)

5.2.2 Raman Scattering Spectroscopy Analysis

As mentioned previously, BNT has rhombohedral symmetry with space group R3c (C^6_{3v}) and BT has tetragonal symmetry with space group P4mm (C^1_{4v}) at room temperature. As far as BT is concerned, in the tetragonal ferroelectric phase of the C^1_{4v} point group, each of the T_{1u} modes splits into a double degenerate E mode and a non-degenerate A_1 mode while the T_{2u} silent mode splits into B_1+E modes. All the A_1 and E modes are Raman and infrared active and B_1 mode is only Raman active. Furthermore, the existence of long-range electrostatic forces in the tetragonal ferroelectric phase splits each of the A_1 and E modes into longitudinal and transverse modes. However, in the present case most of the analysis has been done with respect to the rhombohedral symmetry of BNT. As per the group theory analysis, BNT (rhombohedral, R3c) should show 13 Raman-active modes in irreducible representation $\Gamma_{Raman} = 7A_1+6E$ [49]. However, it is possible to detect only five Raman-active modes observed in the range from 100 to 1,000 cm^{-1} in agreement with the works reported by the Rout *et al*. [88 and Eerd *et al*. [197]. The Raman patterns show roughness or irregularity due to the data taken at high resolution; it makes noise during the collections of data. If we take the data at low resolution, it is impossible to distinguish the closely-bounded molecules.

Fig.5.5 shows the Raman spectra for (1-*x*)BNT-*x*BT solid-solutions with different compositions as well as the band frequencies as a function of composition derived from

spectral deconvolution. Obviously, there is no significant change in the spectra for the compositions of lower x values ($x < 0.05$). The band at around 280 cm^{-1} is assigned to A_1 symmetry, which is associated with vibration of cations in A-site [198, 199]. More specifically, it has been reported that the presence of this Raman mode implies the existence of local $(Bi_{0.5}Na_{0.5})^{2+}TiO_3$ clusters of several unit cells in BNT [45, 198]. According to the "virtual ion" model [200], the 280 cm^{-1} bands should shift progressively when Ba^{2+} substitutes for $(Bi_{0.5}Na_{0.5})^{2+}$ in $(Bi_{0.5}Na_{0.5})^{2+}TiO_3$ clusters, since the "virtual ion" is considered as an ion with the average properties of all cations in the A-sites. The 280 cm^{-1} band is expected to shift to 275 cm^{-1}, which will be downshifted even further when the bigger ionic size of Ba^{2+} is taken into account. However, no detectable change in the frequency of this Raman band was observed, as shown in Fig.5.5.

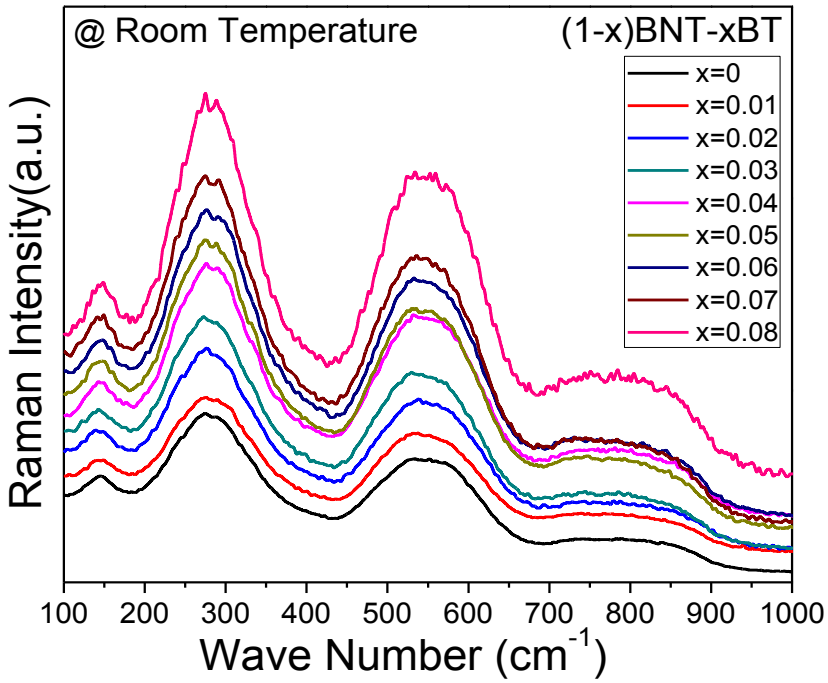

Fig. 5.5: Room temperature Raman spectrum of (1-x)BNT-xBT ($0 \leq x \leq 0.08$) ceramics

Further, interestingly, the 275 $cm^{-1}$and 545 cm^{-1} bands are getting slightly broadened with the increase in *x* value, as indicated by the increase of the full width of half maximum (FWHM) and the shifting of the positions of the Raman bands. The FWHM of a Raman band is inversely proportional to the lifetime of the corresponding phonon [201], which is, in turn, closely related to the size of the local $(Bi_{0.5}Na_{0.5})^{2+}TiO_3$ clusters in the case of present study. When Ba^{2+} substitutes for both Bi and Na, $Ba^{2+}TiO_3$ clusters are formed. As a result, $(Bi_{0.5}Na_{0.5})^{2+}TiO_3$ clusters are reduced in size, giving rise to the peak broadening and intensity weakening of the 280 cm^{-1} band. There is no change in the frequency of this band since both composition and structure remain the same in the $(Bi_{0.5}Na_{0.5})^{2+}TiO_3$ clusters when *x* value is low, which is supported by the observations discussed above. Also, the broad band centered at 280 cm^{-1} is assigned to the A_1 symmetry, which is dominated by a (←O←Ti→O→) vibration. This mode is assigned to stretching arising from the bonds due the presence of octahedral [TiO_6] clusters at short-range. The mode shows anomaly at x = 0.07 and starts splitting into two bands that shift apart from each other with further increase in BT content.

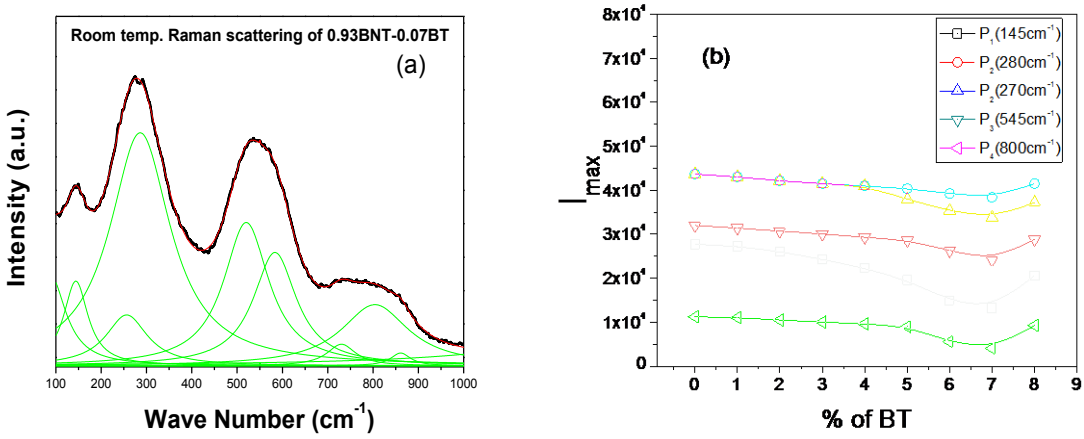

Fig. 5.6: (a) Room temperature Raman spectrum of 0.93BNT-0.07BT (MPB, composition) ceramics and (b) Variation of the maximum intensity of different modes in the Raman spectra with composition (% of BT)

Some drastic changes occur in the Raman spectra when $x > 0.05$. Several new bands, located at 145, 280 (clearly), 545 and 800 cm^{-1}, appear in the spectra. Two of them are underlying bands when x= 0.06 and 0.07, the introduction of which leads to a better overall fit of the spectra shown in the Fig.5.6 (a) for $x = 0.07$. The mode shows anomaly at $x = 0.06$-0.07 (more anomaly at $x = 0.07$) and starts splitting into two bands that shift apart from each other with a further increase in x. The occurrence of these new bands, and observed band splitting, indicates a structural change at $x > 0.05$, which is well in line with the studies of XRD phase analysis. All bands that appear in the spectra at $x > 0.05$ can be assigned to the Raman modes for a tetragonal symmetry [202]. $Ba^{2+}TiO_3$ clusters tend to form a stable tetragonal structure, but they are constrained by $(Bi_{0.5}Na_{0.5})^{2+}TiO_3$ clusters. With the increase in x value and the size of $Ba^{2+}TiO_3$ clusters, such constraining effect become less significant and the phase transition then occur. On the basis of this consideration, it is plausible to conclude that the rhombohedral-tetragonal phase transition is observed at around $x = 0.05$-0.07. This is indeed confirmed by the dramatically enhanced intensity of the Raman bands when the x value is increased further ($x = 0.08$), as shown in Fig.5.6 (b). A strong enhancement in the Raman band intensity suggests the occurrence of a long range ordering of the corresponding phases involved [201-204]. This shows that the minimum intensity occurs at $x = 0.07$ due to the existence of MPB, which are well aligned with the studies of XRD phase analysis.

5.2.3 Microstructure Analysis

Fig.5.7 (a-h) shows the SEM micrographs of natural surface for $(1-x)(Bi_{0.5}Na_{0.5})TiO_3$-$x$ $BaTiO_3$ ceramics. The pure BNT sample presents rectangular grain morphology while the BT addition changes the grain shape towards quasi-spherical shape. All sample surface grains present regular geometry with compact structure.

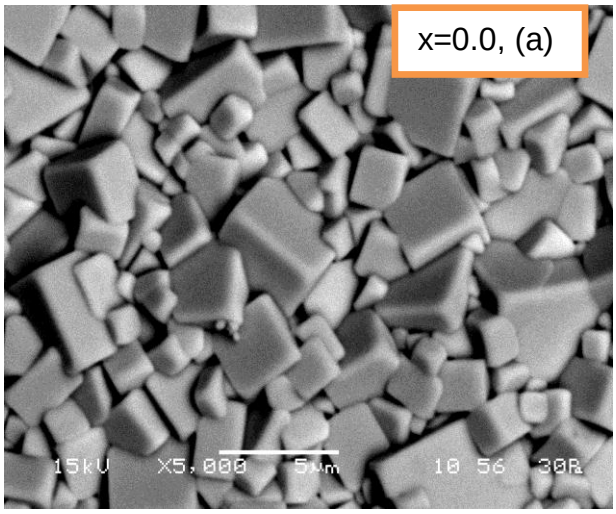
x=0.0, (a)
15kV X5,000 5μm 10 56 30R

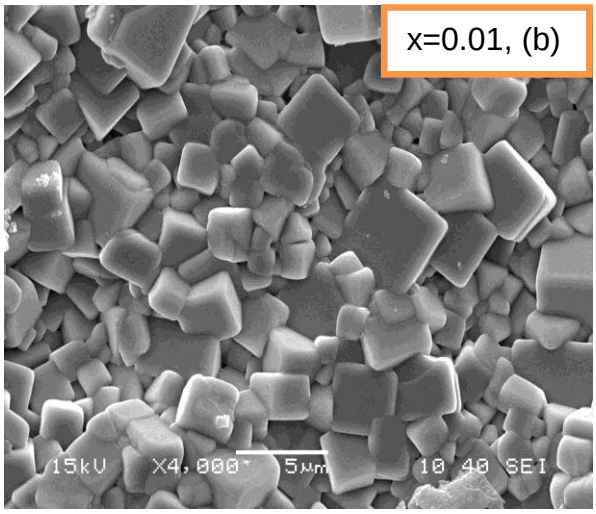
x=0.01, (b)
15kV X4,000 5μm 10 40 SEI

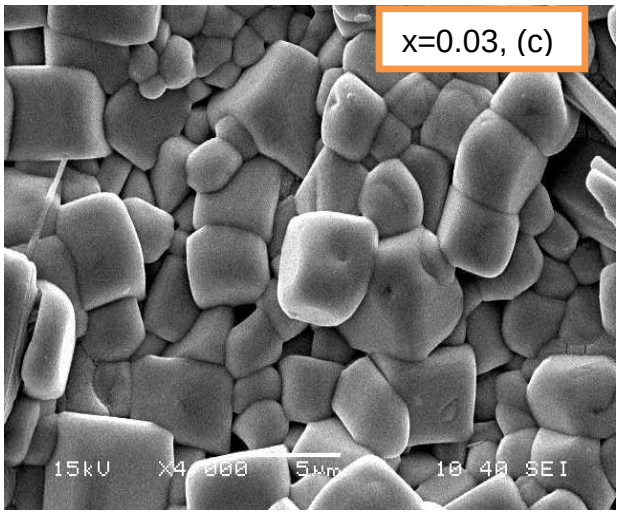
x=0.03, (c)
15kV X4,000 5μm 10 40 SEI

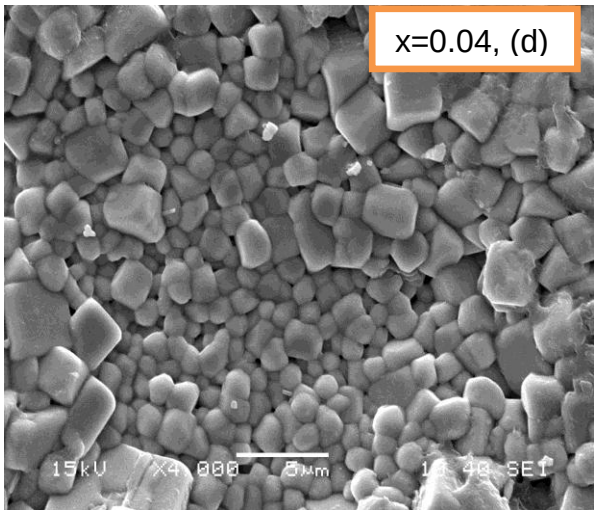
x=0.04, (d)
15kV X4,000 5μm 10 40 SEI

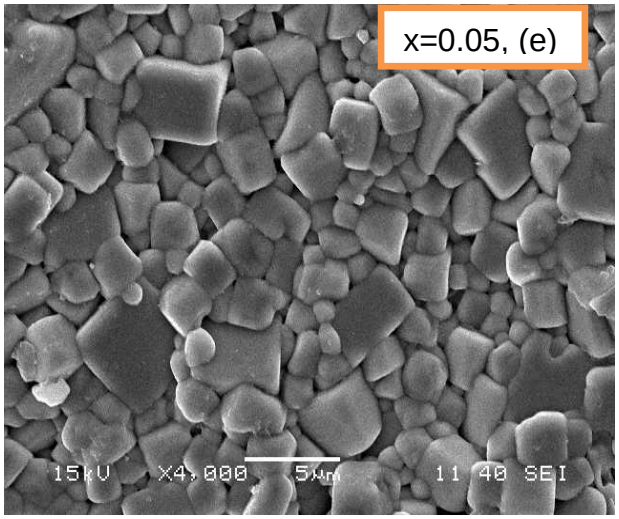
x=0.05, (e)
15kV X4,000 5μm 11 40 SEI

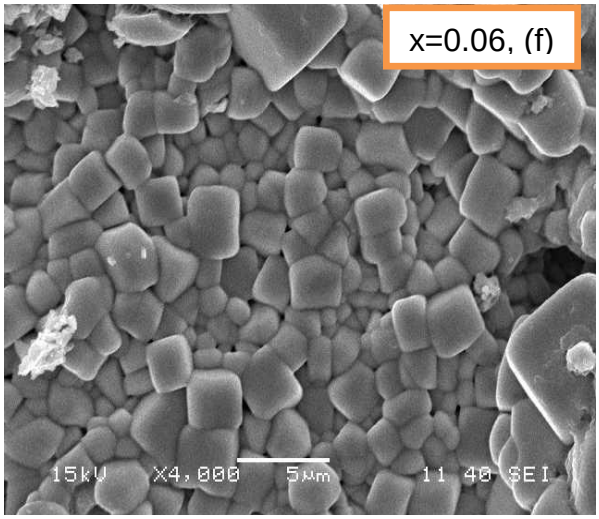
x=0.06, (f)
15kV X4,000 5μm 11 40 SEI

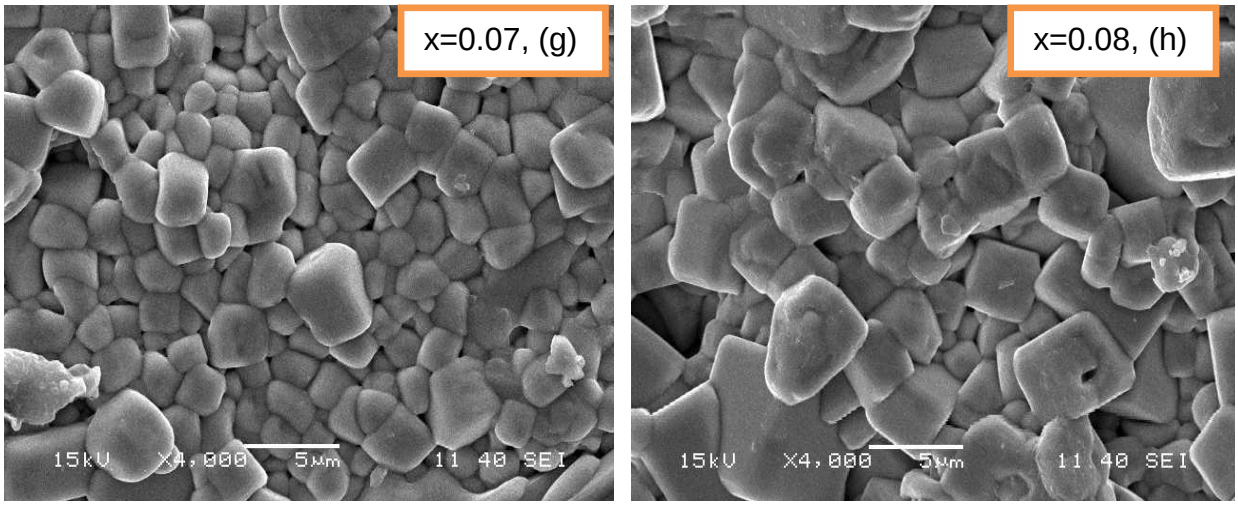

Fig.5.7: (a-h) SEM micrographs of (1-*x*)($Bi_{0.5}Na_{0.5}$)TiO_3-*x*$BaTiO_3$ ceramic

BNT disk appears to be poly-dispersed in both size and shape due to inhomogeneous grain growth. On the contrary, the addition of BT results in the inhibition of grain growth, so the crystals of the BNT-BT appear to be more uniform in both size and shape. Several possible mechanisms have been reported to show how the liquid-phase could homogenize the microstructure [205]. It can also be seen that the grain size reduces with increase in BT content in the compositions as determined by linear intersecting method. The reason may be that Ba^{2+} abounds in crystal boundary, which prevents the ion from migrating and restrains the growing of grains.

Energy dispersive x-ray spectroscopy (EDS) is a chemical microanalysis technique used in conjunction with SEM and is not a surface science technique. The EDS technique detects x-rays emitted from the sample during bombardment by an electron beam to characterize the elemental composition of the analyzed volume. Fig.5.8: (a-e) shows the energy dispersive x-ray spectroscopy compositional patterns of the (1-*x*)BNT-*x*BT ceramics. Although a reliable quantitative analysis is difficult to obtain through EDX, an increase in the composition of $BaTiO_3$ indicates that the Ba^{2+} ions are incorporated into the BNT lattice. The approximate

compositions estimated from EDX data agree well with the stochtiometric chemical compositions shown in Table 5.5. Therefore the energy dispersive x- ray analysis (EDS) (Fig. 5.8 and Table 5.5) confirmed that all the samples are in stochtiometric ratio.

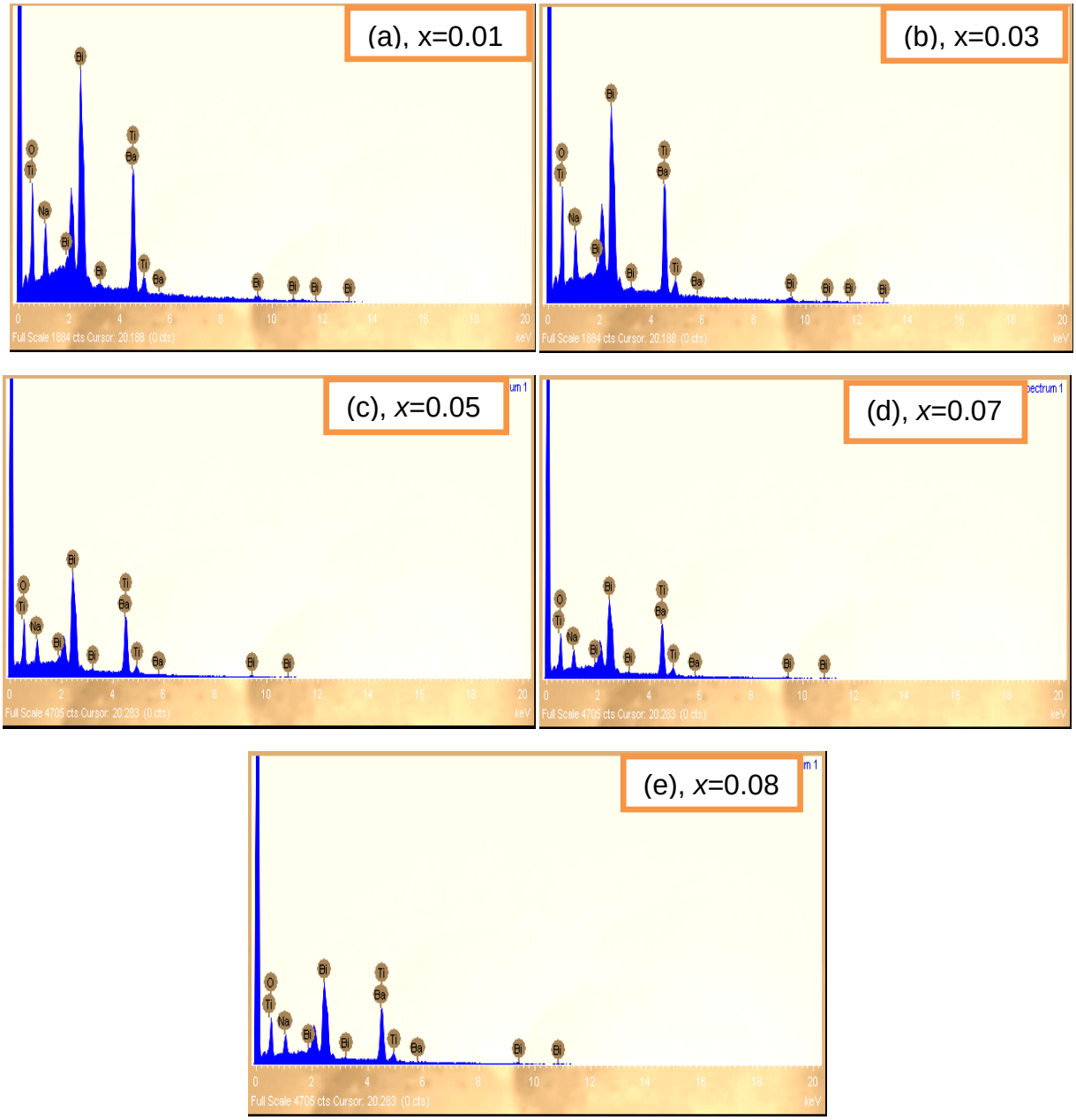

Fig.5.8: (a-e) Energy dispersive x-ray spectroscopy compositional patterns of the (1-*x*)BNT-*x*BT ceramics sintered at 1150^{o}C for 4 hrs

Table 5.5: Compositional analysis of (1-*x*)BNT-*x*BT ceramics from energy dispersive x-ray spectroscopy

Composition (*x*)	Element	Theoretical Weight%	Weight% from EDS
0	O K	25.6554	26.01
	Na K	5.4256	5.33
	Ti K	19.6	19.45
	Bi M	49.32	49.21
0.01	O K	25.63466	25.85
	Na K	5.37	5.36
	Ti K	19.5788	19.55
	Ba L	0.59	0.57
	Bi M	48.83	48.67
0.03	O K	25.593	25.78
	Na K	5.263	5.27
	Ti K	19.5374	19.67
	Ba L	1.77	1.72
	Bi M	47.84	47.56
0.05	O K	25.55	25.72
	Na K	5.1833	5.10
	Ti K	19.496	19.3
	Ba L	2.944	2.87
	Bi M	46.85365	47.01
0.07	O K	25.51	25.7
	Na K	5.0458	5.04
	Ti K	19.45468	19.59
	Ba L	4.122	4.10
	Bi M	45.867	45.97
0.08	O K	25.489	25.6
	Na K	4.991	4.99
	Ti K	19.434	19.44
	Ba L	4.71	4.7
	Bi M	45.374	45.174

5.3 OPTICAL PROPERTIES STUDY

5.3.1 Ultraviolet-Visible Absorption Spectroscopy Analysis

Fig.5.9 (a-h) shows the UV-Visible absorbance spectrum of (1-*x*) $(Bi_{0.5}Na_{0.5})TiO_3$-*x*$BaTiO_3$ (abbreviated as BNT-BT) ceramic powders with *x* = 0.01-0.08.

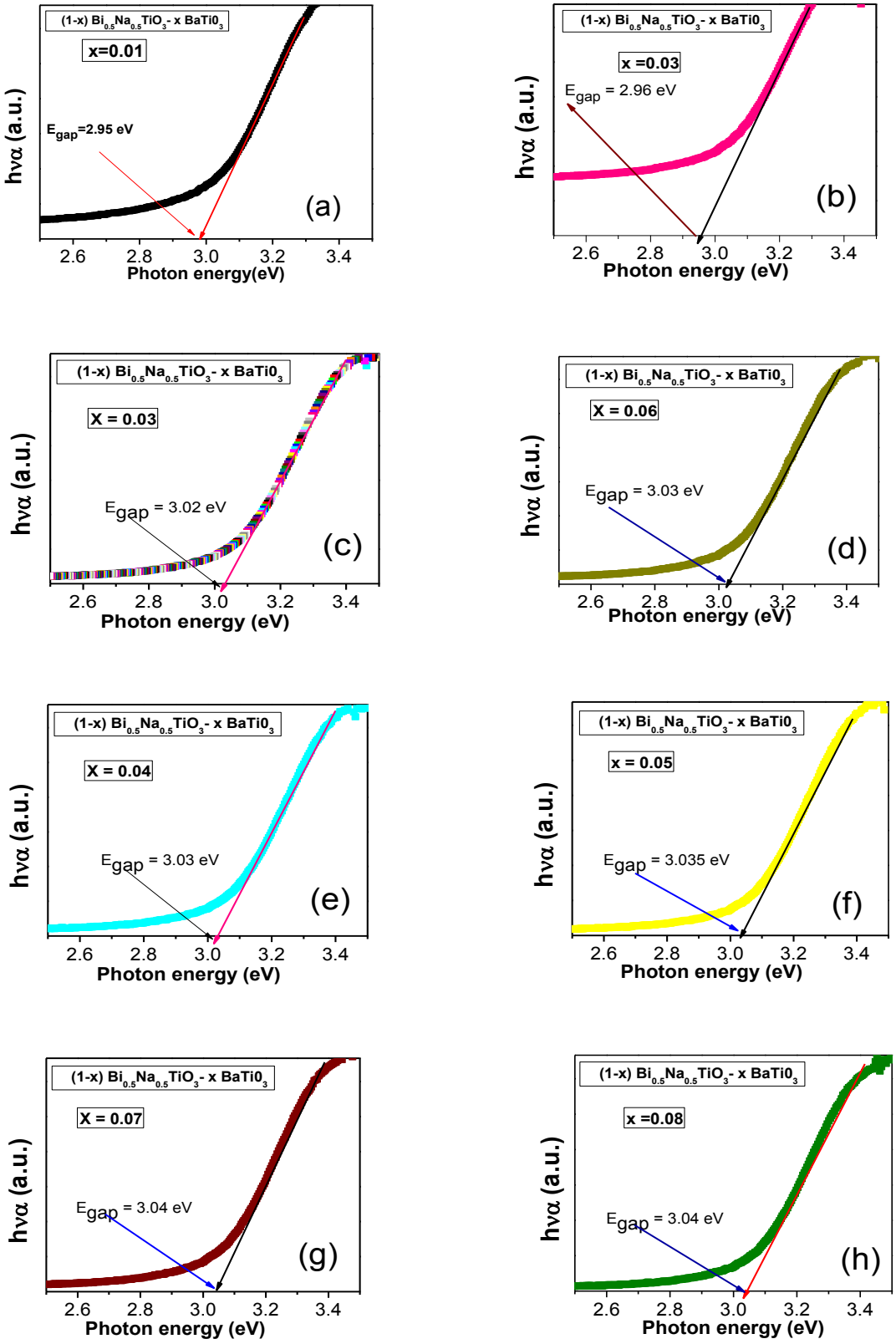

Fig.5.9: (a-h) UV-Visible spectrum of (1-*x*)($Bi_{0.5}Na_{0.5}$)TiO_3-*x*$BaTiO_3$ ceramics

The optical band gap energy (E_{gap}) was estimated by the method proposed by Wood and Tauc and described earlier in Chapter 3 (Section 3.3.1). Thus, the E_{gap} value for BNT-BT powders was evaluated by extrapolating the linear portion of the curve or tail when [y = 0] in the UV-Visible absorbance spectrum. The enhanced optical band gap is observed with the increase in BT content in BNT-BT solid-solutions.

In principle, this behavior indicates the existence of different intermediary energy levels within the band gap of these materials, which can be arising from the structural order-disorder into the lattice. Generally, the origin of these energy states is caused by the formation of oxygen vacancies into the structure, as a consequence of a symmetry break between the (lattice former)-O bonds. Thus, the increase of BT content leads to the formation of oxygen vacancies into the structure, which induces a structural rearrangement, reducing the presence of these energy levels within the band gap and increasing the E_{gap} values. Based on this hypothesis, we believe that the intermediary energy levels are composed of deep and shallow holes [179].

5.4 DIELECTRIC PROPERTIES STUDY

5.4.1 Temperature-Dependent Dielectric Constant (ε') and Loss (tanδ)

The temperature dependence of dielectric constant (ε') and dielectric loss (tanδ) of (1-*x*)BNT-*x*BT solid solutions at 100 kHz are shown in Fig.5.10 (a, b). It is seen from Fig.5.10 (a) that two dielectric peaks have been observed in each composition. The value of T_d and T_m are found to decrease with increasing the concentration of BT, indicating that the conductivity of the materials is decreased compared with BNT. The MPB compositions exhibit a lower depolarization temperature, which implies a reduction of the stability of ferroelectric domains. Compared with the compositions consisting of one single phase, the coexistence of a mixed

rhombohedral-tetragonal phase could lead to more powerful stress in the MPB compositions due to the incompatibility of their crystal lattices, resulting in a decrease of the thermal stability in the long range ferroelectric domains [206, 207]. This can be regarded as the origin of the lower depolarization temperature at the MPB compositions.

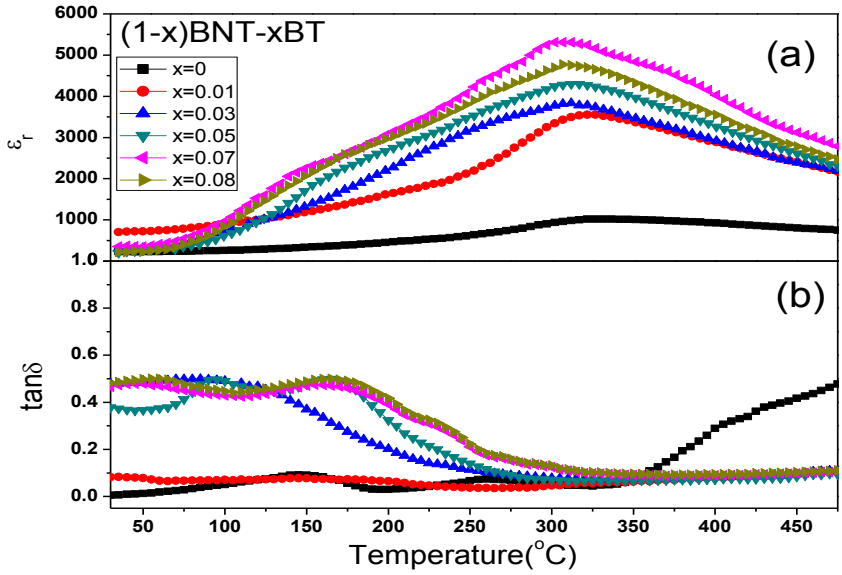

Fig.5.10: Temperature-dependence (a) dielectric constant (ε_r) and (b) dielectric loss (tanδ) of (1-*x*)($Bi_{0.5}Na_{0.5}$)TiO_3-*x*$BaTiO_3$ ceramics at 100 kHz

The dielectric behavior indicates a transformation between a normal and a relaxor ferroelectric state in our material. It can, therefore, be suggested that the phase transition should be divided into two parts. One part exhibits the abrupt increase of the electric permittivity; it is associated with the structural change of a first-order phase transition and the characteristic hysteresis. The second part is a ‘‘diffuse’’ part associated with small tetragonal (polar) regions existing in a matrix of rhombohedral symmetry. Such small regions of the low-temperature ferroelectric phase exist already at temperatures far above T_m. In this temperature range, there are unstable fluctuations which do not interact. With decreasing temperature, these regions grow and start interacting and are expected to become the nuclei of low-temperature ferroelectric phase. The local tetragonal regions are small and have random orientations of the tetragonal axis. From

this point of view, the maximum of the electric permittivity may originate from relaxation processes connected with both electrical and mechanical interactions between polar regions and the non-polar matrix, as for pure BNT.

The ionic radius of Ba^{2+} is 0.160 nm when its coordination number is 12, and ionic radii of Na^{1+}, Bi^{3+} and Ti^{4+} are 0.139, 0.128 and 0.061 nm, respectively, so Ba^{2+} ions are most likely to occupy A- site of perovskite structure (ABO_3).

$$BaO \xrightarrow{Na_2O} Ba_{Na} + V'_{Na} + O_o \qquad (5.1)$$

The above Eq. (5.1) shows that the defect reactions mainly occurred in the BNT-BT system. Ba^{2+} is more likely to substitute the ions whose radius is closer to Ba^{2+}. So reaction (5.4) will occur in the initial period. The V'_{Na} will decrease the lattice density, so the lattice structure becomes incompact, which is favorable for domain wall motion, so the relative permittivity increases. Meanwhile, Ba^{2+} doping also leads to a series of space charge centers. As we know, weak-bonded ions play an important role in dielectric loss, and the space charge centers can disorder the distribution of electric potential, which can increase the potential barrier and the migration of the ions are restrained, so the loss tangent declines. When x is more than 0.05, ε_r begins to decline, because Ba^{2+} begins to replace Bi^{3+}, which will create oxygen vacancies, when the content of Ba^{2+} reaches certain critical value. It has been known that oxygen vacancies are the main cause of wall domain clamping [208]. This clamping will restrain the macro-micro domain switching in some degree; this is the reason that both the relative permittivity and loss tangent declined. The temperature co-efficient of permittivity is calculated by the formula given in equation 4.2 and the values are given in Table 5.6 below.

The value of dielectric loss (tan δ) in the compositions is found to be the order of 10^{-2} indicating the low-loss materials. The important mechanism of conductivity in these ceramics

is the movement of ions present in the current carrying conductor. It is well known that the alkali ions are good current carriers in ceramics; because these ions play an important role in the conductivity of BNT-BT ceramics. The Na^{+} ions in BNT move easily upon heating, resulting in the increase in conductivity with increasing temperature. In the present Ba substituted ceramics, Ba^{2+} (large ion) occupies the A-site of BNT, which possibly blocks the passage of Na^{+} current carriers. When the temperature is increased above T_m, the value of tanδ is found to increase drastically.

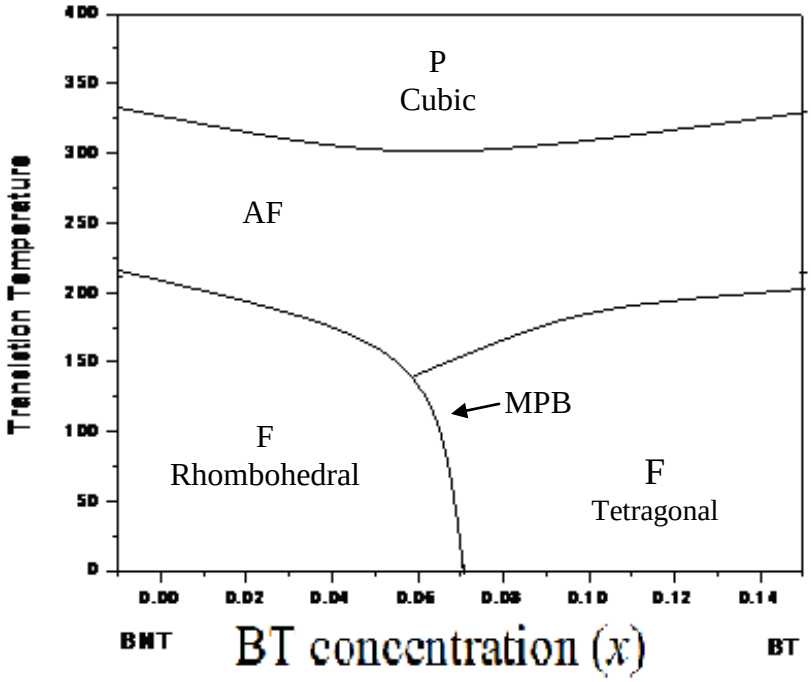

Fig.5.11: Temperature vs. composition phase-diagram of (1-*x*) BNT-*x*BT ceramics

Fig.5.11: shows temperature-composition phase diagram for BNT-BT ceramic where P is the paraelectric (cubic phase), F is the ferroelectric (tetragonal phase) and ferroelectric (rhombohedral phase) and AF is the anti-ferroelectric region. The nearly horizontal line represents the boundary between the paraelectric phase and the ferroelectric phase while the nearly vertical line represents the MPB between the tetragonal and the rhombohedral phase.

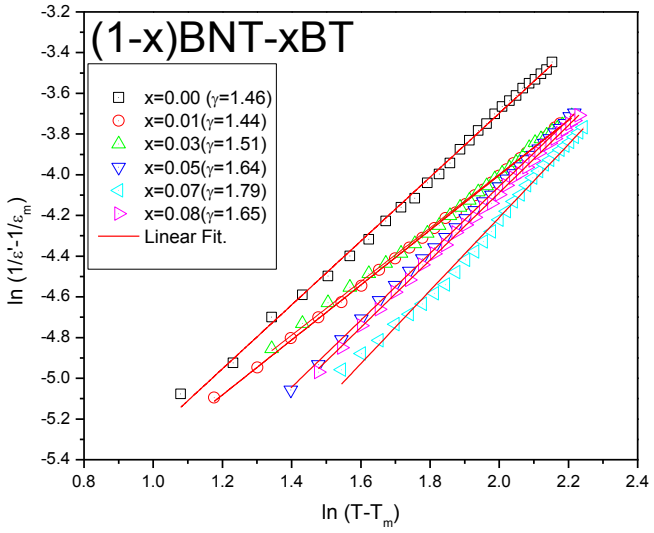

Fig. 5.12: $\ln(1/\varepsilon'-1/\varepsilon_m)$ vs. $(T-T_m)$ for 100 kHz of $(1-x)(Bi_{0.5}Na_{0.5})TiO_3$-$xBaTiO_3$ ceramics

The plots of $\ln(1/\varepsilon' - 1/\varepsilon_m)$ as a function of $\ln(T - T_m)$ for all the compositions are shown in Fig. 5.12. The substitution of Ba^{2+} for $(Na_{0.5}Bi_{0.5})^{2+}$ in the A-site of the perovskite structure is the main factor that induces some order in the cationic octahedral sub-lattice due to the large difference in the radii of Ba^{2+} (1.35A°) and $(Na_{0.5}Bi_{0.5})^{2+}$ (0.97A°), and then produces an increase of the diffusive factor as increasing BT concentration till MPB composition (x = 0.07) (Table 5.6). After MPB composition, the diffusivity factor decreases with increasing BT concentration. These results imply an enhancement of the diffuse phase transition feature.

Table 5.6: Dielectric coefficient of $(1-x)$ $(Bi_{0.5}Na_{0.5})TiO_3$-$xBaTiO_3$ ceramics

Composition (x)	T_d (°C)	T_m (°C)	α (°C^{-1})	ε_m	γ	tanδ
x = 0.00	210	333	2.17 X 10^{-3}	1020	1.42	0.046
x = 0.01	200	320	4.43 X 10^{-3}	3555	1.44	0.0565
x = 0.03	190	315	23.5 X 10^{-3}	3836	1.51	0.0748
x = 0.05	175	310	29.9 X 10^{-3}	4300	1.64	0.066
x = 0.07	150	300	45.7 X 10^{-3}	5312	1.79	0.072
x = 0.08	165	305	28.4 X 10^{-3}	4773	1.65	0.0922

5.4.2 Frequency-Dependent Dielectric Constant (ε') and Loss (tanδ)

Fig.5.13 (a) shows the frequency-dependence of the relative permittivity of (1-*x*) $(Bi_{0.5}Na_{0.5})TiO_3$- *x* $BaTiO_3$ ceramics with $0 \leq x \leq 0.08$ at room temperature. The relative permittivity slowly decreases with the increase of frequency up to (1-5) kHz for all compositions. Beyond the frequency range (1-5) kHz, the relative permittivity sharply fall down due to the release of space-charge polarization and then remains constant beyond the frequency 100 kHz for all the compositions. Fig.5.12 (b) shows the frequency dependence of the dielectric loss of (1-*x*)$(Bi_{0.5}Na_{0.5})TiO_3$-*x*$BaTiO_3$ ceramics with $0 \leq x \leq 0.07$ at room temperature. Initially, the dielectric loss increases non linearly between (1-50) kHz for all compositions, and then suddenly falls down.

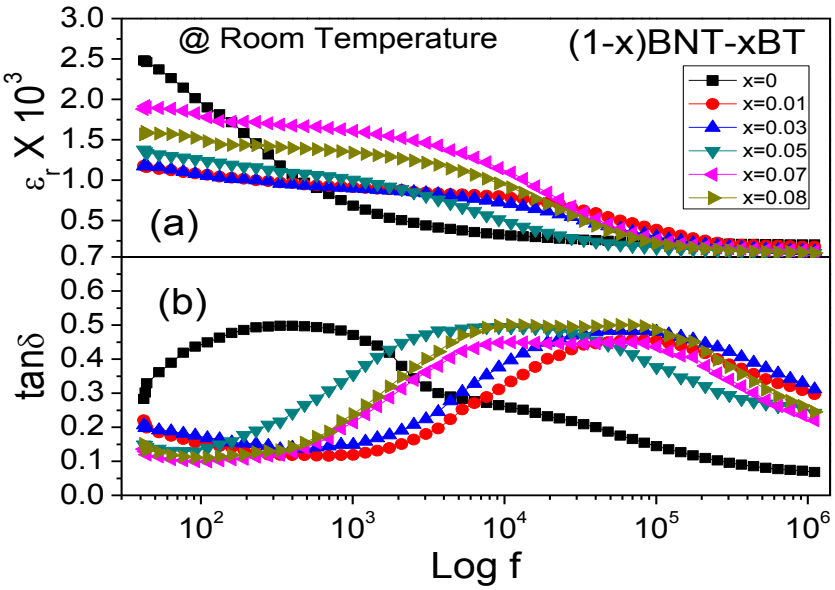

Fig.5.13: (a,b) Frequency-dependence of relative permittivity (ε_r) and dielectric loss (tan δ) at room temperature of (1-*x*)$(Ba_{0.5}Na_{0.5})TiO_3$-*x*$BaTiO_3$ ceramics

Dielectric constants (ε_r) and dielectric losses (tan δ) of BNT-BT ceramics are plotted as a function of frequency at temperatures 450^{o}C in Fig.5.14 (a, b) with $0 \leq x \leq 0.07$. Dielectric constants sharply decrease with increasing frequency (<1 kHz), and the rate of decrease levels

off in a certain frequency range (>1 kHz). But, at relatively low frequency, the dielectric constant depends on frequency strongly, showing a dielectric dispersion evidently. Such a strong dispersion seems to be a common feature in ferroelectric materials concerned with ionic conductivity, which is referred as low-frequency dielectric dispersion. When the frequency increases, the relative effect of ionic conductivity becomes small and, as a result, the frequency dependence of dielectric constant becomes weak. At lower frequencies, the dipolar complexes will be able to keep up with the applied field and reorient with each half-cycle.

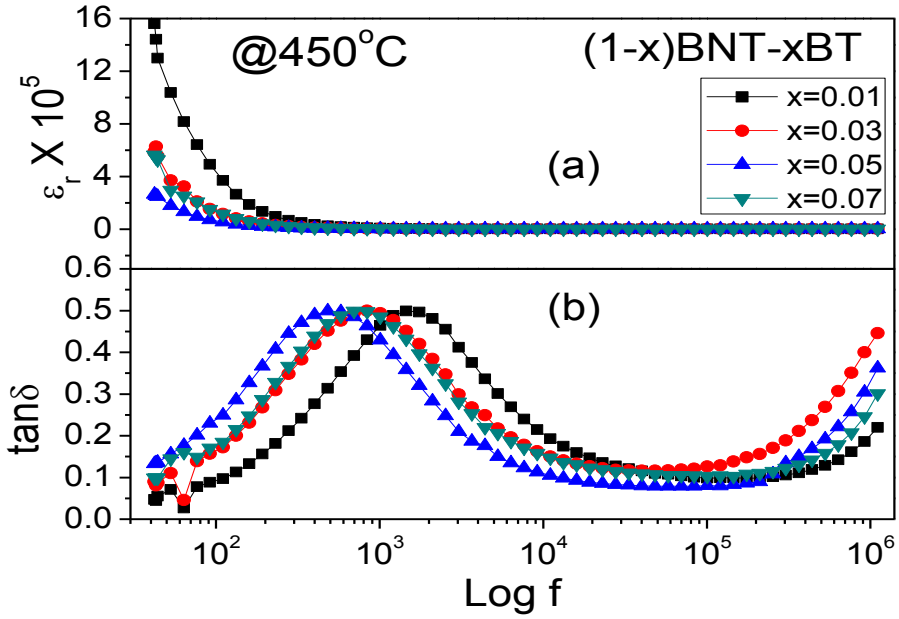

Fig.5.14: (a, b) Frequency-dependent of relative permittivity (ε_r) and dielectric loss (tan δ) at 450°C of (1-*x*)($Bi_{0.5}Na_{0.5}$)TiO_3-*x*$BaTiO_3$ ceramics

The full effect of the polarization reversal will contribute to the dielectric constant. At intermediate frequencies, the dipoles will be able to partially respond to the changing field direction, but will increasingly lag behind as the frequency increases. The dipolar contribution will drop off with frequency, and the dielectric losses reach a peak at the mid-point of this intermediate frequency range. The losses below 100 Hz are directly proportional to the BT

content (*x*), implying that the loosely bounded oxygen vacancies may migrate to the grain and may, thus, contribute to the space charge polarization. However, it should be noted that the loss peaks shift to higher frequencies with increasing BT content (*x*). The peaks are attributed to a reorientation of the oxygen vacancies associated with cation defect centres in the dipolar defect complex where the oxygen vacancy is the most mobile species. But the peak is again shifted to lower frequency region at $x = 0.07$, which may be due to the MPB region.

5.5 ELECTRICAL CONDUCTIVITY STUDY

5.5.1 Impedance Study

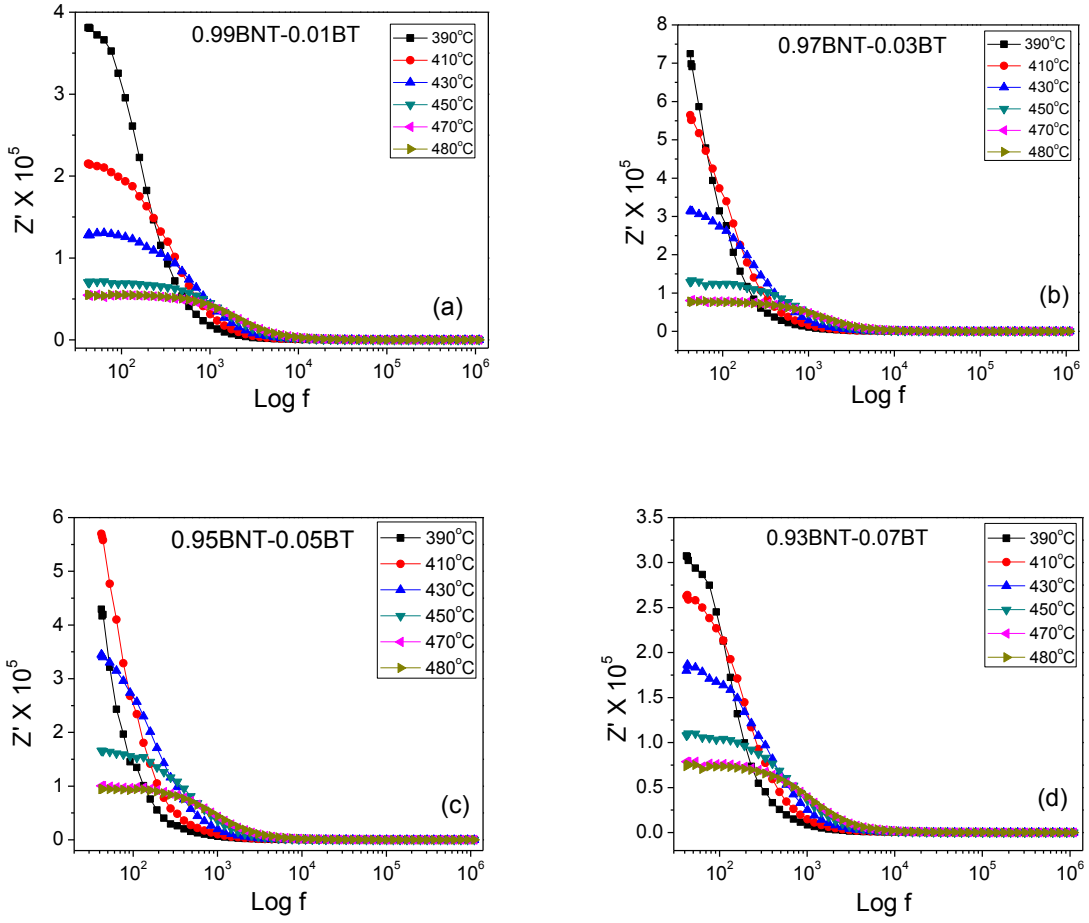

Fig.5.15: Frequency explicit plot of Z' of (a) $x = 0.01$, (b) $x = 0.03$, (c) $x = 0.05$, (d) $x = 0.07$, for (1-*x*) BNT-*x*BT specimens at different temperatures

Fig.5.15 (a-d) shows the variation of the real part of the impedance (Z') versus frequency at different temperatures. The magnitude of Z' (i.e. resistance) is observed to decrease with increasing temperature and frequency, which indicates the possibility of an increase in the ac conductivity with increasing temperature and frequency [187]. The Z' values at all temperatures merge in the higher-frequency region (≥10 kHz). Further, at low frequencies, the Z' values decrease with increasing temperature, and the compound exhibits a negative temperature coefficient of resistance (NTCR)-type behavior like that of semiconductors [188].

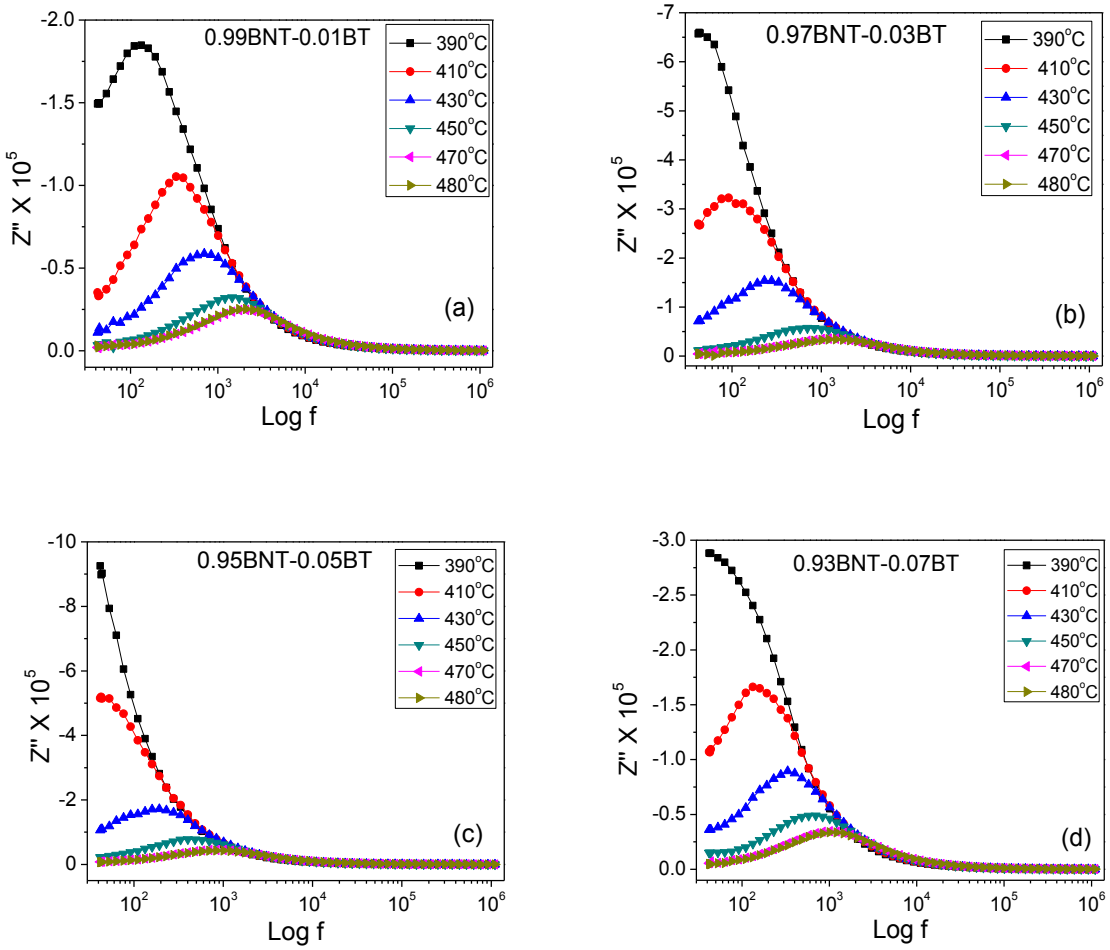

Fig.5.16: Frequency explicit plot of Z" for (a) x = 0.01, (b) x = 0.03, (c) x = 0.05, (d) x = 0.07, of (1-x)BNT-xBT specimens at different temperatures

Fig. 5.16 (a-d) shows the imaginary part of the impedance (*Z''*) as a function of frequency at different temperatures. In addition, the broadening of the peak has shifted towards higher frequencies as the temperature increases. A significant broadening of the peak with increasing temperature suggests the presence of electrical processes in the material with the spread of relaxation time**.** This may be due to the presence of immobile species at low temperatures and defects at high temperatures. Since these observations are made at higher temperatures, some relaxation species, such as defects, may be responsible for electrical conduction in the material by hopping of electrons/ oxygen ion vacancy/defects among the available localized sites. The heights of peaks are found to decrease gradually with the increase in frequency as well as temperature, and finally, they merge in the high frequency domain. It indicates the presence of space charge polarization at lower frequency and its disappearance at higher frequency.

The frequency dependence of *Z''* for all compositions at various temperatures is shown in Fig.5.17 (a-c). The peaks appearing in the pattern area are symmetric and their positions appear to be shifting towards the higher frequency side on substitution of BT in BNT systems upto $x = 0.05$ and then shift towards lower frequency for $x = 0.07$. It gives an indication that the electrical process occurring in the material is slowed down with lower BT substitution due to accumulation of space charge. The merger of spectrum in the high-frequency region irrespective of BT concentration provides an evidence of space charge in the material that governs the electrical process in the region of high frequency.

In such a situation, one can determine the most probable relaxation time τ_m ($= 1/\omega_m$) from the position of the peak in the Z" vs. logω plots. The most probable relaxation time follows the Arrhenius law, given by

$$\omega_m = \omega_0 \, exp\left(\frac{-E_a}{k_B T}\right) \tag{5.2}$$

where ω_o is the pre-exponential factor and Ea is the activation energy. Fig.5.17 (d) shows a plot of the $\log\omega_m$ vs. 1/T. The activation energy E_a of all the compositions has been calculated from the least-squares fit to the points and given in the Table-5.8.

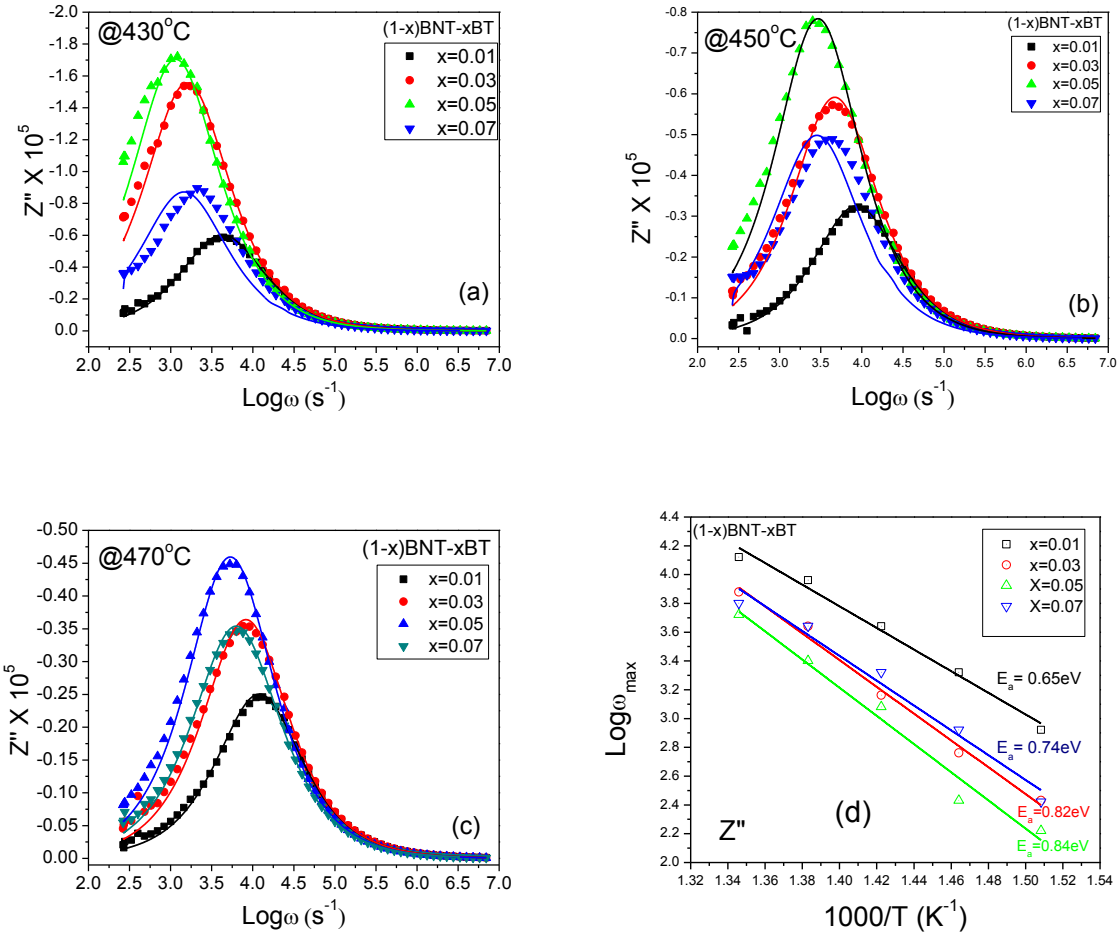

Fig.5.17: (a-c) Frequency explicit plot of Z" of (1-*x*)BNT-*x*BT ceramics at various compositions in different temperatures, and (d) Arrhenius plot of log ω_{max} from imaginary part of impedance Z" of (1-*x*)BNT-*x*BT ceramics at various compositions

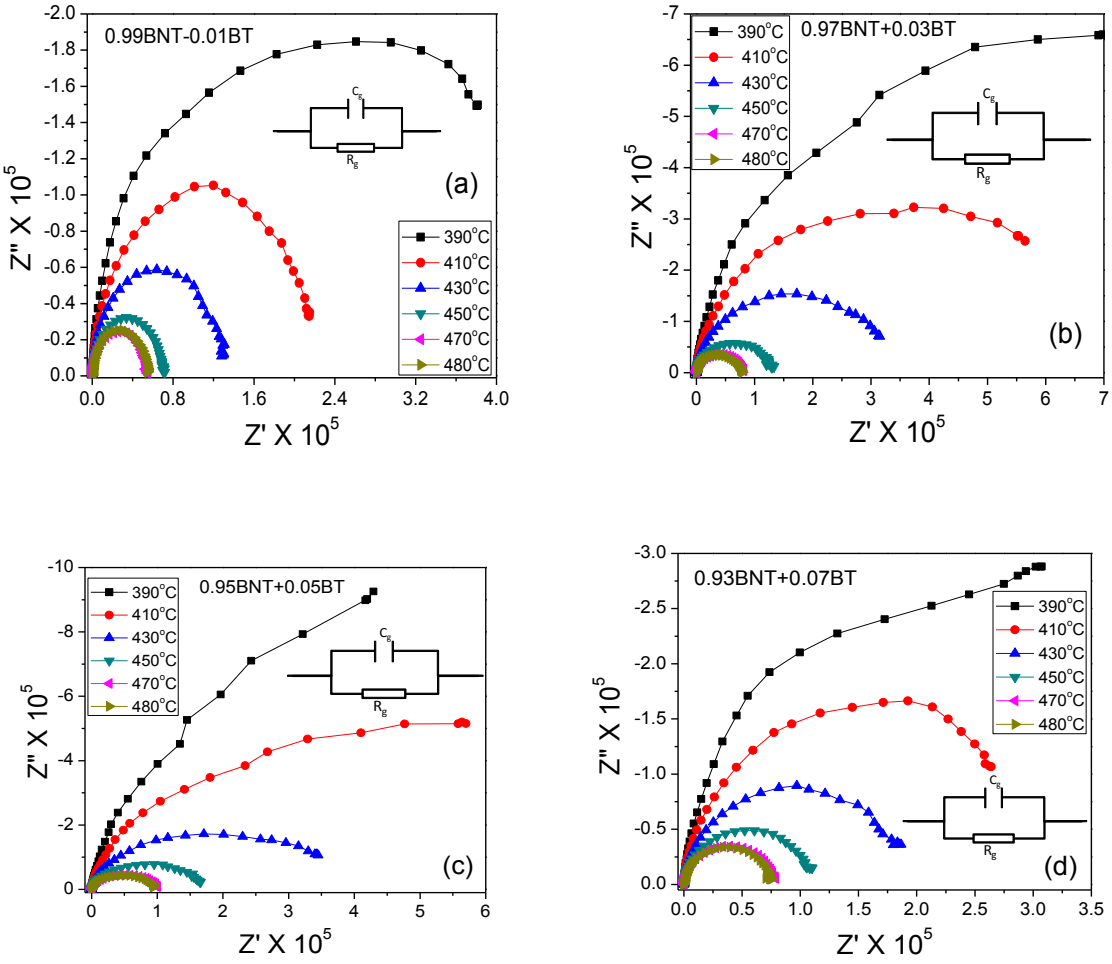

Fig.5.18: (a-d) Cole-Cole plots between Z' and Z'' for (1-*x*)BNT-*x*BT ceramic measured at various temperatures and inset shows the appropriate equivalent electrical circuit

Fig.5.18 (a-d) shows the complex impedance spectrum (Cole-Cole plots) of the (1-*x*)BNT-*x*BT ceramic with $0.01 \leq x \leq 0.07$ at different temperatures . These samples follow Maxwell-Wagner relaxations. Cole-Cole plot shows a single semicircular arc with a single relaxation process which confirms that the impedance contribution is mainly due to the grains. As the temperature increases, the intercept of the prominent semicircles at the Z' axis shift toward lower Z' value, which indicates a reduction of conductivity with increase in temperature. The Cole- Cole plot also shows that there is a decrease in conductivity with increase in BT content upto $x = 0.05$ and then it increases at $x = 0.07$. The impedance representation can also be

obtained from a model-equivalent electrical circuit with resistance R and capacitance C, as shown in the insert of Fig.5.18. The parameters obtained from Cole-Cole plots given in Table 5.7 below.

Table 5.7: Parameters obtained from Cole-Cole plots of (1-*x*)BNT-*x*BT ceramics at different temperatures

x	Temperature (^{o}C)	C_g (nF)	R_g (MΩ)	ω_{max} (rad/s)	σ_g (μS/cm)
0.01	430	2.66	0.13	4384	1.21
	450	2.53	0.07	9158	2.22
	470	2.49	0.05	13238	2.85
0.03	430	2.66	0.33	1452	0.48
	450	2.52	0.13	4383	1.18
	470	2.44	0.08	7618	1.96
0.05	430	3.37	0.37	1207	0.37
	450	2.85	0.17	3032	0.83
	470	2.96	0.10	5270	1.38
0.07	430	3.78	0.19	2098	0.74
	450	3.57	0.11	4383	1.30
	470	3.56	0.08	6336	1.81

Fig.5.19 (a-c) shows Cole-Cole plots between Z' and Z" for BNT-BT ceramic measured for the studied compositions at various temperatures. The area of the peak increases with increasing BT content up to x = 0.05 and then suddenly decreases at x = 0.07. The peaks are attributed to a reorientation of the oxygen vacancies associated with cation defect centers in the dipolar defect complex where the oxygen vacancy is the most mobile species. But the peak is again shifted to lower frequency region at x = 0.07, which may be due to the existing of morphotropic phase boundary region.

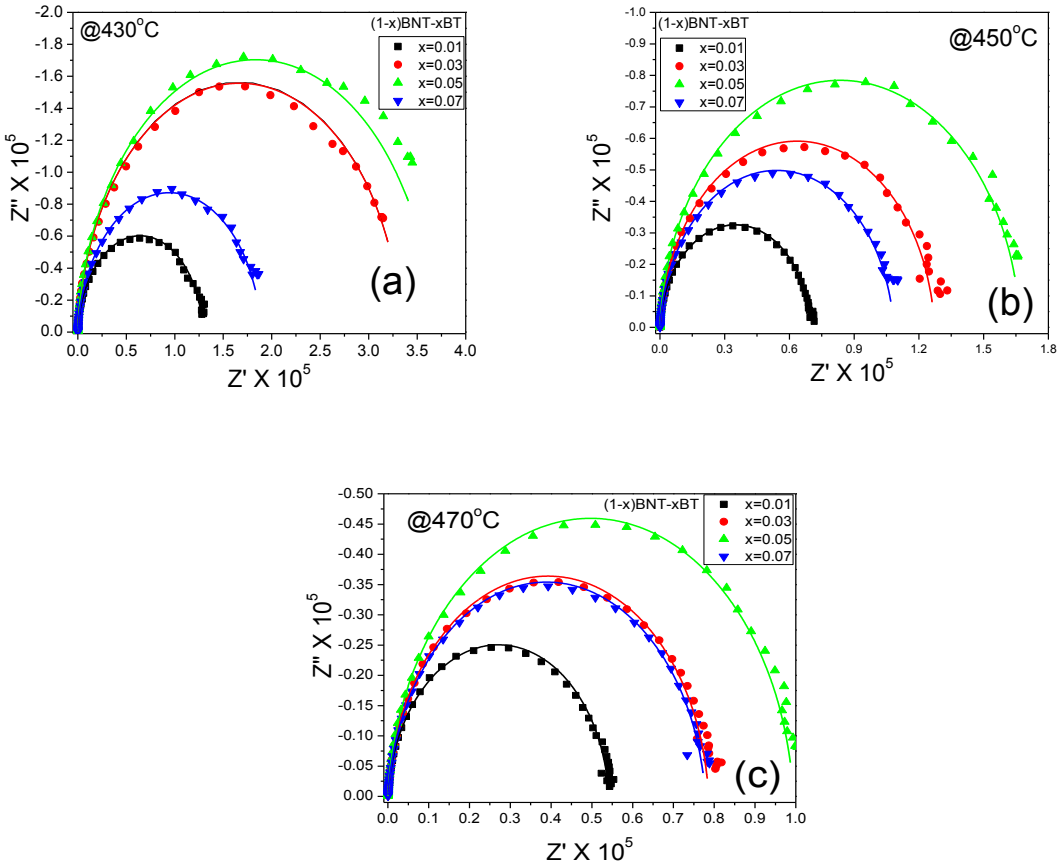

Fig.5.19: (a-c) Cole-Cole plots between Z' and Z'' for (1-*x*)BNT-*x*BT ceramic measured at various compositions at different temperatures

5.5.2 Modulus Analysis

Fig.5.20 (a-d) shows the variation of real part of electrical modulus $M^{'}$ as a function of frequency at various temperatures for all the studied compositions. It is evident from that for each temperature, at lower frequencies the real part of impedance M' approaches to zero confirming the presence of an appreciable electrode and/or ionic polarization in the studied samples. With increasing temperature, the peak shifts towards higher frequencies for all the compositions indicating that a thermally-activated process is responsible (i.e., long range oxygen vacancy motion is responsible for the process).

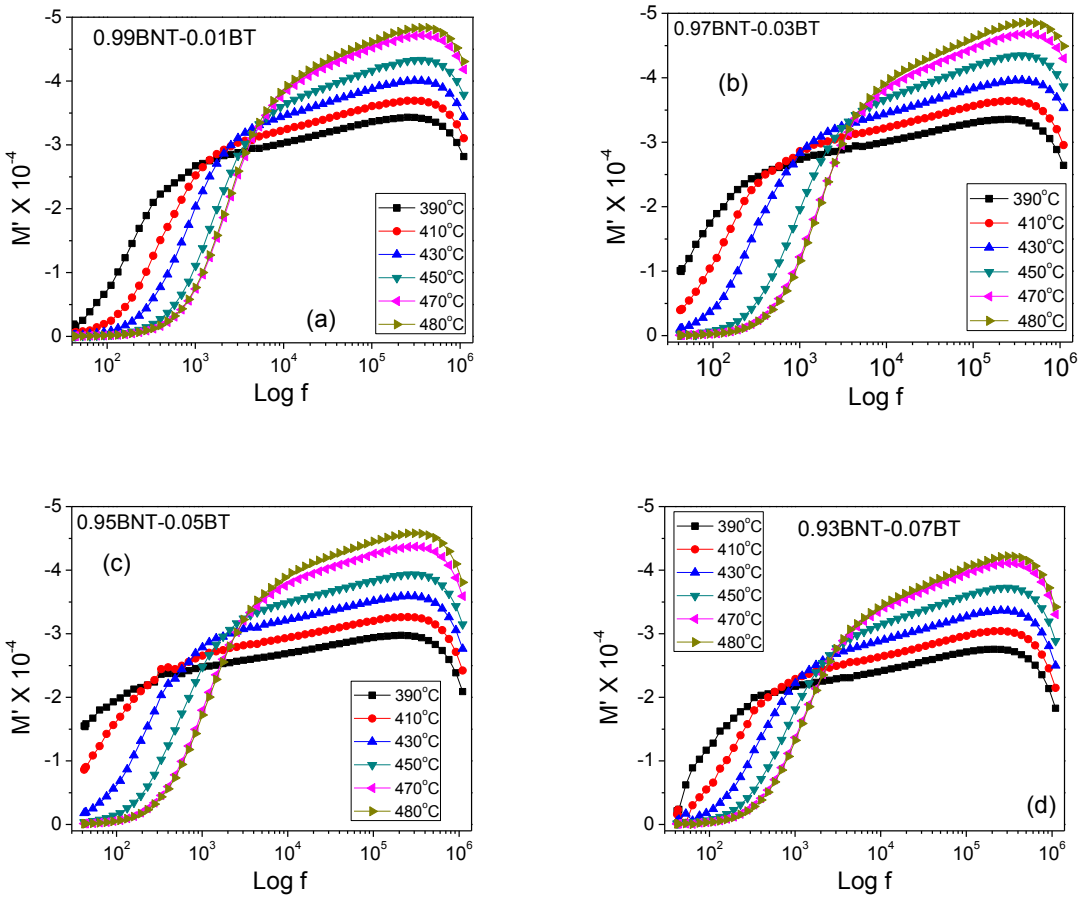

Fig.5.20: Frequency explicit plot of *M'* for (a) x = 0.01, (b) x = 0.03, (c) x = 0.05, (d) x = 0.07, of (1-x)BNT-xBT specimens at different temperatures

Fig.5.21 (a-d) shows the frequency (angular) dependence of *M"* for the (1-x)BNT-xBT (x = 0.01, 0.03, 0.05, 0.07) ceramic measured at different temperatures. It is evident from Fig.5.20 (a-d) that there is a shift in the peak frequencies of *M"* to higher frequency side as temperature increases. Increasing temperature, the dc conduction is attributed to long range motion of ions that are thermally activated. The low frequency side of the peak represents the range of frequency in which the ions can move long range, i.e., ions can perform successfully hopping from one site to the neighboring site. The high frequency side of the M'' represents the range of frequencies in which the ions are separately confined to their potential wells, and the ions can make only the localized motion within the well [209-212].

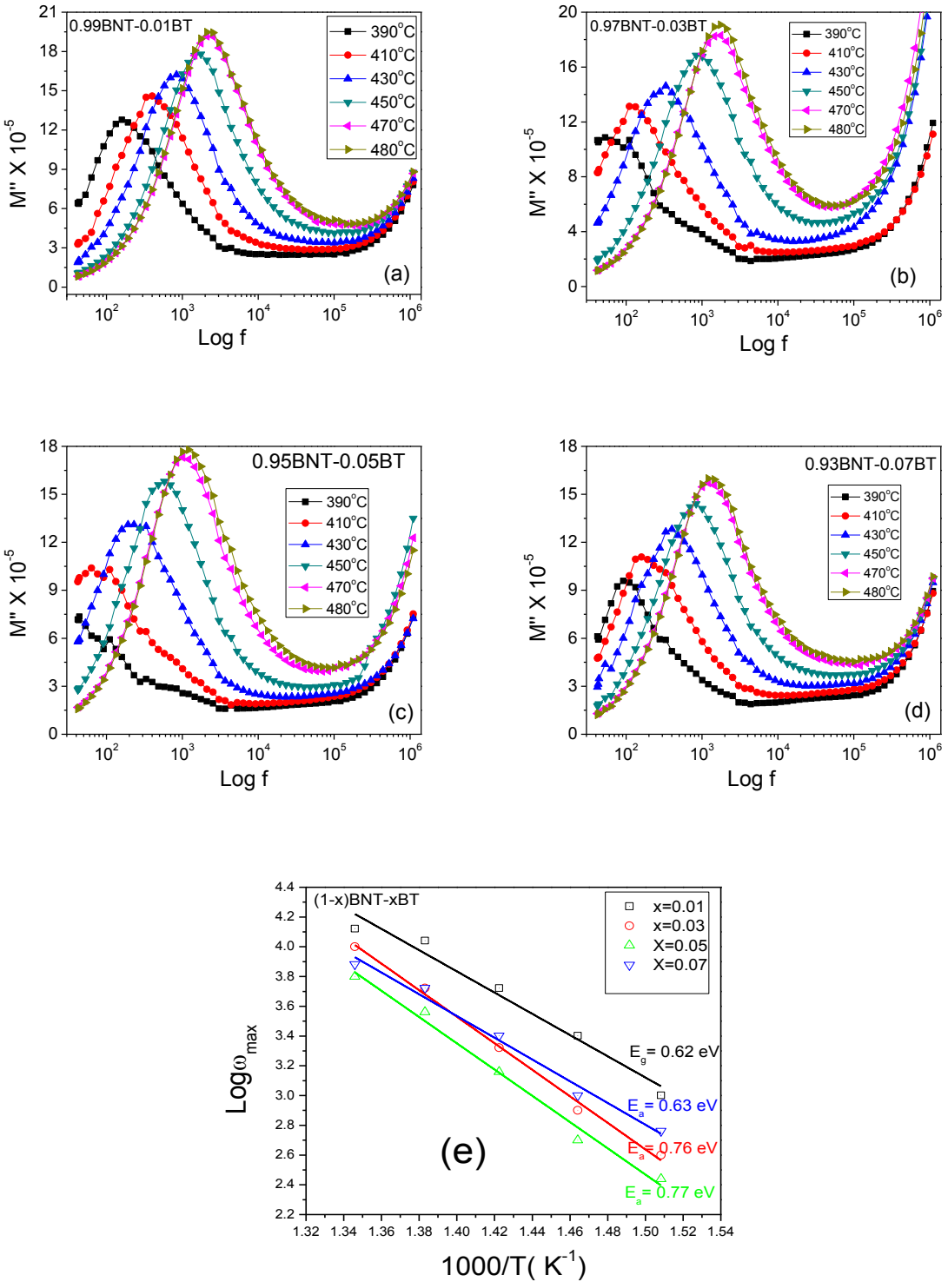

Fig.5.21: (a-d) Frequency explicit plot of M" of (a) x = 0.01, (b) x = 0.03, (c) x = 0.05, (d) x = 0.07, for (1-x)BNT-xBT ceramics at different temperatures, and (e) Arrhenius plot of log ω_{max} from imaginary part of modulus of (1-x)BNT-xBT ceramics of studied compositions

With increasing the BT content, the M'' peak is shifted towards lower frequency up to x = 0.05 and then shifted towards higher angle for x = 0.07; it indicates that the relaxation time increases in the material. Also, M'' peak frequencies increase with increase in temperature and the shift in frequency of M'' peaks correspond to the so-called conductivity relaxation. The most probable relaxation time also obeys the Arrhenius relation and the activation energy of all the compositions is given in Table-5.8 and shown in Fig.5.21 (e), which is close to the activation energy E_a calculated from peak of Z''_{max}.

5.5.3 AC and DC Conductivity

Fig.5.22 (a-d) shows the variation of ac conductivity as a function of frequency at different temperatures in (1-x)BNT-xBT ceramic (x = 0.01, 0.03, 0.05 and 0.07). The electric conductivity in ceramics is mainly controlled by the migration of charge species under the action of electric field and by the defect-ion complexes, the polarization field, the relaxation, etc. The plot of electrical conductivity vs. frequency at different temperatures in Fig.5.22 (a-d) shows that the conductivity increases with increasing of temperature for various compositions. The σ (ω) curves are found to be merging in high frequency and high temperature regions, suggesting the less defect mobility and low conductivity in the material. Frequency-independent behavior of the conductivity in the low frequency region is observed, but that becomes sensitive in the high frequency region, which is generally known as the hopping frequency, shifted towards higher frequency side with increase of temperature. In the higher frequency region, the conductivity increase is caused due to the hopping of charge carriers in finite clusters. Therefore, very small amount of energy is required to activate the charge carriers/electrons for electrical conduction. It has been shown that the value of activation energy depends on ionization level of the oxygen vacancy. Usually, activation energy less than

1.0 eV is connected to singly ionized vacancies and/or electronic mobility in space-charge regions. Thus, the conduction process within this temperature range may be due to the hopping of charge carriers and/or singly ionized oxygen vacancies of the ceramics. The steady or constant conductivity value goes towards lower frequency with increasing of BT content in BNT. Also, the conductivity is slightly decreased with increasing BT content in BNT, which may be due to an enhancement in barrier properties, suppression of lattice conduction path and local lattice distortion [213-215].

The dc conductivity estimated from the bulk response of the material has been observed as a function of temperature, as shown in the Fig. 5.22 (e). At higher temperatures, the conductivity vs. temperature response is linear and can be explained by a thermally activated transport of Arrhenius-type governed by the relation:

$$\sigma_{dc} = \sigma_0 exp(E_a | k_B T) \quad (5.3)$$

where $\boldsymbol{\sigma_0}$, Ea and k_B represent the pre-exponential factor, the activation energy of the mobile charge carriers and Boltzmann constant, respectively. The activation energy Ea of all the compositions has been calculated from the least-squares fit to the points and given in the Table 5.8. This result revealed that the activation energy increases with increasing of BT content, but at x = 0.07, suddenly the activation energy has decreased due to the MPB region. It is found that the value of activation energy does not show any appreciable change with increasing BT content. The substitution of Ba^{2+} may alter the long-range polar order with TiO_6 octahedra and this may result in a disturbance in local polarizations in the lattice. The samples contain defects, or impurity-defect complexes and these would have a corresponding effect on relaxation.

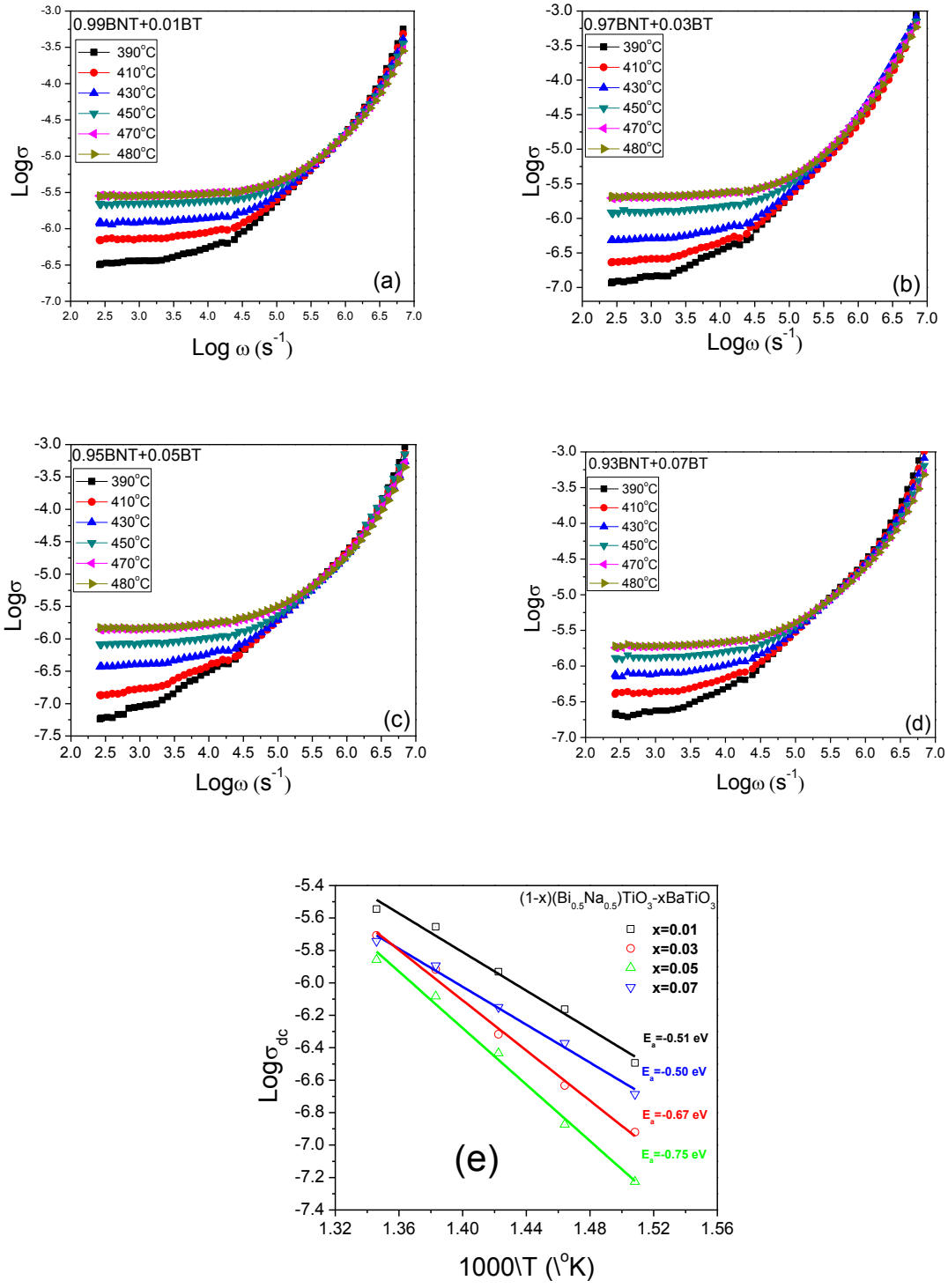

Fig.5.22: Frequency-dependence of the ac conductivity of (1-*x*)BNT-*x*BT ceramic with (a) *x* = 0.01, (b) *x* = 0.03, (c) *x* = 0.05, (d) *x* = 0.07 at various temperatures and (e) Temperature dependence of the dc conductivity for (1-*x*)BNT-*x*BT ceramics. The dots are the experimental points and the solid line is the least-squares straight-line fit

Table 5.8: Activation energy calculated from impedance, modulus and conductivity of (1-*x*)BNT-*x*BT ceramic

Composition (*x*)	Activation Energy (E_a) from Z" (eV)	Activation Energy (E_a) from M" (eV)	Activation Energy (E_a) from σ_{dc} (eV)
0.01	0.65	0.62	0.51
0.03	0.82	0.76	0.67
0.05	0.84	0.77	0.75
0.07	0.74	0.63	0.50

5.6 POLARIZATION AND PIEZOELECTRIC STUDY

The ferroelectric properties of the BNT system ceramics were investigated in terms of their P ~E hysteresis loops. Saturated P~E hysteresis loops were obtained for the BNT-BT ceramics, as shown in Fig. 5.23. The values of remanent polarization (P_r) and coercive field (Ec) determined from the loops are shown in Table 5.9. In comparison with BNT ceramic, BNT-BT ceramic shows an enhanced remanent polarization and an apparently reduced coercive field, indicating a modification of ferroelectric properties. This can be attributed to the fact that BNT-BT has a composition near the MPB, where rhombohedral and tetragonal phases coexist. Due to the coexistence of the two phases, BNT-BT has more possible spontaneous polarization directions than the compositions in the rhombohedral or tetragonal sides of the MPB [168]. Moreover, the coexistence of the two phases created a structural relaxation, benefiting the reorientation of ferroelectric domains under electrical field. These are considered to be the main reason for the remarkable improvement of ferroelectric properties in BNT-BT ceramic at MPB composition (x = 0.07).

Examining the ferroelectric and piezoelectric properties of the ceramics, it was noticed that the variation trend of piezoelectric properties with compositional change is rather consistent with that of ferroelectric properties.

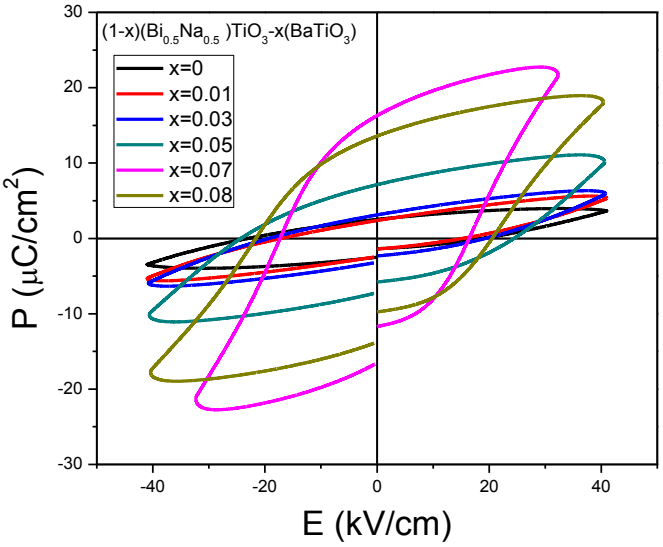

Fig.5.23: The P~E hysteresis loops of (1-*x*)($Bi_{0.5}Na_{0.5}$)TiO_3-*x*$BaTiO_3$ ceramics at room temperature.

Table 5.9: Ferroelectric and piezoelectric coefficient of (1-*x*)($Ba_{0.5}Na_{0.5}$)TiO_3-*x*$BaTiO_3$ ceramics

Composition (*x*)	E_c (kV/cm)	P_r (μC/cm^2)	d_{33} (pC/N)
0.00	20	2.5	41
0.01	17	2.4	63
0.03	19.25	3.2	84
0.05	24.35	7.2	123
0.07	16.8	16.4	134
0.08	20	13.6	125

Compared with BNT ceramic, BNT-BT ceramic provides considerably enhanced piezoelectric properties accompanied by a remarkable modification of ferroelectric properties. Among the ceramics, the preferred piezoelectric properties were obtained for x = 0.07 ceramic, which shows the largest remanent polarization and lowest coercive field at the same time. These imply an essential relation between the piezoelectric properties and the ferroelectric nature of the ceramics. This phenomenon can be qualitatively explained as follows. On one hand, a low

coercive field facilitates the sufficient reorientation of ferroelectric domains during electrical poling, benefiting the achievement of desired piezoelectric properties. On the other hand, a large remanent polarization indicates a strong ferroelectricity, which enhances piezoelectric properties [216]. The various piezoelectric parameters are calculated by the IEEE standard by using the equations (2.33), (2.34) and (2.35) (Chapter 2).

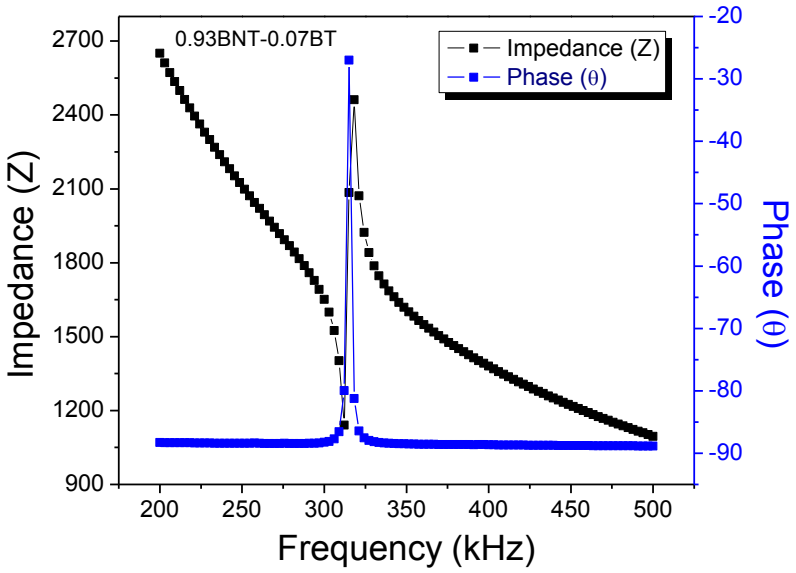

Fig.5.24: The frequency vs. impedance/phase spectrum of 0.93BNT-0.07BT ceramic (MPB composition)

Fig. 5.24 shows the frequency impedance/phase spectra of the BNT-BT solid-solution at its MPB composition. The various piezoelectric and electromechanical properties are shown in Fig.5.25 (a, b). It is observed that the piezoelectric properties are strongly exhibit a strong compositional dependence. Similar to other MPB systems, it can be seen that the piezoelectric properties increases with increases in solid-solution and maximum near at the MPB as shown in the Fig. 5.25 (a, b). The BNT-BT solid solution show peak values of piezoelectric constant d_{33}=134 pC/N, planar electromechanical coupling coefficient k_p= 22%, quality factor Q_m= 41

and frequency constant N_p = 2711 for the sample with x = 0.07 confirming the presence of MPB. The increase in the piezoelectric constant d_{33} in the MPB composition may be attributed to an increase in the domain wall flexibility. The ceramics crystal structure is considered to be a coexistence of rhombohedral and tetragonal phases in the MPB composition as shown in Reitveld refinement and Raman spectroscopy. Therefore, a flipping of polarization between two phases is possible on application of electric field. Enhanced piezoelectric coefficients are obtained in MPB regions and are attributed to an easy switch in the polarization vector between all allowed polarization orientations. In addition, the best piezoelectric constant (d_{33}) and electromechanical coupling factor (k_p) are always near the side of the tetragonal phase of the MPB. The reason can be interpreted the more domains of the tetragonal crystalline can be transformed applied strong poling electric field.

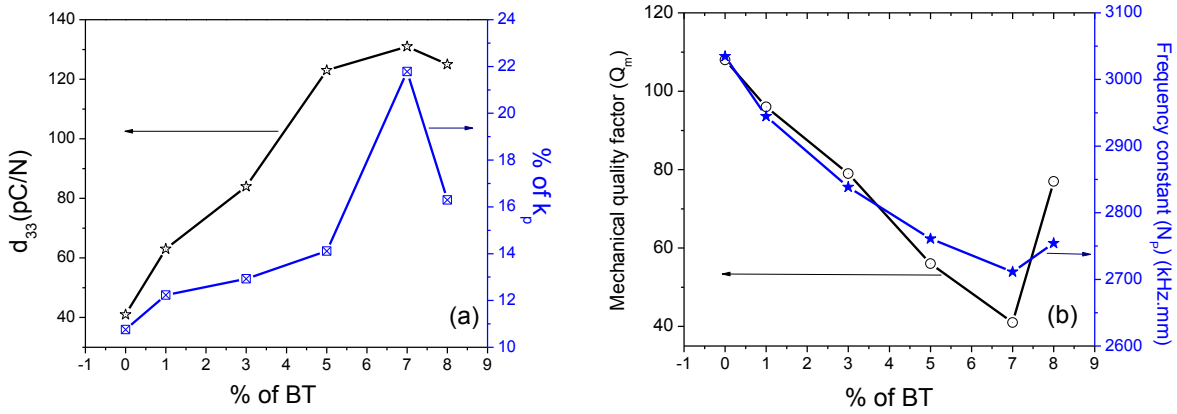

Fig. 5.25: (a) piezoelectric co-efficient (d_{33}) and electromechanical coupling factor (k_p) and (b) Mechanical quality factor (Q_m) and frequency constant (N_p) of BNT-BT ceramics with % of BT concentration

Main result of this chapter have been published in

1. Journal of Advanced Dielectrics, Vol. 2, No. 2 (2012) 1250008

2. *Journal of Materials Science: Materials in Electronics, Vol 24, Issue 1 (2013), Page 402-410*

CHAPTER 6

STRUCTURAL, ELECTRICAL AND OPTICAL STUDTY OF $(Bi_{0.5}Na_{0.5})TiO_3$-$Ba(Zr_{0.25}Ti_{0.75})O_3$ LEAD-FREE PIEZOELECTRIC CERAMIC SYSTEM

OUTLINE: In this chapter the influence of $Ba(Zr_{0.25}Ti_{0.75})O_3$ content on $(Bi_{0.5}Na_{0.5})TiO_3$ ceramic with regards to structural, electrical and optical properties has been studied. Particular emphasis has been given to study enhanced properties at morphotropic phase boundary (MPB) region.

6.1 SAMPLE PREPARATION

The samples were prepared by a conventional mixed oxide process. In the first step $(Bi_{0.5}Na_{0.5})TiO_3$ (BNT) and $Ba(Zr_{0.25}Ti_{0.75})O_3$ (BZT) master batches were made from Barium Carbonate-$BaCO_3$ (reagent grade, Meark, India), Zirconium Oxide-ZrO_2 (reagent grade, Loba Chem.), Titanium Oxide-TiO_2 (reagent grade, Merck, India), Bismuth Oxide - Bi_2O_3 (reagent grade Meark, India) and Sodium Carbonate-Na_2CO_3 (reagent grade, Merck, India). Appropriate amounts of reagents were mixed in a zirconia media for 12 hrs using a laboratory designed ball milling unit. The BNT sample was calcined at 850^{o}C for 4 hrs with intermediate grinding and mixing. The BZT sample was calcined at 1250^{o}C for 4 hrs with intermediate grinding and mixing. The phase purity of both the master samples was investigated using x-ray diffraction (XRD), (Xpert MPD, Philips, UK). Appropriate amounts of BNT and BZT were mixed thoroughly in agate mortar using IPA to obtain $(1-x)(Bi_{0.5}Na_{0.5})TiO_3$-$xBa(Zr_{0.25}Ti_{0.75})O_3$ (abbreviated as BNT-BZT) ceramics, where x is ranging from 0.01 to 0.08.

The mixed powders were ball milled for 12 hrs in acetone medium. After ball milling, the powders were dried at room temperature. Then the dried powders were again grinded for 2 hrs in agate mortar. The granules were made by adding 3% polyvinyl alcohol (PVA) as a binder. The granules were sieved and uniaxially cold-pressed with a load of 6 tonnes to obtain discs with a diameter of 11 mm. The discs were decarbonized at 550°C and then sintered between 1050 and 1175°C for 4 hrs. The optimum sintering temperature was determined by investigating the linear shrinkage and bulk density of the sintered pellets. The bulk density and apparent porosity were investigated using Archimedes principle (water immersion technique).The pellets were sintered at optimized temperature of $1150^{o}C$ for 4 hrs in a programmable furnace (Table 6.1).

Table 6.1: The optimized sintering temperature, bulk density and apparent porosity of (1-x)($Bi_{0.5}Na_{0.5}$)TiO_3-xBa($Zr_{0.25}Ti_{0.75}$)O_3 ceramic

Composition (x)	Sintering Temperature (°C)	Bulk Density (g/cm^3)	Apparent Porosity
0.01	1150	5.91	0.001
0.02	1150	5.992	0.001
0.03	1150	5.815	0.001
0.04	1150	5.913	0.001
0.05	1150	5.711	0.001
0.06	1150	5.634	0.002
0.07	1150	5.544	0.003
0.08	1150	5.536	0.003

For electrical measurement disk shaped samples were prepared and fired at elevated temperatures. The linear shrinkage of different compositions as a function of temperature was

recorded and is shown in Fig.6.1. The diameters of all the pallets were found decreasing with increasing temperature and showed stable behavior above 1150°C. The bulk density of the pellets sintered at 1150°C was measured using water immersion technique and found to be ~97% of their theoretical density. This is signifying that all the compositions of BNT-BZT are well sintered at around 1150°C. There is not much change in sintering temperature with the addition of BZT with BNT.

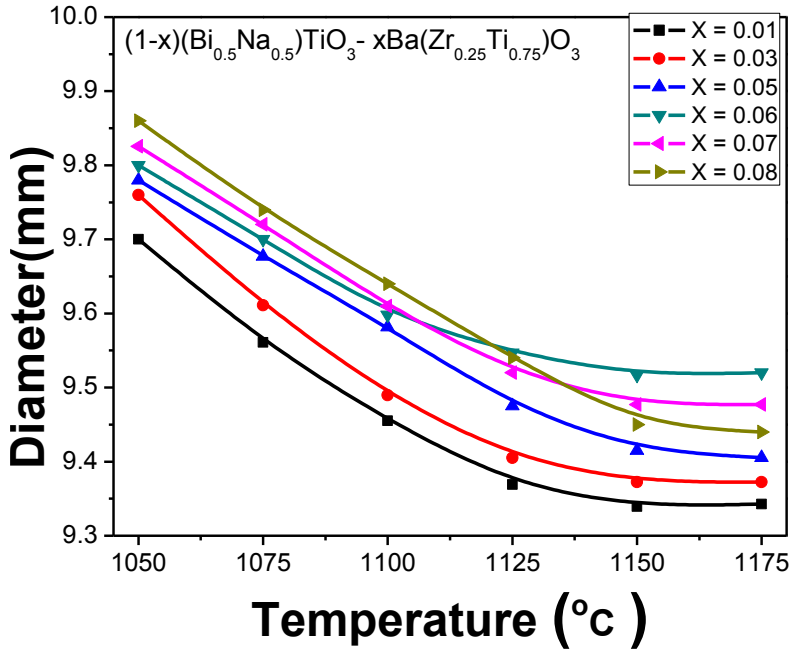

Fig.6.1: Linear shrinkage of (1-*x*)($Bi_{0.5}Na_{0.5}$)TiO_3-*x* Ba($Zr_{0.25}Ti_{0.75}$)O_3 ceramics

6.2 STRUCTURAL CHARACTERIZATION

The selected samples were characterized by the following tools and the results are discussed.

6.2.1 Phase Formation and Rietveld-Refinement

The rhombohedral structure of ($Bi_{0.5}Na_{0.5}$)TiO_3 ceramics and cubic structure of Ba($Zr_{0.25}Ti_{0.75}$)O_3 ceramics were structurally refined in Materials Analysis Using Diffraction (MAUD) software version 2.33 by the Rietveld-refinement method as shown in Fig.3.2(a)

(Chapter3) and Fig.6.2 (a), respectively. The results obtained from the Rietveld-refinement method show a good agreement between the observed XRD patterns and theoretical results. The lattice parameters and atomic positions obtained from the Rietveld-refinement are presented in Table 6.2. In this table, the fit parameters (R_p, R_{wp}, R_{exp}, and χ^2) suggest that the refinement results are well-reliable.

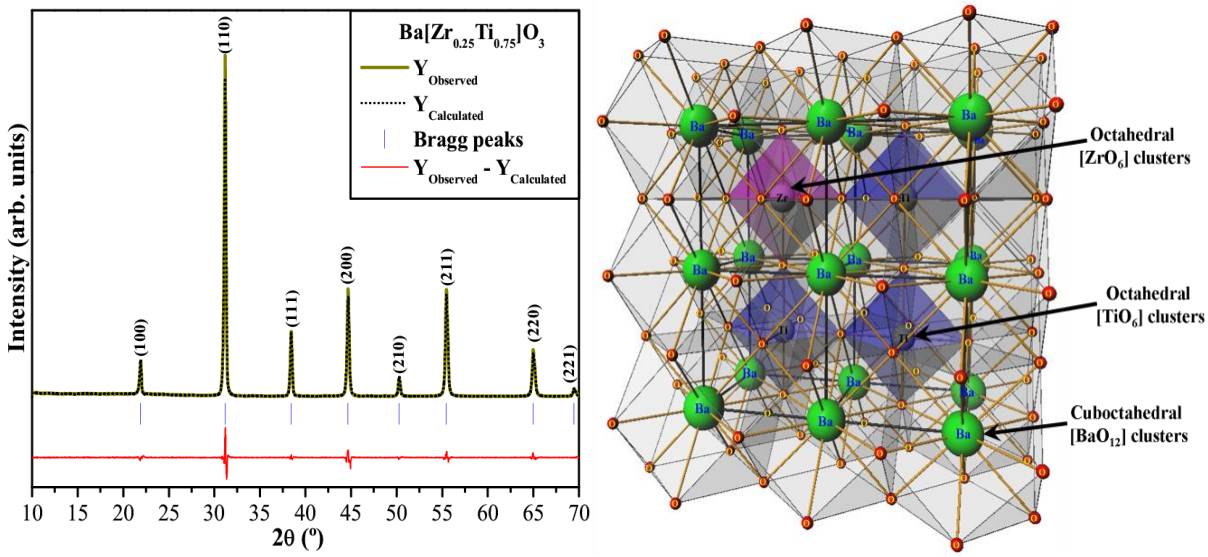

(a) (b)

Fig 6.2: (a) Rietveld-refinement plots and (b) Schematic representation of the unit cell corresponding to $Ba(Zr_{0.25}Ti_{0.75})O_3$ ceramics, respectively

Table 6.2: Lattice parameters, unit cell volume, atomic coordinates and site occupation obtained by Rietveld-refinement for the $Ba(Zr_{0.25}Ti_{0.75})O_3$ ceramic.

Atom	Wyckoff	Site	*x*	*y*	*z*
Ba	1a	*m*-3*m*	0	0	0
Ti	1b	*m*-3*m*	0.5	0.5	0.5
Zr	1b	*m*-3*m*	0.5	0.5	0.5
O	3c	*mm*2..	0	0.5	0.5

$Pm\bar{3}m$ (221) - cubic ($a = b = c = 4.0563(4)$ Å; $c/a = 1$; V = 66.74 Å^3), R_p = 3.97%; R_{wp} = 6.45%; R_{exp} = 2.6% and χ^2 = 2.48

Fig.6. 2(b) shows the representations of BZT unit cells. The rhombohedral structure of the BNT ceramics given in Fig.3.2 (b) (Chapter 3) is characterized by exhibiting a space group ($R\bar{3}c$), point-group symmetry (C_{3v}^{6}) and two clusters per unit cell (Z = 2). In Fig.6.2 (b), it's possible to observe a cubic structure for the BZT ceramic. This lattice presents a space group ($Pm\bar{3}m$), point-group symmetry (O_{h}^{1}) and one cluster per unit cell (Z = 2). In these supercells, the Ba^{2+} atoms (lattice modifier) are coordinated to twelve oxygen atoms forming a cuboctahedron [BaO_{12}] cluster. The cuboctahedron presents twelve identical vertices, formed by the meeting of two triangles and two squares, fourteen faces and twenty-four identical edges, each separating a triangle from a square [217]. The bonds between Ba and O atoms present a higher ionic-bond character in the lattice. While the Ti and Zr atoms (lattice formers) are both bonded to six O atoms, forming a polyhedron called octaedron which is written as [TiO_6] and [ZrO_6] clusters (Fig.6.2(b)).This octahedron presents six vertices, eight faces and twelve edges, formed by the meeting of eight triangles [218]. The bonds between Ti/Zr and O atoms present an ionic character less than (Ba-O) in the lattice.

Fig.6.3(a,b) illustrate the XRD patterns of the (1-*x*)BNT-*x*BZT ceramics with different *x* compositions from 0 to 0.08 and reduced XRD patterns from 44 to 49º of these ceramics, respectively. According to the XRD patterns, all the (1-*x*)BNT-*x*BZT ceramics can be indexed to a perovskite-type rhombohedral structure with the space group ($R\bar{3}c$). Moreover, we have observed that all the compositions are monophasic without the presence of deleterious phases (Fig.6.3 (a)). This characteristic indicates that the BZT ceramic has been introduced completely into the BNT lattice matrix forming a homogeneous (1-*x*)(BNT)-*x*(BZT) solid solutions. In function of BZT ceramics addition into BNT lattice matrix, we can observe an

increase of lattice parameter and cell volume due to the large radius of Ba^{2+} (1.61 Å) in relation to the $[Bi_{0.5}Na_{0.5}]^{2+}$ (~ 1.40 Å) [219].

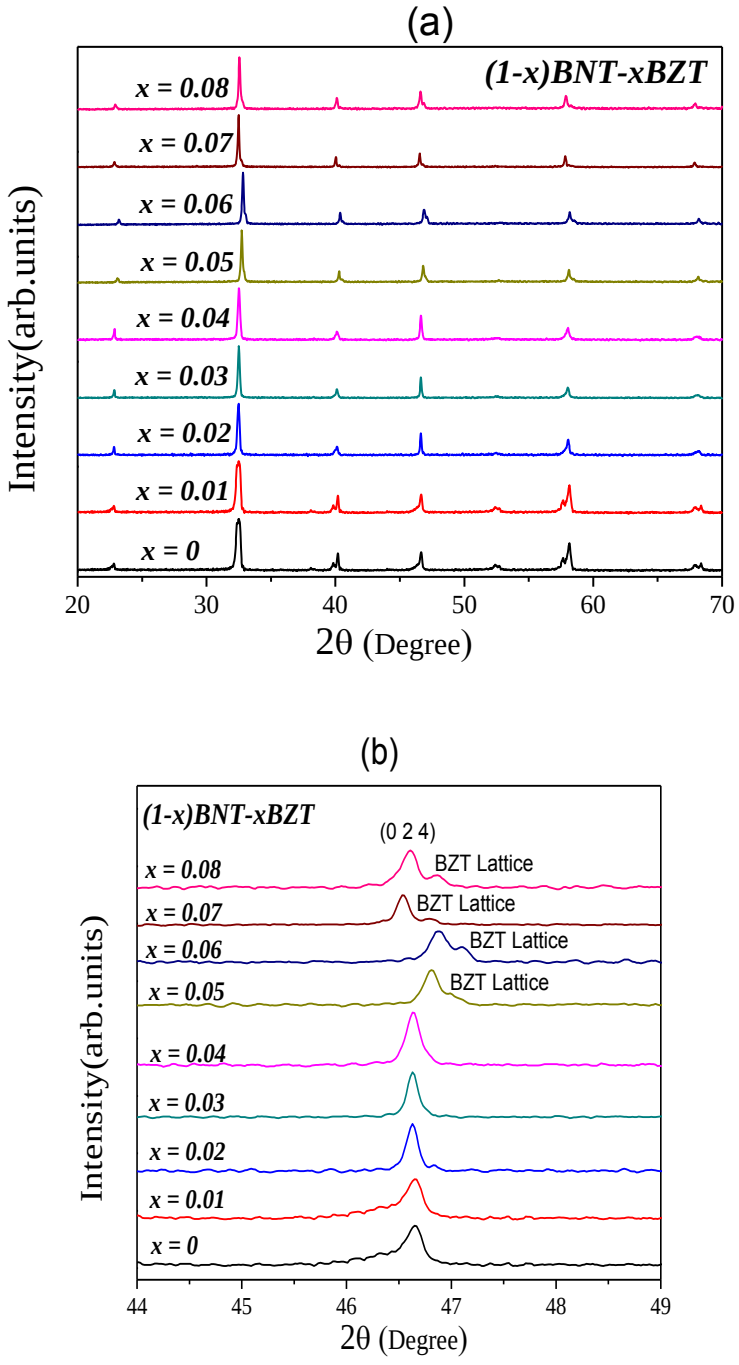

Fig.6.3: (a) x-ray diffraction and (b) Reduced x-ray diffraction pattern of (1-*x*)$(Bi_{0.5}Na_{0.5})TiO_3$-*x* $Ba(Zr_{0.25}Ti_{0.75})O_3$ ceramics

To verify with more clarity the reduction of lattice parameters, the XRD patterns from 44º to 49º are shown in Fig.6.3 (b). It has been observed that a small shift occurs in the (0 2 4) peak in almost all (1-*x*)(BNT)-*x*(BZT) ceramics, which exhibit only a rhombohedral structure and also the manifestation of cubic BZT lattice at long-range near at 46º, probably refering to (2 0 0) peak. However, the XRD patterns for (1-*x*)(BNT)-*x*(BZT) with x = 0.05 presented a considerable shift 2θ(º) and consequently a reduction of lattice parameters.

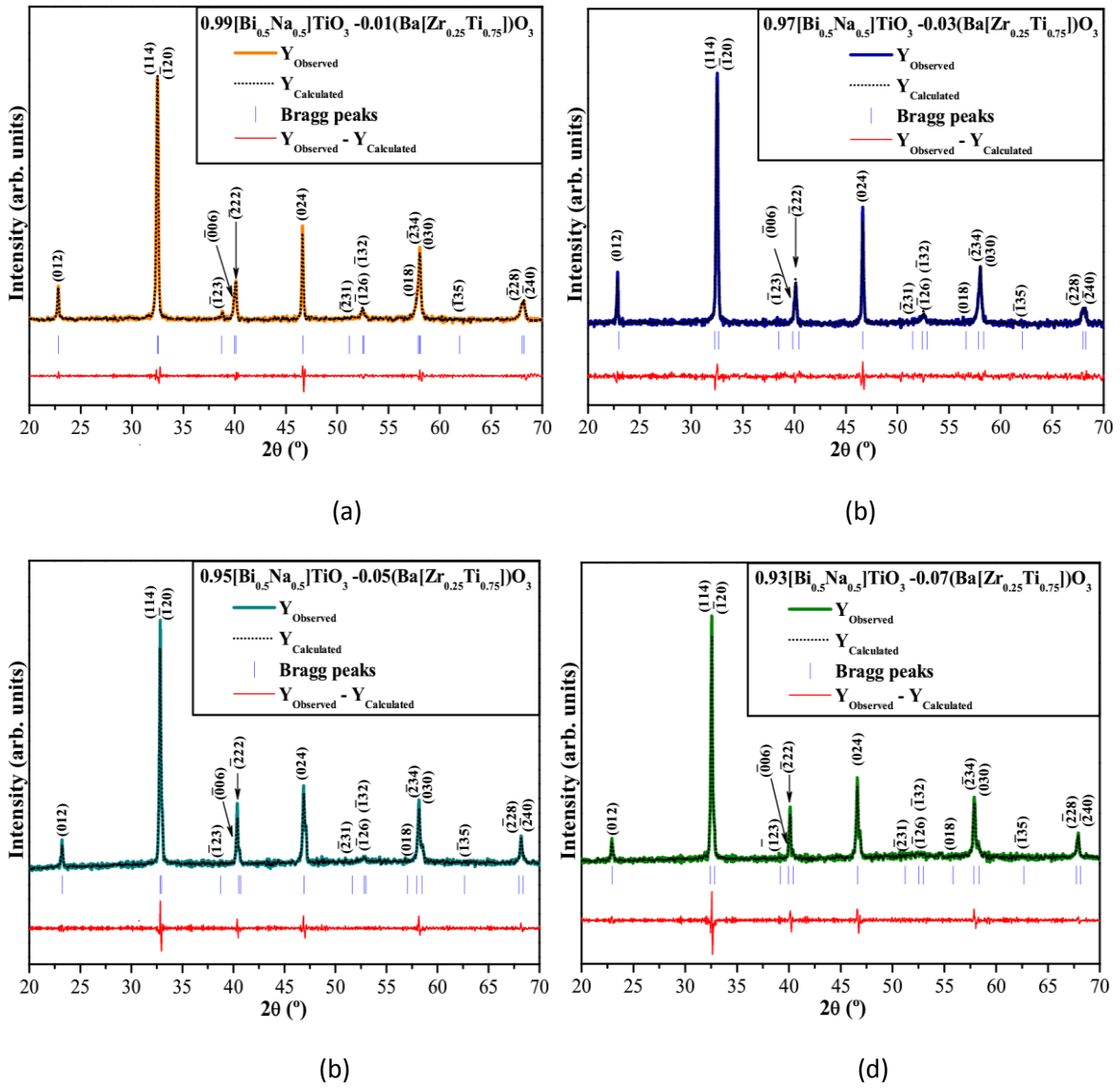

Fig 6.4: (a-d) Rietveld-refinement plot of (1-*x*)BNT-*x*BZT ceramics with [(a); x = 0,01; (b); x = 0.03; (c); x = 0.05; and (d); x = 0.07], respectively

The structural refinement of the (1-*x*)BNT-*x*BZT ceramics with different compositions (*x* = 0.01, 0.03, 0.05 and 0.07) were performed using the Rietveld-refinement method [139] as shown in Fig.6.4(a-d). The results obtained from the Rietveld-refinement method show a good agreement between to the XRD patterns experimentally measured and theoretical line profile of (1-*x*)BNT-*x*BZT ceramic solid-solutions with BNT and BZT Rietveld-refinement pattern.

6.2.2 Raman Spectroscopy Analysis

As reported previously, BNT has rhombohedral symmetry with space group R3c (C^6_{3v}) and BZT has cubic symmetry with space group Pm3m (O^1_h) at room temperature. The rhombohedral structure of BNT presents 13 Raman-active modes, which can be represented as (Γ_{Raman} = $7A_1$ + 6E). All the A_1 and E modes are classified into longitudinal (LO) and transverse (TO) components because of the electronic structure with polar character of lattice. Furthermore, the existence of long-range electrostatic forces in the cubic ferroelectric phase split each of the A_1 and E modes into longitudinal and transverse modes also. However, in the present case most of the analysis has been done with respect to the rhombohedral symmetry of BNT.

Fig.6.5 represents the Raman spectroscopy study of (1-*x*)$(Bi_{0.5}Na_{0.5})TiO_3$-*x* $Ba(Zr_{0.25}Ti_{0.75})O_3$ ceramics with $0 \leq x \leq 0.08$. In BNT, rhombohedral structure with space group $R\bar{3}c$ (Z = 2) and two cluster units, it is possible to observe 13 Raman-active modes, which can be represented as (Γ_{Raman} = 7A1+6E). However, it is possible to detect only five Raman-active modes observed in the range from 100 to 1,000 cm^{-1} in agreement with the works reported by the Rout *et al*. [88] and Eerd *et al*. [197]. Due to the disorder into-A site related to distorted octahedral [BiO_6] and [NaO_6] clusters given in Fig.3.3 (Chapter 3), these BNT ceramics with rhombohedral structure present 13 Raman-active modes by the following representation:

(Γ_{Raman} = 4A1+9E) that have been seen analyzed and reported by the Petzelt *et al*. [159]. In Fig.6.5, the Raman peaks of BNT and BNT-BZT solid-solutions are relatively broad, which can be caused by the distorted octahedral [BiO_6] and [NaO_6] clusters or disorder in A-site of rhombohedral structure. Also this behavior can be provoked possibly due to the presence of the disorder in structural or distorted octahedral [TiO_6] clusters at short-range in both (rhombohedral-BNT and cubic-BZT) lattices.

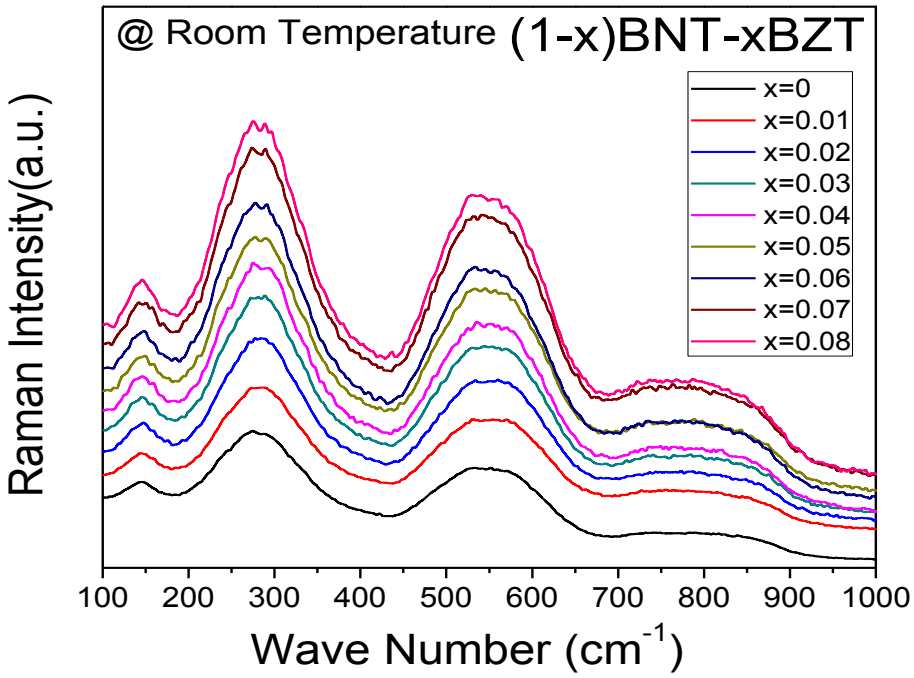

Fig.6.5: Room temperature Raman spectra of (1-*x*)($Bi_{0.5}Na_{0.5}$)TiO_3-*x*Ba($Zr_{0.25}Ti_{0.75}$)O_3 ceramic

The first Raman-active mode at around (146 cm^{-1}) is related to network modifiers or distorted octahedral [BiO_6] and [NaO_6] clusters. The second Raman-active mode can be deconvoluted in three Raman peaks in the regions of 279 cm^{-1}. This mode is assigned to stretching arising from the bonds due the presence of octahedral [TiO_6] clusters at short-range. The mode shows anomaly at x = 0.05 and starts splitting into two bands that shift apart from each other with

further increase in BZT content. The third Raman-active mode with low intensity is related to short-range electrostatic forces associated with the lattice ionicity [155]. According to Dobal *et al*. [160], the modes situated at around 542 cm^{-1} is ascribed to the (←O←Ti→O→) stretching symmetric vibrations of the octahedral [TiO_6] clusters. This mode is common in materials with perovskite-type structure. However, the spectral signature of bands shows a change at x = 0.05 and separates into two distinct bands at x = 0.07. Finally, the mode found at 812 cm^{-1} is due to the presence of the sites within the rhombohedral lattice pre-containing octahedral distorted [TiO_6] clusters [161].

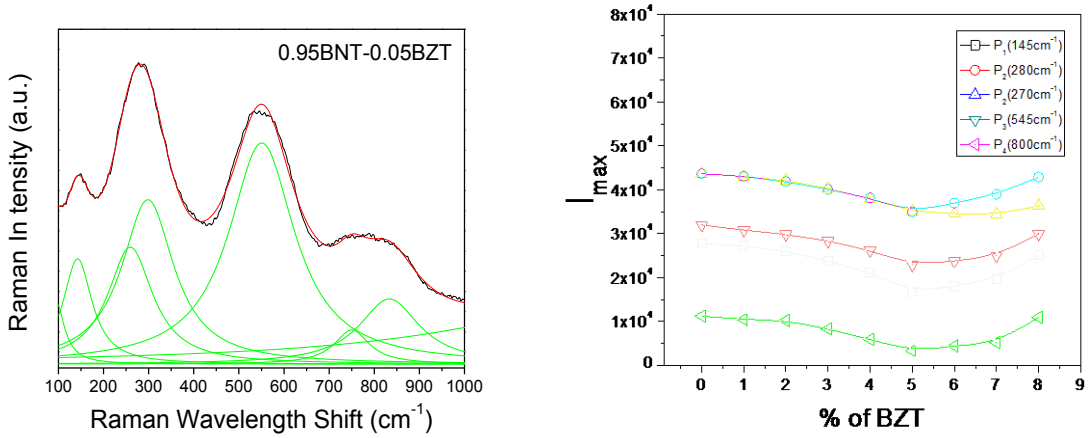

Fig.6.6: (a) Room temperature Raman spectrum of 0.95BNT-0.05BZT (MPB, composition) ceramics and (b)Variation of the maximum intensity of different modes in the Raman spectra with % of BZT concentration

Fig.6.6 (a), fitted by Lorentzian area function for MPB composition of BNT-BZT solid-solutions, clearly shows the overlapping of Raman bands due to anharmonicity in lattice during molecular vibrations. Fig.6.6 (b) shows that the minimum intensity occurs at x = 0.05 due to the maximum strain in the lattice, consequently reduction of lattice parameters and co-existing of BNT and BZT phase, which is well aligned with x-ray diffraction study. The dramatically enhanced maximum intensity of the Raman bands, when the x value is increased

further, suggests the occurrence of a long-range ordering of the corresponding phases involved [201-204].

6.2.3 Microstructure Analysis

Fig.6.7 shows the SEM images of natural surface for (1-*x*)BNT-*x*BZT ceramics sintered at 1150^0 C for 4 hrs. The pure BNT sample presents rectangular grain morphology while the BZT addition changes the grain shape to quasi-spherical. All sample surface grains present regular geometry with compact structure. BNT disks appear to be poly-dispersed in both size and shape due to inhomogeneous grain growth. On the contrary, the addition of BZT results in the inhibition of grain growth, so the crystals of the BNT-BZT appear to be more uniform in both size and shape. Several possible mechanisms have been reported to show how the liquid-phase could homogenize the microstructure [205]. The first possibility is that the liquid-phase assists rearrangement of the matrix particles at the inclusion/matrix interface into a more efficient packing configuration. The second possibility is that the liquid-phase goes into the polycrystalline inclusions by capillary action to break them up and homogenize the microstructure.

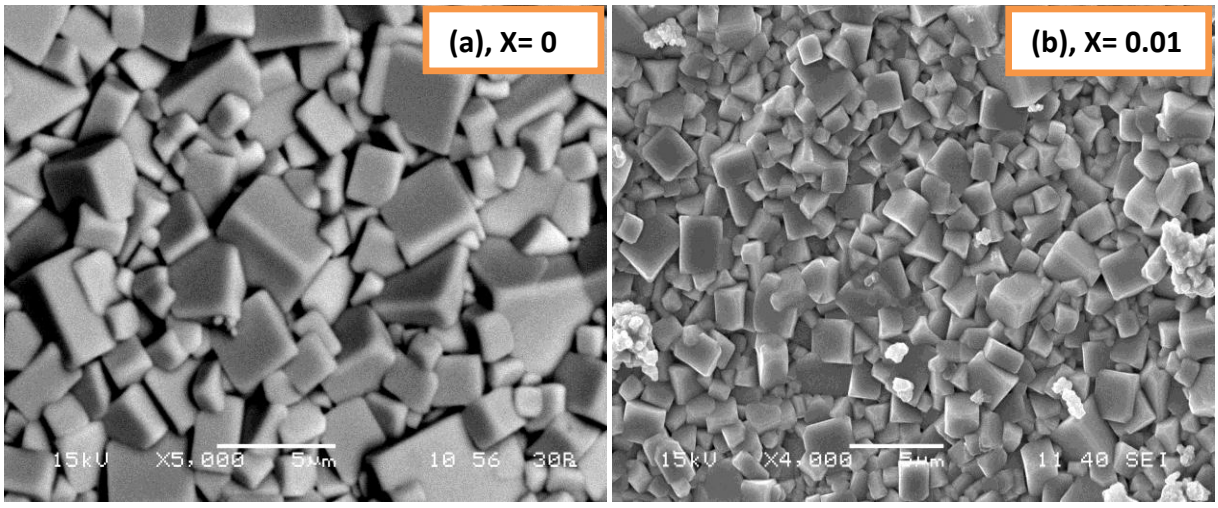

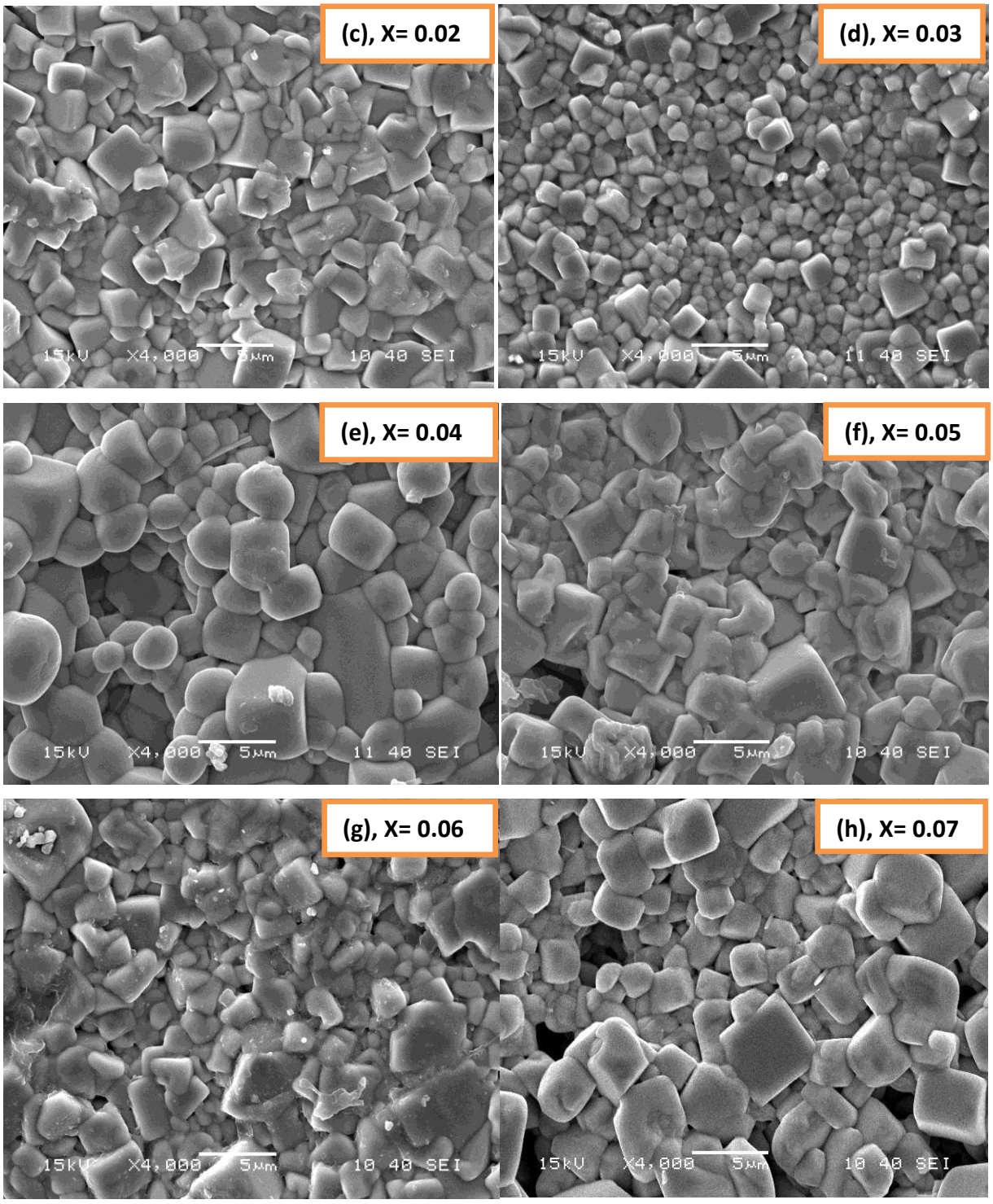

Fig.6.7: (a-h) SEM micrographs of (1-*x*)($Bi_{0.5}Na_{0.5}$)TiO_3- *x* $Ba(Zr_{0.25}Ti_{0.75})O_3$ ceramic

It can also be seen that the grain size reduces with increase in BZT content in the compositions up to x = 0.03, which was determined by linear interception method. The reason may be that

Ba^{2+} abounds in crystal boundary, which prevents the ion from migrating and restrains the growing of grains. The SEM observation confirms that the (1-*x*) BNT- (*x*) BZT ceramics are densely sintered and all compositions have high density between 5.67 and 5.83 g/cm^3, about more than 96% of the theoretical density.

Energy dispersive x-ray spectroscopy (EDS) is a chemical microanalysis technique used in conjunction with SEM and is not a surface science technique. Fig.6.8 (a-d) give the Energy dispersive x-ray spectroscopy (EDS) of BZT substituted BNT compositions. The spectra show that the elements present in the prepared compositions are Na, Ba, Bi, Zr, Ti and O only. With increasing BZT, content weight percentage of Ba and Zr increases in the composition. Hence, energy dispersive x-ray analysis (EDS) (Fig. 6.8 and Table 6.3) confirmed that all the samples are in stoichiometric ratio.

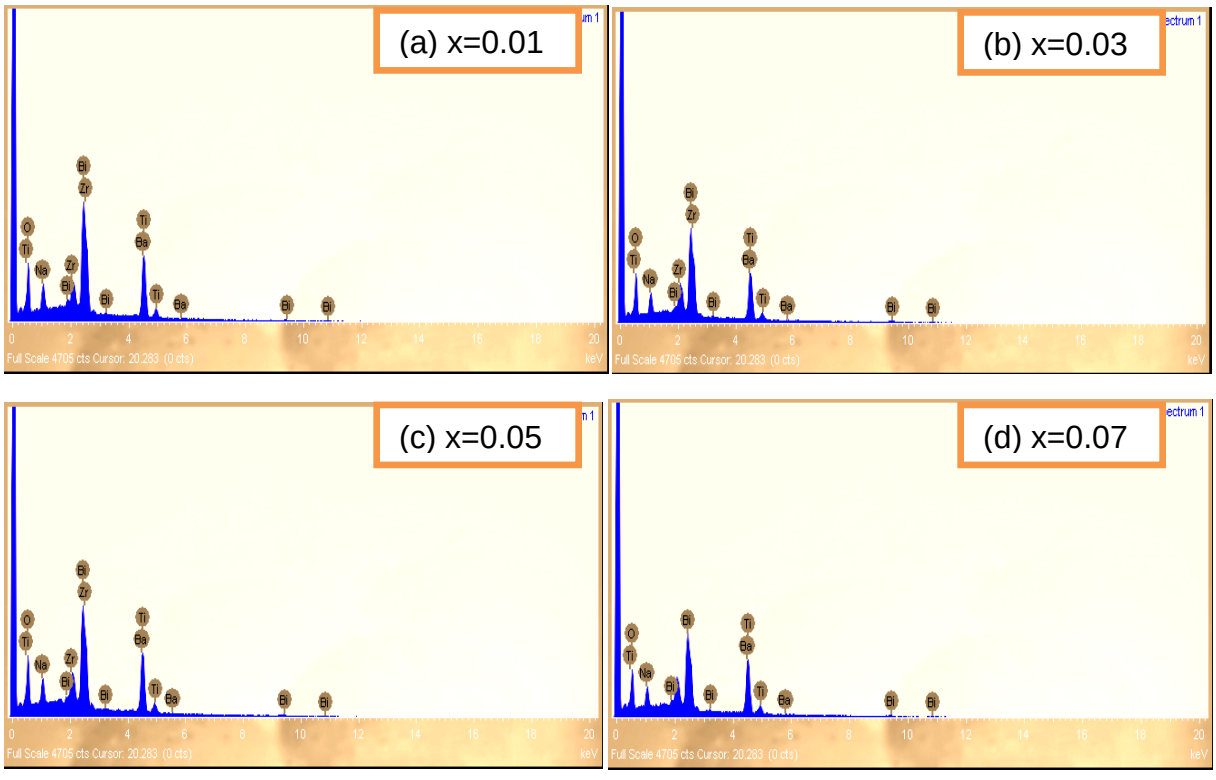

Fig.6.8: (a-d) Energy dispersive x-Ray spectroscopy compositional patterns of the (1-*x*)($Bi_{0.5}Na_{0.5}$)TiO_3- *x* $Ba(Zr_{0.25}Ti_{0.75})O_3$ ceramics sintered at 1150^oC for 4 hrs

Table 6.3: Compositional analysis of (1-*x*)BNT-*x*BZT ceramics from energy dispersive x-ray spectroscopy

Composition (*x*)	Element	Theoretical Weight%	Weight% from EDS
0	O K	25.6554	26.01
	Na K	5.4256	5.33
	Ti K	19.6	19.45
	Bi M	49.32	49.21
0.01	O K	25.626	25.66
	Na K	5.37	5.22
	Ti K	19.52	19.48
	Zr L	0.0936	0.09
	Ba L	0.5635	0.54
	Bi M	48.8264	49.01
0.03	O K	25.5657	25.33
	Na K	5.263	5.64
	Ti K	19.3635	19.00
	Zr L	0.28	0.25
	Ba L	1.69	1.66
	Bi M	47.84	48.12
0.05	O K	25.507	25.28
	Na K	5.1833	5.23
	Ti K	19.2	19.27
	Zr L	0.468	0.46
	Ba L	2.82	2.79
	Bi M	46.85365	46.97
0.07	O K	25.448	25.18
	Na K	5.0458	5.08
	Ti K	19.05	19.27
	Zr L	0.655	0.63
	Ba L	3.944	3.89
	Bi M	45.867	45.95

6.3 OPTICAL PROPERTIES STUDY

6.3.1 Ultraviolet-Visible Absorption Spectroscopy Analysis

The optical band gap energy (E_{gap}) was calculated by the method proposed by Kubelka and Munk [220]. This methodology is based on the transformation of diffuse reflectance measurements to estimate E_{gap} values with good accuracy within the limits of assumptions,

when modeled in three dimensions [221]. Particularly, it is useful in limiting cases of an infinitely-thick sample layer. The Kubelka-Munk equation (6.1) for any wavelength is written as:

$$F(R_\infty) = \frac{(1 - R_\infty)^2}{2R_\infty}\frac{k}{s} \tag{6.1}$$

where $F(R_\infty)$ is the Kubelka-Munk function or absolute reflectance of the sample. In our case, the barium sulphate ($BaSO_4$) was the standard sample in the reflectance measurements. $R_\infty = R_{sample}/R_{BaSO4}$ (R_∞ is the reflectance when the sample is infinitely thick), k is the molar absorption coefficient, and s is the scattering coefficient. In a parabolic band structure, the optical band gap and absorption coefficient of semiconductor oxides [222] can be calculated by the following Eq. (6.2):

$$\alpha h\nu = C_1(h\nu - E_{gap})^n \tag{6.2}$$

where α is the linear absorption coefficient of the material, $h\nu$ is the photon energy, C_1 is a proportionality constant, E_{gap} is the optical band gap and n is a constant associated to the different kinds of electronic transitions (n = 0.5 for a direct allowed, n = 2 for an indirect allowed, n = 1.5 for a direct forbidden and n = 3 for an indirect forbidden transition). According to Meng *et al*. [223], the BNT crystals exhibit optical absorption spectra governed by direct allowed electronic transitions between the valence band and conduction band, while the BNT films prepared experimentally by Bousquet *et al*. [224] showed optical band gap of direct transition (E_{gap} = 3.3 eV) and its theoretical calculation presented six electronic structures over eight present an indirect band gap, with a E_{gap} falling in the range 3.90-4.60 eV. Therefore, we have attributed that our rhombohedral BNT-BZT ceramics have E_{gap}

experimental results very close to direct allowed transitions. In this characteristic, it is observed that after electronic absorption process, the electrons located in the maximum-energy states in the valence band fall back to the minimum-energy states in the conduction band under the same point in the Brillouin zone [223, 224]. Based on this information, the E_{gap} values of BNT-BZT ceramics were calculated using n = 0.5 in equation (6.2). Finally, using the remission function described in equation (6.2) and with the term $k = 2\alpha$ and C_2 is proportionality constant, we obtain the modified Kubelka-Munk equation as shown in equation (6.3):

$$[F(R_\infty)h\nu]^2 = C_2(h\nu - E_{gap}) \tag{6.3}$$

Therefore, finding the $F(R_\infty)$ value from equation (6.3) and plotting a graph of $[F(R_\infty)h\nu]^2$ (represented as absorbance in the figure along y-axis) against $h\nu$, it is possible to determine the E_{gap} of BNT-BZT ceramics.

Fig.6.9 (a-h) illustrate the UV-Visible spectrum of (1-*x*)(BNT)-*x*(BZT) ceramics with ($0.01 \leq x \leq 0.08$), respectively. Fig.6.9 (a-d) revealed that the optical band gaps for all the (1-*x*)(BNT)-*x*(BZT) ceramics are characterized by well-defined direct electronic transitions, which is typical nature of crystalline semiconductor materials [225]. The exponential optical absorption edge and the optical band gap energy are controlled by the degree of structural disorder in the lattice. The optical energy band gap for pure BNT (x = 0) is found to be 2.94 eV as given in Chapter 3 (Section 3.3.4). The increase in the E_{gap} values with BZT content can be attributed to the reduction of the defects into local lattice distortions and localized electronic levels within the forbidden band gap [178].

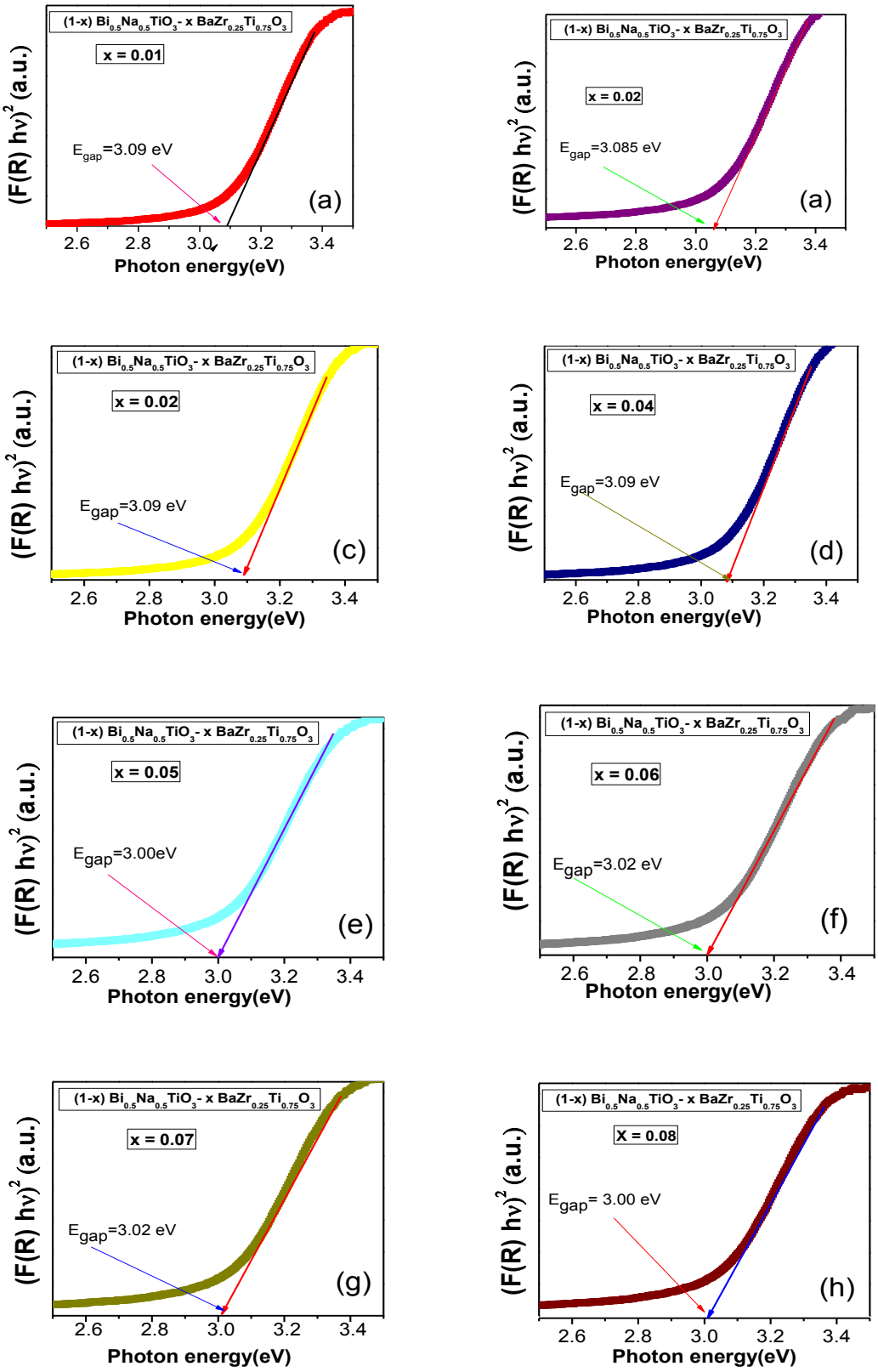

Fig.6.9: (a-h) UV-Visible spectrum of (1-*x*)($Bi_{0.5}Na_{0.5}$)TiO_3-*x* Ba($Zr_{0.25}Ti_{0.75}$)O_3 ceramics

Moreover, we believe that these differences in the E_{gap} (2.94 to 3.09 eV) values may be mainly attributed to the different levels of distortions on both $[BiO_6]$-$[NaO_6]$-$[TiO_6]$ clusters in BNT ceramics and/or $[BaO_{12}]$-$[ZrO_6]$-$[TiO_6]$ clusters in BZT ceramics at short and medium-range. Another interesting point that can be noticed is a slight increase in the E_{gap} = 3.09 eV value for the (1-*x*)BNT-*x*BZT ceramics with (*x* = 0.01 -0.04). This behavior can be possibly related to a slight increase in structural disorder, level of distortion of the clusters and electronic intermediary levels between the valence band and conduction band. Moreover, with the further increase of $[BaO_{12}]$-$[ZrO_6]$-$[TiO_6]$ clusters in (1-*x*)BNT-*x*BZT ceramics (*x* >0.04) are observed oscillations in E_{gap} values, which can be related to interaction between distorted octahedral $[BiO_6]$/$[NaO_6]$ and undistorted octahedral $[ZrO_6]$ and cuboctahedral $[BaO_{12}]$ clusters.

6.4DIELECTRIC PROPERTIES STUDY

6.4.1 Temperature-Dependent Dielectric Constant (ε') and Loss (tanδ)

Fig.6.10 (a) shows the temperature-dependent dielectric behavior of (1-*x*)BNT-*x*BZT ceramic system at 100 kHz. It can be seen that BZT doping can improve the dielectric properties remarkably. The variation of dielectric constant with different BZT fractions is given in Table 6.5. When *x* is less than 0.05, the dielectric permittivity becomes higher with the increasing of *x*. When *x* is 0.05, the ε_r reaches its maximum value (3533); and when the *x* value increases to more than 0.05, the ε_r decreases. The ionic radius of Ba^{2+} is 0.160 nm when its coordination number is 12, and ionic radii of Na^{1+}, Bi^{3+} and Ti^{4+} are 0.139, 0.128 and 0.061 nm, respectively, so Ba^{2+} ions are most likely to occupy A- site of perovskite structure (ABO_3). Here Ba^{2+} can occupy $(Bi_{0.5}Na_{0.5})^{2+}$ site and $(Zr_{0.25}Ti_{0.75})^{4+}$ can enter the Ti^{4+} site of BNT. The substitution of BZT will decrease the lattice density, so the lattice structure becomes

incompact, which is favorable for domain wall motion [226], so the relative permittivity increases. Meanwhile, Ba^{2+} doping also leads to a series of space charge centers. As we know, weak-bonded ions play an important role in dielectric and the space charge centers can disorder the distribution of electric potential, which can increase the potential barrier and the migration of the ions is restrained. When x is more than 0.05, ε_r begins to decline, because Ba^{2+} begins to replace Bi^{3+}, which will create oxygen vacancies, when the content of Ba^{2+} reaches certain critical value. It has been known that oxygen vacancies are the main cause of domain wall clamping [227]. This clamping will restrain the macro-micro domain switching in some degree; this is the reason that the relative permittivity declined.

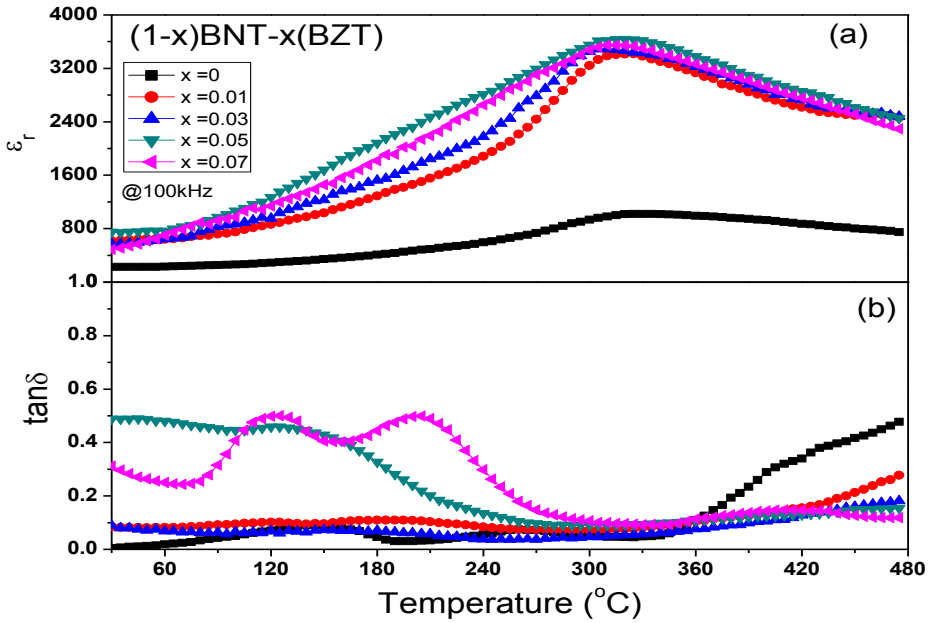

Fig.6.10: Temperature-dependence of (a) dielectric constant (ε_r) and (b) dielectric loss (tanδ) of $(1-x)(Bi_{0.5}Na_{0.5})TiO_3$- x $Ba(Zr_{0.25}Ti_{0.75})O_3$ ceramics

The temperature co-efficient of permittivity is calculated by the formula (equation 4.2) and its values ate given in Table 6.4. Fig.6.10 (b) shows the temperature-dependence of dielectric loss of $(1-x)(Bi_{0.5}Na_{0.5})TiO_3$-$x$ $Ba(Zr_{0.25}Ti_{0.75})O_3$ ceramics with $0 \leq x \leq 0.07$. Two loss peaks appear in the temperature range of 100～150°C and 225～275°C. With increase of

temperature beyond 275°C, the loss falls abruptly and then slightly increases, due to the domain wall motion in the ferroelectric region and leakage current dominant in the materials. With the increasing of $Ba(Zr_{0.25}Ti_{0.75})O_3$ ceramics, the two loss peaks sifted towards lower temperature in most of the compositions. This phenomenon may be related to the existence of polar micro-region [183]. The materials undergo transition from ferroelectric state to anti-ferroelectric state and the anti-ferroelectric state changes macro-domain to micro-domain until polar micro-region is formed.

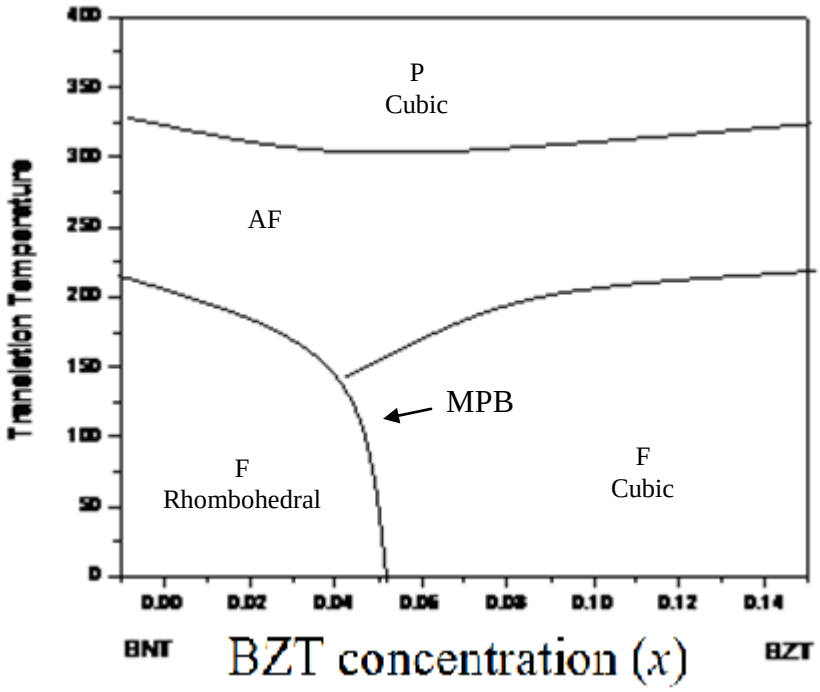

Fig.6.11: Temperature vs. composition phase-diagram of (1-*x*) BNT-*x*BZT ceramics

Fig.6.11: shows temperature-composition phase diagram for BNT-BZT ceramic where P is the paraelectric (cubic phase), F is the ferroelectric (cubic phase) and ferroelectric (rhombohedral phase) and AF is the anti-ferroelectric. The nearly horizontal line represents the boundary between the paraelectric phase and the ferroelectric phase while the nearly vertical line represents the MPB between the cubic and the rhombohedral phase.

The plots of $\ln(1/\varepsilon'-1/\varepsilon_m)$ as a function of $\ln(T-T_m)$ on the basis of the modified Curie-Weiss law for all the compositions are shown in Fig.6.12. The diffusion factor increased slightly at low fraction of BZT in the compounds and then sharply increased up to x = 0.05 and then decreased. The results show that the degree of diffuseness of the phase transition is higher for the samples at x = 0.05 in BNT-BZT solid-solution, which may be due to a considerable shift of peak towards lower angle and consequently a reduction of lattice parameters. The compositional dependence of diffusion factor is shown in Table 6.4.

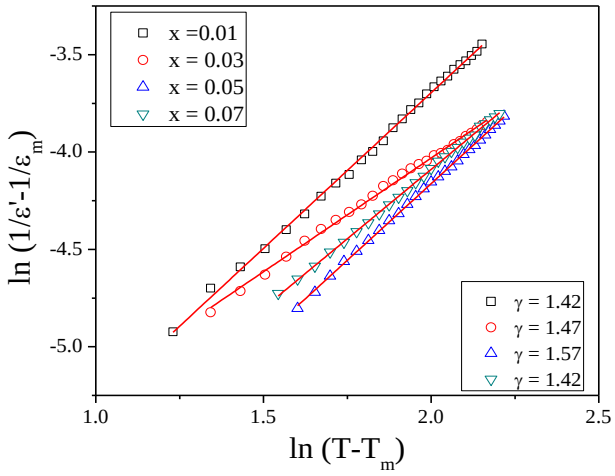

Fig.6.12: $\ln(T-T_m)$ vs. $\ln(1/\varepsilon'-1/\varepsilon_m)$ for 100 KHz of $(1-x)(Bi_{0.5}Na_{0.5})TiO_3$-$xBa(Zr_{0.25}Ti_{0.75})O_3$ ceramics at 100 kHz

Table 6.4: Dielectric coefficient of (1-x)BNT-x BZT ceramic

Composition(x)	T_d (^oC)	T_C (^oC)	α ($^oC^{-1}$)	ε_m	γ	tanδ
0.00	210	333	2.17×10^{-3}	1115	1.4	0.045
0.01	190	327	3.21×10^{-3}	3382	1.42	0.0765
0.03	175	319	5.12×10^{-3}	3427	1.47	0.0812
0.05	155	310	4.8×10^{-3}	3533	1.57	0.092
0.07	165	319	5.9×10^{-3}	3416	1.42	0.0956

6.4.2 Frequency-Dependent Dielectric constant (ε') and Loss (tanδ)

Fig.6.13 shows the frequency-dependence of (a) relative permittivity and (b) dielectric loss of (1-*x*)($Bi_{0.5}Na_{0.5}$)TiO_3- *x*Ba($Zr_{0.25}Ti_{0.75}$)O_3 ceramics with *x* = 0.0, 0.01, 0.03, 0.05 and 0.07 at room temperature. For all the compositions the relative permittivity non-linearly decreases due to the drop out of space charge and orientation polarization with increasing frequency.

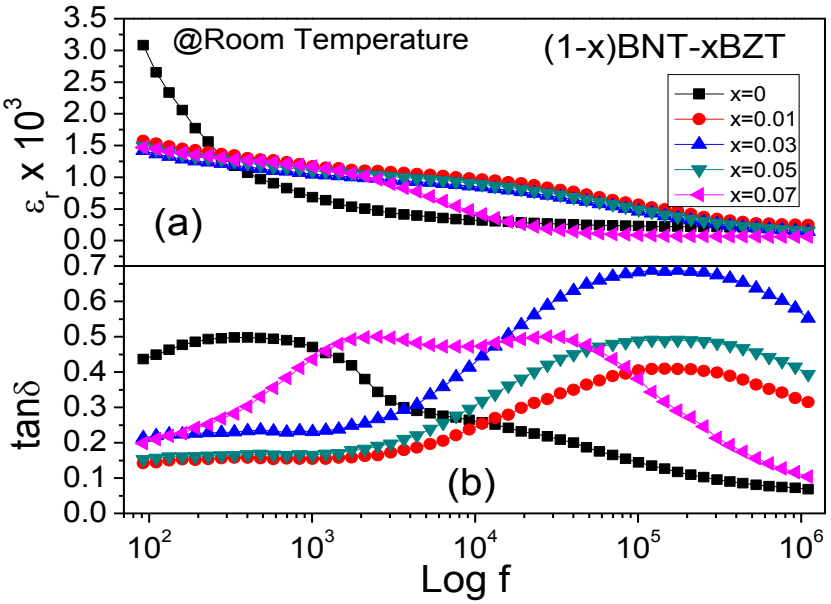

Fig.6.13: Frequency-dependence of relative permittivity and dielectric loss of (1-*x*)($Bi_{0.5}Na_{0.5}$)TiO_3- *x*Ba($Zr_{0.25}Ti_{0.75}$)O_3 ceramics at room temperature

The dielectric loss decreases and dielectric constant increases at higher frequency for all the compositions due to the inductive effect generated in the material at room temperature. The dielectric constant increases and dielectric loss reduces with increasing the BZT concentration up to *x* = 0.05.

Fig.6.14 (a-f) shows the frequency dependence of relative permittivity (ε') and dielectric loss (tanδ) of (1-*x*) ($Bi_{0.5}Na_{0.5}$)TiO_3-*x*Ba($Zr_{0.25}Ti_{0.75}$)O_3 ceramics at different temperatures for studied samples. For frequency ranging between 10 and 100 kHz, a sudden decrease in ε' was

observed at different temperatures for all samples, and this becomes more diffuse and shifts to higher frequency range with increasing temperature and vice-versa in increasing BZT content.

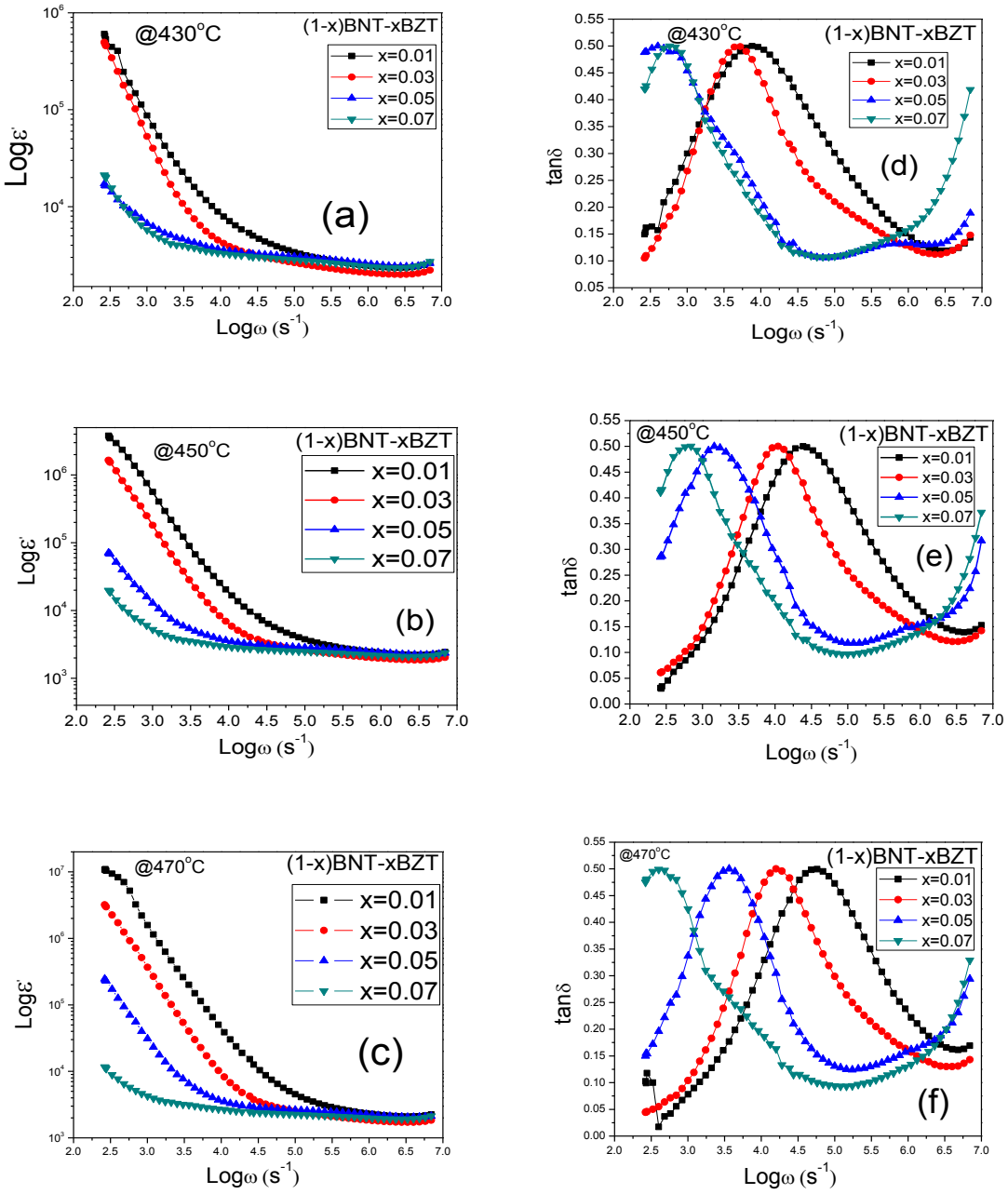

Fig.6.14: Frequency-dependence of (a-c) relative permittivity (ε') and (d-f) dielectric loss (tanδ) of (1-*x*) $(Bi_{0.5}Na_{0.5})TiO_3$- *x* $Ba(Zr_{0.25}Ti_{0.75})O_3$ ceramics at different temperature

In the low frequency range, the permittivity increases with increase in temperature. This may be caused due to grain boundary effect and the presence of all types of polarization in the materials. The observed high value of permittivity, both at low frequency and high temperature, is probably due to some kind of surface layer formed by the diffusion of the electrode materials [228]. The peak occurred in the same frequency range where the sudden decrease in the dielectric constant was also noticed and it shifted towards higher frequencies as the temperature increased. However, the peaks shifted towards the lower frequency side and the tanδ did not change appreciably by increasing the BZT content. The linearly decreasing region of ε' (and also the tanδ peak itself) could not have been a consequence of a Debye relaxation. The frequency dependence of the dielectric loss spectrum, shown in Fig.6.13 (d-f), implies that the hopping of charge carriers plays an important role in their transport processes because a loss peak is an essential feature of the charge carrier hopping transport [229].

6.5 ELECTRICAL CONDUCTIVITY STUDY

6.5.1 Impedance Spectroscopy Study

Fig.6.15 shows the variation of the real part of the impedance (Z') versus frequency at different temperatures. The magnitude of Z' (i.e., resistance) is observed to decrease with increasing temperature and frequency, which indicates the possibility of an increase in the ac conductivity with increasing temperature and frequency [187]. The Z' values of all temperatures and compositions merge in the higher-frequency region due to short range hopping mechanism. Further, at low frequencies, the Z' values decrease with increasing temperature, and the compound exhibits a negative temperature coefficient of resistance (NTCR)-type behavior like that of semiconductors [188]. The peaks disappeared with

increasing BZT content throughout the studied temperatures due to the increasing inhomogenity in the material indicated the induction of grain boundary effect.

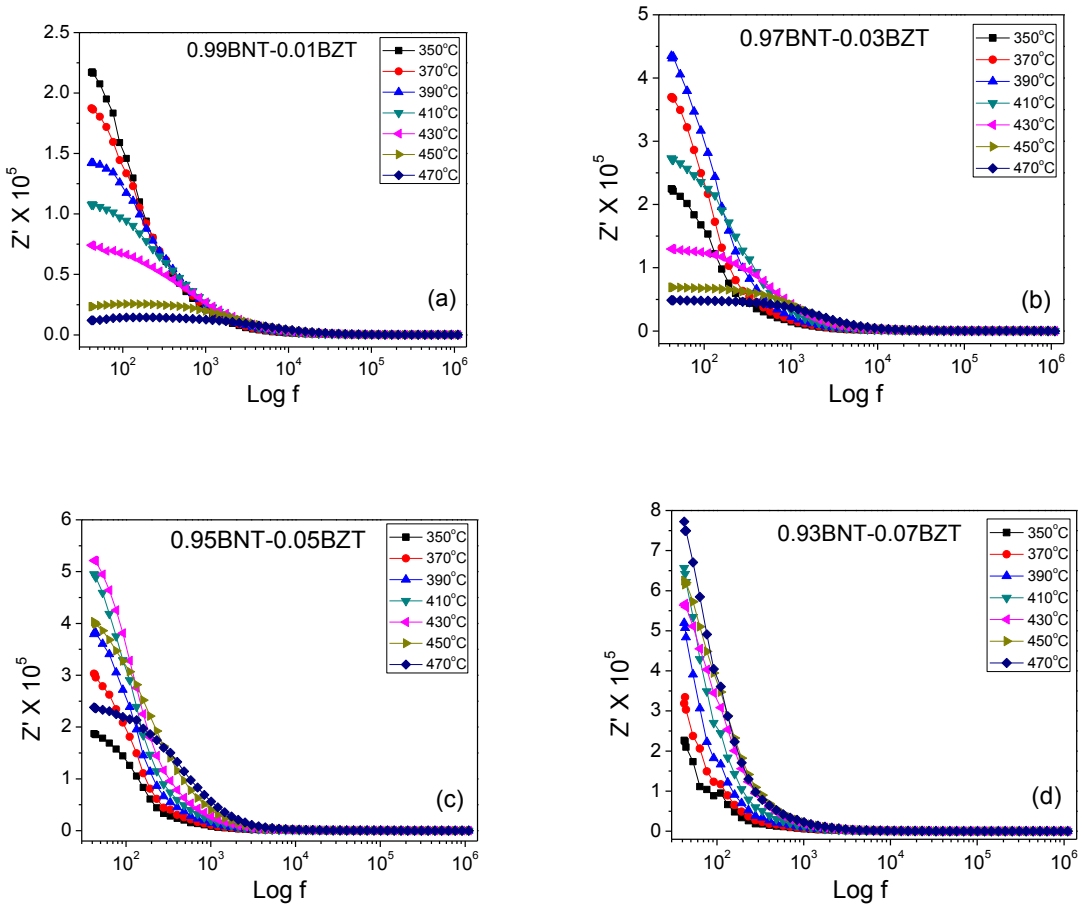

Fig.6.15: Variation of the imaginary part (*Z'*) of impedance with frequency at various temperatures for all the compositions

Fig.6.16 (a-d) shows the variation of Z″ with frequency at different temperatures of (1-*x*)BNT-*x*BZT (for *x* = 0.01, 0.03, 0.05 and 0.07). It is observed that the magnitude of Z'' decreases with increasing temperature as well as frequency, which shows negative temperature coefficient of resistance (NTCR)-type behavior of BNT-BZT. The plots show that Z″ values attain a peak (Z''_{max}) for studied compositions at all the measured temperatures, which shifts to higher frequency with increasing temperature and shifts to lower frequency with increasing BZT content, and also all the curves merge at higher frequencies. The shifting of peaks

towards higher frequency indicates that the relaxation time is decreasing with the increase of temperature [230] and the relaxation time increases with increasing BZT content. The peak broadening with increasing temperature suggests the presence of temperature dependent electrical relaxation phenomenon in the material [231]. The asymmetric broadening of peaks in frequency-explicit plots of Z'' suggests that there is a spread of relaxation times, i.e. the existence of a temperature-dependent electrical relaxation phenomenon in the material [232]. The relaxation process is due to the presence of space charges whose mobility increases at higher temperature [233].

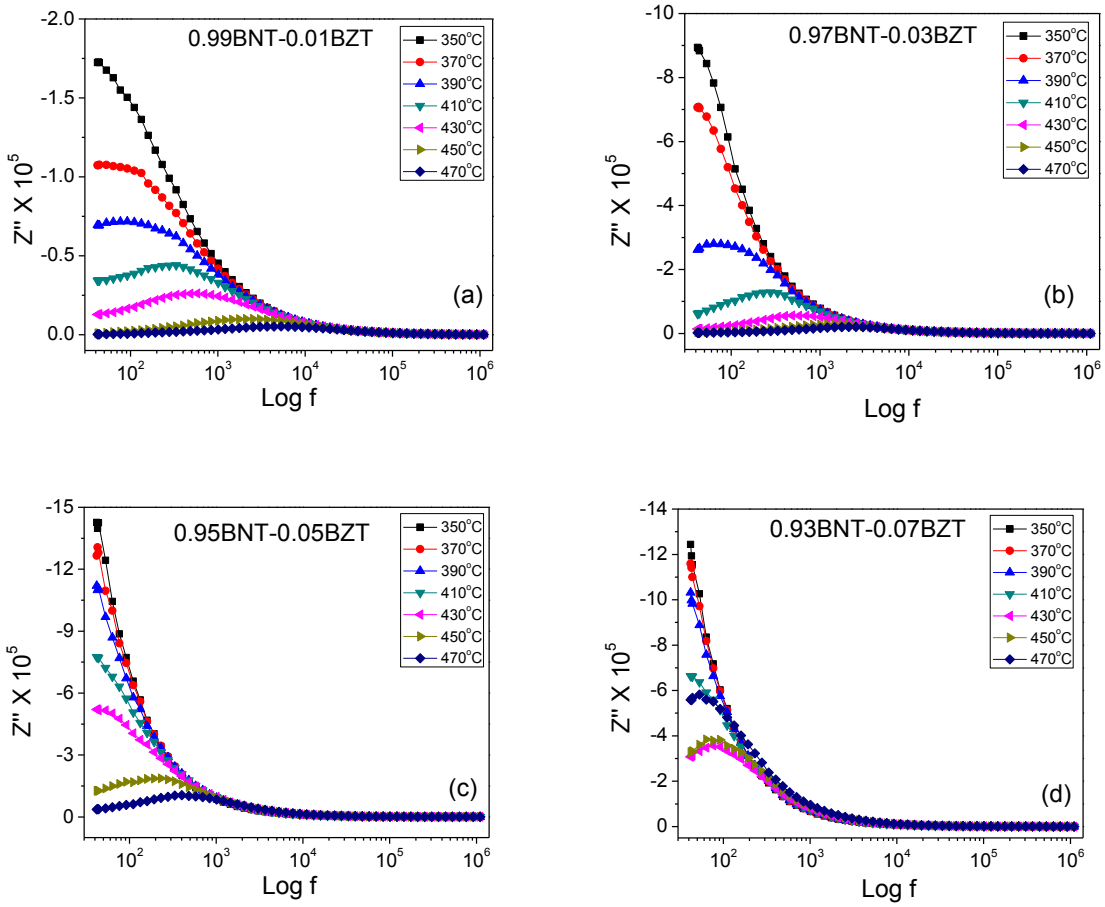

Fig.6.16: (a-d) Variation of imaginary part of impedance (Z″) with frequency at different temperatures for studied sample

Fig.6.17 (a) shows the frequency-dependent imaginary parts of impedance for studied samples at 450°C, which clearly exhibited that the peak (Z''_{max}) shifted to lower frequency with increasing BZT content. The fact that the peak shifted to lower frequency side signifies that the relaxation time increases and inhomogenity develops in the material, thus the grain boundary effect appears. At all temperatures, the compositions x = 0.01, 0.03, 0.05 and 0.07, have given a linear Arrhenius plot (Fig.6.17 (b)) with activation energy 1.06 eV, 1.08 eV, 0.82 eV and 0.76 eV, respectively (Table-6.6).

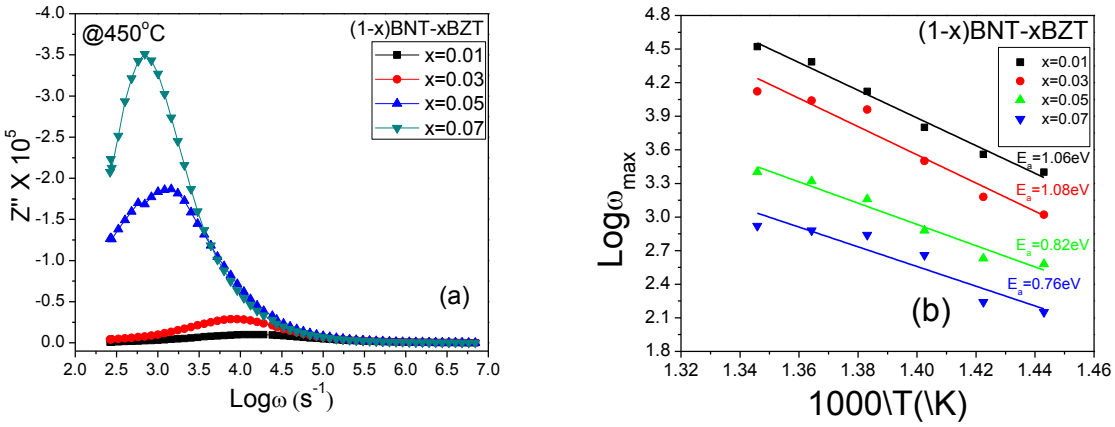

Fig.6.17: (a) Frequency explicit plot of Z" of (1-*x*)BNT-*x*BZT in various compositions at 450°C and (b) Arrhenius plot of logω_{max} from imaginary part of impedance Z"

Fig.6. 18(a-d) shows Cole-Cole plots (a plot drawn between imaginary and real parts of the impedance) at the various temperatures. It is clear that with the increasing of BZT content Cole-Cole plots become stretched and/or split into two discrete semicircles at certain high temperatures, inferring the possible average profile of various Cole-Cole semicircles. The split as well as stretched semicircles may be due to secondary factors like interfacial capacitance or defects. As temperature increases, the graphs turn from a pitch arc to semicircles for all the specimens. Although not all the plots are depressed semicircles, it also can be seen that the centers of the circles do not fall on the real axis, but fall on a straight line below the real axis.

The relaxation time τ is then not single-valued, but is distributed continuously or discretely around a mean value of τ, i.e. τ_m. The angle by which such a semicircular arc is depressed below the real axis is related to the width of the relaxation time distribution. This indicates the non-Debye nature of these samples. These samples follow Maxwell-Wagner relaxations.

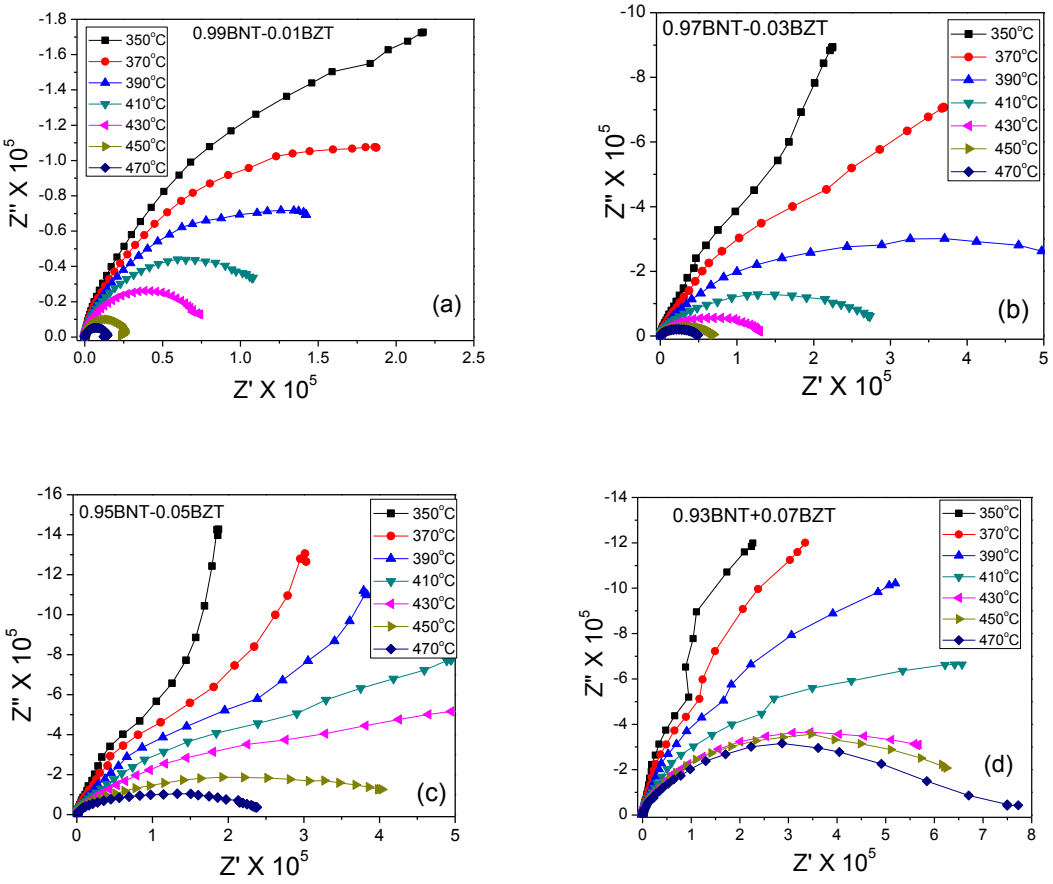

Fig.6.18: (a-d) Cole-Cole (*Z*'-*Z*") plots of (1-*x*)BNT-*x*BZT specimens at different temperature for *x* = 0.01, 0.03, 0.05 and 0.07

Cole-Cole plots for all the samples with increasing temperature show smaller semicircles, i.e. areas under the curves decrease with increasing temperature. The inverse of the frequency, corresponding to the maximum value of the imaginary component of the impedance curves, indicates the relaxation time, and the intercept of the semi-circle in the complex impedance plane on the real axis indicates the true resistance of the material [234]. For *x* = 0.05, two

semicircles could be traced at all the frequencies with different values of resistance for grain (R_g) and grain boundary (R_{gb}). The values of R_g and R_{gb} can directly be obtained from the intercept on the Z'-axis. It can be noticed that the values of R_g as well as R_{gb} decrease with the increase in frequency.

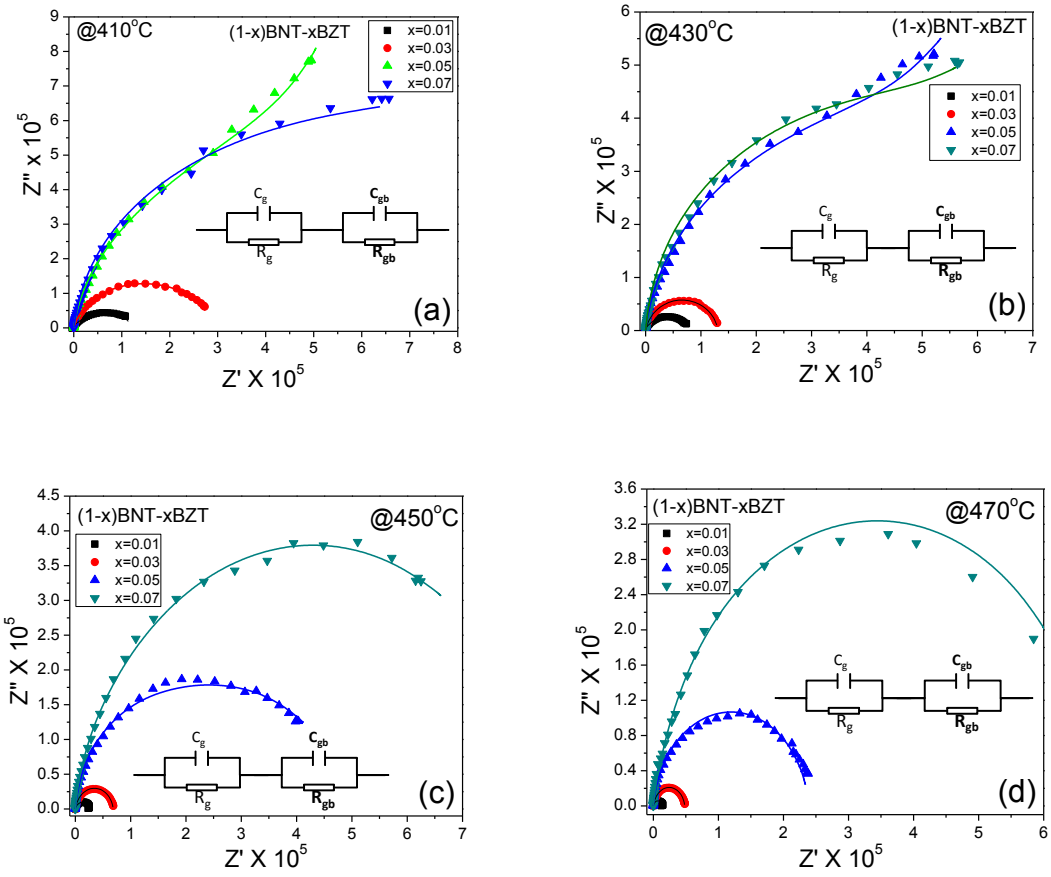

Fig.6.19: (a-d) Cole-Cole (*Z*'-*Z*") plots of (1-*x*)BNT-*x*BZT ceramics at various temperatures of studied samples

Cole-Cole plots (Z'vs. Z'') of (1-*x*)BNT-*x*BZT at different temperatures (410^0C-470^0C) have been shown in Fig.6.19(a-d) for the studied samples. As the BZT content increases, a turn into semi-circles is observed with an increase in size. This trend indicates the enhancement of grain (R_g), grain boundary (R_{gb}) resistance and negative temperatures coefficient of resistance (NTCR) behavior like semi-conducting materials [235-237]. At higher temperatures and for all

the compositions, the Cole-Cole plots are resolved into two overlapping arcs which suggest the contribution of two relaxation mechanisms due to grain and grain boundary. The centre of semi-circles lies below the x-axis at an angle 'ø' indicating non-Debye type relaxation process. The observed data are indicating that the conduction in (1-*x*)BNT-*x*BZT is predominant through grain boundary, and giving a scope for a variety of device applications. The poor separation of this overlapped semicircle is ascribed to the blocker (pore) size. Dessemond [238] described the influence of the blocker size on the interference between the semicircles arising out of the contributions from the bulk and the blockers, in other words on the relative values of their relaxation frequencies. The blockers in the present study are referred to as the pores that exist at the grain boundaries.

Table-6.5: Parameters obtained from Cole-Cole plots of (1-*x*)BNT-*x*BZT at different temperatures

x	Temperature (^{o}C)	C_g (nF)	R_g(MΩ)	C_{gb} (nF)	R_{gb}(MΩ)	σ_g (μS/cm)
0.01	410	4.335	0.09852	2.3	0.01125	1.3
	430	3.963	0.06143	2.146	0.007672	2.12
	450	3.117	0.02178	2.143	0.002971	6.98
	470	3.121	0.01138	1.887	0.002161	13.97
0.03	410	3.051	0.005666	2.068	0.2669	0.566
	430	2.88	0.003010	1.856	0.1219	1.23
	450	2.671	0.002073	1.704	0.06392	2.34
	470	2.453	0.001606	1.552	0.04502	3.33
0.05	410	2.37	0.9882	2.266	1.667	0.118
	430	2.598	0.06162	2.402	0.0541	0.197
	450	2.806	0.000847	1.362	0.3984	0.477
	470	2.47	0.000421	1.181	0.2255	0.864
0.07	410	2.103	1.217	4.176	0.0007159	0.115
	430	1.832	0.9149	3.753	0.000412	0.21
	450	1.983	0.7607	3.65	0.013	0.306
	470	1.887	0.6539	3.148	0.01324	0.434

6.5.2 Modulus Spectroscopy Study

Fig.6.20 (a-d) shows the variation of real part of electrical modulus M' as a function of frequency at various temperatures for all the studied compositions. It is evident that for each temperature, at lower frequencies the real part of impedance M' approaches to zero confirming the presence of an appreciable electrode and/or ionic polarization in the studied samples.

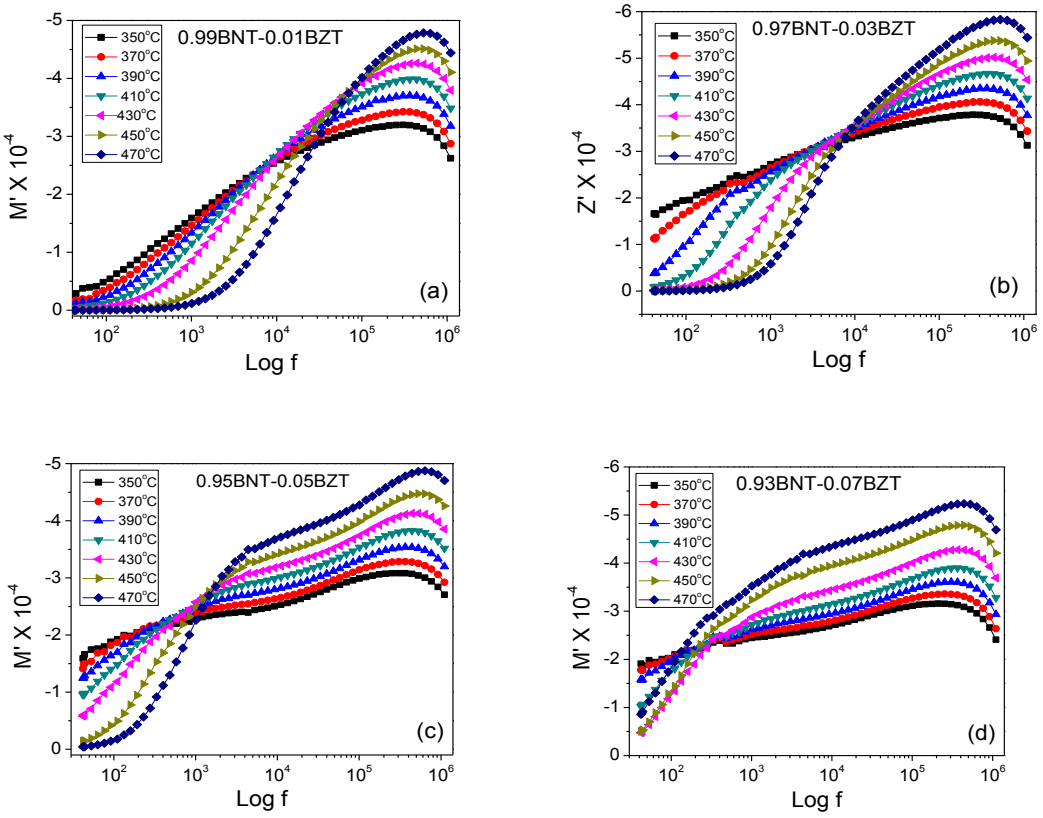

Fig.6.20: (a-d) Variation of peal part of electrical modulus M' as a function of frequency at various temperatures

With increasing the BZT content the grain boundary effects have appeared and have been clearly indicated in the compositions x = 0.05 and 0.07 in Fig.6.20(c, d), by the double relaxations. The low frequency relaxation may be due to grain and high frequency relaxation due to grain-boundary effects. It is evident from the variation of M'' with frequency at various

temperatures, in Fig.6.21 (a-d); that there is a shift in peak frequencies of M'' to higher frequency side as temperature increases. The low frequency side of the peak represents the long-range motion, i.e., ions making successful hopping from one site to neighboring site. The high frequency side of M'' represents the localized motion of the ions confined to their potential wells. The grain-boundary effect appears with increasing the BZT content. Fig.6.21(c, d) clearly shows the double relaxation of two peaks, the first peak due to grain-boundary effect and the second peak due to the effects of grain. The imaginary part of modulus shows a marked change in its shape with rise in BZT concentration, suggesting a change in the value of capacitance of the material with BZT content. The coincidence of all the peaks for a particular composition at different temperatures indicates the temperature-independent dynamic processes [239]. The low frequency side of the M'' peak represents the range of frequencies in which charge carriers can move over a long distance, i.e., charge carriers can perform successful hopping from one site to the neighboring site. The high frequency side of the M'' peak represents the range of frequencies in which the charge carriers are spatially confined to their potential wells and thus could only make localized motion within the well. The region where peak occurs is indicative of the transition from long-range to short-range mobility with increasing frequency [66]. Fig.6.21 (e) shows Arrhenius plot of log ω_{max} from imaginary part of Modulus of BNT-BZT ceramics. The calculated activation energy (E_a) from modulus spectroscopy due to the grain effect is given in Table 6.6. This result revealed that the activation energy increases with increasing of BZT content, but from x = 0.05, suddenly the activation energy decreased due to consequent reduction of lattice parameters. Also, the activation energy due to grain boundary effect is calculated as 0.78 eV and 0.42 eV for the composition x = 0.05 and 0.07, respectively, and inserted in Fig.6.21 (e).

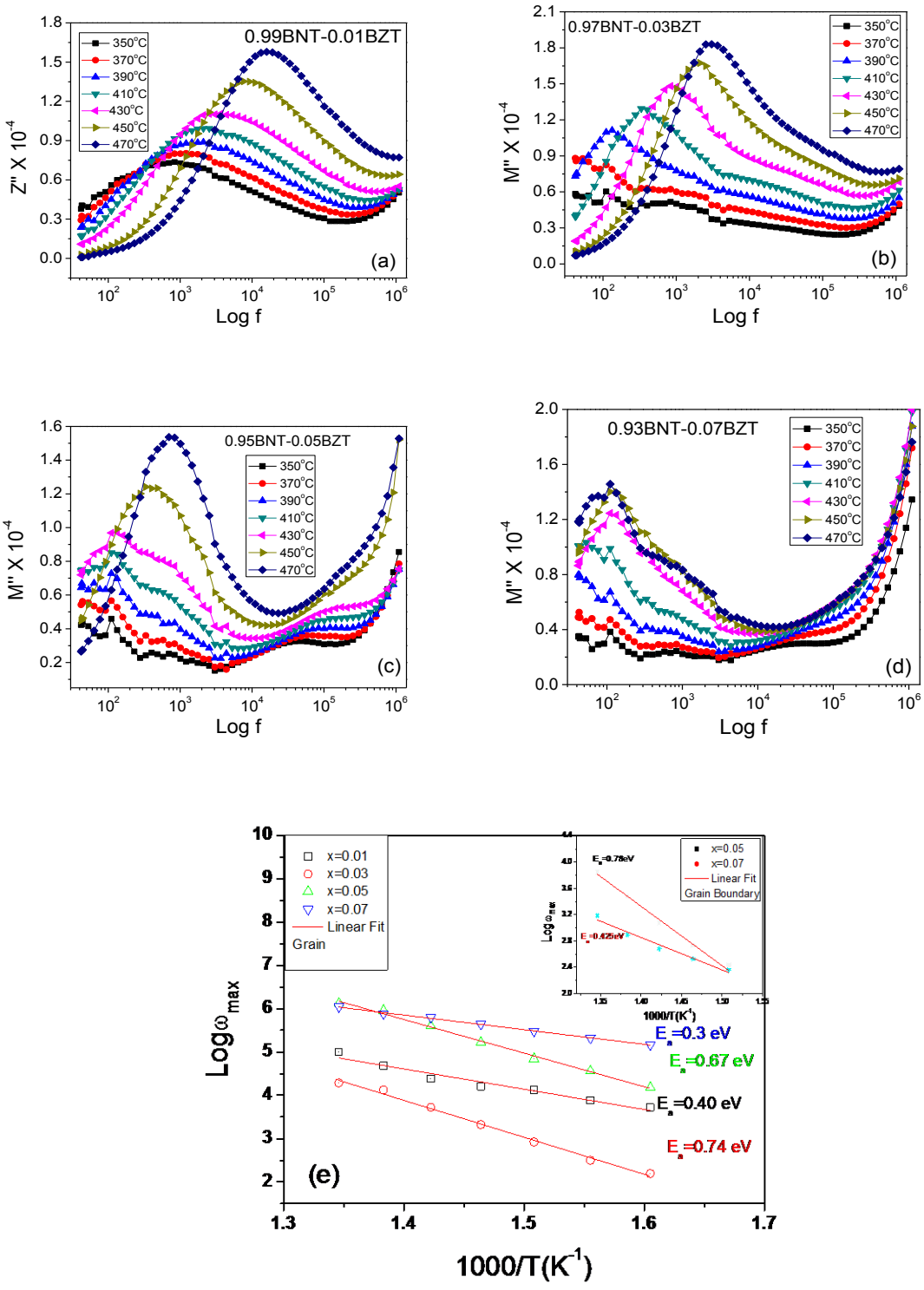

Fig.6.21: Fig.6.20: (a-d) Variation of imaginary part of electrical modulus M'' as a function of frequency at various temperatures. (e) Arrhenius plot of log ω_{max} from imaginary part of Modulus of (1-*x*)BNT-*x*BZT ceramics of studied compositions

6.5.3 AC and DC Conductivity Analysis

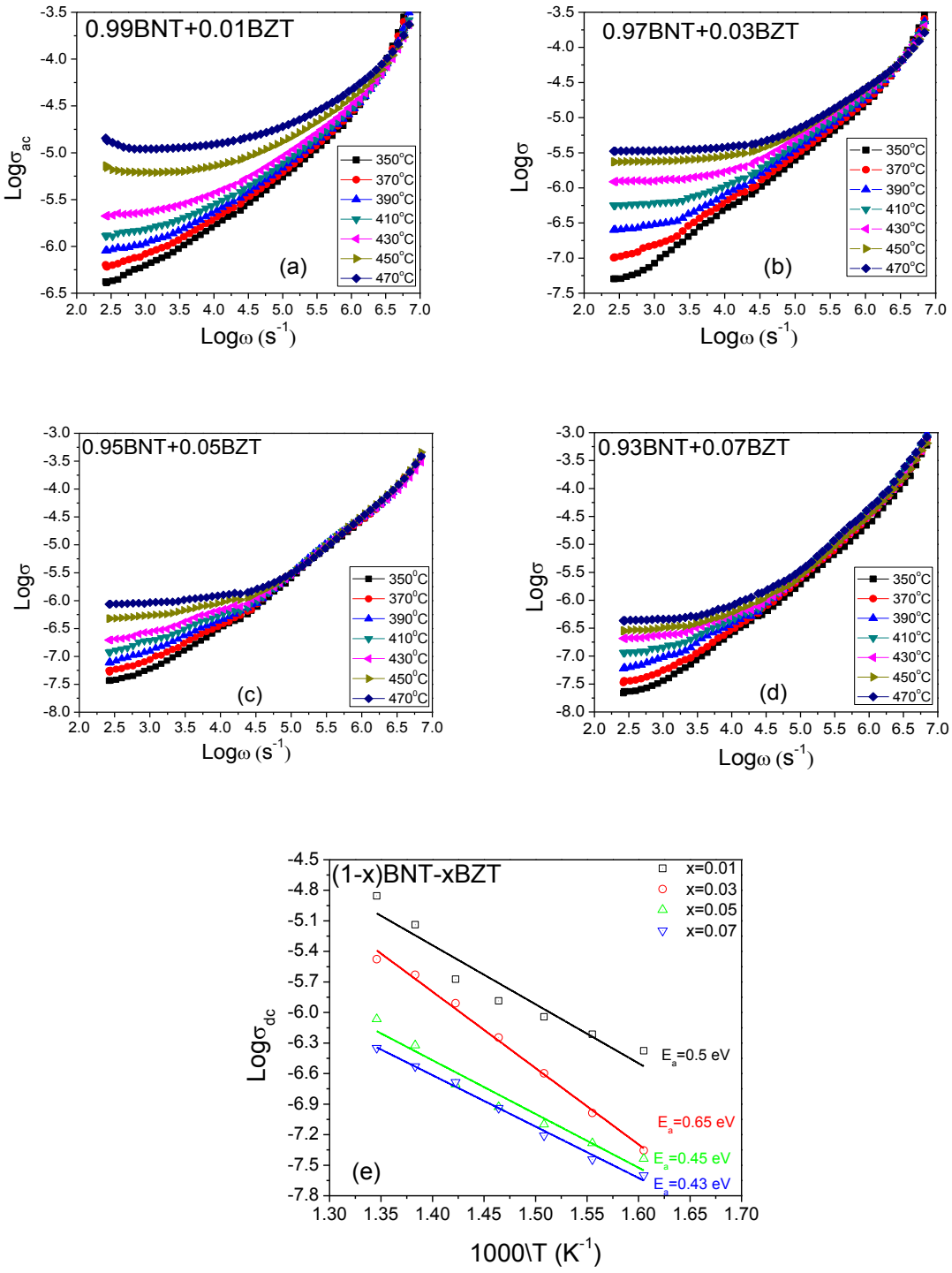

Fig.6.22:(a-d) Frequency-dependence of the real conductivity σ(ω) for (1-*x*)BNT-*x*BZT ceramics at several temperatures.(e) Temperature-dependence of the dc conductivity (Arrhenius plot) for (1-*x*)BNT-*x*BZT ceramics

The log-log plot of electrical conductivity vs. frequency at different temperatures is shown in Fig.6.22 (a-d). The plot shows that conductivity increases with increase of temperature for all the compositions. This indicates that the conduction process is a thermally activated process. Frequency-independent behavior of the conductivity in the low frequency region is observed, but that becomes sensitive in the high frequency region, which is generally known as hopping frequency, and shifted towards higher frequency side with increase of temperature for all the compositions. In the higher frequency region, the conductivity increase is caused due to the hopping of charge carriers in finite clusters. Frequency-independent ac conductivity observed at high temperatures indicates the long-range movement of mobile charge carriers. The conductivity decreases with increasing the BZT content, as shown in Table-6.5.

Table 6.6: Activation energy calculated from impedance, modulus and conductivity of (1-*x*)BNT-*x*BZT ceramics

Composition (*x*)	Activation Energy (E_a) from Z" (eV)	Activation Energy (E_a) from M" (eV)	Activation Energy (E_a) from σ_{dc} (eV)
0.01	1.06	0.47	0.50
0.03	1.08	0.75	0.65
0.05	0.82	0.64	0.45
0.07	0.76	0.42	0.43

The dc conductivity estimated from the bulk response of the material has been observed as a function of temperature as shown in the Fig.6.22 (e). The nature of variation shows the negative temperature coefficient of resistance (NTCR) behavior of BNT-BZT ceramic. The activation energy (E_a) of all the compositions has been calculated from the least-squares fitting of the data in the higher temperature region and given in the Table 6.6. This result revealed that the activation energy increases with increasing of BZT content, but again at x = 0.05,

suddenly the activation energy decreased due to the co-existence of BNT and BZT phases. It is found that the value of activation energy does not show any appreciable change with increasing BZT content. The substitution of Ba^{2+} and Zr^{4+} may alter the long-range polar order with TiO_6 octahedra and this may result in a disturbance in local polarizations in the lattice. The samples contain defects, or impurity-defect complexes, and these would have a corresponding effect on relaxation. At lower temperatures, the complexes do not have orientation effect. The relaxation species may not relax at lower temperatures, as there is a polarization field in the lattice. [77]. It is observed that the activation energies obtained from impedance, modulus and ac conductivity studies in para and ferro regions are typical values for ionic conductors. From lattice dynamic theory the restoring force tends to become zero at ferro-para electric phase transition due to weakening of soft modes. Therefore, it is expected that charge carriers become mobile at phase transition temperature [240]. The low value of activation energy obtained in $x = 0.05$ region might be attributed to the influence of electronic contribution to the conductivity.

6.6 POLARIZATION AND PIEZOELECTRIC STUDY

Fig.6.23 shows P~E loops of (1-*x*)BNT-(*x*)BZT ceramics with a maximum field of 42 kV/cm at room temperature different values of *x*. With the increasing of BZT content the maximum breakdown field increases, accordingly the coercive field (E_c) and remnant polarization (P_r) also increase. The well-behaved hysteresis loops are obtained with the highest remanent polarization value of 12 $\mu C/cm^2$ and corresponding coercive field of about 29 kV/cm at $x = 0.05$. Beyond the BZT content 5% ($x = 0.05$), the coercive field and remanent polarization reduce given in Table 6.7. It suggested that the composition $x = 0.05$ is near the MPB of BNT-BZT solid-solution.

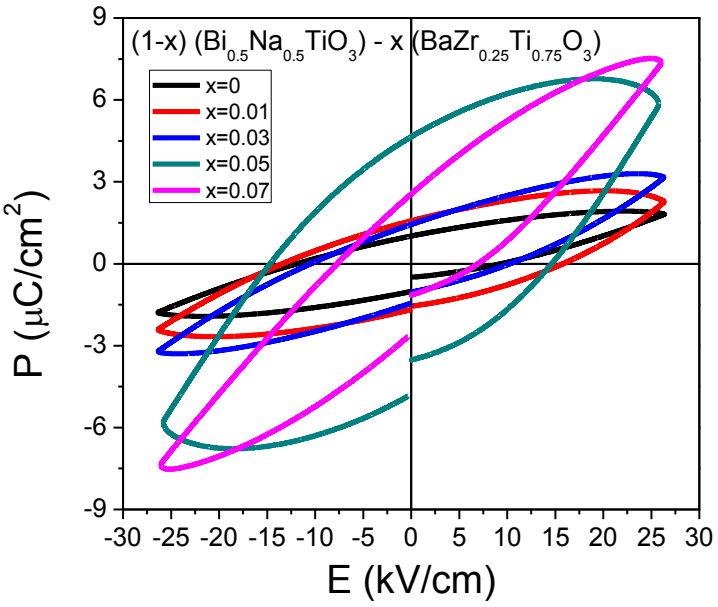

Fig.6.23: The P~E hysteresis loops of (1-*x*)BNT-*x*BZT ceramics at room temperature

Table: 6.7: Ferroelectric and piezoelectric coefficient of (1-*x*)BNT-*x*BZT ceramic

Composition(*x*)	E_c (kV/cm)	P_r (μC/cm^2)	d_{33} (pC/N)
0.00	20	2.55	41
0.01	22.5	4.2	60
0.03	25.2	5.8	87
0.05	29.7	12	131
0.07	12.6	5.7	113

Fig. 6.24 shows the frequency impedance/spectra of the BNT-BZT solid solution at its MPB composition. Fig.6.25 (a) presents the piezoelectric and electromechanical properties of (1-*x*) BNT-*x*BZT ceramics. The piezoelectric constant d_{33} and electromechanical coupling factor k_p display a similar variation, enhancing with the increasing of *x* through a maximum value in a composition near the MPB and then tending to decrease.

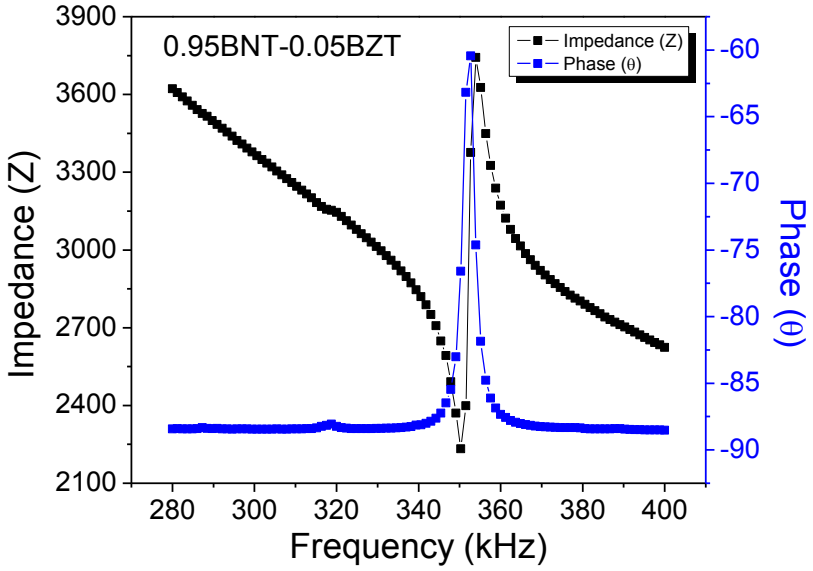

Fig.6.24: The frequency vs. impedance/phase spectrum of 0.95BNT-0.05BZT ceramic (MPB composition)

The piezoelectric constant d_{33} attains a maximum value of 131 pC/N at x = 0.05 and the electromechanical coupling factor k_p reaches to the maximum value of 23 % at x = 0.05. A similar tendency is also observed in BNT-BT solid solution as described in chapter-5. From Fig.6.25 (b), it can be seen that the mechanical quality factor Q_m of the specimens decreases with increasing x, reaches the minimum value at x = 0.05 and then shows a slight increase with more values of x. A tendency of frequency constant N_p of the specimens similar to the Q_m can be seen, which confirms the MPB at x = 0.05. From the above electromechanical properties of the solid solution BNT-BZT systems, it can be concluded that the good piezoelectric and electromechanical properties lie in near MPB composition range similar to other systems. It is attributed to an increase in the number of possible spontaneous polarization direction for the compositions near the MPB due to the coexistence of rhombohedral and cubic phases. This is also explained by having equivalent energy for the coexistence of rhombohedral and cubic

phases can be transformed each other in poling process, which enhance the piezoelectric and electromechanical activities.

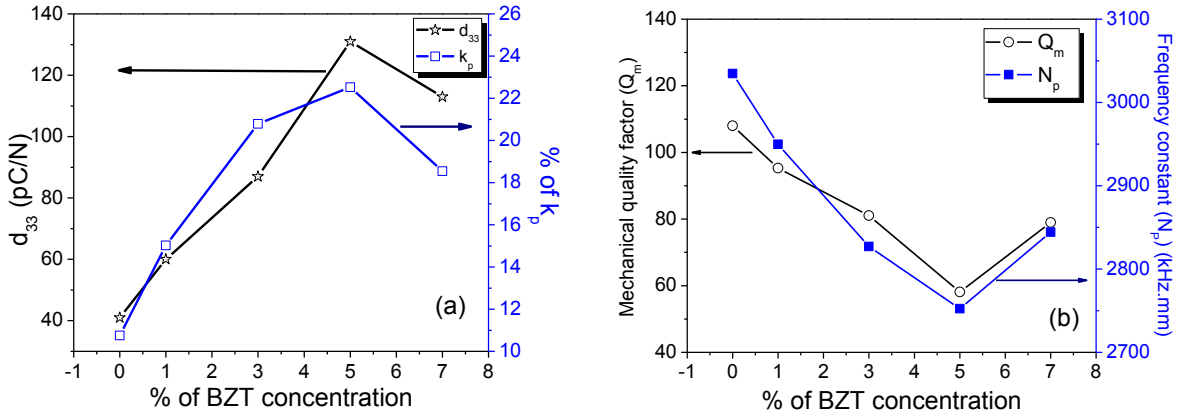

Fig. 6.25: (a) piezoelectric co-efficient (d_{33}) and electromechanical coupling factor (k_p) and (b) Mechanical quality factor (Q_m) and frequency constant (N_p) of BNT-BZT ceramics with % of BZT concentration

Main result of this chapter have been accepted and published in

1. **Ceramic International (Accepted)**
2. **Ferroelectrics Letters, 39 (1-3) (2012) 38-55**

CHAPTER 7

CONCLUSION AND FUTURE DIRECTIONS

7.1 CONCLUSION

The BNT based solutions BNT-ST, BNT-BT and BNT-BZT have been synthesised by solid state reaction route. Their structural, microstructural, optical and electrical characterization has been studied. The major outcomes of the works are discussed as follows:

- The phase formation and structural analysis of solid-solutions prepared by solid-state reaction were carried out by x-ray diffraction and its Reitveld-refinement study. A morphotropic phase boundary (MPB) exists in (1-*x*)BNT-(*x*)BT and (1-*x*)BNT-(*x*)BZT solid-solution at $x = 0.07$ and $x = 0.05$ respectively. The similar kinds of results are also observed in Raman spectroscopy study.
- The temperature-dependent dielectric study shows an increase in dielectric constant and decrease of phase transition temperature in all compositions. The maximum dielectric constant in BNT-ST, BNT-BT, BNT-BZT solid-solutions is 2332, 5312, 3533 and the corresponding transition temperatures are 315^{o}C, 300^{o}C, 310^{o}C at the region $x = 0.09$, 0.07 and 0.05 respectively. The maximum dielectric constant and phase transition temperature in BNT-BT and BNT-BZT occurs near the morphotropic phase boundary. The high dielectric constant and phase transition temperature of around 330^{0}C is comparable with that of commercial PZT ceramics. The dielectric loss decreases with the increase in solid-solution content in high temperature region. The diffusivity of the ceramics increases with higher content of solid-solution implying that

the solid-solution introduces defects and localized strain field. The maximum diffusivity occurs in BNT-BZT solid-solution at $x = 0.05$.

- The impedance spectroscopy study of all compositions shows non-Debye type dielectric relaxation and the relaxation frequency is shifted to higher frequency side with the increase of temperature and lower frequency side with increasing the concentrations. In BNT, BNT-ST and BNT-BT only grain effect is observed indicating the uniform distribution and homogeneity in the specimen under study, whereas in BNT-BZT, grain and grain boundary effect are observed. The activation energy, obtained from the impedance, modulus and conductivity analysis, increases with increasing non BNT compound in the solid-solution. The electrical conductivity studies showed the NTCR character. The optical study shows a slight change in the optical band gap, conformed by UV-Visible spectroscopy, in all the studied solid-solutions.
- The ferroelectric properties of all the compositions were studied at room temperature polarization-electric field (P-E) hysteresis loops at 42 kV/cm. It can be seen that well-saturated hysteresis loops are obtained in all compositions. In BNT-ST solid-solution the coercive field E_c and remnant polarization P_r increases with increase in ST content. While in case BNT-BT and BNT-BZT E_c decreases and P_r increases near the MPB region. The E_c value decreases from 20 kV/cm to 16.8 kV/cm and P_r increase from 2.5 $\mu C/cm^2$ to 16.4 $\mu C/cm^2$ at $x = 0.07$ in BNT-BT where as in BNT-BZT the E_c decreases to 12.6 kV/cm and P_r increases to 12 $\mu C/cm^2$ at $x = 0.05$.
- The piezoelectric properties are found to be degenerated in BNT-ST solid-solutions, while in the solid-solutions of BNT-BT and BNT-BZT the piezoelectric properties are

found to be increase with rise in solid-solution and maximum near the MPB region. The maximum piezoelectric constant in BNT-BT and BNT-BZT is found 134 pC/N at x = 0.07 and 131 pC/N at x =0.05 respectively. The electromechanical properties also increase with rise in solid-solution in BNT-BT and BNT-BZT. In BNT-BT the maximum k_p = 22% and minimum Q_m = 41 occurs at x = 0.07, whereas in BNT-BZT the maximum k_p = 23% and minimum Q_m = 58 occurs at x = 0.05.

It is reported in the literature that the maximum piezoelectric constant is 147 pC/N which occurred in 0.91BNT-0.09Ba($Ti_{0.942}Zr_{0.058}$)O_3 composition [105]. The piezoelectric constant observed by us is 134 pC/N which is close to the maximum value reported in literature. The maximum k_p as reported in the literature is 0.314 which occurred in 0.84BNT-0.16($Bi_{0.5}K_{0.5}$)TiO_3 composition [99]. The highest k_p value observed in our solid-solution is 0.23 which is comparable to other repots available in literature given in Table 1.1. All the above results indicate that the solid-solutions (BNT-ST, BNT-BT, and BNT-BZT) improve the properties of BNT. In BNT-ST solid-solution the dielectric properties increases abrobtly with increase in solid solution which can be used as a capacitors and other storage deivices. In BNT-BT and BNT-BZT solid solution the dielectric, ferroelectric and piezoelectric properties enhance which might be a promising lead-free piezoelectric material for various kinds of actuators and transducers. The most improved dielectric, ferroelectric and piezoelectric properties occur near the MPB region in BNT-BT and BNT-BZT solid-solution. Among all the composition BNT-BZT at x = 0.05 shows the best ferroelectric and piezoelectric properties which makes the material suitable for industrial applications.

7.2 FUTURE DIRECTIONS

The present research work examined three different solid-solutions, namely, (1-*x*)$(Bi_{0.5}Na_{0.5})TiO_3$-*x*$SrTiO_3$, (1-*x*)$(Bi_{0.5}Na_{0.5})TiO_3$-*x*$BaTiO_3$, and (1-*x*)$(Bi_{0.5}Na_{0.5})TiO_3$-*x*$Ba(Zr_{0.25}Ti_{0.75})O_3$, with limited concentration (*x* = 0-0.08) of non BNT compounds. The result shows greater improvement in structural, electrical and optical properties. The number of possible combinations for BNT-based compositions is virtually endless, and the time required to synthesize and characterize them all is impractical. So the thesis is limited to only three series of different solid-solutions. However, the future directions are fast expanding.

It is worthwhile to examine some high concentrations of non BNT compounds. This will definitely provide more insights in the nature of modification of parent compound BNT with different solid-solutions of non BNT compounds. Some more non BNT solid-solutions may be doped to investigate the improvement of similar properties. The ionic-radii-based tolerance factor with different non BNT solid-solution at and above the critical state may provide some more interesting results in the present study. Further, the neutron diffraction experiments may be performed to relate the bond-valence-based tolerance factor and lattice parameter for description of structural modification and comparison with theoretical value. The present work is limited to single non BNT compound solid-solutions; however, the work in future can be extended to multi-component non BNT solid-solutions with BNT for fabrication of multilayer capacitor (MLC) in electronic applications.

Besides experimental studies, equally important is the theoretical description of diffuse phase transition and its correlation with the experimental result. Application of piezoelectric stress tensor to electro-mechanical and electro- optic effect provides another room for expansion of the experimental work to theoretical domain.

REFERENCES

1 Rainer Waser, editeur. "*Nanoelectronics and information technology*", Wiley-VCH, Verlag GmbH and Co. KGaA, Weinheim, (2003).

2 Charles Kittel. Úvod do fyzikypevnýchlátek. Academia,nakl. CSAV, Praha, 1st edition, (1985). orig.: *Introduction to Solid State Physics* (John Wiley and Sons, Inc.), 5th ed.

3 A.J.Moulson and J.M.Herbert, *Electroceramics*. 2nd Ed., John Wiley and Sons, Inc., New York, (2003)

4 Muller, O. and Roy, R., *The Major Ternary Structural Families. Springer,* New York, (1974).

5 D. Jones, S. Prasad, and J. Wallace., *Adv. Ceram. Mater.*, 122-124 (1996) 71.

6 A. Safari, R. Panda and V. Janas., *Key. Eng. Mater.*, 122-124 (1996) 35-70.

7 http://www.bostonpiezooptics.com/files/Intro_to_Piezo.pdf

8 B. Jaffe, W. R. Cook, and H. Jaffe. "Piezoelectric Ceramics", Academic Press Limited, New York, NY (1971).

9 T. Ikeda. "*Fundamentals of Piezoelectricity*", Oxford University Press, Oxford, UK, (1990).

10 J. Valasek., *Phys. Rev.*, 17 (1921) 475.

11 W. Kanzig. "*Ferroelectrics and Anti-ferroelectrics"*, Academic Press, New York, (1957).

12 J. C. Burfoot. "*Ferroelectrics",* Van Nostrand, New York (1967).

13 M.E. Lines, A.M.Glass. "*Principles and Applications of Ferroelectrics and Related Materials",* Clarendon Press, Oxford (1977).

14 F. Jona, G. Shirane. "*Ferroelectric Crystals",* Pergamon Press, Oxford (1962).

15 M. A. Torghabeh, (Thesis) "*Development of lead-free piezoelectric thin films by pulsed laser deposition "* New Brunswick, New Jersey, May, (2010)

16 M. E. Lines, A. M. Glass. "*Principles and Applications of Ferroelectrics and Related Materials",* Oxford: Clarendon, (1979).

17 D. Damjanovic, *Rep. Prog. Phys.*, 61 (1998) 1267.

18 M. J. Haun, E. Furman, S. J. Jang, H. A. McKinstry, L. E. Cross, *J. Appl. Phys.* 62 (1987) 3331.

19 D.R. Askeland, *The Science and Engineering of Materials*, third edition, Chapman & Hall, London, UK. (1996).

20 S. Stemmer, S. K. Streiffer, F. Ernst, M. Ruhle, *Phil. Mag. A*, 71 (1995) 713.

21 R. E. Newnham."*Structure-Property Relations",* Berlin: Springer (1975).

22 A. J. Burggraaf, Proc. 9th Int. *Cong.on Sci. of Ceramics*, Noordwijkerhout, Netherland (1977).

23 C.G.F Stenger, A.J.Burggraaf, *J. Phys. Chem. Solids*, 41 (1980) 25.

24 W. Kanzig, *Helv. Phys. Acta*, 24 (1951) 175.

25 J. Fritesberg, Proc. 4th Int. *Meeting on Ferroelectricity*, Leningrad (1977).

26 A.G. Smolensky, *J. Phys. Soc. Japan* 18 (1970) 26.

27 B.N Rolov, *Soviet Phys. Solid state*, 6 (1965) 1676.

28 A.G. Smolensky, *J. Ferroelectricity*, 53 (1984) 129.

29 V.S. Tiwari and D. Pandey, *J. Am. Ceram. Soc. II*, 77 (1994) 1819.

30 V.V. Kirollov and V.A. Isupov, *Ferroelectrics*, 5 (1973) 3.

31 L. E. Cross, *Ferroelectrics*, 76 (1987) 241.

32 Y. Xu. "*Ferroelectric Materials and Their Applications*", North-Holland *Elsevier Sci. Publ.*, Amsterdam (1991).

33 T. Shrout and S. Swartz, *Processing of ferroelectric and related materials: a review*, in Proceedings of the Eighth IEEE International Symposium on Applications of Ferroelectrics, ISAF, (1992).

34 G. Smolenskii, V. Isupov, A. Agranovskaya and N. Krainik., *Soviet Phys. Solid state*, 2 (11) (1961) 2651.

35 A. S. Bhalla, R. Guo, R. Roy, *Mater. Res. Innovations, 4* (2000) 326.

36 L.E. Cross, S. J. Jang and R. E. Newnham, *Ferroelectrics*, 23 (1980) 187.

37 S. Nomura, and K. Uchino, *Ferroelectrics*, 50 (1983) 197.

38 K.Uchino, "*Ferroelectric Devices"*. Marcel Dekker, Inc., New York, (2000).

39 Jean-Richard Gomah-Pettry, Senda Saıd, Pascal Marchet, Jean-Pierre Mercurio,*J. Eur. Ceram. Soc.*, 24 (2004) 1165.

40 J.Suchanicz, W.S.Ptak, *Ferroelectrics Lett. Sect., 12* (**1990**) 71.

41 J.Suchanicz, A.Jezowski, R.Poprawski, *Phys. Status Solidi A-Appl. Res. 169 (***1998)** 209.

42 C.S.Tu, I.G.Siny, V.H.Schmidt, *Phys. Rev. B 49 (***1994)** 11550.

43 V. A. Isuprov and A. F. Ioffe, *Ferroelectrics*, 315 (2005) 123.

44 J. East and D. C. Sinclair, *J. Mater. Sci. Lett.*, 16 (1997) 422.

45 J. Kreisel, A. M. Glazer, P. Bouvier and G. Lucazeau, *Phys. Rev. B.*, 63 (2001) 174106.

46 B.V. BahugunaSaradhi, K. Srinivas, G. Prasad, S. V. Surynarayan and T. Bhimasankaram, *Mater. Sci. Eng. B*, 98 (2003) 10.

47 V. H. Schmidt, C. S. Tu and I. G. Siny, DOI: 10.1109/**ISAF** (1994) 522294.

48 J. Suchanicz, *Ferroelectric*, 190 (1997) 77.

49 J. Suchanicz, *Ferroectrics*, 209 (1998) 561.

50 Y. Watanabe, Y. Hiruma, H. Nagata and T. Takenaka, *Ceram. Int.*, 34 (2008) 761.

51 J. K. Lee, K. S. Hong, C. K. Kim and S. E. Park, *J. Appl. Phys.*, 91 (2002) 4538.

52 S. E. Park and K. S. Hong, *J. Mater. Res.*, 12 (1997) 2152.

53 V. Dorcet, G. Trolliardand P. Boullay, *J. Magn. Magn. Mater.*, 321 (2009) 1758.

54 P. A. Thomas, S. Trujillo, M. Boudard, S. Gorfman and J. Kreisel, *Solid State Sci.*, 12 (2010) 311.

55 R. Ranjan and A. Dviwedi, *Solid State Commun.*, 135 (2005) 394

56 Y. Lin, C. W. Nan, J. Wang, G. Liu, J. Wu and N. Cai, *J. Am. Ceram. Soc.*, 87 (2004) 742.

57 J. S. Kim, B. C. Choi, J. H. Jeong, K. S. Lee and S. B. Cho, *Ferroelectrics*, 384 (2009) 120.

58 C. Zhou, X. Liu, W. Li and C. Yuan, *Mater. Res. Bull.*, 44 (2009) 724.

59 J. Y. Yi, J. K. Lee and K. S. Hong, *J. Am. Ceram. Soc.*, 85 (2002) 3004.

60 B.K. Barick, R.N.P. Choudhary, Dillip K. Pradhan,*Mater. Chem. Phys*., 132 (2012) 1007

61 X. X. Wang, K. W. Kwok, X. G. Tang, H. L. W. Chan and C. L. Choy, *Solid State Commun.*, 129 (2004) 319.

62 M. Raghavender, G. S. Kumar and G. Prasad, *Pramana-J. Phys.*, 72 (2009) 999.

63 M. Raghavender, G. S. Kumar and G. Prasad, *J. Phys. Chem. Solids.*, 67 (2006) 1803.

64 K. Kumari and K. Prasad, *Braz. J. Phys.*, 39 (2009) 297.

65 P. Jaiban, A. Rachakom, S. Jiansirisomboon and A. Watcharapasorn, Nanoscale Res. Lett., 7 (2012) 45.

66 Lily, K Kumari, K Prasada and R. N. P. Choudhary, *Indian J. Eng. Mater. Sci.*, 15 (2008) 147.

67 A. Watcharapasorn, S. Jiansirisomboon and T. Tunkasiri, *Chiang Mai J. Sci.*, 33 (2006) 169.

68 M. Davies, E. Aksel and J. L. Jones, *J. Am. Ceram. Soc.*, 94 (2011) 1314.

69 H. Liu, W. Ge, X. Jiang, X. Zhao and H. Luo, *Mater. Lett.*, 62 (2008) 2721.

70 H. Nagata and T. Takenaka, *J. Eur. Ceram. Soc.*, 21 (2001) 1299.

71 K. Prasad, K. Kumari, Lily, K. P. Chandra, K. L. Yadav, and S. Sen, *Solid State Commun*, 144 (2007) 42.

72 C. R. Zhou and X. Y. Liu, *J. Alloys Compd.*, 466 (2008) 563.

73 Z. C. Rong, L. X. Yu, L. W. Zhou and Y. C. Lai. *Bull. Mater. Sci.*, 32 (2009) 99.

74 S. Senda and J. P. Mercurio, *J. Eur. Ceram. Soc.*, 21 (2001) 1333.

75 S. Zhao, G. Li, A. Ding, T. Wang and Q. Yin. *J. Phys. D. Appl. Phys.*, 39 (2006) 2277.

76 C. F. Buhrer, *J. Chem. Phys.*, 36 (1962) 798.

77 Y. M. Li, R. H. Liao, X. P. Jiang and Y. P. Zhang, *J. Alloys Compd.*,484 (2009) 961.

78 Y. Hiruma, K. Yoshii, H. Nagata and T. Takenaka, *J. Appl. Phys.*, 103 (2008) 084121.

79 J. Kun Lee, Yi, Jae Yun, Hong and Kug Sun, *J. Solid State Chem.*, 177 (2004) 2850.

80 Y. Hiruma, H. Nagata and T. Takenaka, *J. Appl. Phys.*, 104 (2008) 124106.

81 H. Yu and Z. Ye, *Appl. Phys. Lett.*, 93 (2008) 112902.

82 E. Boucher, P. Marchet and J. P. Mercurio, *J. de Phys. IV: J.Phys*, 128 (2005) 3.

83 R. Selvamani, G. Singh, V. Sathe, V. S. Tiwari and P. K. Gupta, *J. Phys. Condens. Matter.*, 23 (2011) 055901.

84 C. R. Zhou and X. Y. Liu, *Bull. Mater. Sci.*, 30 (2007) 575.

85 Y. Li, W. Chen, Q. Xu and J. Zhou, *J. Mater. Sci.*, 40 (2005) 3625.

86 H. Y. Tian, D. Y. Wang, D. M. Lin, J. T. Zeng, K. W. Kwok and H. L. W. Chan, *Solid State Commun.*, 142 (2007) 10.

87 K. Sakata and Y. Masuda, *Ferroelectrics*, 7 (1974) 347.

88 D. Rout, K. S. Moon, S. J. L. Kang and I. W. Kim, *J. Appl. Phys.*, 108 (2010) 084102.

89 B. J. Chu, D. R. Chen, G. R. Li and Q. R. Yin. *J. Eur. Ceram. Soc.*, 22 (2002) 2115.

90 B. H. Kim, S. J. Han, J. H. Kim, J. H. Lee B. K. Ahn and Q. Xu, *Ceram. Int.*, 33 (2007) 447.

91 Z. Chen and J. Hu, *Ceram. Int.*, 35 (2009) 111.

92 P. Setasuwon and S. Kijamnajsuk, *Sci. Technol. Adv. Mater.*, 7 (2006) 780.

93 M. Zhu, H. Hu, N. Lei, Y. Hou and H. Yan, *Appl. Phys. Lett.*, 94 (2009) 182901.

94 Y. Li, W. Chen, Q. Xu, J. Zhou and X. Gu, *Mater. Lett.*, 59 (2005) 1361.

95 M. Dunce, E. Birks, M. Antonova, M. Kundzinsh and A. Sternberg, *Integr. Ferroelectr.*, 108 (2009) 125.

96 Z. Yang, Y. Hou, B. Liu and L. Wei, *Ceram. Int.*, 35 (2009) 1423.

97 C. R. Zhou, X. Y. Liu, W. Z. Li and C. L. Yuan, *Solid State Commun.*, 149 (2009) 481.

98 Y. Wu, H. Zhang, Y. Zhang, J. Ma and D. Xie, *J. Mater. Sci.*, 38 (2003) 987.

99 A.Sasaki, T.Chiba, Y.Mamiya, E.Otsuki, *Jpn. J. Appl. Phys.*, 38 *(1999)* 5564.

100 Y.R.Zhang, J.F.Li, B.P.Zhang, *J. Amer. Ceram. Soc.*, *91* (2008) 2716.

101 A.B.Kounga, S.T.Zhang, W.Jo, T.Granzow, J.Rodel, *Appl. Phys. Lett.92 (2008)* 222902.

102 J. Suchanicz, J. Kusz, H. Bohm and G. Stopa, *J. Mater. Sci.*, 42 (2007) 7827.

103 R.Z.Zuo, X.S.Fang, C.Ye, *Appl. Phys. Lett. 90 (2007)* 092904.

104 T. Takenaka, K. Maruyama and K. Sakata, *Jpn. J. Appl. Phys.*, 30 (1991) 2236.

105 C. Peng, J. F. Li and W. Gong, *Mater. Lett.*, 59 (2005) 1576.

106 Z. W. Chen, A. Z. Sui, Z. Y. Lu and P. A. Liu, *J. Ceram. Soc. Jpn.*, 114 (2006) 857.

107 Y. Li, W. Chenb, Q. Xub, J. Zhoub, X. Gua and S. Fanga. *Mater. Chem. Phys.*, 94 (2005) 328.

108 J. Shieh, K. C. Wu and C. S. Chen, *Acta Mater.*, 55 (2007) 3081.

109 C. Zhou, X. Liu, W. Li and C. Yuan. *Mater. Chem. Phys.*, 114 (2009) 832.

110 S.Mahboob, G.Prasad, G.S.Kumar, *J Mater Sci*, 42 (2007) 10275.

111 Y.M.Li, W.Chen, Q.Xu, J.Zhou, H.J.Sun, R.Xu, *Mater Sci Eng B*, 112 (2004) 5.

112 T.Takenaka, H.Nagata, *J Eur Ceram Soc.*, 25 (2005) 2693.

113 J.Yoo , D.Oh, Y.Jeong, J.Hong, M.Jung, *Mater Lett.*, 58 (2004) 3831.

114 W.Zuo,R. Zuon, W.Zhao, *Ceramics International*, 39 (2013) 725.

115 F.Guo, B.Yang,S.Zhang,X.Liu, L.Zheng, Z.Wang, Fe.Wu, D.Wang, and W.Cao, *J. Appl. Phys.*, 111 (2012)124113.

116 K.Sakata, T.Takenaka, and Y.Naitou, *Ferroelectrics*, 131 (1992) 219-226**.**

117 Y.Li, W.Chen, Q.Xu, J.Zhou, and X.Gu, *Mater. Lett.*,**59** (2004) 1361-1364.

118 T. Takenaka, K. Sakata, and K. Toda, *Ferroelectrics*, 106 (1990) 375.

119 T. Takenaka and H. Nagata, *J. Eur. Ceram. Soc*., 25 (2005) 2693.

120 H. Nagata, N. Koizumi, and T. Takenaka, *Key. Eng. Mater*., 37(1999) 169.

121 A. Sasaki, T. Chiba, Y. Mamiya, and E. Otsuki, *Jpn. J. Appl. Phys*., 38 (1999) 5564.

122 X. X. Wang, S. H. Choy, X. G. Tang, and H. L. W. Chan, *J. Appl. Phys*., 97 (2005) 104101.

123 S. Fuentes, R.A. Zarate, E. Chavez, P. Muñoz, D. Díaz-Droguett, P. Leyton, *J. Mater. Sci.*, 45 (2010) 1448.

124 W. Jauch, A. Palmer, *Phys. Rev. B*, 60 (1999) 2961.

125 P.K. Petrov, E.F. Carlsson, P. Larsson, M. Friesel, Z.G. Ivanov, *J. Appl. Phys*., 84 (1998) 3134.

126 O. Saburi, *j. Phys. Soc. Japan*, 14 (1959) 1159.

127 G.G. Harman, *Phys. Rev.*, 106 (1957) 1358.

128 W.J. Merz, *Phys. Rev*., 76 (1949) 1221.

129 F. Jona, G. Shirane, "Ferroelectric Crystals*"*, *Elsevier, Amsterdam*, (1963).

130 B.J.Chu, D.R.Chen, G.R.Li and Q.R.Yin, *J. Eur. Ceram. Soc*., 22 (2002) 2115.

131 K.Pengpat, S.Hanphimol, S.Eitssayeam, U.Intatha, G.Rujijanagul and T.Tunkasiri, *J. Electroceram*, 16, (2006) 301.

132 T.Takenaka, K.Maruyama, K.Sakata, *J. Appl. Phys.*,30 (1991) 2236.

133 Y.Hosono, K.Harada and Y.Yamashita, *Jpn. J. Appl. Phys.*, 40 (2001) 5722.

134 Y.Zhi, A.Chen, R.Guo and A.S.Bhalla, *Appl. Phys. Lett.*, 81 (2002) 1285.

135 T.Tsurumi, Y.Yamamoto, H.Kakemoto and S.Wada,*J. Mater. Res.*,17 (2002) 755.

136 J.Ravez, C.Broustera and A.Simon, *J. Mater. Chem.*, 9 (1999)1609.

137 Z.Yu, R.Guo, and A.S.Bhalla, *Appl. Phys. Lett.*77 (2000) 1535.

138 T. Badapanda, S.K. Rout, L.S. Cavalcante, J.C. Sczancoski, S. Panigrahi, E. Longo, M.S. Li, J. Phys. D: Appl. Phys. 42 (2009) 175414.

139 H.M.Rietveld, J. Appl. Crystallogr., 2 (1969) 65.

140 A.C.Larson, R.B.VonDreele, "*Generalized structure analysis system (GSAS)"*, Los Alamos National Laboratory Report, USA, LAUR (2000) 86.

141 L.W.Finger, D.E.Cox, A.P.Jephcoat, *J. Appl. Crystallogr.*, 27 (1994) 892.

142 P.W.Stephens, *J. Appl. Crystallogr*. 32 (1999) 281.

143 D. Lin, D. Xizo, J. Zhu, P. Yu,H. Yan, L. Li, and W. Zhang, *Cryst. Res. Technol.*, 39 (1) (2004) 30.

144 H.d.Li, C.d. Feng, W.l. Yao, *Mater. Lett.*, 58 (7) (2004) 1194.

145 X. Wang, S. Or, X. Tang, H. Chan, P. Choy and P. Liu, *Solid State Commun.*,134 (10) (2005b) 659.

146 D. Xiao, D. Lin, J. Zhu and P. Yu, *J. Electrochemistry*, 16 (4) (2006) 271.

147 M. Matsubara, T. Yamaguchi, W. Sakamoto, K. Kikuta, T. Yogo, S. Hirano, *J. Am. Ceram. Soc.* 88, 1190 (2005) 1196.

148 JCPDS powder diffraction file card No. 36-0340.

149 http://www.ing.unitn.it/~maud/

150 M. Ferrari, L. Lutterotti, *J. Appl. Phys*. 76 (1994) 7246.

151 H.M. Rietveld, *Acta Cryst.*,2 (1967) 65.

152 L. Lutterotti, M. Bortolotti, G. Ischia, I. Lonardelli, H.R. Wenk, *Z. Kristallogr. Suppl.*, 26 (2007) 125.

153 H.R. Wenk, L. Lutterotti, S.C. Vogel, *Powder Diffract*., 25 (2010) 283.

154 I. Lonardelli, H.-R. Wenk, L. Lutterotti, M. Goodwin. *J. Synchrotr. Rad*., 12 (2005) 354.

155 A.Z. Simões, L.S. Cavalcante, F. Moura, E. Longo, J.A. Varela, *J. Alloys Compd*., 509 (2011) 5326.

156 http://www.crystalimpact.com/diamond/

157 J. Petzelt, S. Kamba, J. Fábry, D. Noujni, V. Porokhonskyy, A. Pashkin, I. Franke, K. Roleder, J. Suchanicz, R. Klein, G.E. Kugel, *J. Phys. Condens. Matter*., 16 (2004) 2719.

158 http://en.wikipedia.org/wiki/Octahedron

159 M.D. Domenico Jr., S.H. Wemple, S.P.S. Porto P.R. Buman, *Phys. Rev*., 174 (1968) 522.

160 P.S. Dobal, A. Dixit, R.S. Katiyar, Z. Yu, R. Guo, A.S. Bhalla, *J. Appl. Phys.*, 89 (2001) 8085.

161 T. Badapanda, S.K. Rout, L.S. Cavalcante, J.C. Sczancoski, S. Panigrahi, E. Longo, M.S. Li, *J. Phys. D. Appl. Phys*., 42 (2009) 175414.

162 P.Zhao, B.P. Zhang, J.F. Li, *Appl. Phys. Lett*., 90 (2007) 242909.

163 Y.Zhen, J.F. Li, *J. Am. Ceram. Soc*., 89 (2006) 3669.

164 D.L.Wood, J. Tauc, Phys. Rev. B, 5 (1972) 3144.

165 T.Kimura, T. Takahashi, T. Tani, Y. Saito, *Ceram. Int.,* 30 (2004) 1161.

166 K.Uchino, S. Nomura, *Ferroelectrics*, 44 (1982) 55.

167 A. Kumar, N.M. Kumari, R.S. Katiyar, *J. Alloys Compd*., 469 (1-2) (2009) 433.

168 Y. Hosono, K.Harada, Y.Yamashita, *Jpn.J.Appl.Phys*., 40 (2001) 5722.

169 J.R. Macdonald (Ed.), "*Impedance Spectroscopy: Emphasizing Solid Materials and Systems*", Wiley, New York, (1987).

170 K.S. Cole, R.H. Cole, *J. Chem. Phys.*, 9 (1941) 341.

171 J. Zhu, X.B. Chen, J.H. He, J.C. Shen, *Phys. Lett. A*, 362 (2007) 471

172 B K Barick, K K Mishra, A K Arora, R N P Choudharyand Dillip K Pradhan, *J. Phys. D: Appl. Phys*., 44 (2011) 355402.

173 O.Raymond, R.Font, N.S.Almodovar, J. Portellesand J.M.Siqueiros, *J. Appl.Phys.* 97 (2005) 084107.

174 W. Krauss, D Schutz, F.A.Mautner, A. Feteira, K.Reichnamm, *J Euro. Ceram.Soc.*, 30 (2010) 1827.

175 Y.A. Abramov, V.G. Tsirelson, V.E. Zavodnik, S.A. Ivanov, I.D. Brown, *Acta*

Crystallogr. B, 39 (1983) 942.

176 V.M. Longo, M.G.S. Costa, A.Z Simões, I.L.V. Rosa, C.O.P. Santos, J. Andrés, E. Longo,J.A. Varela, *Phys. Chem. Chem. Phys*., 12 (2010) 7566.

177 L.S. Cavalcante, V.S. Marques, J.C. Sczancoski, M.T. Escote, M.R. Joya, J.A. Varela, M.R.M.C. Santos, P.S. Pizani, E. Longo, *Chem. Eng. J.*, 143 (2008) 299.

178 L.S. Cavalcante, J.C. Sczancoski, F.S. De Vicente, M.T. Fabbro, M.S. Li, J.A. Varela, E. Longo, J. *Sol-Gel Sci. Technol.,* 49 (2009) 35.

179 S.K.Rout, L.S.Cavalcante, J.C.Sczancoski, T.Badapanda, S.Panigrahi, M.SiuLi, E.Longo, *Physica B*, 404 (2009) 3341.

180 T. wang, H. Du, X. Shi, *J. Phys: Conference Series*, 152 (2009) 012065.

181 D. Lin, K.W. Kwok, H.L.W. Chan, *J. Alloys Compd.,* 481 (2009) 310.

182 Y. Hiruma, Y. Imai, Y. Watanabe, H. Nagata, T. Takenaka, *Appl. Phys. Lett*., 92 (2008) 262904.

183 D. Viehland, S.J. Jang, L.E. Cross, M. Wuttig, *J. Appl. Phys*., 68 (1990) 2916.

184 S.K. Rout, P.K. Barhai, S. Panigrahi, I.W. Kim, J. Electroceram., 23 (2009) 37.

185 J. Bera, S.K. Rout, J. Electroceram., 18 (2007) 33.

186 L.I. Maissel, R. Glang, "*Handbook of Thin Film Technology*", McGraw-Hill, New York, Chap. 16; (1970).

187 S. Selvasekarapandian and M. Vijaykumar, *Mater. Chem. Phys.,* 80 (2003) 29.

188 C. K. Suman, K. Prasad and R. N. P. Choudhary, *J. Mater. Sci.,* 41 (2006) 369.

189 S. K. Barik, P. K. Mahapatra and R. N. P. Choudhary, *Appl. Phys. A*, 85 (2006) 199.

190 N. Lei, M. Zhu, P. Yang, L. Wang, L. Wang, Y. Hou, H. Yan, J. Appl. Phys., 109 (2011) 054102.

191 P. Jaita, A. Watcharapasorn, S. Jiansirisomboon, *Curr. Appl. Phys*., 11 (2011) 77.

192 R. Dittmer, W. Jo, J. Daniels, S. Schaab, *J. Am. Ceram. Soc.*, 94 (2011) 4283.

193 Q. Zhou, C. Zhou, W.Z. Li, J. Cheng, H. Wang, C. Yuan, *J. Phys. Chem. Solids*, 72 (2011) 909.

194 J. Yoo, D. Oh, Y. Jeong, J. Hong, M. Junge, *Mater.Lett.*,58 (2004) 3831.

195 S.E.Park and S.J. Chung, *Proceedings of the* 9*th IEEE International Symposium*, ISAF'94, (1994) 265.

196 Y.F Liu, Y.N. Lv, M. Xu, S.Z Shi, H.Q. Xu, and X.D. Yang, J. Wuhan Univ. *Technol.-Mater. Sci. Ed.*, 22 (2) (2007) 315

197 B.W.V. Eerd, D. Damjanovic, N. Klein, N. Setter, J. Trodahl, *Phys. Rev. B*, 82 (2010) 104112.

198 J.Kreisel, A.M.Glazer, G.Jones, P.A.Thomas, L.Abllo and G.Lucazeau, *J. Phys: Condens. Matter.*, 12 (2000) 3267.

199 M.S. Zhang, J.F. Scott, *Ferroelectr. Lett.*,6 (1986) 147.

200 A.S. Barker, A.J. Sievers, *Rev. Mod. Phys.*, 47 (1975) *S1–S179.*

201 J. Kreisel, B. Dkhil, P. Bouvier, J.M. Kiat, *Phys. Rev. B*, 65 (2002) 172101.

202 J.A. Sanjurjo, E. Lopez-Cruz, *Phys. Rev. B*, 28 (1983) 7260.

203 M.E. Marssi, R. Farhi, X. Dai, A. Morell, D. Viehland, *J. Appl. Phys*., 80 (1996) 1079.

204 H. Uwe, K.B. Lyons, H.L. Carter, P.A. Fleury, Phys. Rev. B, 33 (1986) 6436.

205 R.M.German, "*Liquid Phase Sintering"*, Plenum Press, New York (1985).

206 X. H Dai, A. Digiovanni, and D. Viehland, *J. Appl. Phys.*, 74 (1993) 3399.

207 M. S Yoon,H. M. Jang and S.Kim, *Jpn. J. Appl. Phys.*, 4 (1995) 1916.

208 P.R. Chowdury, and S.B. Deshpande, *Indian J. Pure Appl. Phys.*, 22 (1984) 708.

209 R.L. Nagai and C. Leon, *Solid State Ionics*, 125 (1999) 81.

210 P. Pisssis and A. Kyritsis, *Solid State Ionics*, 97 (1997) 105.

211 V.V. Shilov, V.V. Shevchenko, P. Pissis, A. Kyritsis, G. Georgeoussis, Y. Gommza, S.D. Nesin and N.S. Klimenko, *J. Non-cryst. Solids*, 375 (2000) 116.

212 D.L. Sidebottom, P.F. Green and R.K. Brow. *J. Non-cryst. Solids*, 151 (1995) 183.

213 A. Kumar, B.P. Singh, R.N.P. Choudary, and A.K. Thakur, *J. Alloys Compd.*, 394 (1-

2) (2005) 292.

214 B.A. Scott, E.A. Geiss, B.L. Olson, G. Burns, A.W. Smith, and D.F. O'Kane, *Mater. Res. Bull.*, 5(1) (1970) 47.

215 F. A. Kroger, and H. J. Vink, *Solid State Phys.*, 3 (1956) 307.

216 X. Wang, H. L. W. Chan and C. l. Choy, *Solid State Commun.* 125 (2003) 395.

217 http://polyhedra.org/poly/show/71/triangular-rthobicupola.

218 http://polyhedra.org/poly/show/2/octahedron.

219 C.H. Wang, *J. Ceram. Soc. Jpn*., 116 (2008) 632.

220 P. Kubelka, F. Munk-Aussig, *Zeit.Fur.Tech. Physik*, 12 (1931) 593.

221 M.L. Myrick, M.N. Simcock, M. Baranowski, H. Brooke, S.L. Morgan, J.N. Mccutcheon, *Appl. Spectrosc. Rev.*, 46 (2011) 140.

222 R.A. Smith. *Semiconductors*, 2nd edition. Cambridge University Press, London, (1978) 434.

223 M. Zeng, S. Wing, H.L.W. Chan, *J. Appl. Phys*., 107 (2010) 043513.

224 M. Bousquet, J.R. Duclère,, E. Orhan, A. Boulle, C. Bachelet, C. Champeaux, *J. Appl. Phys*., 107 (2010) 104107.

225 L.S. Cavalcante, M.F.C. Gurgel, A.Z. Simões, E. Longo, J.A. Varela, M.R. Joya, P.S. Pizani, *Appl. Phys. Lett.*, 90 (2007) 011901.

226 D.L. West, D.A. Payne, *J. Am. Ceram. Soc*., 86 (2003) 1132.

227 A.J. Moulson, J.M. Herbert, "*Eletronic Ceamic Materials and their Applications"*, Chapman and Hall, London, (1990).

228 S.K. Rout, Ali Hussian, J.S. Lee, I.W. Kim, S.I.Woo, *J. Alloys Compd.*, *477* (2009) 706.

229 Alo Dutta, T.P. Sinha, Phys. Rev. B, 76 (2007) 155113.

230 B.Behera, P.Nayak and R.N.P.Choudhary, *Mater. Res. Bull*., 43 (2008) 401.

231 B.Behera, P.Nayakand R.N.P.Choudhary, *J. Alloys Compd*., 436 (2007) 226.

232 C.K. Suman, K. Prasad, R.N.P. Choudhary, *Adv. Appl. Ceram.*, 104 (2005) 294.

233 S.Sen, P.Pramanik and R.N.P.Choudhary, Physica B, 52 (2007) 387.

234 Y. Feldman, A. Puzenko, Y. Ryabov, Chem. Phys., 284 (1-2) (2002) 139.

235 M. A. L. Nobre, S. L. Fredi, *Mater .Lett*.,50 (2001) 322.

236 M. A. L. Nobre, S. L.Fredi, *J. Phys. Chem Solids,* 62 (2001) 1999.

237 M. A. L. Nobre, S. L. Fredi, *Matter. Lett*.,47 (2001) 362.

238 L. DESSEMOND, Thesis, Grenoble, (1992).

239 S. Saha, T.P. Sinha, Phys. Rev. B, 65 (2002) 134103.

240 K. S. Rao, P. M. Krishna, D.M. Prasad, D. Gangadharudu, *J. Mater. Sci.*, 42 (2007) 4801.

LIST OF PUBLICATION/ACCEPTED/COMMUNICATED PAPERS BASED ON THE RESEARCH WORK

1 **B.Parija**, T.Badpanda, V.Senthil, S.K.Rout, S.Panigrahi and T.P.Sihna "Diffuse phase transition, Piezoelectric and Optical study of $Bi_{0.5}Na_{0.5}TiO_3$ ceramic", ***Bull. Mater. Sci.,*** **35 (2) (2012) 197**.

2 **B.Parija**, T.Badpanda, S.K.Rout, S.Panigrahi and T.P.Sihna, "Dielectric dispersion and impedance spectroscopy of lead-free $(Bi_{0.5}Na_{0.5})TiO_3$ ferroelectric ceramics", ***Phys. Express,*** **2 (2012) 21.**

3 **B.Parija**, T.Badpanda, S.Panigrahi and T.P.Sihna, "Morphotropic phase boundary and dielectric relaxation study of $(Bi_{0.5}Na_{0.5})TiO_3$-$BaTiO_3$ Lead-Free Ceramic", ***J. Adv. Dielectric.,*** **2 (2) (2012) 1250008**.

4 **B.Parija**, T. Badapanda, S. Panigrahi1, T.P.Sinha "Ferroelectric and Piezoelectric properties of $(1-x)(Ba_{0.5}Na_{0.5})TiO_3$-$xBaTiO_3$ Ceramics", ***J. Mater. Sci.: Mater. Electron., (2013) 24:402-410.***

5 **B.Parija** and S. Panigrahi,"Impedance and AC Conductivity Study of $(Bi_{0.5}Na_{0.5})TiO_3$-$Ba(Zr_{0.25}Ti_{0.75})O_3$ Lead-Free Ceramics", ***Ferroelectrics Lett.,*** **39 (1-3) (2012) 38-55.**

6 **B.Parija**, and S.Panigrahi, "Impedance-Spectroscopy Analysis of $(1-x)(Bi_{0.5}Na_{0.5})TiO_3$-$xSrTiO_3$ Lead-free ceramic systems", ***Asian J. Phys***., (**Accepted**).

7 **B.Parija,** T. Badapanda, S.K.Rout, S. Panigrahi, L.S.Cavalcante, E. Longo, T.P.Sinha, "Structural, Electrical and Optical study of $(Bi_{0.5}Na_{0.5})TiO_3$-$Ba(Zr_{0.25}Ti_{0.75})O_3$ lead free piezoelectric ceramics" ***Ceramic International,*** **(Accepted).**

8 **B.Parija**, S.K. Rout, L.S Cavalcante, A.Z. Simões, S. Panigrahi, E. Longo, "Structure, microstructure and dielectric properties of $(1-x)(Bi_{0.5}Na_{0.5})TiO_3$-$xSrTiO_3$ composites ceramics" ***Appl. Phys. A,*** **109 (3) (2012) 715-723.**

REVIEW PAPERS

1 **B.Parija** and S.Panigrahi, "Lead-Free Piezoceramic: A Review", ***PCE Journal,*** **1 (2010) 53.**

2 **B.Parija** and S.Panigrahi, "A brief review on Lead-free Bismuth Sodium Titanate (BNT) based ceramics", ***PCE Journal,*** **(Accepted).**

CONFERENCE PAPERS

1 **B.Parija**, T.Badpanda, S.K.Rout, and S.Panigrahi, "Synthesis and characterization of $(Bi_{0.5}Na_{0.5})TiO_3$ by solid-state reaction method". *[Presented, National Conference on **CMDAYS** on August 26-28, 2009 at Jadavpur University, Kolkata]*.

2 **B.Parija** and S.Panigrahi, "Sources of Lead-poissionic and its prevention in present society". *[Presented, National Conference on **Advances in Environmental Engineering** on November 14-15, 2009 at NIT, Rourkela]*.

3 **B.Parija**, T.Badpanda, V.Senthil, S.K.Rout, and S.Panigrahi, "Impedance Spectroscopy Study of Lead-Free Perovskite $(Bi_{0.5}\ Na_{0.5}\ )TiO_3$ ceramic" *[Presented, National Conference on **CMDAYS** on August 24-26, 2011 at Gauhati University, Gauhati, Assam, India]*.

4 **B.Parija**, T.Badpanda, V.Senthil, and S.Panigrahi "Ferroelectric, piezoelectric and optical properties of $(Bi_{0.5}Na_{0.5})TiO_3$–$Ba(Zr_{0.25}Ti_{0.75})O_3$ Lead-Free Ceramics". *[5th International Conference on **Electroceramics,** Sydney, **Australia**, December 12-16, 2011, University of New South Wales, P12]*.

5 **B.Parija**, T.Badpanda, and S.Panigrahi, "Impedance-Spectroscopy Analysis of $(1-x)(Bi_{0.5}Na_{0.5})TiO_3$-$xSrTiO_3$ Lead-free ceramic systems", [**PTNM** II-2012, March 10-11, 2012, Sambalpur University, PP-05].

6 **B.Parija,**M.R.Kar, P.K.Sahu, T.Badpanda, S.K.Rout, S.Panigrahi, "Phase transition in $(Bi_{0.5}Na_{0.5})TiO_3$-$BaTiO_3$ solid-solutions"*[Presented, National Conference on **CMDAYS** on August 29-31, 2012 at BIT, Mesra, Ranchi, Orissa, India]*.